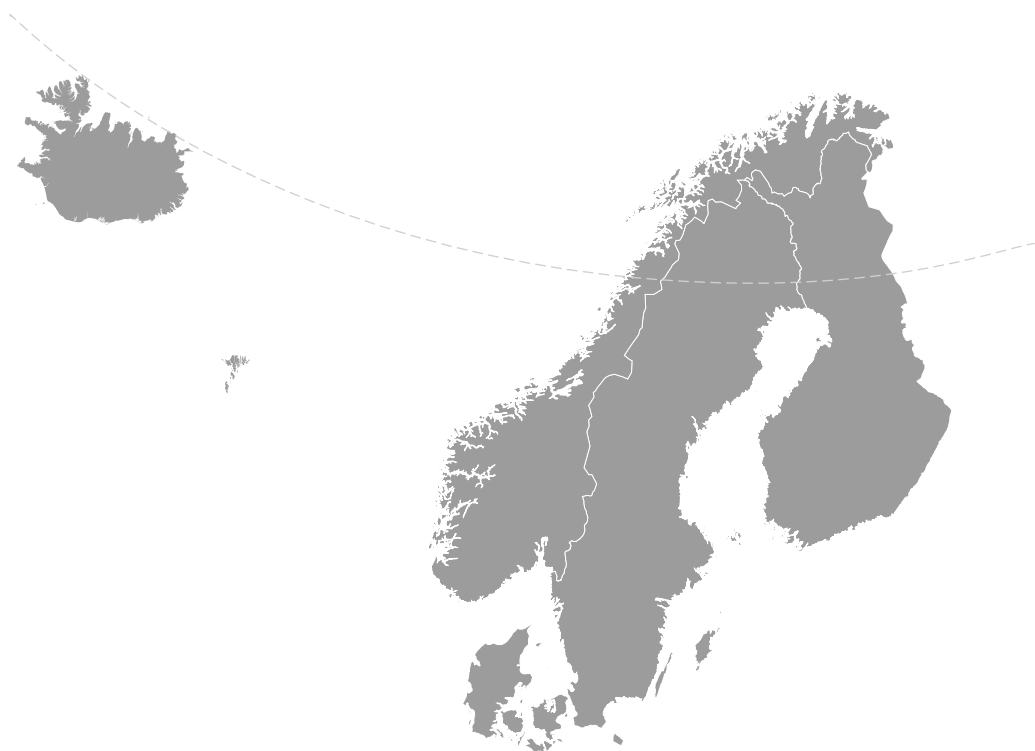


Nordic Concrete Research



Nordic
Concrete
Federation

PUBLICATION NO. 49 1/2014

NORDIC CONCRETE RESEARCH

**EDITED BY
THE NORDIC CONCRETE FEDERATION**

**CONCRETE ASSOCIATIONS OF: DENMARK
FINLAND
ICELAND
NORWAY
SWEDEN**

**PUBLISHER: NORSK BETONGFORENING
POSTBOKS 2312, SOLLI
N - 0201 OSLO
NORWAY**

VODSKOV, JUNE 2014

Preface

Nordic Concrete Research is since 1982 the leading scientific journal concerning concrete research in the five Nordic countries, e.g., Denmark, Finland, Iceland, Norway and Sweden. The content of Nordic Concrete Research reflects the major trends in the concrete research.

Nordic Concrete Research is published by the Nordic Concrete Federation which also organizes the Nordic Concrete Research Symposia that have constituted a continuous series since 1953 in Stockholm. The Symposium circulates between the five countries and takes normally place every third year. The next symposium, no. XXII, will be held Reykjavik, Iceland 13 - 15 August 2014, in parallel with the ECO-CRETE conference. More information on the research symposium can be found on www.rheo.is. More than 110 papers will be presented.

Since 1982, 414 papers have been published in the journal. Since 1994 the abstracts and from 1998 both the abstracts and the full papers can be found on the Nordic Concrete Federation's homepage: www.nordicconcrete.net. The journal thus contributes to dissemination of Nordic concrete research, both within the Nordic countries and internationally. The abstracts and papers can be downloaded for free.

The high quality of the papers in NCR are ensured by the group of reviewers presented on the last page. All papers are reviewed by three of these, chosen according to their expert knowledge.

Since 1975, 76 Nordic Miniseminars have been held – it is the experience of the Research Council of the Nordic Concrete Federation, that these Miniseminars have a marked influence on concrete research in the Nordic countries. In some cases, the information gathered during such Miniseminars has been used as Nordic input to CEN activities. The latest Miniseminar concerning Alkali Silica Reactions was held in Riga in an attempt to involve the Baltic countries in our Nordic activities.

We look forward to welcome You to the XXII Nordic Concrete Research Symposium in Reykjavik 13. - 15. August 2014.

Vodskov, June 2014

Dirch H. Bager
Editor, Nordic Concrete Research

Reykjavik, June 2014

Olafur H. Wallevik
Chairman, Research Council of the Nordic Concrete Federation &
Chairman of the Organizing Committee for the XXII Research Symposium

CONTENTS

1	Gunvor Marie Kirkelund, Mette Rica Geiker & Pernille Erland Jensen Electrodiallytically Treated MSWI APC Residue as Substitute for Cement in Mortar	1
2	Oldrich Svec, Lars Nyholm Thrane & Henrik Stang Linking the Fibre Orientation Factor with the Mechanical Response of the fibre reinforced Self-compacting Concrete	17
3	Ya Peng, Klaartje de Weerd, Bård Pedersen & Stefan Jacobsen Measuring sedimentation and bleeding of fresh paste with hydrostatic pressure	27
4	Mahdi M. Kioumars, Max A.N. Hendriks & Mette R. Geiker Quantification of the interference of localised corrosion on adjacent reinforcement bars in a concrete beam in bending	39
5	Håvard Nedrelid & Terje Kanstad Shear Resistance of Steel-Fibre Reinforced RC Beams with Small Circular Openings	59
6	Richard Mc Carthy & Johan Silfwerbrand Is It Possible to Predict Formwork Pressure When Using SCC? – A Field Study	73
7	Jonas Carlsvärd & Mats Emborg Avoiding undesirable end results of bonded steel fibre concrete overlays – observations from tests and theoretical calculations	93
8	Björn Täljsten, Gabriel Sas & Thomas Blanksvärd Strengthening of concrete structures with FRP – a guideline	113
9	Anders Hösthagen, Jan-Erik Jonasson, Mats Emborg, Hans Hedlund & Kjell Wallin Thermal Crack Risk Estimations for Tunnel - Equivalent Restraint Method Correlated to Empirical Observations.	127
10	Dimitrios Boubitsas & Tang Luping Electrochemical monitoring of Corrosion Initiation of Reinforcement Steel in Concrete and Chloride Threshold Values	145
11	Martin Persson, Ulf Ohlsson & Mats Emborg Bridge deck concrete overlays – full scale studies	163
12	Arezou Babaahmadi, Luping Tang & Zareen Abbas Mineralogical, Physical and Chemical Characterization of Cementitious Materials Subjected to Accelerated Decalcification by an Electro-Chemical Method	181
	Research Council and Editorial Board of NCR	199
	Review Group for NCR	201

Electrodiallytically Treated MSWI APC Residue as Substitute for Cement in Mortar



Gunvor Marie Kirkelund
PhD, Researcher
Department of Civil Engineering
Technical University of Denmark
DK – 2800 Lyngby
E-mail: gunki@byg.dtu.dk



Mette Rica Geiker
PhD, Professor
Department of Structural Engineering
Norwegian University of Science and Technology
Richard Birkelands Vei 1a
N – 7491 Trondheim
E-mail: mette.geiker@ntnu.no



Pernille Erland Jensen
PhD, Associate Professor
Department of Civil Engineering
Technical University of Denmark
DK – 2800 Lyngby
E-mail: pej@byg.dtu.dk

ABSTRACT

Air pollution control (APC) residues from municipal solid waste incineration (MSWI) are considered hazardous waste and need pre-treatment prior to possible reuse. Here, two MSWI APC residues, from which the most mobile fraction of heavy metals and salts has been removed by carbonation and/or electrodialytic remediation, were used in Portland cement mortar. Mortar bars with 15 % weight replacement of cement by APC residues showed compressive strengths up to 40 MPa after 28/32 days. Heavy metal and salt leaching from both crushed and monolithic mortars with APC residues was generally similar and comparable to both the reference mortar and mortar with coal fly ash. These results indicate that electrodialytic remediation could be used a pre-treatment method for MSWI APC residues prior to reuse in mortar.

Keywords: electrokinetic remediation, mortar, leaching, fly ash, heavy metal

1. INTRODUCTION

In Denmark municipal solid waste incinerators (MSWI) have air pollution control (APC) systems which generate residues with a high content of salt and leachable heavy metals. Currently, MSWI APC residue is classified as hazardous waste and stabilized and disposed of abroad. Current practice in other countries are either temporary disposal until a treatment method has been found or permanent disposal in hazardous waste landfills, often with pre-treatment (solidification, stabilisation or extraction) of the APC residue [1].

Contrarily to the MSWI APC residue, fly ash from coal combustion is considered a valuable resource to be used in production of cement and as a supplementary cementitious material (SCM) in mortar and concrete. Mortar consists of binder (cement), water and fine aggregate (sand) at a given ratio and is the basis for concrete which is a mix of mortar and coarse aggregate. Up to 5 % of the total global anthropogenic CO₂ is emitted by Portland cement production and the replacement of Portland cement by other binders such as industrial by-products have gained increasing interest [2]. MSWI fly ash or APC residues could potentially be used as binder in mortar and concrete [3], but the content of heavy metals restricts/limits this possibility, mainly due to their mobility [4]. Only a few studies have been made where MSWI APC residue is tested for direct reuse in mortar and concrete, most studies report results for fly ash, without the APC products [1].

Pre-treatment of MSWI APC residues prior to reuse has shown to be difficult, as the method should be able to keep the desired material characteristics and treat the contaminants. Generally two approaches are considered when treating heavy metals in MSWI APC residues prior to potential reuse: stabilization or extraction of heavy metals. Stabilization methods include carbonation, thermal treatments or chemical stabilizations, such as stabilization with phosphates, chelating agents or ferrous compounds. In stabilization, the material characteristics are only altered slightly and the heavy metals are still present in the same quantity but are less available [1, 4]. Extraction techniques include different washing and chemical extraction methods. Acid washing is efficient for removing heavy metals, but drastically alters the pH and material characteristics [1, 4].

An electrodialytic (ED) upgrading method, where the mobile fraction of heavy metals is removed by an electric current at the MSWI APC residues' original alkaline pH, has shown potential for reducing heavy metal and salt leaching and keeping an alkaline pH in the MSWI APC residue both bench [5] and pilot scale [6]. The principle of electrodialytic (ED) upgrading is illustrated in Fig. 1.

ED is widely used e.g. for desalination of solutions in industrial scale, but not for suspensions of solid matter. MSWI APC residues in suspension (up to 10% DM) have been subjected to ED. The ED system consists of an ED stack with multiple concentrate compartments (concentrate) and compartments containing the APC residue suspension (diluate). The concentrate and the diluate are pumped through the ED stack and the compartments are separated by ion exchange membranes and anions and cations from the diluate are removed to the concentrate by the applied current. Dewatering is required prior to reuse of the upgraded APC residue as a constituent in construction materials.

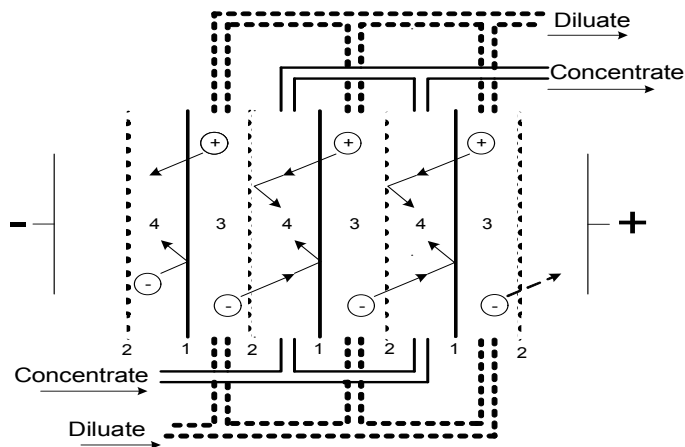


Figure 1 – Principle of electrochemical upgrading of APC residue. 1/2- ion exchange membranes, 3- diluate compartments, 4- APC residue suspension (diluate) compartments

ED differs from another treatment set-up developed by the same research group by aiming at lower final metal leaching while maintaining the alkaline pH instead of obtaining the highest possible heavy metal removal. The latter may be time-consuming and take weeks [7, 8] and result in high matrix changes by either acidification of the residue [9] or by the addition of chemical complexing agents. Although few studies of the electrochemical method have focused on reducing heavy metal leaching instead of the total content, those that exist indicate that this can be achieved with treatment times in the order of hours, simultaneously reducing the salt concentration significantly [5, 6]. This last approach was recently also recommended by Lima et al. [10].

In this paper, the properties of MSWI APC residues after electrochemical upgrading were studied to evaluate if the residues can qualify as secondary resources and if the electrochemical upgrading method has potential as a pre-treatment method prior to reuse. Focus was on the technical and environmental properties of the electrochemically upgraded residue as a secondary raw material that could partially replace Portland cement in mortar.

2. MATERIALS AND METHODS

2.1 Experimental APC residue

Five experimental APC residues were used in this study:

- Coal: coal fly ash from Dong Energy A/S, Avedøreværket blok 1.
- Raw: raw semi-dry MSWI APC residue. The residue was collected after a semi-dry flue gas cleaning process from a Danish waste incineration plant, REFA I/S.
- Carb: raw MSWI APC carbonized by letting it react with atmospheric CO₂ under humid conditions.
- EDU: raw MSWI APC residue upgraded in electrochemical pilot scale experiments according to Kirkelund et al. [6]

- EDUcarb: carbonized MSWI APC residue upgraded in an electrodialytic pilot scale experiment according to Kirkelund et al. [6].

2.2 Analytical procedures

Total heavy metal and minor element concentrations (Al, As, Ba, Cd, Cr, Cu, Mn, Ni, Pb, Zn) in the APC residue were measured by ICP-OES (induced coupled plasma – optical emission spectrometry) after pre-treatment by DS259 [11] where 1 g of APC residue and 20 ml 7.3 M HNO₃ were heated at 200 kPa (120°C) for 30 min. The liquid was subsequently separated by vacuum filtration through a 45 µm filter and diluted to 100 ml. The units used in this paper are mg/kg for concentrations in dry matter. Major oxide composition was estimated from semi-quantitative analysis by X-ray fluorescence (XRF) on powder samples. Loss on ignition was measured after heating at 550°C for one hour. The pH was measured in 1 M KCl at a liquid-to-solid ratio (L/S) of 5 and after 1 hour of agitation, pH was measured by a Radiometer Analytical pH electrode. The amount of water soluble APC residue was estimated as mass reduction when mixing 1 g APC residue with 20 ml distilled water, agitated for 24 hours.

Leaching experiments were made according to DS/EN 12457-3 part 1 [12] at L/S 2, mixing 40 g APC residue and 80 ml distilled water. The suspension was shaken for 6 hours on an end-over shaker before vacuum filtration through a 45 µm filter and the filtrate was divided into two subsamples. One subsample for analysis of anions (Cl, SO₄) by ion chromatography (IC) and the other subsample was acidified by addition of concentrated HNO₃ before analysis of heavy metals and minor elements on ICP-OES.

Scanning electron microscope (SEM) and energy-dispersive X-ray spectroscopy (EDX) analyses for main morphology were performed on the samples. For the SEM/EDX analysis, a small subsample of the residue (<0.5 g) was placed directly on carbon tape. No further pre-treatment of the samples was made. The accelerating voltage of the SEM was 30 keV with large field detector (and X-ray cone). Different areas of the samples were investigated by SEM and the element distribution was examined by element mapping using EDX on unpolished samples. Residue mineralogy was studied by X-ray powder diffraction (XRD), for identification of major crystalline phases. The instrument was a PANalytical X'Pert Pro operating at 45 kV and 40 mA applying Cu K α radiation with a 2 Θ X'Celerator detector. The samples were scanned in the range of 4-100 2 Θ within 8 hours. The diffractograms were interpreted using the ICDD PDF-4 database for minerals.

2.3 Mortar

For preparation of mortar, low alkali sulphate resistant cement (CEM I 42.5 N) from Aalborg Portland and 0/4 mm quartz sand of class E from RN Sten & Grus, Hvidovre, Denmark were used. The mortar was mixed according to EN 196-1 [13] at a water/binder-ratio of 0.5 and a sand/cement ratio of 3 (reference mix). The cement was substituted 15 % by weight with APC residue, which is within the acceptable replacement range between 5-25 % from previous studies [10, 14, 15]. Six experimental mortars were made, five with substitution of the different APC residues and a reference mortar without APC residue. The 6 cm · 12 cm cylindrical mortar bars were cast in PEH molds and demolded after 1 day. The mortars were cured in separate water baths to avoid cross contamination.

Compressive strength was tested after 7 and 28 days at 20°C on mortars prepared and cured according to DS/EN 12390-3 [16] in triplicate for each mortar, except for the raw and EDU which was tested after 32 and 56 days. Adiabatic heat development was measured after DS 423.37 [17] with slight modifications on reference, coal, raw, EDU and EDUcarb mortars continuously during 7 days after mixing. For simple workability assessment, slump tests by using a 75 mm cone were made on the reference, raw, EDU and EDUcarb mortars according to Bartos [18].

Leaching experiments were made on crushed and monolithic (ca. 3 cm · 3 cm) samples of the mortar cured for 28/32 days following the same procedure as for the APC residues. Leaching of the crushed samples represents the worst case scenario if the material is disposed of after its service life and monolithic samples represent leaching that could occur during service life time [15]. The mortars were stored in sealed bags at room temperature until the leaching experiments were made.

3. RESULTS AND DISCUSSION

3.1 APC residue characteristics

APC residue characteristics for the five residues are shown in Table 1. The minor element concentrations in the MSWI APC residues were generally higher than in the coal residue. This was expected due to the different fuel conditions during incineration. Up to 50 % of the residue was water soluble. This explains why the metal concentrations in the ED upgraded residues were higher than in the untreated: when the residues are mixed with water, soluble salts dissolve and are removed; and even though parts of the metals are removed by the electro-dialytic treatment, the total concentration increases due to the larger decrease in total mass.

The results for major elements confirmed the difference in composition between the coal fly ash and the APC residues. The APC residues, as also seen by other authors consist mainly of Ca and Cl [19, 20], which is due to addition of lime during the acid gas cleaning. Also, the Ca concentration was 10 times higher in the MSWI residues than the coal fly ash and almost half of the content of what is be found in cement [15]. The sulfate content increased when the APC residues were electro-dialytically treated and the Na, K and Cl content decreased. The Cl content in the ED upgraded residues were, however, still a factor 10 higher than in the coal residue. High chloride content in MSWI APC residue is considered a limiting factor for reuse as Cl can cause corrosion in reinforced steel [21]. The limit for reuse in mortar according to DS/EN 450 [22] is a chloride content below 0.1 %, which could be met for the upgraded MSWI APC residues by adjusting the electro-dialytic treatment process [6].

Due to the carbonation processes, pH in the Carb and EDUcarb samples was two pH units lower than in the coal, raw and EDU residues, which is due to the introduction and further reaction of H_2CO_3 in the residue [23]. Despite the carbonization and electro-dialytic upgrading, all residues were alkaline. The loss on ignition (LOI) of the carbonized residues were higher than of the raw, probably due to bound lattice water in the carbonized residues, as the LOI results would be expected to be in the same range as the raw and EDU samples. Lattice water is removed when heating a sample between 450-600 °C [24] and will not be removed by the temperature used for drying (105°C) prior to LOI analysis. The limit value for LOI is maximum 9% according to DS/EN 450 [22], which was met by the coal, Raw and EDU samples.

Table 1 – Characteristics of the different APC residues.

	Parameter	Coal	Raw	Carb	EDU	EDUcarb
Minor element content (mg/kg)	LOI (%)	1.6	0.7	8.1	0.9	9.5
	Water solubility (%)	11	42	50	20	13
	pH _{KCl}	12.5	12.2	10.0	12.4	9.9
	Al	26,450	23,450	14,050	22,650	20,000
	As	24.3	127	138	192	257
	Ba	1,100	370	349	448	299
	Cd	1.5	170	190	245	287
	Cr	45.7	93	96	150	196
	Cu	31.7	575	572	807	744
	Mn	198	411	372	664	603
	Ni	31.7	32	30	47	142
	Pb	19.1	2,200	3,150	2,150	4,400
	Zn	87.7	14,650	20,200	21,600	32,400
Major oxide content (%)	CaO	7.0	64.4	36.4	40.6	43.4
	Na ₂ O	1.8	10.2	7.1	0.7	0.7
	K ₂ O	2.9	7.7	3.1	0.4	0.4
	SO ₃	1.3	6.2	5.2	12.5	10.2
	Al ₂ O ₃	22.7	2.1	2.1	3.0	3.8
	Si ₂ O	53.5	2.6	3.0	7.1	7.7
	Fe ₂ O ₃	7.6	1.0	0.8	1.2	1.6
	MgO	2.2	0.6	0.3	1.4	1.3
	MnO	0.05	0.06	0.04	0.08	0.09
	P ₂ O ₅	0.7	0.2	0.1	0.7	0.8
	TiO ₂	1.0	0.7	0.4	0.8	1.0
	Cl	0.01	24	19	0.7	0.4

Leaching of heavy metals and salts from the different residues is shown in Table 2, together with the Category 3 values for leaching and these values represent the maximum allowed values for reuse of waste materials in construction [25]. The results from leaching and the discussion on the effect of the carbonization and the electrodialytic treatment have been presented previously [6]. The conclusions from this study regarding leaching, which is also apparent in Table 2, are:

- Carbonization leads to increased Cd, Cr and Cu leaching but a reduces leaching of other heavy metals, especially Pb and Zn
- Electrodialytic upgrading of both the raw and carbonized APC residue significantly reduces the leaching of most heavy metals, except Cr which increases.
- Cl leaching is drastically reduced due to electrodialytic upgrading

Table 2 – Element leaching from the residues. *N.m.* – not measured. ^a[6].

Element	Coal	Raw ^a	Carb ^a	EDU ^a	EDUcarb ^a	Category 3 [25]
pH _{leachate}	12.3	12.0	9.0	12.3	8.3	-
Al (mg/l)	2.6	n.m	3.0	n.m	0.4	-
As (µg/l)	<25	110	<25	<25	<25	50
Ba (mg/l)	0.7	34	17	0.45	0.1	4
Cd (µg/l)	1.2	22	1,860	0.1	0.7	40
Cr (mg/l)	1.0	0.06	0.9	0.24	1.6	0.5
Cu (µg/l)	7.0	2.9	833	15.3	8.8	2000
Mn (µg/l)	<25	<25	<25	<25	<25	1000
Ni (µg/l)	<25	<25	<25	<25	<25	70
Pb (µg/l)	31	535,300	586	3,780	27	100
Zn(µg/l)	77	49,800	303	1,660	160	1500
Ca (g/l)	1.2	36	26	1.6	0.9	-
Na (g/l)	0.3	11.5	13.9	0.3	0.6	1.5
Cl (g/l)	0.003	88	84	2	1.3	3
SO ₄ (g/l)	0.04	1.3	0.7	1.1	1.8	4

Leaching of Cr increased significantly in both upgraded residues compared to the raw residues. This suggests a shift from Cr (III) to Cr (VI), the latter which is more mobile at alkaline conditions. Cr leaching in the coal residue also exceeded the values of category 3. Thus, according to the Category 3 guidelines none of the residues comply with the values regarding leaching. However, at the final pH of the ED treated compared to the untreated (Table 1), the difference in leaching could not be equally reduced just by pH alone, which could be seen from pH-dependent leaching experiments by Kirkelund et al. [6] for the same raw and carb APC residues. Gao et al. [26] found higher leached concentrations in waterwashed fly ash than was seen here for the EDUcarb, both samples which were similar in pH. This shows that the electrodialytic treatment is beneficial for reducing the leachability of heavy metals. Leaching behaviour of electrodialytically treated harbour sediments showed similar pH dependent leaching patterns before and after electrodialytic treatment, even if up to 95 % of heavy metals were removed, despite matrix changes of the sediment and a significant change of pH due to electrodialytic treatment [27]. Thus, further changes in the pH of the electrodialytic treated APC residues could change the leaching properties.

Scanning electron microscopy analysis (SEM) of the coal, raw, carb and EDU APC residues showed different morphology. Typical SEM images of the APC residues are shown in Fig. 2.

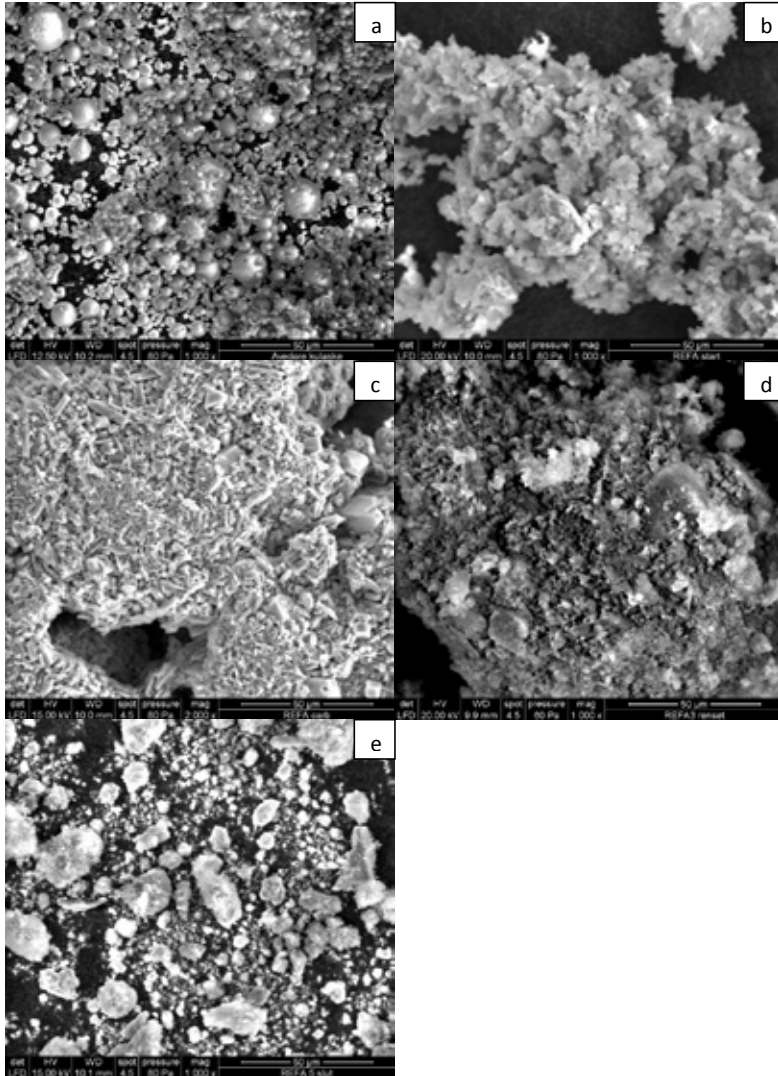


Figure 2 – SEM images of the APC residues, a) coal, b) raw, c) carb, d) EDU, e) EDUcarb

In the coal APC residue (Fig. 2 a) the typical spherical fly ash particles dominated. This finding was also seen by e.g. Brown et al. [28] who also showed that the elemental composition of the fly ash particles is dependent on coal feed and incineration temperature. The raw and the carbonated APC residue both consisted of particles of different sizes; however, agglomerates dominated the samples. The elemental mapping by SEM/EDX (results not shown) showed that the major constituents found in the raw and carbonized APC residue were O, Cl and Ca; while Ca, O and S were most abundant in the ED treated residues, which was also seen by the XRF analysis. The only distinct element overlap was seen in the raw and carb sample, by Na and K together with Cl. No clear overlapping patterns were found for heavy metal speciation. Fig. 2 b) shows a more granular and porous surface of the raw sample, with what looked like salts

between the grains, which changed to a more crystalline and less porous surface of the carbonated sample (Fig. 2 c). A similar change was also observed by Jiang et al. [29], where the crystallinity was caused by reaction products from the carbonization reaction. Both the raw and carbonized APC residue changed when electrochemically upgraded. The EDU residues lost some of the granularly and crystalline appearances, which could be due to the removal of soluble salts.

The XRD diffractograms are seen in Fig. 3. from where the major crystalline phases in the different APC residues are specified based on interpretation.

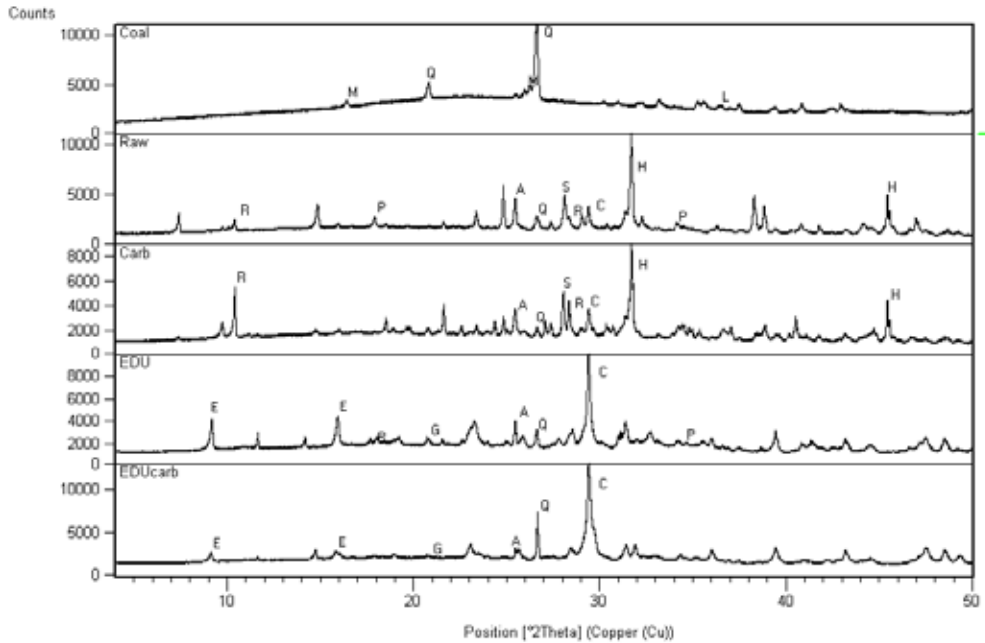


Figure 3 – XRD diffractograms with main minerals. M-mullite, Q-quartz, L-lime, R-richterite, P-portlandite, A-anhydrite, S-sylvite, C-calcite, H-hallite, E-ettringite, G-gypsum

The diffractograms for the MSWI residues were noisy due to the complex mineralogy and heterogeneity of the samples. The main minerals in the coal residue were identified as quartz, lime and mullite, which are typical minerals in coal fly ashes [28]. The main mineral compounds in the raw and carbonated residues were sylvite (KCl) and halite (NaCl) which were not identified in the ED upgraded residues. Contrarily to the coal APC residue, CaO was not identified as a Ca mineral in the MSWI residues, which was also expected as the acid gas treatment typically results in calcium carbonates, chlorides, hydroxides or sulphates. Thus, Ca minerals such as CaCO_3 , CaSO_4 , Ca(OH)_2 and $\text{CaSO}_4 \cdot \text{H}_2\text{O}$ were identified. Calcite (CaCO_3) and anhydrite (CaSO_4) were present in all the four MSWI residues, portlandite (Ca(OH)_2) was present only in the non-carbonized residues, and gypsum ($\text{CaSO}_4 \cdot \text{H}_2\text{O}$) only in the EDU treated residues. The peaks for calcite had higher counts in the ED upgraded residues which indicate

that carbonate was not dissolved during ED treatment. A further carbonation of the residue during ED treatment is also possible, which would produce more calcite. Also, the total Ca content was at similar level in the ED upgraded residues compared to the untreated. Richerite ($\text{Na}(\text{CaNa})\text{Mg}_5\text{Si}_8\text{O}_{22}(\text{OH})_2$) was most likely present in the raw and carbonated residues, but was not seen in the ED upgraded. Indications of formation of ettringite ($\text{Ca}_6\text{Al}_2(\text{SO}_4)_3 \cdot 26\text{H}_2\text{O}$) were seen after ED treatment and ettringite has been shown to effectively immobilize oxyanions such as Cr (VI) [30]. However, Cr was not stabilised by the ED treatment as the Cr leaching was higher in the residue after ED. This may suggest that ettringite could not immobilize Cr as seen by the other authors.

In the ED upgraded residues it was clearly seen that the soluble KCl and NaCl salts were removed by the ED process, which was also seen in another study where MSWI fly ash was investigated by XRD after EDR [31] and also corresponds with the reduced leaching. The final obtained Cl concentrations in the ED treated residues were lower (0.3 – 0.5 %) than what has been reported for simply washing MSWI fly ash by water (1.3 – 1.8 %) [26, 32]. Thus, ED treatment enhanced removal of chloride from MSWI APC residues compared to washing.

Water solubility of up to 20 % of the electrodialytically treated APC residue was seen, despite the significant removal of soluble minerals such as sylvite and halite. On the other hand, 11 % of the coal fly ash was also soluble. This suggests that there could be soluble phases also in the amorphous phase of the fly ash and APC residues, which could not be determined by the SEM/EDX.

3.3 Mortars

Compressive strength, heat development and workability

All the mortars containing APC residue exhibited lower compressive strength than the reference mortar (Table 3).

Table 3 – Compressive strength and slump test of mortars.

Mortar sample	Compressive strength (MPa)				Slump (mm)
	7 days	28 days	32 days	56 days	
Mref	35 ± 1	45 ± 3		56 ± 1	12.0
Mcoal	29 ± 2	42 ± 2		44 ± 2	
Mraw	27 ± 2		41 ± 0	41 ± 10	11.0
Mcarb	27 ± 1	26 ± 0			
MEDU	34 ± 1		40 ± 2	45 ± 1	7.5
MEDUcarb	31 ± 5	41 ± 6			4.5

The results showed a larger strength increase from 32 to 56 days for the reference mortar, but limited strength change for the mortars containing carb and EDUcarb residue. The compressive strength for the mortars with EDU, EDUcarb and coal residue were similar during the whole period and only slightly higher than the compressive strength of the mortar with raw residue. The only mortar which showed significantly lower strength after 28 days was the Mcarb mortar.

During the mortar mixing, it was observed that the workability decreased when MSWI APC was added. These observations were also confirmed by the slump test, see results in Table 3. The decrease in workability is most likely linked to the porosity of the APC residues, as was also observed to be higher in the MSWI residues than in the coal residue in the SEM analysis (Fig. 2). Porous particles will adsorb water in the mortar mix and reduce the workability, which should be compensated for by adding water or superplasticizer [28]. The workability of the mortar pastes increased when adding coal residue to the paste compared to the reference mortar paste without APC residues. Other factors than porosity influencing the workability could be the particle size, shape and surface characteristics. The circular shape of the coal APC residue was significantly different than the granular shape of the MSWI residues. The EDU residue showed higher workability than the EDUcarb residue, which also appeared more porous (Fig. 2d).

Metallic Al and sulphate in MSWI APC residue is regarded as important factors to lower compressive strengths when added in mortars due to crack formation [15]. However, the compressive strengths in this study are similar to what has been observed in other studies [10, 14, 15]. Contrary to Geiker et al. [14] no visible crack formation was observed in the mortars in this study. To make a contribution to reducing the CO₂ emissions from the concrete industry, it is necessary that the residues are substituting the cement and not the aggregate, even if aggregate substitution has shown better compressive strengths compared to reference, for untreated MSWI fly ash (e.g. [10]).

The heat development of the mortars is illustrated in Fig. 4.

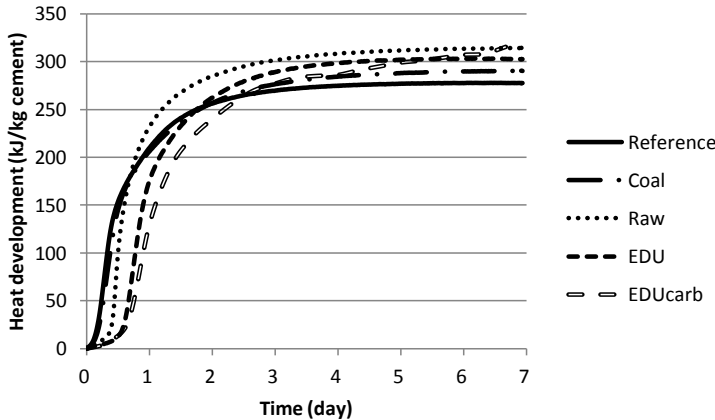


Figure 4 – Adiabatic heat development in mortars with and without fly ash and APC residues

The initial hydration was delayed in the mortars containing APC residue compared to the reference, but the highest heat acceleration period for all mortars occurred within the first days. The cumulative heat development measured within the first seven days was higher for all the mortars containing APC, which indicates that the APC either acted pozzolanic or induced a possible filler effect.

The initial setting times were found from the heat development curves, as the time where the extension of the linear part of the curve in acceleration period crosses the abscissa and found to be: reference (3 h); coal (3 – 4 h); raw (9 h), EDU (13 h) and EDUcarb (18 – 19 h). The initial setting times were delayed when adding APC residue to the mortar, however to a lesser extent than a similar study with MSWI APC residue from a wet process [14]. This indicates a dependence on the composition of the APC residue. Taylor [33] claims that salts of Pb and Zn as well as phosphates can cause hydration retardation. Soluble Zn can be a hydration retarder because it can form amorphous layers on cement grains and Pb has been observed to coat cement grains and precipitate on silicate surfaces [34]. It was seen that the observed setting times increased with increasing total Zn and Pb content. However, for the MSWI APC residues, the raw APC residue with the highest leachable amount of Zn showed the shortest delay of the two, which suggests that the formation of Zn(OH)_2 is not the controlling mechanism. Addition of Cl to mortars can act as an accelerator or retarder depending on the concentration for the initial hydration and according to Brough et al. [35] as an accelerator at concentrations below 4 %. Here, the contrary occurred; adding the upgraded MSWI APC residue with a low Cl content (0.4 – 0.7 %) retarded hydration compared to the raw MSWI APC residue with high Cl content (24 %). At present the combined effect of soluble components on the setting time is not well described.

Leaching from mortars

Leaching from mortars cured for 28/32 days are shown in Table 4. For most elements leaching from the crushed samples was higher than from the monolithic, except for Ca and Na. Substitution of cement by APC residues did not significantly increase metal leaching. The Danish legislation for the maximum leaching concentrations for disposing inert waste [36] is also seen in Table 4.

Table 4 – Element leaching ($\mu\text{g/l}$) from mortars cured for 28¹/32² days. A-Mref, B-Mcoal, C-Mraw, D-Mcarb, E-MEDU, F-MEDUcarb

Element	Crushed						Monolithic						Inert waste
	A ¹	B ¹	C ²	D ¹	E ²	F ¹	A ¹	B ¹	C ²	D ¹	E ²	F ¹	
pH	12.6	12.6	12.6	12.6	12.5	12.6	12.6	12.6	12.5	12.5	12.5	12.5	
Al	195	241	311	65	91	142	148	261	250	194	459	187	-
As	5	5	9	6	<5	<5	<5	14	11	<5	<5	6	50
Ba	1,700	2,100	900	4,900	500	3,100	1000	1,100	600	2,600	400	1,600	3500
Cd	<5	<5	<5	<5	<5	<5	<5	<5	<5	<5	<5	<5	15
Cr	28	18	20	6	41	14	33	21	17	7	31	12	100
Cu	16	13	28	<5	27	12	22	14	12	10	18	6	450
Mn	<5	<5	<5	<5	<5	<5	<5	12	<5	17	<10	6	-
Ni	7	7	<5	14	9	7	6	<5	<5	7	7	10	100
Pb	58	53	159	92	69	209	58	49	90	59	76	128	100
Zn	38	46	101	55	44	153	26	37	155	34	65	76	1000
Ca(mg/l)	750	690	1,370	1,184	747	753	701	716	978	1,111	734	775	-
Na(mg/l)	97	11	134	201	42	136	48	48	95	121	37	45	-
Cl (mg/l)	23	25	1,484	1,216	66	26	26	21	948	744	49	11	275
SO4(mg/l)	18	11	52	7	60	5	3	3	47	5	57	6	280

Only four mortar samples exceeded the threshold values for heavy metals. This indicates that the heavy metals are incorporated in the mortar matrix with time or water soluble metals are released during curing. The EDUcarb residue showed the highest leaching from the mortar compared to the initial amount available for leaching from the residue, which is most likely due to the increased pH in the mortar that changes the heavy metal leachability. Comparing the MEDU and MEDUcarb to the Mcoal samples, similar leaching levels were observed, even though the total concentration of Pb and Zn in the EDU samples was a factor 100 and 1000 higher respectively.

The pH in the mortar was generally higher than in the residues and at a level where the heavy metals are expected to be stable in the matrix [7]. The slight increase in Cr leaching in the upgraded residues (Table 2) suggests a shift from Cr (III) to Cr (VI) during ED treatment. Higher Cr leaching was also seen from the mortars with upgraded residues compared to raw, which was also seen in the leaching of the APC residues alone. When comparing the amount of leached heavy metals from the APC residues to the amount leached from the mortars, it can be seen that the mortars generally incorporates the heavy metals. This also includes Cr, where 14 and 1 % of the total leachable Cr in the APC residues is leached from the mortars containing EDU and EDUcarb, respectively. Cr leaching was high in the reference mortar, which has also been seen in other studies [10, 15]. The Cr leaching from mortars containing EDU samples were lower than leaching from the reference and coal mortar. This is an improvement to what was seen by Aubert et al. [15] where a higher Cr leaching was seen from mortars with MSWI fly ash compared to a reference sample and also exceeded the limits for inert waste disposal. A study where concrete samples containing fly ash with a higher Cr content than cement were carbonated, did not show increased leaching of Cr compared to reference samples [37]. Contrarily, the same concretes with fly ash subjected to NaCl and Na₂SO₄ solutions increased Cr leaching compared to reference concrete.

This suggests that the choice of final application for concrete containing waste incineration residues should be carefully considered. As MSWI APC residue is considered hazardous waste in most countries, direct reuse will probably not be allowed, so even if the metal leaching from the mortars with untreated and upgraded residue were similar, this would probably not be an argument that would promote reuse of untreated APC residue. Most importantly, the total Cl concentration and the Cl leaching decreased significantly when introducing electrolytic upgrading. Regarding long term leaching of metals it would be expected that in mortar samples containing untreated residue the leaching would increase due to the higher water solubility of the residue.

4. CONCLUSION

Two electrodiolytically (ED) treated MSWI APC residues were evaluated for use in mortar as Portland cement replacement, i.e. a potential alternative use of these residues compared to disposal in hazardous waste disposal sites. One of the residues was carbonated followed by electrodiolytic treatment. The carbonated ED treated residue shows lower leaching of heavy metals compared to the only ED treated residue before use in mortar. However, when the carbonated ED treated residue is incorporated in mortar, the heavy metal leaching increases due to a higher pH in the mortar than in the residue itself. The heavy metal leaching from the mortars with ED treated MSWI APC residues is similar to reference mortar without added APC residue. Mortars with ED treated residues show similar compressive strengths compared to

mortars with coal fly ash, where the compressive strengths are up to 45 MPa, but lower than the reference mortar. The initial setting times are delayed with up to 16 hours in mortar with ED treated residues compared to reference mortar and the workability also decreases in these mortars, which should be considered for application of such mortar. The high salt content suggests that the ED treated MSWI APC residues are most applicable to unreinforced concrete.

From an environmental and mechanical point of view, electrochemical upgrading has potential as a pre-treatment method prior to reuse of APC residue. Carbonation of the APC residue prior to ED does not improve the quality of the residue neither for technical nor environmental performance in mortar. There seems to be a potential for using electrochemically upgraded APC residue in mortar, however, long term leaching and the durability should be investigated further.

Acknowledgement

We are grateful to REFA I/S for providing the experimental MSWI APC residue and hosting the pilot plant facilities. The Danish Agency for Science Technology and Innovation financed the pilot plant test period through Proof of Concept funding.

REFERENCES

1. Quina, M.J., Bordado, J.C., Quinta-Ferreira, R.M., "Treatment and use of air pollution control residues from MSW incineration: An overview", *Waste Management*, Vol 28, 2008, pp. 2097-2121.
2. Gartner, E., "Industrially interesting approaches to "low-CO₂" cements", *Cement Concrete Research*, Vol 34, 2004, pp. 1489-1498.
3. Ferreira, C., Ribeiro, A., Ottosen, L., "Possible applications for municipal solid waste fly ash", *Journal of Hazardous Materials*, Vol B96, 2003, pp. 201-216.
4. Todorovic, J., Ecke, H., "Treatment of MSWI residues for utilization as secondary construction minerals: a review of methods", *Minerals Energy – Raw Materials Report*, Vol. 3-4, 2006, pp. 45-59.
5. Jensen, P.E., Ferreira, C.M.D., Hansen, H.K., Rype, J.U., Ottosen, L.M., Villumsen, A., "Electroremediation of air pollution control residues in a continuous reactor", *Journal of Applied Electrochemistry*, Vol. 40, 2010, pp. 1173-1181.
6. Kirkelund, G.M., Jensen, P.E., Villumsen, A., Ottosen, L.M., "Test of electrochemical upgrading of MSWI APC residue in pilot scale: focus on reduced metal and salt leaching", *Journal of Applied Electrochemistry*, Vol. 40, 2010, pp.1049-1060.
7. Pedersen, A.J., Ottosen, L.M., Villumsen, A., "Electrochemical removal of heavy metals from municipal solid waste incineration fly ash using ammonium citrate as assisting agent", *Journal of Hazardous Materials*, Vol. B122, 2005, pp.103–109.
8. Ottosen, L.M., Lima, A.T., Pedersen, A.J., Ribeiro, A.B., "Electrochemical extraction of Cu, Pb and Cl from municipal solid waste incineration fly ash suspended in water", *Journal of Chemical Technology and Biotechnology*, Vol. 81, 2006, pp. 553–559.
9. Ferreira, C.D., Jensen, P., Ottosen, L., Ribeiro, A., "Preliminary treatment of MSW fly ash as a way of improving electrochemical remediation", *Journal of Environmental Science and Health Part A*, Vol. 43, 2008, pp. 837–843.
10. Lima, A.T., Ottosen, L.M., Ribeiro, A.B., "Assessing fly ash treatment: Remediation and stabilization of heavy metals", *Journal of Environmental Management*, Vol. 95, 2012, pp. S110-115.

11. DS 259, "Determination of metals in water, sludge and sediments - General guidelines for determination by atomic absorption spectrophotometry in flame", 2003.
12. DS/EN 12457-3, "Characterisation of waste - Leaching - Compliance test for leaching of granular waste materials and sludges - Part 3: Two stage batch test at a liquid to solid ratio of 2 l/kg and 8 l/kg for materials with high solid content and with particle size below 4 mm (without or with size reduction)", 2002.
13. DS/EN 196-1, "Methods of testing cement - Part 1: Determination of strength", 2005.
14. Geiker, M.R., Kjeldsen, A.M., Galluci, E., Bager, D.H., "Preliminary investigations of the effect of air-pollution-control residue from waste incineration on the properties of cement paste and mortar", Proceedings for Advances in cement and concrete X, Sustainability, Davos Switzerland, 2006.
15. Aubert, J.E., Husson, B., Sarramone, N., "Utilization of municipal solid waste incineration (MSWI) fly ash in blended cement. Part 2. Mechanical strength of mortars and environmental impact", *Journal of Hazardous Materials*, Vol. 146, 2007, pp. 12-19.
16. DS/EN 12390-3, "Testing hardened concrete - Part 3: Compressive strength of test specimens", 2009.
17. DS 423.37, "Testing fresh concrete – generation of heat", 2001
18. Bartos, P., "Fresh concrete: properties and tests", Elsevier, London, 1992.
19. Hjelm, O., Johnson, A., Comas, R., "Incineration: Solid residues", In: Christensen, T.H., "Solid Waste Technology and Management", Wiley, 2011. pp. 430-462.
20. Del Valle-Zermeño, R., Formosa, J., Chimenos, J.M., Martínez, M., Fernández, A.I., "Aggregate material formulated with MSWI bottom ash and APC fly ash for use as secondary building material" *Waste Management*, Vol. 33, 2013, pp. 621-627.
21. Wang, K-S., Chiang, K-Y., Lin, K-L., Sun, C-J., "Effects of a water-extraction process on heavy metals behaviour in municipal solid waste incinerator fly ash", *Hydrometallurgy*, Vol. 62, 2001, pp. 73-81.
22. DS/EN 450-1 + A1, "Fly ash for concrete - Part 1: Definition, specifications and conformity criteria", 2007.
23. Jiang, J., Chen, M., Zhang, Y., Xu, X., "Pb stabilization in fresh fly ash from municipal solid waste incinerator using accelerated carbonation technology", *Journal of Hazardous Materials*, Vol. 161, 2009, pp. 1046-1051.
24. American Geological Institute "Dictionary of mining, mineral and related terms", American Geological Institute in cooperation with the Society for Mining, Metallurgy and Exploration, Inc., Alexandria, Va, 1997.
25. Danish Ministry of the Environment, "Bekendtgørelse om genanvendelse af restprodukter og jord til bygge- og anlægsarbejder", BEK nr 1480 af 12/12/2007, 2007. (In Danish).
26. Gao, X., Wang, W., Ye, T., Wang, F., Lan, Y., "Utilization of washed MSWI fly ash as partial cement substitute with the addition of dithiocarbamic chelate", *Journal of Environmental Management*, Vol. 88, 2008, pp. 293-299.
27. Gardner, K.H., Nystroem, G.M., Aulisio, D.A., "Leaching properties of estuarine harbour sediment before and after electrodialytic remediation", *Environmental Engineering Science*, Vol. 24 (4), 2007, pp. 424-433.
28. Brown, P., Jones, T., Bérubé, K., "The internal microstructure and fibrous mineralogy of fly ash from coal-burning power stations", *Environmental Pollution*, Vol. 159, 2011, pp. 3324-3333.
29. Jiang, J., Du, X., Chen, M., Zhang, C., "Continuous CO₂ capture and MSWI fly ash stabilization, utilizing novel dynamic equipment", *Environmental Pollution*, Vol. 157, 2009, pp. 2933-2938.

30. Chrysochoou, M., Dermatas, D., "Evaluation of ettringite and hydrocalumite formation for heavy metal immobilization: Literature review and experimental study", *Journal of Hazardous Materials*, Vol. 136, 2006, pp. 20-33.
31. Pedersen, A.J., Gardner, K.H., "Characterization of municipal solid waste incineration fly ash before and after electrochemical remediation", *Journal de Physique IV France*, Vol. 107, 2003, pp. 1029-1032.
32. Chen, W-S., Chang, F-C., Shen, Y-H., Tsai, S., Ko, C-H., "Removal of chloride from MSWI fly ash", *Journal of Hazardous Materials*, Vol. 237-238, 2012, pp. 116-120.
33. Taylor, H.F.W., "Cement chemistry", Second Ed., Thomas Telford, London 1997.
34. Polettini, A., Pomi, R., Sirini, P., "Fractional factorial design to investigate the influence of heavy metals and anions on acid neutralization behavior of cement-based products", *Environmental Science and Technology*, Vol. 36, 2002, pp. 1584-1591.
35. Brough, A.R., Atkinson, A., "Automated identification of the aggregate-paste interfacial transition zone in mortars of silica sand with Portland or alkali-activated slag cement paste", *Cement Concrete Research*, Vol. 30, 2000, pp. 1375-1379.
36. Danish Ministry of the Environment, "Bekendtgørelse deponeringsanlæg", BEK nr 719 af 24/06/2011, 2011. (In Danish).
37. Müllauer, W., Beddoe, R.E., Heinz, D., "Effect of carbonation, chloride and external sulphates on the leaching behaviour of major and trace metals from concrete", *Cement and Concrete Composites*, Vol. 34, 2012, pp. 6186-26.

Linking the Fibre Orientation Factor with the Mechanical Response of the Fibre Reinforced Self-Compacting Concrete



Oldrich Svec
M.Sc., Ph.D., Consultant
Concrete Centre, Danish Technological Institute
Gregersensvej, DK-2630 Taastrup
E-mail: osv@teknologisk.dk



Lars Nyholm Thrane
M.Sc., Ph.D., Senior Consultant
Concrete Centre, Danish Technological Institute
Gregersensvej, DK-2630 Taastrup
E-mail: lnth@teknologisk.dk



Henrik Stang
Professor
Technical University of Denmark
Anker Engelunds Vej 1, DK 2800 Kgs. Lyngby
E-mail: hs@byg.dtu.dk

ABSTRACT

Steel fibre reinforced self-compacting concrete is a promising construction material. One of the features of the concrete is the fact that the immersed steel fibres orient under the flow of the concrete. The fibre orientation can be represented by the fibre orientation factor. Different approaches exist to link the fibre orientation factor with the mechanical response of the structure. In this article, we show two different existing approaches that link the fibre orientation factor with the residual tensile strength of the material. We propose an alternative relation. The proposed relation is compared to the existing solutions and validated by experimental results obtained from casting of a slab made of the steel fibre reinforced self-compacting concrete.

Key words: Steel fibre, fibre orientation, orientation factor, SFRC, SFRSCC

1. INTRODUCTION

Steel fibre reinforced self-compacting concrete is a material composed of steel fibres immersed in the self-compacting concrete. During the casting process, the self-compacting concrete flows and fills the formwork without the need of vibration or any other type of agitation. The immersed steel fibres together with the ability of the concrete to flow then bring new challenges and possibilities into the design process of the material.

Fibres immersed in the self-compacting concrete orient according to the flow of the material. This has been observed by many researchers, e.g. [1, 2]. Martinie and Roussel [3] describe the various origins of the fibre orientation. A range of analytical, empirical, experimental and numerical techniques exists that aim to obtain the fibre orientation in the material [4–7]. The fibre orientation is often represented by the fibre orientation factor [8–10]

$$\alpha = \frac{n_f A_f}{v_f A_c}, \quad (1)$$

where n_f , A_f , v_f and A_c stand for the number of fibres at the cut plane, cross-sectional area of one fibre, fibre volume fraction and the area of the cut plane, respectively.

Fibre orientation can have a significant impact on the resulting mechanical behaviour of the steel fibre reinforced self-compacting concrete. The impact of the fibre orientation on the mechanical response is a very complex topic dealing with parameters such as fibre pull-out curve, fibre inclination, fibre embedment length, fibre type, fibre shape and concrete type. A range of analytical, empirical and numerical techniques exists that put all these parameters together in order to describe the overall mechanical response of the material [11–13].

Stang et al. [14] suggest a linear relation between the fibre orientation factor and the residual tensile strength of the material of the following shape

$$f_{\text{struct}} = f_{\text{ref}} \alpha_{\text{struct}}, \quad (2)$$

where f_{struct} , f_{ref} and α_{struct} stand for the mechanical strength of the material in the given point of the structure, the referential strength of the material and the fibre orientation factor in the given point of the structure, respectively. The referential strength, f_{ref} , is commonly defined experimentally, e.g. by the three point bending test. The presented linear relation assumes zero strength of the material for fibre orientation factor equal to zero.

Kanstad et al. [15] and Thorenfeldt [16] introduced a linear relation of the following shape

$$f_{\text{struct}} = f_{\text{ref}} (4\alpha_{\text{struct}} - 1). \quad (3)$$

The presented linear relation assumes zero strength of the material for fibre orientation factor below the value of 0.25.

2. MATERIAL AND METHODS

2.1 Proposed approach

We propose an alternative relation to Stang et al. and Kanstad et al. linking the fibre orientation factor with the mechanical strength of the material in the following shape

$$f_{\text{struct}} = f_{\text{ref}} \alpha_{\text{struct}} \sin \left(\frac{\pi}{2} \alpha_{\text{struct}} \right). \quad (4)$$

The proposed relation was deduced in the following manner. The mechanical strength of the material at a given point of structure and normal to a given fracture plane can be estimated as

$$f_{\text{struct}} = \overline{f_{\text{struct}}} n_f, \quad (5)$$

where $\overline{f_{\text{struct}}}$ stands for the average of the fibre pull-out strengths at the given fracture plane and at a given crack opening displacement. The value of n_f stands for the number of fibres at the given fracture plane. Equation (1) can be used to replace the number of fibres, n_f , by the fibre orientation factor, α , as

$$f_{\text{struct}} = \overline{f_{\text{struct}}} n_f = \overline{f_{\text{struct}}} \alpha \frac{v_f A_c}{A_f} = C_1 \alpha \overline{f_{\text{struct}}}, \quad (6)$$

where C_1 is in this context a constant. The average of the fibre pull-out strengths, $\overline{f_{\text{struct}}}$, is assumed to be primarily defined by the average fibre inclination, γ , at the given fracture plane. When a fibre is parallel to the fracture plane the pull-out strength diminishes. When the fibre is close to normal to the fracture plane, the pull-out strength reaches its maximum. A linear relation between the fibre orientation factor and the average fibre inclination at the fracture plane, $\gamma = \frac{\pi}{2} \alpha$, was assumed. The fibre orientation factors 0, 0.5, 1 then correspond to the average fibre inclinations of 0°, 45°, 90°. Finally, we assumed that the function linking the average pull-out strength with the average fibre inclination has a sinus form, $\overline{f_{\text{struct}}} = C_2 \sin(\gamma)$. This corresponds to the state where only the projection of the fibre normal to the fracture plane is active in the pull-out process. The average of the fibre pull-out strengths is then

$$\overline{f_{\text{struct}}} = C_2 \sin \left(\frac{\pi}{2} \alpha \right), \quad (7)$$

where C_2 is in this context a constant. The total mechanical strength of the fibre reinforced self-compacting concrete at the given fracture plane is then computed as

$$f_{\text{struct}} = C_1 \alpha \overline{f_{\text{struct}}} = C_1 \alpha C_2 \sin \left(\frac{\pi}{2} \alpha \right) = f_{\text{ref}} \alpha \sin \left(\frac{\pi}{2} \alpha \right), \quad (8)$$

where f_{ref} is the constant coefficient to be determined experimentally.

Figure 1 compares the three presented relations linking the mechanical strength of the material with the fibre orientation factor. Figure 1 left shows the three relations with common point of $[0.6, 0.45]$ whereas Figure 1 right highlights the three relations with the common point of $[1, 1]$.

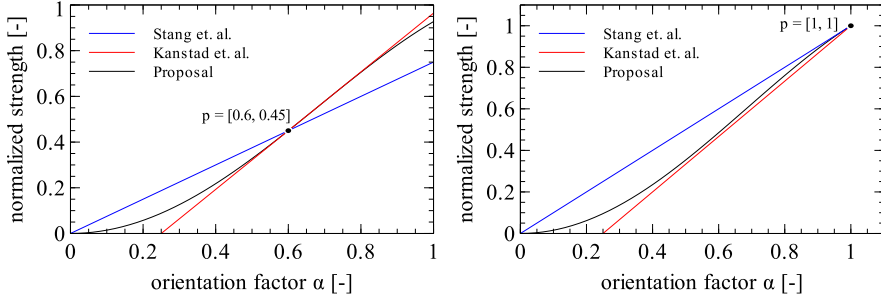


Figure 1 – Comparison of the three proposed relations linking orientation factor with the mechanical response of the material. Left: Common point $p = [0.6, 0.45]$. Right: Common point $p = [1, 1]$.

2.2 Experiment – slab

An experiment was performed to show performance of the individual presented relations. A slab of dimensions $1.6 \times 1.6 \times 0.15$ m was cast with steel fibre reinforced self-compacting concrete [7]. The casting process was performed from a rubber circular inlet positioned at a distance of 0.3 m from one of the corners of the slab (Figure 2). The point of discharge was located 0.3 m above the bottom of the slab. The casting was performed into a smooth oiled glue-laminated plywood formwork.

Density of the fibre reinforced self-compacting concrete was approximately 2300 kg/m^3 . Plastic viscosity and yield stress of the suspension were measured using 4C Rheometer [17]. The averaged resulting values at the time of casting were 45 Pa and 75 Pa·s for the yield stress and for the plastic viscosity, respectively.

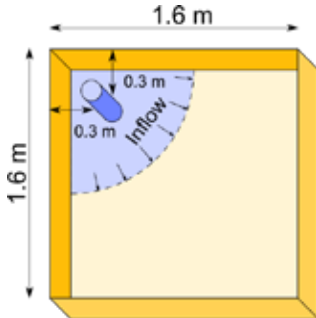


Figure 2 – Layout of the slab casting. Blue cylinder denotes the inlet whereas the orange box denotes the formwork.

Hooked end steel fibres (Bekaert Dramix RL 80/60 BN) were added to the concrete during the mixing process. The fibre volume ratio was 0.5%, corresponding to approximately 40 kg/m^3 .

The fibre length and the fibre diameter were 60 mm and 0.75 mm, respectively. Density of the steel fibres was 7850 kg/m³.

After the casting, the slab was left to harden for a period of 28 days. The slab was subsequently cut into 24 beam specimens of dimensions 150 × 150 × 550 mm (Figure 3 left). The beam specimens were cut to provide a notch at mid-span and tested in the three-point bending according to EN 14651 to obtain the mechanical response in flexure (Figure 3 right).

The three-point bending tests resulted in a series of curves relating loading forces, F , [kN] to crack mouth opening displacements, CMOD [mm]. The forces, F , were recomputed into flexural stresses, σ , as:

$$\sigma = \frac{3FL}{2b(h-a)^2}, \quad (9)$$

where L , b , h and a stand for the beam length (= 550 mm), beam depth (= 150 mm), beam height (= 150 mm) and notch depth (= 25 mm), respectively.



Figure 3 – Left: The slab saw cut into 24 beam specimens. Right: Three-point bending test.

The tested beam specimens were then cut into two pieces. The cut was performed in the vicinity of the fracture plane. The created cut planes were polished and the number of fibres visible at each plane was manually counted (Figure 4). The fibre orientation factor, α , was computed for each beam of the slab from the number of fibres visible at each cut plane.

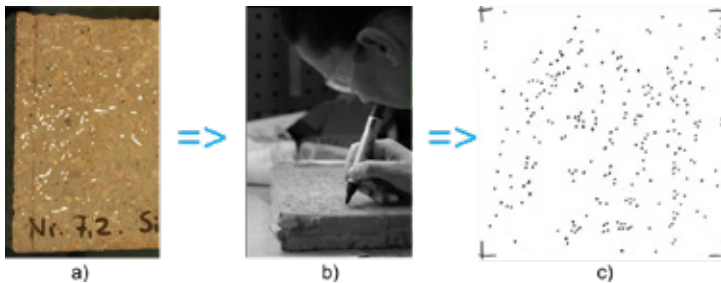


Figure 4 – Manual counting of the number of fibres at the given plane. a) A typical cut plane. b) Counting process. c) Resulting scanned image.

2.3 Numerical simulation

The presented experimental slab casting was simulated using a numerical framework of flow introduced by Svec et al. [18]. The numerical framework is capable of simulating a free surface flow of non-Newtonian fluid with immersed solid particles of an arbitrary shape. An interaction model was implemented to allow for two-way communication between the solid particles and the surrounding fluid. The solid particles are capable of colliding among each other and with the surrounding obstacles such as formwork, reinforcement or aggregates. The numerical framework is devoid of any non-physical input parameters.

The numerical simulation was run with the same physical input parameters, such as fluid density, viscosity, fibre type etc., as presented in Section 2.2. The self-compacting concrete was modelled as a free surface flow of homogeneous Bingham plastic fluid. The immersed steel fibres were modelled explicitly one by one as thin rigid cylinders. The immersed aggregates were modelled implicitly as a part of the fluid since an explicit representation of the aggregates would increase the computational demands significantly. Boundary conditions representing the smooth oiled glue-laminated plywood formwork was modelled as Navier's slip boundary condition [19]. The value of the Navier's slip length was set to 50 mm.

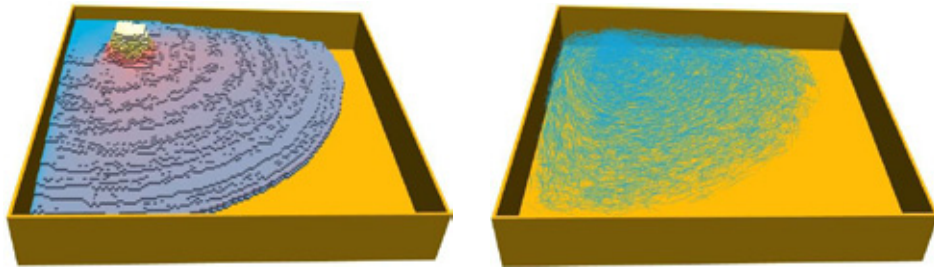


Figure 5— 3D view of an intermediate step of the numerical simulation. Left: Fluid part. Right: Fibres immersed in the concrete.

Figure 5 presents a 3D view of an intermediate step of the numerical simulation. The figure at the left depicts the self-compacting concrete modelled as the free surface flow of the homogeneous Bingham plastic fluid. The figure at the right depicts the corresponding steel fibres immersed in the concrete.

3. RESULTS

3.1 Experiment – slab

Series of curves of all the beam specimens tested in the three-point bending and relating flexural stresses to crack mouth opening displacements are presented in Figure 6. The figure indicates a large variation of the curves among the individual beam specimens ranging from softening curves where the effect of fibres is relatively low to hardening curves where the effect of fibres is substantial.

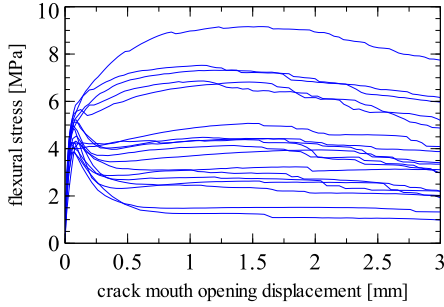


Figure 6 – A series of curves relating flexural stresses to the crack mouth opening displacements for the individual beam specimens.

Figure 7 indicates flexural stresses at three different crack mouth opening displacements CMOD = 0.5, 1.5, 2.5 mm as a function of the orientation factor, α . Black circular marks denote the experimentally obtained results. The experimentally obtained flexural stresses were obtained by the three-point bending tests. The experimentally obtained orientation factors were obtained by the manual counting of the number of fibres at the fracture plane. Our proposed relation together with the two relations by Stang et al. and Kanstad et al. were fitted to the experimental data by maximizing the coefficient of determination, R^2 .

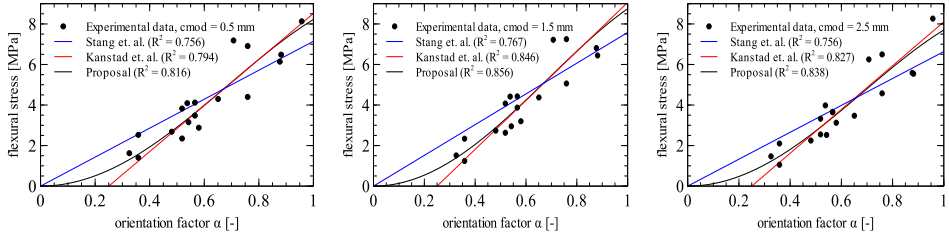


Figure 7 – Flexural stresses at CMOD = 0.5, 1.5 and 2.5 mm as a function of the fibre orientation factor, α .

Figure 7 shows a rather minor difference between our proposed relation and relation by Kanstad et al. The difference between the two relations can be primarily observed for low values of $\alpha < 0.4$. Coefficient of determination, R^2 , of the two relations oscillates above the value of 0.8. Relation proposed by Stang et al. on the other hand exhibits a slightly lower coefficient of determination oscillating around the value of 0.76. Accuracy of the individual proposed relations correlates with the complexity of the formulas.

3.2 Numerical simulation

At the end of the numerical simulation, position and orientation of each individual fibre was averaged into a set of orientation ellipses [7]. The orientation ellipses can be seen in Figure 8 as grey ellipses in the background. Fibre orientation factors were computed in planes normal to X, Y and Z direction. Each fibre orientation factor corresponds to the average of 50 fibre orientation factors obtained from sections equally spaced in a region of dimensions $200 \times 200 \times 150$ mm (X, Y, Z). The individual fibre orientation factors were subsequently recomputed into

the flexural stresses by Equation (4) where f_{ref} was set to 7.7 MPa (black curve in Figure 7 right).

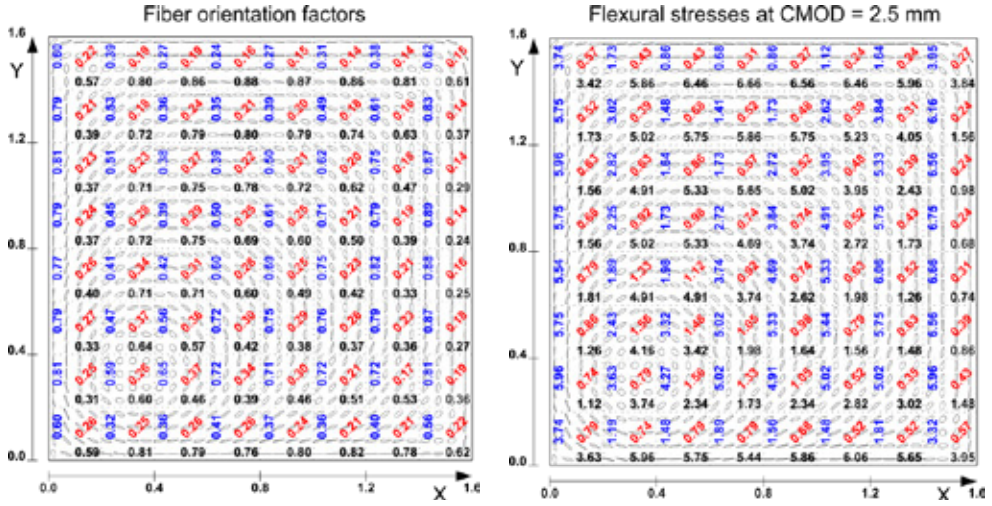


Figure 8 – Left: Fibre orientation factors normal to X (black numbers), Y (blue numbers) and Z (red numbers) direction. Right: Their respective flexural stresses [MPa] computed by the proposed relation.

4. CONCLUSIONS

This article presented two existing relations linking the fibre orientation factor with the mechanical response of the fibre reinforced self-compacting concrete. In this article, an alternative relation was proposed. The three relations were compared to the experimentally obtained data. All the three relations exhibited a relatively high accuracy in terms of the coefficient of determination. The highest accuracy was obtained by our newly proposed relation, tightly followed by the proposal by Kanstad et al. and subsequently followed by the relation proposed by Stang et al. Accuracy of the individual proposed relations correlates with the complexity of the individual formulas.

This article further showed that at least for this particular case and material the complex field of fracture mechanics can be avoided and replaced by a simplified linear relation. Once the referential strength of the particular fibre reinforced self-compacting concrete, f_{ref} , is known, the knowledge of the fibre orientation factor is satisfactory for estimating the mechanical response of the material in a structure. We have shown that the fibre orientation factors can be easily obtained in all position and directions of the structure by the numerical simulations of flow. This gives a huge potential in a relatively fast and cheap design process of structures made of the fibre reinforced self-compacting concrete.

REFERENCES

1. Stähli, P., Custer, R and Mier, J. G. M. "On flow properties, fibre distribution, fibre orientation and flexural behaviour of FRC", *Mater. Struct.*, vol. 41, no. 1, pp. 189–196, Feb. 2007.
2. Zerbino, R., Tobes, J. M., Bossio, M. E. and Giaccio, G. "On the orientation of fibres in structural members fabricated with self compacting fibre reinforced concrete", *Cem. Concr. Compos.*, vol. 34, no. 2, pp. 191–200, Feb. 2012.
3. Martinie, L. and Roussel, N. "Simple tools for fiber orientation prediction in industrial practice", *Cem. Concr. Res.*, vol. 41, no. 10, pp. 993–1000, Oct. 2011.
4. Žirgulis, G., Geiker, M. R., Švec, O. and Kanstad, T. "Potential methods for quality control of fibre distribution in FRC SCC", in *Proceedings of 7th international conference on self compacting concrete*, 2013, pp. 1–8.
5. Lee, Y., Lee, S., Youn, J., Chung, K. and Kang, T. "Characterization of fiber orientation in short fiber reinforced composites with an image processing technique", *Mater. Res. Innov.*, vol. 6, no. 2, pp. 65–72, Sep. 2002.
6. Barnett, S. J., Lataste, J.-F., Parry, T., Millard, S. G. and Soutsos, M. N. "Assessment of fibre orientation in ultra high performance fibre reinforced concrete and its effect on flexural strength", *Mater. Struct.*, vol. 43, no. 7, pp. 1009–1023, Oct. 2009.
7. Švec, O., Stang, H., Olesen, J. F. and Thrane, L. N. "Application of the fluid dynamics model to the field of fibre reinforced self-compacting concrete", in *Proceedings of the International Conference on Numerical Modeling Strategies for Sustainable Concrete Structures (SSCS)*, P. Rossi and J.-L. Tailhan, eds., Aix-en-Provence, France (on CD-ROM), 2012, pp. 1–9.
8. Advani, S. G. "The Use of Tensors to Describe and Predict Fiber Orientation in Short Fiber Composites", *Journal of Rheology*, 31(8), 751, 1987.
9. Krenchel, H. "Fibre spacing and specific fibre surface", A. Nev. (Ed.), *Fibre Reinf. Cem. Concr. Constr. Press*. UK, pp. 69–79, 1975.
10. Stroeven, P. "Morphometry of fibre reinforced cementitious materials", *Matériaux Constr.*, 1979.
11. Bolander, J. E., Choi, S. and Duddukuri, S. R. "Fracture of fiber-reinforced cement composites: effects of fiber dispersion", *Int. J. Fract.*, vol. 154, no. 1–2, pp. 73–86, Feb. 2008.
12. Laranjeira, F., Molins, C. and Aguado, A. "Predicting the pullout response of inclined hooked steel fibers", *Cem. Concr. Res.*, vol. 40, no. 10, pp. 1471–1487, Oct. 2010.
13. De Oliveira, F. L. "Design-oriented constitutive model for steel fiber reinforced concrete", *Thesis, ISBN 9788469347010*, 2010.
14. Stang, H., Kasper, T., Mjoernell, P., Slot, H., Vitt, G., Thrane, L. N., Reimer, L. "Design guideline for structural applications of steel fibre reinforced concrete – Background document", *SFRC Consortium*, Sep. 2013
15. Kanstad, T., Arve, J. D., Vatnar, A., Mathisen, A. E., Sandbakk, S., Vikan, H., Nikolaisen, E., Dossland, A., Leirud, N. and Overrein, O. G. "Forslag til retningslinjer for dimensjonering, utførelse og kontroll av fiberarmerte betongkonstruksjoner", *COIN Project report 29*, Oslo SINTEF Building and Infrastructure, 2011.

16. Thorenfeldt, E. "Theoretical tensile strength after cracking. Fibre orientation and average stress in fibres", in *Proceedings of the Nordic Concrete Federation Workshop on Design Rules for Steel Fibre Reinforced Concrete Structures*, 2003, pp. 43–60.
17. Thrane, L. N., Pade, C., Nielsen, C. V., Jeknavorian, A. A., Schemmel, J. J. and Dean, S. W. "Determination of Rheology of Self-Consolidating Concrete Using the 4C-Rheometer and How to Make Use of the Results," *J. ASTM Int.*, vol. 7, no. 1, p. 102003, 2010.
18. Švec, O., Skoček, J., Stang, H., Geiker, M. R. and Roussel, N. "Free surface flow of a suspension of rigid particles in a non-Newtonian fluid: a Lattice Boltzmann approach", *J. Non-newton. Fluid Mech.*, vol. 179–180, pp. 32–42, Jun. 2012.
19. Švec, O. and Skoček, J. "Simple Navier's slip boundary condition for the non-Newtonian Lattice Boltzmann fluid dynamics solver", *J. Non-newton. Fluid Mech.*, vol. 199, pp. 61–69, Sep. 2013

Measuring sedimentation and bleeding of fresh paste with hydrostatic pressure



Ya Peng*
Dr.ing, Researcher
Dept. of Structural Eng., NTNU
N-7491 Trondheim
ya.peng@ntnu.no



Klaartje de Weerd
Dr. ing, associate professor, senior scientist
Dept. of Structural Eng., NTNU, Sintef
N-7491 Trondheim
klaartje.d.weerd@ntnu.no



Bård Pedersen
Dr.ing, Senior principal Engineer
Norwegian Public Roads Administration (NPRA)
N-0033 Oslo
baard.pedersen@vegvesen.no



Stefan Jacobsen
Professor
Dept of Structural Eng., NTNU
N-7491 Trondheim
stefan.jacobsen@ntnu.no
(* corresponding author)

ABSTRACT

The matrix instability affects the robustness and the total bleeding of the concrete remarkably. This paper focuses on the fundamental research of the stability of cement paste. Particle sedimentation and low yield stress of the fluid cause instability of cement paste in the form of particle segregation and bleeding. The origin of the problem is the density differences between the different phases, and thus 100 % effective solutions to stable SCC, which are usually attempted by adding powder and/or Viscosity Modifying Admixtures (VMA), are hard to achieve. A sensitive HYdroStatic Pressure Test (HYSPT) was developed at the concrete laboratory of NTNU to detect the density differences over time and depth in fresh cement paste due to sedimentation and bleeding. Based on review and analyzing the dp/dt plots from HYSPT, a conceptual model for progress of segregation was proposed. It was validated by parallel experiments such as bleeding and in situ solid fraction measurements that HYSPT can be applied to evaluate the sedimentation process and the flocculation state of paste or matrix. Furthermore, the sedimentation rate by HYSPT measurements was found to coincide with bleeding measurements and estimates from

the Kozeny-Carman equation. By use of HYSPT the stabilizing effect of various powders and admixtures can be analyzed and compared. Four different bleeding values were obtained for each of two different pastes with $w/c = 0.50$ and 0.60 . The flow values were based on visual bleeding measurements, HYSPT, laser (TurbidScan) and the Kozeny-Carman Equation, respectively showing consistent rankings. However, the bleeding rate from TurbiScan was lower since this “front” was defined as completely clear liquid, whereas visual bleeding and HYSPT rely on both clear and turbid layers. Therefore, HYSPT helps to understand the basic mechanism of the stability and can be looked upon as a good tool to study the stability of cement paste and the effect of different materials, such as chemical admixtures and powder additives, on stability.

Key words: stability, sedimentation, bleeding, hydrostatic pressure

1. INTRODUCTION

Self-compacting concrete (SCC) has been described as one of the most innovative developments in the field of concrete technology for its reduced construction costs and improved working environment [1]. Unfortunately, SCC cast in-situ in Norway has stagnated at a very low market share. One of the main reasons is probably the low stability and robustness against fluctuations in the concrete production [2]. The origin of the problem is the density difference between the particles and the fluid phase. Consequently, 100 % effective solutions to stable SCC, which are usually attempted by adding powder and/or Viscosity Modifying Admixtures (VMA), are hard to achieve. Particularly for SCC, in order to obtain the high fluidity, the lower yield stress, higher dosage of water reducer and/or higher matrix volume than in the ordinary concrete can lead to the problem of instability. This is one of the major challenges facing full scale use of Self-Compacting Concrete (SCC) on site. Mørtzell et al. [3] simplified concrete into a two-phase material with the particle-matrix model. This assumes aggregates $>125\ \mu\text{m}$ to be in the suspended particle phase while all liquids and particles $\leq 125\ \mu\text{m}$ are in the matrix phase. Accordingly the instability of concrete can generally be looked upon as coarse aggregate segregation within the matrix as well as the bleeding. However, as a multi-phase material, the filler modified cement paste itself also experiences instability as a particle sedimentation process before setting. The stability of the cement matrix also affects the segregation of the coarse aggregates, and influences the total bleeding and inhomogeneity of the hardened concrete. The investigation on the stability of cement paste thus helps to understand the concrete stability. This investigation is also important to ensure the quality of injectable cement grouts which are of great use in many construction domains such as pre-stressed cable coating, repair and consolidation of masonry, soil grouting etc. The instability of cement paste is a result of particle sedimentation and is mainly affected by the solid fraction, the fresh properties of the fluid phase, various particle sizes, the mineralogy of the powders, the flocculation between particles and density differences between the particles and the fluid. The sedimentation of cement paste is more complicate than that of the suspensions with inert particles because of the reaction between the particles and the fluid phase. It results in structural build-up, chemical shrinkage and bleeding water re-suction etc.

Some investigations have been performed on the relationship between fresh properties and stability of cement paste. Perrot et al. [4] focused on a potential correlation between yield stress

and bleeding of cement paste. It was concluded that for most cementitious materials in the industry, a percolated network of interacting particles appears within the suspension which is affected by solid volume fraction and polymer surface coverage for a given polymer. However, the consequences of cement hydration were neglected in this study. Kwan et al. [5] studied the effect of superplasticizer (SP) on the cohesiveness of cement paste by sieve segregation measurements, but there is still no generally adopted acceptance criterion for the sieve segregation index (SSI). In this research Kwan suggested a combined evaluation by observing the bleeding water along the edge of the cement paste after the mini slump cone test. A bigger range of research has also been focused on the development of test methods for bleeding measurements. Schokker et al. [6] estimated the bleeding resistance of the grout by using a pressure filter test. Jossierand and de Larrard [7] developed the bleeding water collecting method by making tracks on the surface of the sample; however, this is hard to carry out for the paste of SCC due to the soft surface. It was also suggested to put a stainless steel sphere and a pre-humidified filter paper on the sample surface to collect the bleeding water, but no available data have yet showed the repeatability and the accuracy. Sawaide and Iketani [8] designed the bleeding apparatus, but it was found by Kaplan [9] that water bubbles may be trapped in the apparatus, which affects the measured bleeding volume and thus the accuracy of the method. There are also several standardized methods for bleeding measurements such as a Swedish test (Swedish standard B5 6.3310 [10]) and an ASTM method C243-95 [11] (withdrawn 2001 without replacement). Most of these methods can hardly be applied to the cement paste of SCC, with fine mineral fillers and high dosages of chemical admixtures such as SP. The main reason is the difficulty to collect clear bleeding water due to the existence of turbid bleeding and the transit layer as investigated in our previous research [12]. It was also found that the classic term “bleeding” seems not always to describe stability of cement paste well because the inhomogeneity of the remaining cement paste is not taken into account. Therefore, particle sedimentation and the consequent bleeding should both be studied when looking into the stability of fresh cement paste. Rosquoët et al. [13] studied the particle sedimentation process with density measurements from top to bottom of the paste samples by using γ -rays from a radioactive source. Chen et al. [14] used the Turbiscan test more recently to investigate the stability of premixed injectable cement paste. The particle sedimentation process can be investigated with a lot of test methods. The radiation scanning methods as mentioned above have been broadly used, but normally professional equipment is needed. Furthermore, there are size resolution problems in the application of micro Computer Tomography for filler characterization. Therefore, research still needs to be applied in paste and matrix stability studies [15]. More direct methods including density and in situ volume fraction measurements were also tried [16]. However, it was found that the in situ sampling was more difficult for cement paste with low w/c ratio, especially after a period of sedimentation. In addition, during in situ sampling it is hard not to disturb the fresh sample. Therefore, some physical properties such as electric conductivity or pressure measurements were recommended by Williams [17] to be better ways to investigate the particle sedimentation of suspensions.

Hydrostatic pressure measurements were applied very early by Steinour [18] in 1944 to study the spherical particle sedimentation for developing a better understanding of the settling of fresh Portland cement paste. The phenomenon of sedimentation was just commonly looked on as “bleeding” for the old cement paste without chemical admixtures and other mineral additives. However, he only investigated solid volume fraction and the particle size effect on the settling of uniform pearl tapioca spheres within a diluted non-flocculated suspension. The interaction and reaction between particles were not considered. Mori et al. [19] characterized the flocculation degree of dense slurry by hydrostatic pressure measurements. The ratio of apparent weight flux of the depositing particles to that of the settling particles was introduced to discuss

the relationship between the results obtained from hydrostatic pressure measurement and the final packing fraction of the sediment. To our knowledge so far, time-dependent hydrostatic pressure measurements was first used by Roffle [20, 21] who studied the settlement of the hydrating cement suspensions. The pressure detection methods were also used to evaluate plastic shrinkage up to the hardening period by Wittmann [22] and Hammer et al. [23]. A similar method was developed by Radocea [24, 25] to investigate the bleeding of cement paste, although with simultaneous evaporation. Amziane [26] applied hydraulic pressure measurements to determine the setting time of pressurized fresh cementitious materials and to evaluate formwork pressure.

In this research, the HYdroStatic Pressure Test (HYSPT) was developed to study particle sedimentation and bleeding of normal cement paste with high solid volume fraction varying from 0.33-0.46 (corresponding to $w/c=0.4-0.7$). However, the HYSPT setup is different from the above measurements which was discussed in [16] from two aspects. Firstly, the experiments only deal with the pressure variations during the early fresh state eliminating the influence of evaporation instead of over longer periods such as 10 hours in [23, 24, 25, 26]. According to our previous research [16], the detected pressure change is mainly governed by the particle sedimentation for normal cement paste before set. The influence of early hydration of the cement, structural build-up and chemical shrinkage is limited and cannot overshadow the big pressure change induced by the particle movement. In addition, commercial pressure sensors for industrial applications with high accuracy and compensation for atmospheric pressure variations were applied in this test setup, so that a pure hydrostatic pressure was determined. The applicability and repeatability were also discussed in [16] by comparing some parallel tests such as in situ volume fraction measurements and bleeding tests. Then further experimental study by this method [12] were carried out to investigate the materials effect such as SP, filler and VMA on sedimentation and bleeding process of cement paste. This paper introduces this test method, summarizes its application and proposes further research with this method.

2. MEASUREMENT METHOD AND MATERIALS

2.1. HYdroStatic Pressure Test (HYSPT)

The schematic diagram of the hydrostatic pressure test setup with data acquisition system is shown in Fig. 1 and a photo for this system is shown in Fig. 2. Two pressure sensors are connected to one end of each glass siphon. The pilot tests on air-free water confirmed the detection accuracy of both pressure sensors (Endress+Hauser Cerabar-S PMC71) used at different levels to be ± 0.75 Pa as presented in the product manual [27]. The atmospheric pressure variation is automatically compensated in the output hydrostatic pressure, and thus a pure hydrostatic pressure signal is produced. The sensors are connected to an electronic controller which monitors the sensor and transfers the data to the computer. The top valve on each siphon is for fluid filling and another valve connects to the end of the pipe that goes into the suspension via holes on the wall of a rigid plastic cylinder containing the paste sample. The plastic cylinder has a height of 25 cm, an inner diameter of 10 cm and 2 cm thick walls which can avoid deformation during tests. There are five holes on each opposite side of the plastic cylinder. Before filling the cement paste into the cylinder, the whole glass pipe is filled with air free water and the system is sealed. The sample is then mixed and poured into the cylinder to the designed height of 22 cm, and slightly shaken to evacuate air bubbles. The air-free water and paste sample are put into contact when opening the lower valve for each pressure detection system. At the same time, the long probe of the temperature sensor is placed into the mixture to

compensate the pressure change due to temperature fluctuation in the mixture. The cylinder is covered on the top to hinder evaporation. The pressure detection is performed in the laboratory condition (approx. 20°C and RH 60%) for around 4 h.

HYSPT relies on the mainly restricted Stokesian settlement of particles causing changes in the solid fraction and thus the fresh density at a given height and time. After casting, the hindered particle settling occurs in the mixed homogenous cement paste due to the density differences between particle and fluid phases. HYSPT measures the instant pressures continuously exerted by the suspended particles and liquid above the designed test levels. Generally, the hydrostatic pressure at the given height of a homogeneous suspension can be calculated as the sum of the pressure due to the fluid and particles above the measurement position $P_m = \rho_m gh$, where ρ_m is the mixture density and h is the height of the suspension above the measurement level. Accordingly the density and thus the volume fraction of the suspension can be calculated by monitoring the hydrostatic pressure. As sedimentation process continues, the densities at the different levels of the suspension are not constant but increase from top to bottom, therefore different zones including homogeneous, various concentration and sediment zones appear. Hence, the above simple equation does not hold any longer. Finally a sediment cake forms at the bottom, all the particles are supported by the bottom of the container and therefore HYSPT can detect plateau pressures which indicate the liquid pressures above the test levels. However, the detected plateau pressures are shown to be not constant because of the compressing of the sediment cake. HYSPT investigates the materials effect on the particle sedimentation process by comparing the gradients of pressure curves dp/dt during hindered settling and studying the different time reaching the plateau. The starting and finishing time of this plateau pressure respectively indicates the completion of the particle settling and setting of cement paste after long compressing process of the sediment cake. Therefore, the experimental study on the density variations in the suspension by HYSPT helps to develop the model of sedimentation and bleeding process, perceive the whole process of particle sedimentation and sediment cake compression, and thus improves the understanding of instability of cement paste due to particle sedimentation.

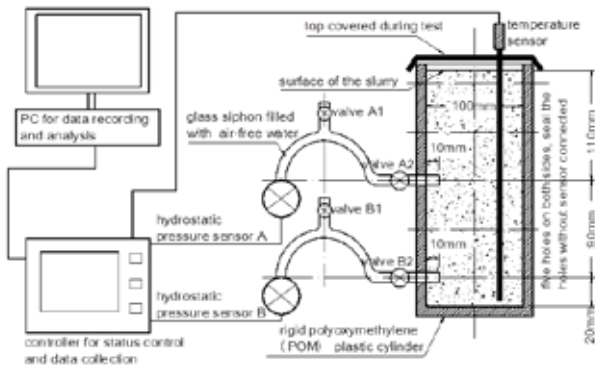


Fig. 1: Hydrostatic pressure test set up for cement paste sedimentation measurement

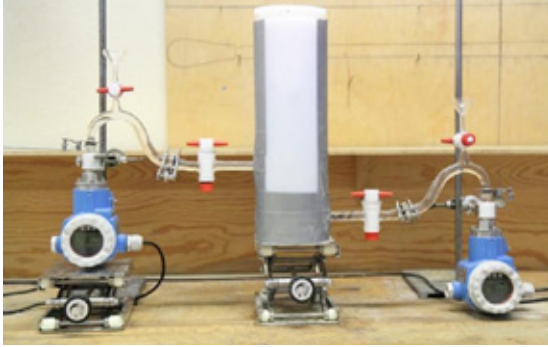


Fig. 2: Hydrostatic pressure test pressure detection system

A range of preliminary tests on limestone slurries and cement pastes have been done to validate the effect of the test set up on the pressure detection. Three different directions of the opening of the intruded glass pipe were investigated: vertically downwards and two horizontal measurements with two different pipe-end designs. It was found [28] that similar pressure changes were observed for all three directions for both limestone slurry and cement paste. Hence, no clear “stress redirection” [29] phenomenon occurs during the test period of HYSPT. The influence of the wall effect on pressure detection was also studied by setting the detection position either near the wall of the cylinder or to the centre of the sample. It seems [16] there is no wall effect even when setting the glass opening at 1cm to the wall of the cylinder. The previous research [16] also investigated the influence of the structural build-up, chemical shrinkage and water re-absorption on the pressure detection. It was found that these affect the pressure change in the magnitude of 100 Pa, which cannot overshadow the main effect of in the order of a thousand Pa pressure drop at a depth of 10 - 20 cm as a result of particle settling during the fresh state of cement paste. In addition, the measurements on the same cement pastes show that HYSPT has a satisfactory repeatability [16] with 1% variation between the detected and the calculated initial pressure, see Fig. 3.

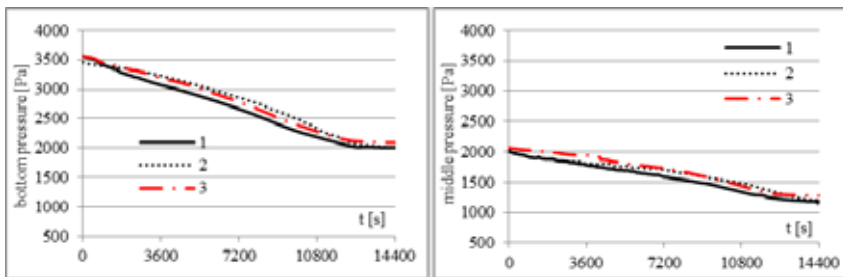


Fig. 3: Repeatability tests for HYSPT for cement pastes with $w/p=0.5$ and 0.3% SP [16]

2.2. Materials

A volume of 2 l cement paste or limestone slurry was prepared. The suspensions were made with a Hobart mixer with the following mixing procedure: the dry cement or limestone powder was mixed at low speed for 1 min; water and superplasticizer was added simultaneously and mixed for 2 min at lower speed 591 rpm; then changed to middle speed 1485 rpm, continued mixing for 1 min, waited for 5 min while using spatula and hand to check the dispersing status and reduce the agglomerates; at last the suspension was mixed at middle speed for 1 min. All

experiments started at around 10 min after water addition to cement. The polycarboxylate superplasticizer (SP) was added to the samples in Fig. 5 and Fig. 6 to investigate the influence of flocculation on sedimentation, see Table 1. The solid content of this PCE SP is 30% and the density is 1090 kg/m^3 ; while lignosulfonate (LS) plasticizer was used for the samples in Table. 2 to study the bleeding of cement paste. Limestone powder ($\rho=2780 \text{ kg/m}^3$) and fly ash cement, CEM-FA, with 20% fly ash (STD-FA CEM II/A-V $\rho=2950 \text{ kg/m}^3$) are used for the samples in Fig. 5 to prepare the suspensions for HYSPT measurements; while Portland cement (STD-CEM I) was used for the samples in Fig. 6 and Table 2. The particle size distributions of the cements and limestone determined by laser diffraction with a Mastersizer2000 are shown in Fig. 4. It can be seen that the cement is finer than the limestone. The recipes of all the tested suspension are shown in Table 1.

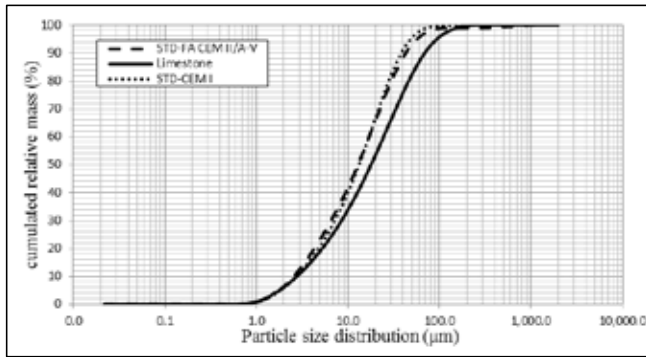


Fig. 4: The particle size distribution of the cement and the limestone powder

Table 1: The recipes of all samples in the following figures with test results

Test No.	Fig. No.	suspension code in the figure	powder type	w/c	w/p	solid vol. fraction Φ	SP type	SP dosage	VMA dosage
1	Fig. 4	cem-sp0.3	CEM-FA	0.625	0.50	0.404	PCE	0.3% lbwp	0
2		cem-no sp	CEM-FA	0.625	0.50	0.404		0.0	0
3		lim-sp0.3	Limestone	0	0.55	0.404	PCE	0.3% lbwp	0
4		lim-no sp	Limestone	0	0.55	0.404		0.0	0
5	Fig. 5	PCE0VMA0	Portland	0.5	0.5	0.388		0	0
6		PCE0VMA2.0	Portland	0.5	0.5	0.388		0	2.0
7		PCE0.6VMA0	Portland	0.5	0.5	0.388	PCE	0.6% lbwc	0
8		PCE0.6VMA2.0	Portland	0.5	0.5	0.388	PCE	0.6% lbwc	2.0
9	Fig. 6	DP24-wc0.5p0.3	Portland	0.5	0.5	0.388	LS	0.3% lbwc	0
10		DP24-wc0.5p0.3	Portland	0.5	0.5	0.388	LS	0.3% lbwc	0
Note:		1. "lbwp" and "lbwc" respectively means liquid by the weight of the powder or cement; 2. the solid fraction is calculated assuming no air voids in the cement pastes.							

3. HYSPT APPLICATION AND DISCUSSION

The previous research [12, 16, 28] indicates that HYSPT measurements can be applied to investigate the sedimentation process, to assess the flocculation state of the suspensions and possibly also to calculate the bleeding rate.

Fig. 5 gives an example of time dependent pressure changes as a result of sedimentation for limestone slurry and cement paste with constant solid volume fraction $\Phi=0.404$ (corresponding to $w/p=0.5$ with fly ash cement). The left plot shows the bottom pressure changes and the right

plot shows pressure changes for the middle level. As particle sedimentation occurs, the pressure decreases due to less particles and thus lower average density for the suspension above the detection level. The sedimentation rates of the suspensions can be assessed with the pressure decreasing gradient dp/dt . It can be seen that the cement pastes and limestone slurries show similar pressure after reaching the plateau, except for the cement paste without SP (cem-no sp). It indicates that the sedimentation processes of cement paste and limestone slurry perform similarly in around 4 h of the test period. A bit lower pressure at the plateau for the cement paste is probably due to the extra pressure drop as a result of cement hydration, structural build-up, bleeding water re-suction etc. The terminal sinking velocity of a particle immersed in a yield stress fluid was reviewed by Roussel [30] based on the Stokes law and the Bingham model. It tells that the particle sinking velocity in a high-concentrated suspension is determined by the density difference of the particle and the fluid, the particle size, the fluid viscosity and the yield stress of the fluid. The classical Richardson-Zaki Equation (R-Z), which explains the particle sinking velocity v_p in a hindered system is also affected by the solid volume fraction of the suspension as shown in Eq. 1:

$$v_p = v_t(1 - \Phi)^n \quad (1)$$

Where v_t is the Stokes terminal sinking velocity of the particle in the laminar flow condition, Φ is the solid volume fraction, n is a coefficient depending on the particle Reynolds Number and will normally be 4.65. However, Fig. 5 shows that the limestone slurries with lower particle density even present high sedimentation rate and thus higher particle sinking velocity. The different flocculation states in cement pastes and limestone slurries cause different sedimentation rates according to our previous research [12]. Therefore, the R-Z is too simplified to take into account both flocculation and solidification for all types of cement and limestone mixes. The reason is that powder types and use of admixtures, especially SP, influence the particle flocculation state and thus change the “effective” particle sizes. Fig. 6 gives a better example for the application of HYSPT to detect the flocculation state of cement paste. The sedimentation process of four cement pastes with the same solid volume fraction ($\Phi=0.388$, $w/c=0.5$ with Portland cement), cement type (Norcem standard cement, CEM I according to EN-197-1) and mixing procedure were compared. The sedimentation rate and the time to reach the plateau indicate the flocculation state of the mixtures. It can be seen that, compared with the reference cement paste without SP (polycarboxylate type in this case, PCE) and VMA (PCE0VMA0), the individual addition of SP (PCE0.6VMA0) induces a lower sedimentation rate although SP can reduce the static yield stress of the liquid phase. It is mainly a result of highly dispersing effect of SP. better dispersed particles have smaller “effective” particle sizes and thus shows lower sedimentation rate. However, the individual addition of VMA (PCE0VMA2.0) results in a higher sedimentation rate, and the combined addition of both SP and VMA (PCE0.6VMA2.0) cause the lowest sedimentation rate. The quite different sedimentation rates between the cement pastes with VMA when combining SP or without SP were concluded to be a result of particle flocculation [12]. VMA increases the viscosity of the fluid phase in cement paste [12, 31] but induces a higher particle sinking velocity. This is mainly because of the flocculation of the high-concentrated mixture. When without combining with SP, The cement paste only with VMA have similar particle flocculation state as those without admixtures. The flocculated particles with much bigger “effective” particle sizes show higher particle sinking velocities even within the liquid with VMA and higher viscosity. The addition of SP overshadows this negative effect from VMA on stability due to the particle dispersing effect as presented previously. Therefore, VMA stabilizes cement paste only when activated by the addition of SP. The combined effect of increased viscosity by VMA and the dispersing effect from SP contribute to stabilize the cement paste more.

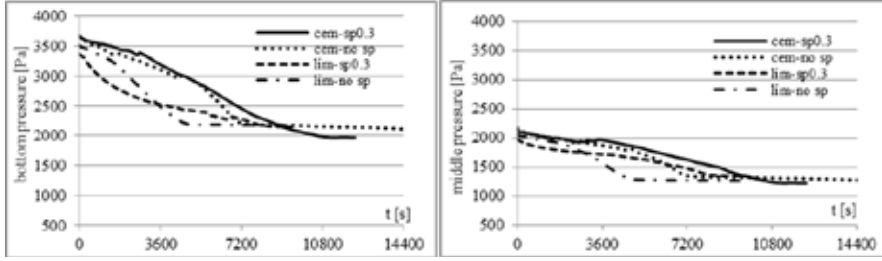


Fig. 5: The pressure vs time curves of cement pastes and limestone slurries (constant volume fraction $\Phi=0.459$) with or without superplasticizer [15]

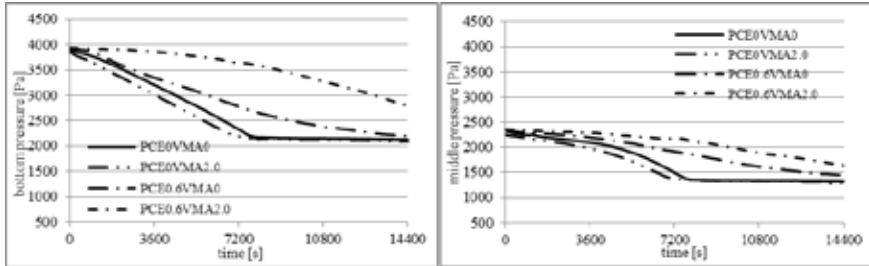


Fig. 6: The pressure vs time curves of cement pastes with or without admixtures including SP and VMA (the number after the admixture is the liquid dosage) [12]

In addition to evaluation of the sedimentation and flocculation state of cement paste and filler modified paste [12, 16, 31], HYSPT was also applied to investigate bleeding of cement paste or matrix. The parallel measurements with HYSPT, in situ volume fraction measurements and bleeding tests shows that it is possible to use the HYSPT results to evaluate the bleeding rate based on proper assumptions [16]. As presented above, the addition of some additives such as SP improves the behaviour compared to the Richardson-Zaki Equation which described that the suspensions with higher solid volume fraction present lower particle sinking velocity. However, they also result in a softer bleeding front and opaque bleeding, which make many classic bleeding measurement methods inapplicable. The evaluation of this turbid bleeding layer could be a difficulty of stability evaluation for cement paste. More recently it was found [28] that the bleeding rate calculated from dp/dt at the position close below the bleeding front by HYSPT are in the same magnitude as the measured bleeding rate from some parallel bleeding measurements, as shown in Table 2. Table 2 compares 4 different values of bleeding: 1) calculated bleeding rate based on top pressure measurements by HYSPT and the assumed sharp front, 2) visual bleeding measurements, 3) Laser detection by TurbidScan for the clear liquid front [32], and 4) Kozeny-carman Equation [33] (see Eq. 2):

$$Q_f = \frac{(1-\Phi)^3}{\Phi} \cdot \frac{(\rho_p - \rho_f) \cdot g}{\mu \cdot k_c \cdot S_0^2} \quad (2)$$

The hydrostatic pressures were measured at around 2cm below the bleeding front (4h) of cement pastes with w/c=0.50 or 0.60 and 0.3% sbwc LS plasticizer (solid dosage by the weight of cement, equal to 0.75% liquid dosage based on 40% concentration of this LS). The calculated bleeding rate from HYSPT results are based on an assumption of the presence of a clear bleeding front and a homogeneous suspension below the bleeding. For the same cement pastes, the bleeding was also measured by the TurbiScan test based on diffraction and penetration of

light and the visual bleeding test. It is also interesting that, based on above assumption, the calculated bleeding rate from dp/dt by the top pressure measurements by HYSPT were found to be closest to the magnitude of the visual bleeding measurements and the theoretical bleeding rate by the classical Kozeny-Carman Equation. The TurbidScan tests show the lowest bleeding value since only the clear bleeding water was considered while the turbid bleeding zone was included into this detection and calculation. Therefore, both the comparison between the parallel measurements and the theoretical calculation indicate the possibility of using HYSPT results to evaluate the bleeding of cement paste.

Table 2: The comparison of the bleeding depths by different measurement methods [28]

time (h)	cement paste	calculated bleeding depth (by HYSPT)				bleeding depth (by TurbidScan)				bleeding depth (by bleeding test)				Calculated bleeding rate by K-C Eq. (m/s)
		absolute (mm)	relative bleeding	linear bleeding rate (m/s)	average linear bleeding rate (m/s)	absolute (mm)	relative bleeding	linear bleeding rate (m/s)	average linear bleeding rate (m/s)	absolute (mm)	relative bleeding	linear bleeding rate (m/s)	average linear bleeding rate (m/s)	
0.5	DP24- w/c 0.5p0.3	3.0	0.015	1.67E-06		0.0	0.000	0.00E+00		1.4	0.007	7.78E-07		
1		4.4	0.022	1.22E-06		0.0	0.000	0.00E+00		2.9	0.015	8.06E-07		
2		5.7	0.029	7.92E-07	9.46E-07	0.0	0.000	0.00E+00	6.02E-09	4.3	0.022	5.97E-07	6.16E-07	1.23E-06
3		6.3	0.032	5.83E-07		0.1	0.002	9.26E-09		5.2	0.026	4.81E-07		
4		6.7	0.034	4.65E-07		0.3	0.007	2.08E-08		6.0	0.030	4.17E-07		
0.5	DP24- w/c 0.6p0.3	3.5	0.018	1.94E-06		1.0	0.022	5.56E-07		--	--	--		
1		5.8	0.029	1.61E-06		1.6	0.036	4.44E-07		3.5	0.018	9.72E-07		
2		7.6	0.038	1.06E-06	1.20E-06	1.9	0.042	2.64E-07	3.20E-07	8.0	0.040	1.11E-06	9.65E-07	1.58E-06
3		8.2	0.041	7.59E-07		2.0	0.044	1.85E-07		10.2	0.051	9.44E-07		
4		9.0	0.045	6.25E-07		2.2	0.049	1.53E-07		12.0	0.060	8.33E-07		

4. CONCLUSION

HYSPT was developed to evaluate particle sedimentation by observing the pressure change and thus the density variation from top to bottom of the suspension. The influences from reactions in the order of one hundred Pa seem to be negligible compared to thousands of Pa pressure drop mainly caused by particle movements. In this paper, by HYSPT measurements, it was found that SP stabilizes the cement paste mainly by dispersing the particles; VMA can also stabilize cement paste only when combined with SP although the viscosity of the fluid is increased. For the turbid bleeding phase of paste, traditional methods are not applicable, but HYSPT measurements seem to give a good indication on the bleeding rate. The calculated bleeding rate based on the top measurements of HYSPT at the level close to the bleeding front shows good correlation to the bleeding measurements and the theoretical bleeding rate calculated with Kozeny-Carman equation.

5. FURTHER RESEARCH

Our previous research [12, 16, 28, 31] has verified that HYSPT can be applied to investigate the sedimentation process of both cement paste, powder suspensions and filler modified paste. HYSPT measurements for filler modified pastes with the same solid fraction show the various flocculation states of the mixtures and thus indicate the effect of different filler additions. The HYSPT results at the top position close to the bleeding front can be used to investigate the bleeding of cement paste.

To understand the stability of SCC, the segregation of coarse aggregate need to be further studied. Some preliminary studies on coarse aggregate sinking within cement paste by HYSPT has been carried out and indicated that the aggregate sinking velocity was very sensitive to the w/c ratio and to the addition of admixtures, especially SP. The pilot tests by HYSPT on coarse

aggregate stability in paste showed a very sharp transition between “floating” and “fast sinking” aggregates. Therefore, the pressure monitoring process should be specially designed to detect the coarse aggregate movement. The other possibility for applying HYSPT to study the coarser particle sinking is to investigate the sedimentation rate of mortar and compare the results with the pressure detection on the corresponding paste. Generally, the study on a combined particle movement process by HYSPT including the coarser aggregate segregation and the fine particle sedimentation can be considered as our further research on this topic and the next step in the further development of HYSPT measurement method. Such investigations will contribute to a better understanding of both aggregate segregation and the impact of cement paste on concrete instability.

ACKNOWLEDGEMENTS

The support from the CONcrete Innovation Center (COIN) and the NTNU concrete laboratory, as well as the discussion with Prof. Erik J. Sellevold, Dr. Tor Arne Hammer and Prof. Sverre Smeplass are gratefully acknowledged.

REFERENCES

1. G. De Schutter, P. J.M. Bartos, P. Domone, J. Gibbs, “Self-Compacting Concrete”, Whittles Publishing, Scotland, UK, 2008
2. H. Vikan, “Means of improving concrete construction productivity – State of the art”, COIN Project report 8, 2008, ISBN 978–82–536–1068–9, 17p.
3. Mørtzell E.; Maage M., Smeplass S., "A Particle-Matrix Model for Prediction of Workability of Concrete", Proceedings from the International Conference on Production Methods and Workability of Fresh Concrete", Glasgow, Scotland 1995
4. Perrot A., Lecompte T., Khelifi H., Brumaud C., Hot J., Roussel N., "Yield stress and bleeding of fresh cement pastes", Cement and Concrete Research, V.42, 2012, pp.937-944
5. Kwan A.K., Fung W.W.S., Chen J.J., “Effects of superplasticizer on rheology and cohesiveness of CSF cement paste”, Advanced in Cement Research, V.24, 2012, pp.125-137
6. Schokker A.J., Hamilton H.R., Schupack M., “Estimating Post-Tensioning Grout Bleeding Resistance Using a Pressure Filter Test”, PCI journal, V.47, 2002, pp.32-39
7. Jossierand L., de Larrard F., “A method for concrete bleeding measurement, Materials and Structures”, V. 37, 2004, pp 666-670
8. Sawaide M., Iketani J., “Rheological analysis of the behavior of bleeding water from freshly cast mortar and concrete”, ACI Materials Journal, V.89, 1992, pp.323-327
9. Kaplan D., “Pompage des betons (concrete pumping)”, research report of LCPC, OA36, 2001, 228p. [in French]
10. Swedish Standard, 'Method for measuring water-separation (Bestämning av betongmassas vattenseparation)', B5-33, 1965 [only available in Swedish].
11. ASTM C 243-95, “Standard test methods for bleeding of cement pastes and mortars”, Annual Book of ASTM Standards, Easton, MD, USA, 1995. 4p.
12. Peng Y.; Jacobsen S., “Influence of water cement ratio, admixtures and filler on sedimentation and bleeding of cement paste”, Cement Concrete Research, V.54, 2013, pp.133-142
13. Rosquoët F., Alexis A., Khelidj A., Phelipot A., “Experimentail study of cement grout: Rheological behavior and sedimentation”, Cement and Concrete Research, V.33, 2003, pp.713-722

14. Chen F.P., Mao Y.H., Liu C.S., "Premixed injectable calcium phosphate cement with excellent suspension stability", *Journal of Material Science: Materials in Medicine*, V.24, 2013, pp.1627-1637
15. Cepuritis R., Wigum B.J., Garboczi E.J., Mørtzell E., Jacobsen S., "Crushed concrete aggregate fines: pore structure, specific surface, particle shape and size distribution", *Cement and Concrete Composite*, accepted and in press, 2014
16. Peng Y.; Jacobsen S., Weerd K. De; Pedersen B., "Model and methods for stability of fresh cement pastes", *ASTM-Advances in Civil Engineering Materials*, V.3, 2013, pp.1-24, doi:10.1520 /ACEM20130097. ISSN 2165-3984
17. Williams R.A.; Xie C.G., Bragg R., Amarasinghe W.P.K., "Experimental techniques for monitoring sedimentation in optically opaque suspensions", *Colloids and Surfaces*, V.43, 1990, pp.1-32
18. Steinour H.H., "Rate of sedimentation: Nonfloculated suspensions of uniform spheres", *Industrial and Engineering Chemistry*, V.36, 1944, pp.618-624
19. Mori T., Kuno K., Ito M., Tsubaki J., Sakurai T., "Slurry characterization by hydrostatic pressure measurement – analysis based on apparent weight flux ratio", *Adv. Powder Tech.*, V.17, No.3, 2006, pp.319-332
20. Roffle J.F., "Pressure variation within concentrated settling suspensions", *Journal of Physics D: Applied Physics*, V.9, No.8, doi:10.1088/0022-3727/9/8/010
21. King A., Roffle J.F., "Studies on the settlement of hydrating cement suspensions", *Journal of Physics D: Applied Physics*, V.9, 1976, pp.1425-1443
22. Wittman F. H., "On the action of capillary pressure in fresh concrete", *Cem. Conc. Res.*, V. 6, 1976, pp.49-56
23. Hammer T. A., "Effect of silica fume on the plastic shrinkage and pore water pressure of high-strength concrete", *Mat. Struc.*, V.34, 2001, pp.273-378
24. Radocea A., "A Study on the Mechanism of Plastic Shrinkage of Cement-Based Materials", PhD thesis, Chalmers University of Technology, Göteborg, 1992, 278p.
25. Radocea A., "A new method for studying bleeding of cement paste", *Cement and Concrete Research*, V.22, 1992, pp.855-868
26. Amziane S., "Setting time determination of cementitious materials based on measurements of the hydrostatic pressure variations", *Cem. Conc. Res.*, V.36, No.2, 2006, pp.295-304
27. Endress + Hauser, "Functional Manual for Cerabar-S PMC71, Process pressure and level measurement with output signal 4...20mA", Maulburg, Germany, 2008, 44p.
28. Peng Y., "Sedimentation and bleeding of cement paste", PhD thesis at Norwegian University of Science and Technology, 2014:89, Trondheim Norway, ISBN 978-82-326-0102-8 (printed ver.), ISBN 978-82-326-0103-5 (electronic ver.)
29. Amziane S., "Setting time determination of cementitious materials based on measurements of the hydrostatic pressure variations", *Cem. Conc. Res.*, V.36, No.2, 2006, pp.295-304
30. Roussel N., "A theoretical frame to study stability of fresh concrete", *Materials and Structures*, 2006, DOI 10.1617/s11527-005-9036-1
31. Peng Y., Jacobsen S., De Weerd K., Pedersen B., Marstrander B. B., "Overview of rheological parameters affecting stability of SCC", *CANMET/ACI SP-288.33, Proceedings of the Tenth International Conference on Superplasticizers and Other Chemical Admixtures in Concrete*, 2012, Prague, pp.481-496
32. Mengual O., Meunier G., Cayre I., Puech K., Snabre P., "TURBISCAN MA 2000: multiple light scattering measurement for concentrated emulsion and suspension instability analysis", *Talanta*, V.50, 1999, pp.445-456
33. Carman P.C., "Fluid flow through granular beds". *MIT Chem Eng.*, V.15, 1937, pp.150-166.

Quantification of the interference of localised corrosion on adjacent reinforcement bars in a concrete beam in bending



Mahdi M. Kioumars
B.Sc. Eng., M.Sc. Eng, PhD Candidate
NTNU, Department of Structural Engineering
Rich. Birkelandsvei 1A,
NO-7491, Trondheim, Norway
E-mail: mohammad.kioumars@ntnu.no



Max A.N. Hendriks
Professor
NTNU, Department of Structural Engineering
Rich. Birkelandsvei 1A,
NO-7491 Trondheim, Norway
TU Delft, Department of Structural Engineering
Stevinweg 1,
NL-2628CN, Delft, the Netherlands
E-mail: max.hendriks@ntnu.no



Mette R. Geiker
Professor
NTNU, Department of Structural Engineering
Rich. Birkelandsvei 1A,
NO-7491, Trondheim, Norway
E-mail: mette.geiker@ntnu.no

ABSTRACT

In this paper, the interference of localised corrosion on adjacent reinforcement bars in a concrete beam in bending is quantified. The focus is on the influence on the bending ultimate limit state. The effect of four parameters was investigated using the response surface method (RSM) and non-linear finite element analysis. The parameters considered are amount of localised corrosion, ratio of pit distance on adjacent bars to rebar distance, concrete compressive strength, and rebar tensile strength. Based on the obtained results, a modified analytical design rule was proposed to calculate the ultimate limit state by taking into account the ratio of pit distance on adjacent bars to rebar distance.

Key words: RSM, Concrete structure, localised corrosion, pitting corrosion, bending ultimate limit state, finite element analysis.

1. INTRODUCTION AND BACKGROUND

The corrosion process of reinforcing bars in Reinforced Concrete (RC) structures transforms steel into rust, leading to uniform and localised loss of rebar cross section, volume expansion

causing cracking and spalling of the concrete cover, bond deterioration, and impaired mechanical properties of corroded rebars [1]. Laboratory and field observations of deteriorated RC show that corrosion damage in structural elements exposed to chlorides is not homogenous, but spatially variable along and around the rebars [2, 3]. Localised corrosion of reinforcing bars of RC structures exposed to chloride environments can cause significant reductions in cross section areas for reinforcing bars, for example around 50% loss of cross section was observed for a 27-year-old naturally corroded beam [2]. Localised corrosion is of particular concern since the loss of cross sectional area can be quite high and may not necessarily be associated with visual damage (cracking).

There are a number of experimental investigations quantifying the effects of the corrosion on the structural behaviour of RC beams or slabs [2-9]. For a review of some of these experimental results for yield load capacity, serviceability limit state and ductility, see Kallias et al. [10]. In the majority of the published experimental investigations, the effect of average corrosion levels on the structural performance is considered.

A summary of available experimental results on the remaining yield capacity and ultimate limit state (ULS) for corroding under-reinforced beams and slabs are presented in Figure 1. In some of the references the average cross section reduction or mass loss were given, in others [2] more detailed data for the extent of corrosion along the rebar were provided from which the average corrosion was calculated. The yield capacity and ULS are presented normalized to the non-corroded capacities and as a function of the average cross section reduction percentage. Substantial scatters in the results are observed: the R-squared statistics of linear regressions are as low as 0.1150 and 0.2175 for the residual ULS and the yield load capacity, respectively. In some of the investigations, for example results presented by Du et al. [6] and Torres et al. [3], beams with similar average cross section reductions did not show similar reduced capacity (see Figure 1a and b). This obstructs the ability of making reliable conclusions on the residual performance of corroding under-reinforced beams by using the average loss in cross sectional area of steel bar. The large scatter of data suggests that other parameters affect the structural performance; the value of maximum cross section reduction might correlate better with the remaining capacities.

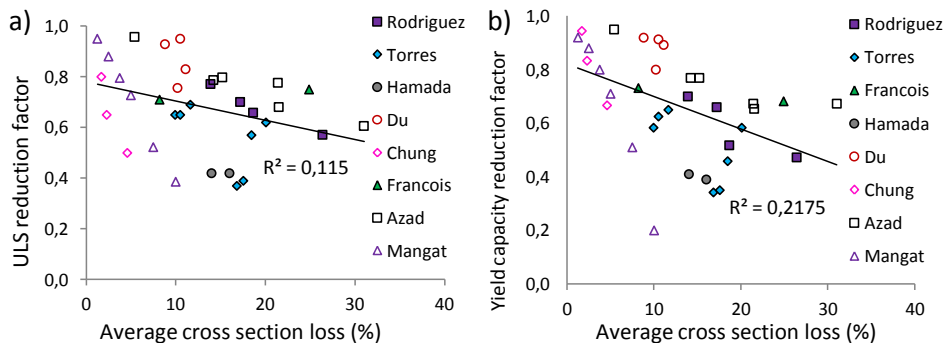


Figure 1 – Reduction factor of the ultimate limit state (ULS) and yield capacity as a function of the average cross section reduction of the rebars. Literature data [2-9].

Figure 2a and b again summarise available data on the normalised reduced ULS and yield capacity, but now, as a function of maximum cross section reduction in the bending zone. The maximum cross section reduction is the sum of average cross section and the localised cross

section loss, deducting the overlapping area (see principle in Figure 3d, which illustrates the calculation for the combination of uniform and localized corrosion). A model by Val and Melchers [11] was used to calculate the cross section reduction due to localised corrosion (A_{pit}) from the maximum pit depth. In Figure 2a and b an improved linear regression is obtained with substantially higher R-squared values. It indicates that the capacity losses are a function of maximum cross section loss of the reinforcing steel. Therefore, to assess the structural performance of corroded RC member in numerical analysis, amount and location of the pitting corrosion should be taken into account in addition to the extent of uniform corrosion.

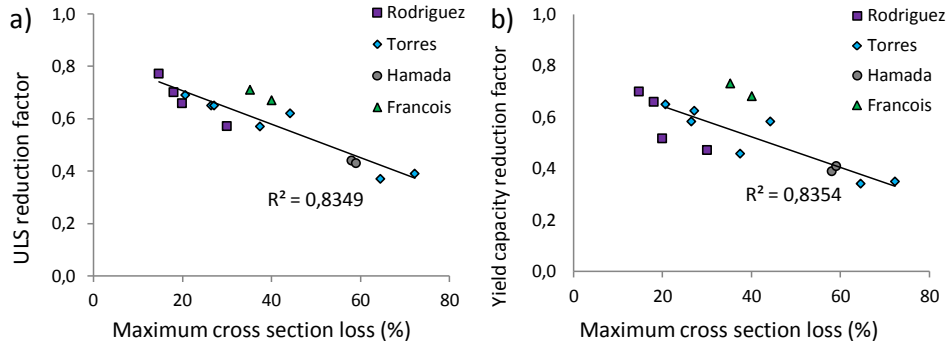


Figure 2 – Reduction factor of the ultimate limit state (ULS) and yield capacity as a function of maximum cross section reduction of rebars. Literature data [2, 3, 7, 9].

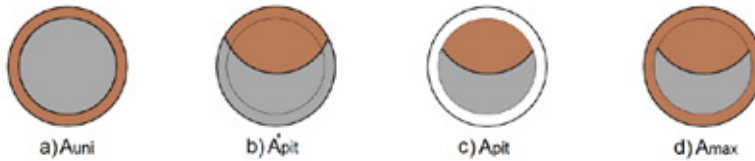


Figure 3 – Cross section reduction due to corrosion, a) uniform cross section reduction, b) pit area loss, c) pit area loss without overlapping uniform corrosion and d) maximum cross section reduction.

Experimental tests reported by Francois et al. [2] (Figure 4) show that in naturally corroded beams not only loss of cross section varies along the tensile rebars, but also loss of cross section differs between rebars. It can be attributed to a variety of reasons, such as heterogeneous quality of concrete, especially at the concrete-steel interface, potential cracks, variation in cover thickness, and the stochastic nature of the corrosion process in the presence of chloride [2].

The dissimilarities of the cross section profiles of adjacent bars, raises the question on how to assess this mechanically. The ratio of the localised cross section reduction (see Figure 3c) to the original area of the rebar (A_{pit}/A_0) and the ratio of the longitudinal pit distances to the rebar distance (l_p/l_r) (see Figure 5) are considered as explanatory parameters both are varying along the corroded RC element.

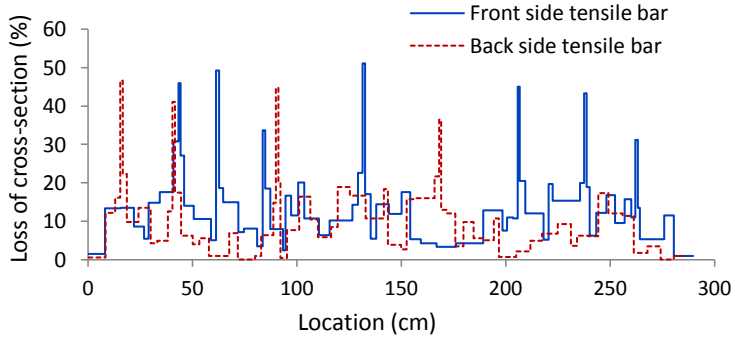


Figure 4 – Loss of cross section due to corrosion along the back tensile rebar and the front tensile rebar [2].

An idealized case introduced in an earlier study of the authors [12] was selected to quantify the interference of localised corrosion on adjacent rebars in an under-reinforced beam subjected to bending. In the idealized case two adjacent rebars each have one corrosion pit and the influence of l_p/l_r with one size of the pit ($A_{pit}/A_0 = 0.26$) on the bending ULS was quantified for a fixed rebar distance ($l_r = 80$ mm). Depending on the longitudinal distance of the two pits, l_p , the interaction of localised corrosion in adjacent bars is analysed. This leads to a gradual reduction of the bending ULS for decreasing distances between the pits, starting at a critical distance.

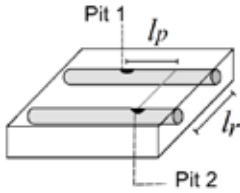


Figure 5 – Pit distance (l_p) and rebar distance (l_r) in an idealized case.

Apart from A_{pit}/A_0 and l_p/l_r , there are other variables which could have an influence on the performance of the corroded structures such as concrete properties and steel properties. It is difficult to design and perform a set of experimental tests to quantify and isolate the effect of each of the variables. Numerical studies are seen as an option to overcome these limitations. Although numerical modelling can achieve reliable results, due to the number of variables and their possible interaction a systematic statistical model is required to analyse the results. Among the many statistical models in literature, the response surface methodology (RSM) has been commonly used in recent years [10, 13, 14]. It allows assessing the (quadratic) interaction of the variables.

The present work adopts the idealized case with two adjacent bars, each having one corrosion pit. The effect of selected variables on the interference of localised corrosion on adjacent reinforcement bars in an under-reinforced concrete beam in bending is quantified. The RSM is used to study the interaction effects of four variables: A_{pit}/A_0 , the l_p/l_r ratio concrete compressive strength and rebar tensile strength. Based on the results, a modification of the analytical design rules to determine the bending ULS of a beam is proposed which takes into account the l_p/l_r ratio. In this paper, to avoid the repetition, “ULS” is used for “bending ULS”.

2. FINITE ELEMENT MODELLING OF CORRODED BEAMS

2.1 Selected experimental case

Since under-reinforced beams are most common in practice only this type of beam was considered. The beams for numerical simulations were selected from experimental tests by Rodriguez et al. [15]. A reference beam (no. 111), a slightly corroded beam (no. 115) and a severely corroded beam (no. 116) were selected. Rodriguez et al. tested the effect of reinforcement corrosion on RC beams loaded in a four-point bending test. Geometry dimensions and rebar detailing of the selected simply supported beams are shown in Figure 6. The amount of the average corrosion and maximum pit depth on the tensile reinforcement was 0.39 mm and 1.0 mm (14% and 2% steel cross section loss) in beam no. 115 and 0.71 mm and 2.1 mm (26% and 8% steel cross section loss) in beam no.116. In the following it is assumed that uniform cross section reduction is equal to average cross section reduction. To calculate the loss of cross section due to localised corrosion (A_{pit}) the model which has been recommended by Val and Melchers [11] was used, which was also used in section 1 to evaluate literature data.

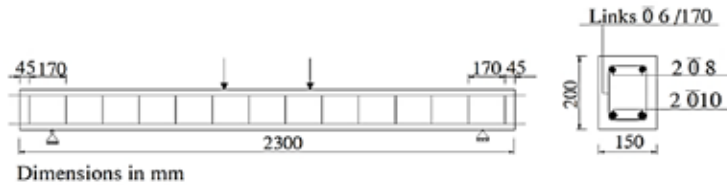


Figure 6 – Geometry of under-reinforced beams investigated by Rodriguez et al. [15].

The reference beam (no. 111) showed flexural failure due to yielding of the reinforcement tensile bars. For increasing level of corrosion, the ULS is reduced and the behaviour became less ductile. The corroded beams (no.115 and 116) failed by failure of the tensile bars at pit locations.

2.2 FE model

Full 3D non-linear finite element (FE) analyses were carried out. The concrete was modelled using eight-node solid elements. The reinforcements were modelled as two-node straight truss elements. Interaction between the reinforcement and the concrete was modelled with 2+2 node line interface elements. Only one half of the beams were modelled to take advantage of the symmetry in geometry and loading conditions, implicitly assuming that also the corrosion damage was symmetric. Vertical displacement increments were applied at the loading point in the model, with step sizes of 1 mm (see Figure 7). The Newton-Raphson iterative approach was selected to solve the non-linear problem.

In all 3D FE models, the corroded reinforcement bars were discretised into a series of small sections with length $L=100$ mm containing elements with 20 mm length. Pit cross section reduction was applied for each tensile reinforcing steel rebar in the middle element of the assigned section. Furthermore, reduction in yield and ultimate strength of the rebar due to localised corrosion were applied along the section containing the pit.

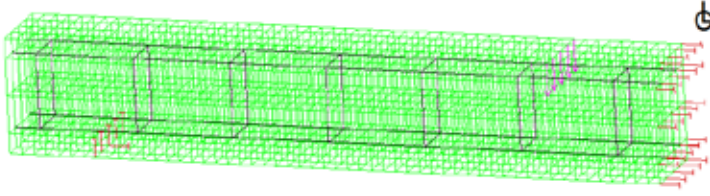


Figure 7 – Mesh size and finite element model of one half of the beam.

2.3 Material properties

For the concrete behaviour a smeared rotating crack model with Hordijk tension softening and an elastic-ideally plastic model in compression were used [16]. The ultimate tensile strain in the Hordijk model is given by:

$$\varepsilon_{nn,ult}^{cr} = 5.136 \frac{G_f^I}{h f_t} \quad (1)$$

where, G_f^I is the Mode-I fracture energy, f_t is the tensile strength of concrete and h is the crack bandwidth taken as the cubic root of the element volume [16]. The concrete had a uniaxial compressive strength of 50 MPa in the reference beam (no. 111) and 34 MPa in the corrosion damaged beams (no. 115 and no. 116). The remaining concrete properties were derived from the compressive strengths using the *fib* model code 2010 [17].

For the constitutive behaviour of the rebars a standard elastic-plastic model with linear hardening was used. The yield strength f_y , the ultimate strength f_u and the elastic modulus E_s for the steel reinforcement are given in Table 1. The ultimate deflection of beam no. 115 is available from the experiment and equals 34.6 mm. In the FE analysis of beam no. 115, a maximum strain in the tensile bars at the ultimate deflection, i.e. 34.6 mm, was recorded. This strain is considered as the ultimate strain of the tensile rebar: $\varepsilon_{su} = 0.08$. The same value was used in the analyses of the other beams. The corresponding load at the ultimate deflection of the beam is considered as the ULS. Note that in the FE model the resulting ductility of a bar is the result of both the ultimate strain and the locally reduced cross section of the bar. As a result of the local reduction of the cross section, due to strain localization at the pit locations, the bars of the severely corroded beams will behave less ductile, even when the ultimate strain of the material is the same. This relatively simple way of taking into account the reduced ductility was selected in absence of experimental data of the ductility of the bars.

Table 1 – material properties of steel for corroded and non-corroded models

Steel Properties	Type of bar	Reference beam (no. 111)	Corroded beam (no. 115)	Corroded beam (no. 116)
Yield / Ultimate strength (MPa)	Stirrups ($\phi 6$)	626 / 760	506 / 610	451 / 550
	Compressive bar ($\phi 8$)	615 / 673	615 / 673	615 / 673
	Tensile bar ($\phi 10$)	575 / 655	569 / 648	552 / 626
Young's modulus (GPa)	All	206	206	206

The presence of localised corrosion may cause significant degradation of the mechanical properties of the rebar due to local stress concentrations [18-20]. In the present study these are taken into account by using reduced yield and ultimate strength properties [20]:

$$f_y^D = (1 - \alpha_y(A_{pit}/A_0)100)f_{yo} \quad (2)$$

$$f_u^D = (1 - \alpha_u(A_{pit}/A_0)100)f_{uo} \quad (3)$$

where f^D and f_0 denote residual and initial strengths respectively, A_{pit} is the pit area, A_0 is the cross sectional area of the non-corroded rebar, $\alpha_y = 0.005$, and $\alpha_u = 0.005$ [20]. As a result of uniform corrosion, the rebar diameter is reduced. The sum of localised (A_{pit}) and uniform corrosion area (A_{uni}) was subtracted from the original steel cross section (A_0). Since the rebars are modelled as truss elements the shape of residual area is not relevant. As it mentioned before, it was assumed that uniform cross section reduction is equal to uniform cross section reduction.

2.4 Bond-slip model

An interface layer was modelled along the tensile rebars, using line-to-solid interface elements, to consider the effect of bond-slip. For corroded and non-corroded beams, bond-slip behaviour based on the *fib* 2010 model code [21] for beams confined with steel stirrups was adopted. In this study, the bond slip behaviour was modified based on the amount of the uniform corrosion and kept constant along the tensile rebar. In addition, the bond strength was calculated using Eq. (4), which describes the effect of concrete and stirrup confinement on bond strength [22].

$$U_{max}^D = R[0.55 + 0.24(c/d_0)]\sqrt{f_c} + 0.191\left(\frac{A_{sw}f_{yt}}{s_s d_0}\right) \quad (4)$$

where, U_{max}^D is the reduced bond strength, c is the thickness of concrete cover, d_0 is the diameter of the anchored rebar, f_c is the concrete compressive strength, A_{sw} and f_{yt} are the stirrups cross section and the stirrup yield strength respectively, s_s is the stirrup spacing and R is a factor which is a function of the amount of corrosion [22]. The value of the R for the corroded beams no. 115 and no. 116 is 0.76 and 0.48 respectively. Considering the limited amount of corrosion products generated by the pits, in this paper it is assumed that a pit has no effect on the local bond behaviour.

2.5 Comparison FE analysis results with experimental data and analytical calculations

Since rebar corrosion affects the ultimate capacity, the ULS of corroded and non-corroded beams were assessed. For the non-corroded (no. 111), less (no. 115) and highly (no. 116) corroded beams the load-displacement curves of the 3D FE analyses indicate good agreement for the ULS with experimental observations, as shown in Figure 8a to c.

To further validate the FE models comparisons were made with analytical analyses. The ULS of the beams were calculated using the ACI code, where the material properties of corroded reinforcement were selected on the basis of the methodology described in Section 2.3. Figure 8 also shows that the analytical calculations are in good agreement with the FE results and experimental data.

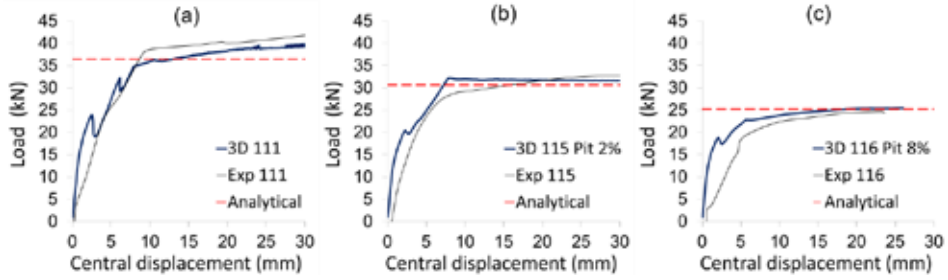


Figure 8 – Load-displacement curve for 3D FE simulation and experimental results of (a) non-corroded beam no. 111, (b) corroded beam no. 115 (14% uniform plus 2% localised steel cross section loss) and (c) corroded beam no. 116 (26% uniform plus 8% localised steel cross section loss); experimental data from [15].

2.6 Variation studies with different pit distances

Different FE analyses with the same ratio $A_{pit}/A_0 = 26\%$ and with varying distances between pits in longitudinal direction by were performed [12]. Figure 9 indicates that reducing the pit distance from 100 mm to 0 mm leads to around 17% reduction of the ULS of the corroded beam. This can be explained by the interference of the localised corrosion in multiple tensile rebars resulting in a different number and orientation of bending cracks. Figure 10 shows the crack pattern in terms of maximum principle strain for three different pit distances on adjacent bars in longitudinal direction, i.e. 0, 40 and 120 mm. When the distances between pits is zero, there is only one main bending crack crossing both pits (Figure 10 a). When the distances between pits increase to 40 mm, a skew crack between the pits appears, still crossing both pits (see Figure 10 b). In contrast, when the pit distance is 120 mm, there is no skew crack between the pits and each pit initiates a separate crack (see Figure 10 c).

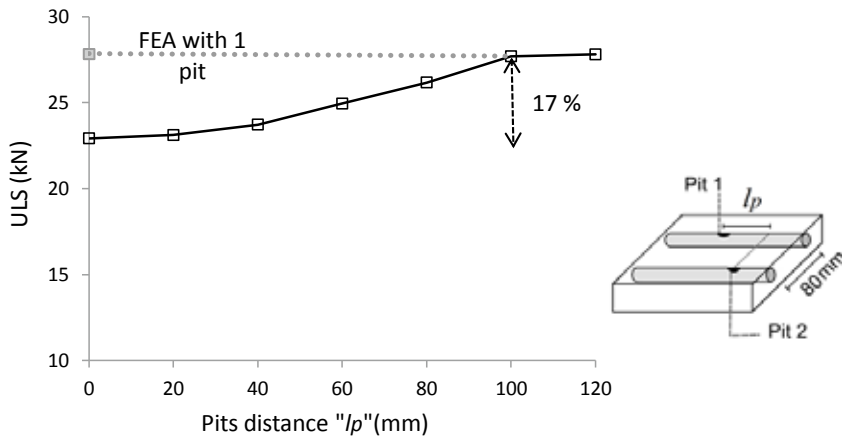


Figure 9 – Effect on ULS of varying pit distance on adjacent bars in longitudinal direction (l_p), 14% uniform plus 26% localised steel cross section loss along each bar [12].

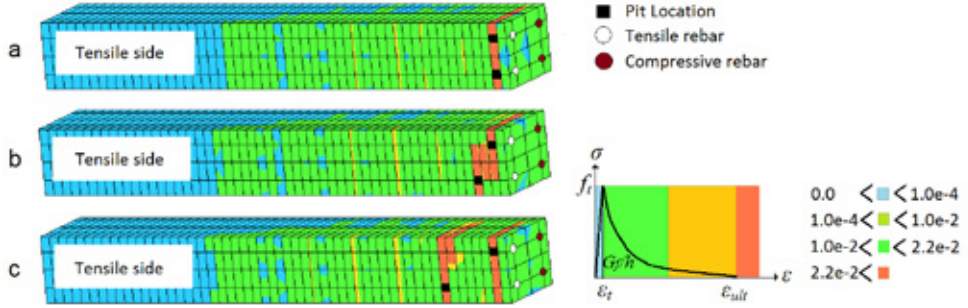


Figure 10 – Crack patterns in terms of maximum principle tensile strains from 3D numerical analyses, pit distance in longitudinal direction on adjacent bars a) 0 mm, b) 40 mm and c) 120 mm [12].

In order to study the possible effect of the mesh alignment in relation to the crack formation and propagation, alternative models with different mesh alignments were explored in a separate study. A limited effect on the crack patterns was observed and the load deflection curve was not altered [23].

3. RESPONSE SURFACE METHOD (RSM)

The Response Surface Method (RSM) is a collection of statistical and mathematical techniques useful for developing, improving, and optimizing processes. It also has important applications in the design, development, and formulation of new products, improvement of existing product designs [6], and more recently in reliability analysis [24, 25]. In this paper RSM is used to approximate and interpret the relationship between the ULS of the corroded beams, termed as “response” and the corrosion pit, concrete properties, and steel properties, termed as (design) “variables”. The approximation of this relationship or performance function is termed “response surface”.

3.1 Design of response surface

In this study the performance function is approximated with a second-order polynomial function, which for k random variables is expressed as:

$$Y = \beta_0 + \sum_{i=1}^k \beta_i X_i + \sum_{i=1}^k \beta_{ii} X_i^2 + \sum_{i < j}^k \beta_{ij} X_i X_j \quad (5)$$

where, Y is the predicted response, X_i is the coded level of a design variable i , k is the total number of variables present in the problem, coefficient β_0 is a constant and β_i , β_{ii} and β_{ij} are the regression coefficients for the linear, quadratic and interaction effects, respectively.

The most popular available design for fitting a second-order model is the central composite design (CCD). The total number of design points in CCD is 2^k factorial points, $2k$ axial points and one centre point. This is illustrated in Figure 11 for $k = 3$. In case, using half fractional factorial points instead of complete factorial points the number of fractional point is reduced to 2^{k-1} .

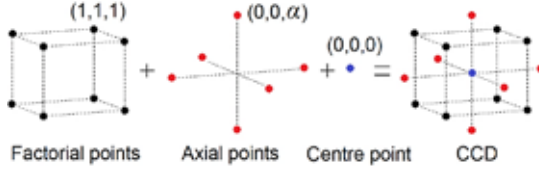


Figure 11 – Experimental design for the fitting of a second-order model for $k = 3$, central composite design (CCD)

In CCD the coded distance of the axial points from the centre point in order to make the design rotatable is given by [26]

$$\alpha = \sqrt[4]{2^k} \quad (6)$$

The specific choices for the variables and its coding are presented in the next section.

3.2 Variables and levels

The ULS of the corroded beams is the response of the RSM. Four basic variables are included in the RSM model: localised corrosion ratio ($A_{pit}/(A_0 - A_{uni})$) (which in the following is approximated to (A_{pit}/A_0)), pit distance to rebar distance ratio (l_p/l_r), concrete compressive strength (f_c) and rebar tensile strength (f_y). (A_{pit}/A_0). In order to study the combined effects of these variables, FE analyses were conducted with different combinations of variables. The CCD uses five levels for each variable: the factorial zero level ($X_i = 0$), the one levels ($X_i = \pm 1$) and the axial points ($X_i = \pm \alpha$), where α equals 2 for four variables. The following upper and lower levels of each uncoded variable x_i are used.

- l_p/l_r : Relevant values for this variable are expected to be in the range of 0.0 to 1.25, see Figure 9. Since the selected RSM model is quadratic in its variables the range for this variable is confined to $x_1^{(-2)} = 0.0$ to $x_1^{(+2)} = 1.0$.
- A_{pit}/A_0 : For $A_{pit}/A_0 = 0$, i.e. no pitting corrosion, the pitting distance l_p/l_r has no physical meaning and consequently the response should not be a function of the l_p/l_r ratio. Since the modelling of interacting variables in the RSM is relatively simple, by a single $X_i X_j$ term, it is not favourable to include $A_{pit}/A_0 = 0$ in the range. Relatively arbitrary, the range for this variable has been set from $x_2^{(-2)} = 0.05$ to $x_2^{(+2)} = 0.45$. In the FE analyses, the pitting corrosion cross section loss (A_{pit}) was added to the uniform cross section loss (A_{uni}).
- f_c & f_y : In the selected under-reinforced beam the actual values for f_c and f_y are 35 and 575 MPa. Since the selected RC beams for this numerical study are supposed to be well-designed leading to a flexural failure mode, relatively small variations of these variables are considered. Changing of the failure mode of the beam will be avoided. For f_c a range from $x_3^{(-2)} = 25$ to $x_3^{(+2)} = 45$ MPa is considered, for f_y the range extends from $x_4^{(-2)} = 500$ to $x_4^{(+2)} = 600$ MPa.

Table 2 lists the variables, and the design of the considered levels. For statistical calculations, the variables x_i were coded linearly as:

$$X_i = 4 \frac{x_i - x_i^{(0)}}{x_i^{(+2)} - x_i^{(-2)}} \quad (7)$$

where X_i is the coded value, x_i the uncoded value, $x_i^{(0)}$ the value of x_i at the centre point.

Table 2 – Uncoded and coded values of independent variables used for the experimental design

No.	Variable	Unit	Notation	Levels				
				Axial (-α)	Factorial			Axial (+α)
					Low (-1)	Centre (0)	High (1)	
1	Pit's distance	-	l_p/l_r	0	0.25	0.5	0.75	1
2	Pit depth/diameter	-	A_{pit}/A_0	0.05	0.15	0.25	0.35	0.45
3	Concrete compressive strength	MPa	f_c	25	30	35	40	45
4	Tensile rebar yield strength	MPa	f_y	500	525	550	575	600
1-4	Coded values (X_i)	-	-	-2	-1	0	1	2

3.3 Overview of the central composite design (CCD)

According to CCD, with four control factors, a total of 25 numerical experiments need to be performed as shown in the first six columns of Table 3. These are the sets of variables which distinguish the various FE analyses. It is assumed that the other concrete properties, i.e. modulus of elasticity (E_c), tensile fracture energy (G_f) and tensile strength (f_{ct}) are fully correlated to the concrete compressive strength.

Table 3 – The used CCD for four variables, FE analysis results for the ULS and the response predicted by the RSM

	Run order	Uncoded variables				ULS	
		l_p/l_r	A_{pit}/A_0	f_c (MPa)	f_y (MPa)	FE anal. (MPa)	Predicted (MPa)
Factorial	1	0.25	0.15	30	525	24.71	24.77
	2	0.75	0.15	30	525	25.93	25.95
	3	0.25	0.35	30	525	17.81	17.80
	4	0.75	0.35	30	525	19.07	19.14
	5	0.25	0.15	40	525	26.40	26.32
	6	0.75	0.15	40	525	27.45	27.49
	7	0.25	0.35	40	525	18.35	18.48
	8	0.75	0.35	40	525	19.80	19.82
	9	0.25	0.15	30	575	26.56	26.54
	10	0.75	0.15	30	575	27.76	27.74
	11	0.25	0.35	30	575	18.95	19.02
	12	0.75	0.35	30	575	20.31	20.38
	13	0.25	0.15	40	575	28.14	28.19
	14	0.75	0.15	40	575	29.38	29.38
	15	0.25	0.35	40	575	19.82	19.80
	16	0.75	0.35	40	575	21.11	21.16
Axial	17	0.00	0.25	35	550	22.70	22.66
	18	1.00	0.25	35	550	25.26	25.19
	19	0.50	0.05	35	550	30.78	30.81
	20	0.50	0.45	35	550	15.75	15.61
	21	0.50	0.25	25	550	21.59	21.52
	22	0.50	0.25	45	550	23.89	23.85
	23	0.50	0.25	35	500	21.69	21.62
	24	0.50	0.25	35	600	24.76	24.73
Centre	25	0.50	0.25	35	550	23.16	23.16

4. RSM RESULTS AND INTERPRETATION

This section presents the predicted responses from the RSM model and discusses the effects of the variables on the ULS of the beam.

4.1 RSM result

The resulting RSM regression model using coded variables is

$$\begin{aligned}
 ULS = 23.16 & \\
 & + 0.633(X_{l_p/l_r}) - 3.799(X_{A_{pit}/A_0}) + 0.581(X_{f_c}) + 0.777(X_{f_y}) \\
 & + 0.192(X_{l_p/l_r}^2) + 0.013(X_{A_{pit}/A_0}^2) - 0.118(X_{f_c}^2) + 0.003(X_{f_y}^2) \\
 & + 0.041(X_{l_p/l_r}X_{A_{pit}/A_0}) - 0.001(X_{l_p/l_r}X_{f_c}) + 0.007(X_{l_p/l_r}X_{f_y}) \\
 & - 0.217(X_{A_{pit}/A_0}X_{f_c}) - 0.137(X_{A_{pit}/A_0}X_{f_y}) + 0.024(X_{f_c}X_{f_y})
 \end{aligned} \tag{8}$$

For the definitions of the coded variables, the reader is referred to the previous section. The last two columns in Table 3 list the FE analyses results for the ULS and the predicted results according to Equation 8. The regression model coincides well with the test data with an adjusted $\bar{R}^2 = 0.994$, within the defined ranges of the variables. Figure 12 indicates the normal probability distribution diagram of the residuals (the difference between FEA results and predicted responses by Eq. 8). According to the plot, the residuals are approximately normally distributed on both sides of 0.0.

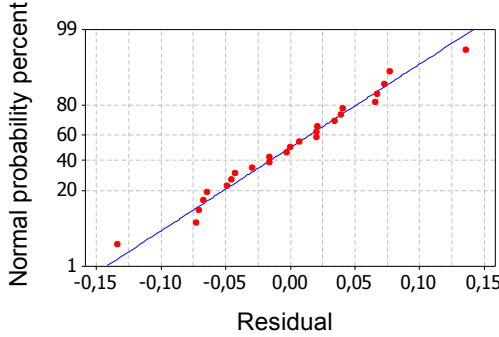


Figure 12 – Normal probability plot of residuals for ultimate load

In the next subsections Equation (8) is interpreted in terms of uncoded variables. The emphasis is on the l_p/l_r variable. The main question is whether the effect of the l_p/l_r variable, as shown in Figure 9, is influenced by the other variables.

4.2 Effect of concrete compressive strength

The influence of f_c on the residual ULS for different amount of localised corrosion is presented in Figure 13a. The graphs have been normalized at $A_{pit}/A_0 = 0.05$. Figure 13a shows that: (i) there is a clear negative linear relationship between the ULS and A_{pit}/A_0 which upon

extrapolation to $A_{pit}/A_0 = 1.0$ will approach 0.0 and (ii) the f_c is not influencing this trend. Both observations are expected from the analytical design rules and are in agreement with previous RSM results [7].

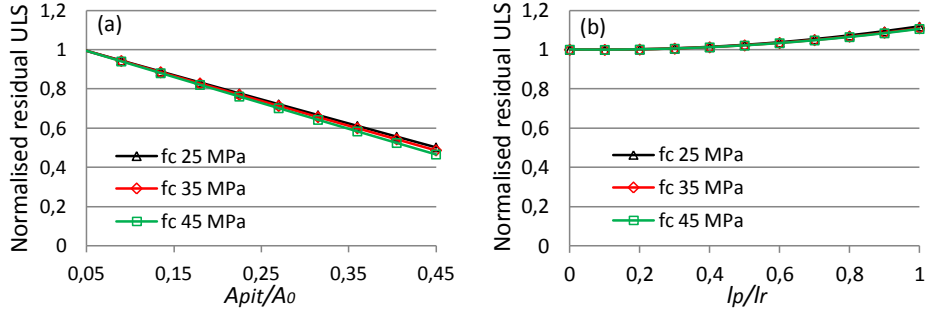


Figure 13 – Effect of f_c on the normalised residual ultimate limit state (ULS) with different amount of localised corrosion and different pit distances. The hold values are a) $l_p/l_r = 1$, $f_y = 575$ MPa and b) $A_{pit}/A_0 = 0.25$, $f_y = 575$ MPa.

Figure 13b presents the effect of f_c on the residual ultimate load for different ratios l_p/l_r . The graphs have been normalized at $l_p/l_r = 0.0$. The rate of the reduction of the ULS, for decreasing distances between the pits, is hardly influenced by f_c . As it is noted before, the fracture energy, module of elasticity and tensile strength are recalculated using the corresponding values of f_c .

4.3 Effect of rebar yield strength

Figures 14a and 14b show similar graphs as Figures 13a and 13b but now for different f_y values instead of f_c . Also the interpretation of these results is similar as for f_c . Again the dependency of the normalised ULS on the A_{pit}/A_0 ratio is in line with the analytical design rules. The f_y values have a limited influence on the trends.

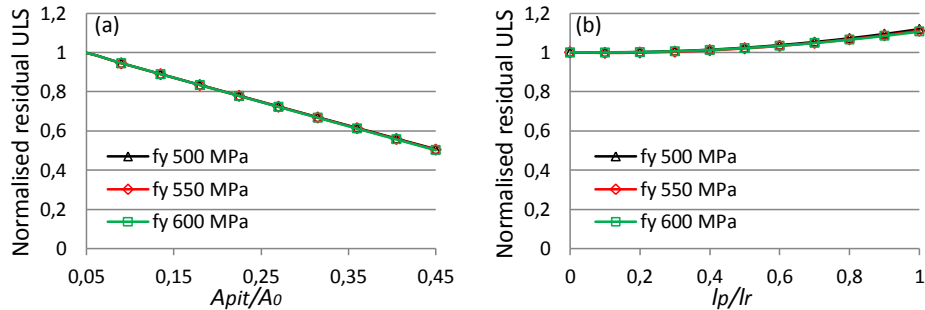


Figure 14 – Effect of f_y on the normalised residual ultimate limit state (ULS) with different amount of localised corrosion and different pit distances. The hold values are a) $l_p/l_r = 0.5$, $f_c = 35$ MPa and b) $A_{pit}/A_0 = 0.25$, $f_c = 35$ MPa.

4.4 Interaction effect of A_{pit}/A_0 and l_p/l_r using RSM

For this study, the A_{pit}/A_0 and l_p/l_r variables are the most interesting variables. Figures 15a and 15b illustrate the interaction effects of these variables on the normalised residual ULS. Figure 15b displays the decrease of the normalised residual ULS for decreasing l_p/l_r using three levels of A_{pit}/A_0 . The interpretation of these graphs is more complicated compared the corresponding graphs for f_c and f_y . Figure 15a again shows the linear decrease of the residual ULS as a function of A_{pit}/A_0 . It is now less obvious whether the influence of the l_p/l_r ratio can be considered as marginal. Figure 15b shows a different rate of the residual ULS for different values of A_{pit}/A_0 . Note that the trend is comparable with the findings of Figure 9. Compared to Figure 9, the considered range of l_p/l_r values is limited as motivated in Section 3.2.

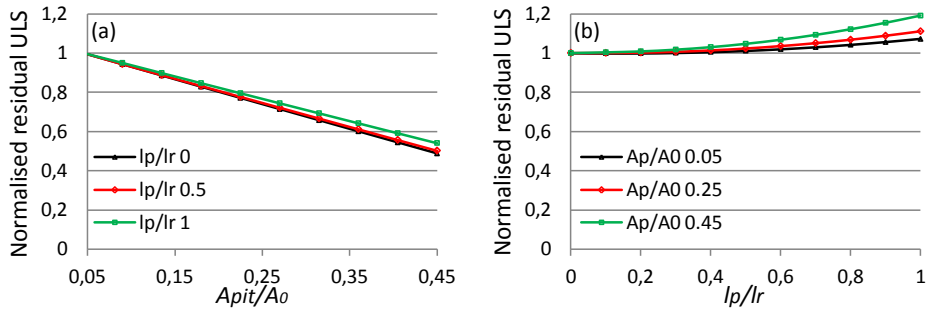


Figure 15 – Effect of A_{pit}/A_0 and l_p/l_r on the normalised residual ultimate limit state (ULS). The hold values are a) and b) $f_y = 575$ MPa and $f_c = 35$ MPa.

A contour plot and a three-dimensional response surface plot of the ULS as a function of l_p/l_r and A_{pit}/A_0 are presented in Figure 16a and b. Both plots suggest an approximate linear dependency of the ULS on A_{pit}/A_0 for a fixed value of l_p/l_r .

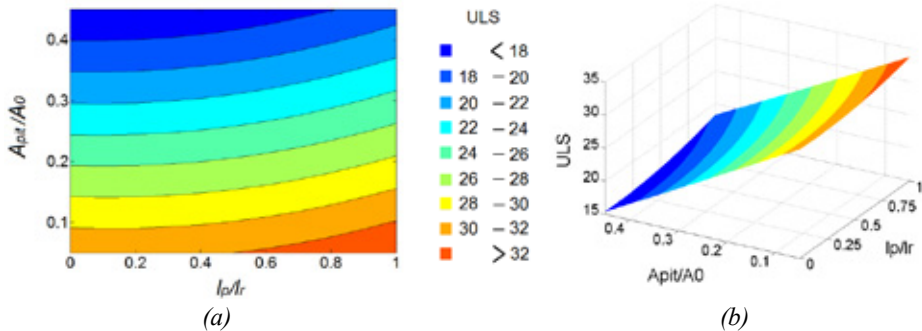


Figure 16 – Contour plot and 3D response surface plot of the ultimate limit state (ULS) versus A_{pit}/A_0 and l_p/l_r . The hold values are $f_c=35$ [MPa] and $f_y=575$ [MPa].

The next two sections will elaborate further on the interaction of the A_{pit}/A_0 and l_p/l_r ratios. First, in section 5, the range of the considered l_p/l_r ratios will be extended such that also

information on the critical l_p/l_r ratio will be obtained. This is, necessarily, done outside the RSM framework. Next, in section 6, a simplified relationship is derived which can be used in analytical formula.

5. CRITICAL RATIO OF PIT DISTANCE TO REBAR DISTANCE $(l_p/l_r)_{crit}$

In order to quantify the influence of the varying pit sizes (A_{pit}/A_0) with larger ratios of pit distance to rebar distance (l_p/l_r) on the reduction of the ULS of the corroded beam, series of FE models with 3 different A_{pit}/A_0 ratios (15%, 20% and 25%) were simulated with l_p/l_r ranging from 0 to 1.5.

Figure 17 shows that decreasing the ratio of l_p/l_r causes a gradual reduction of the ULS of the beam. For all sizes of the pits, a similar critical ratio $(l_p/l_r)_{crit}$ can be observed, which is close to 1.25. For larger l_p/l_r ratios than the critical one, the crack planes starting at the pit locations do no longer coalesce [12]. It should be noted that the rebar distance (l_r) in all models is equal to 80 mm.

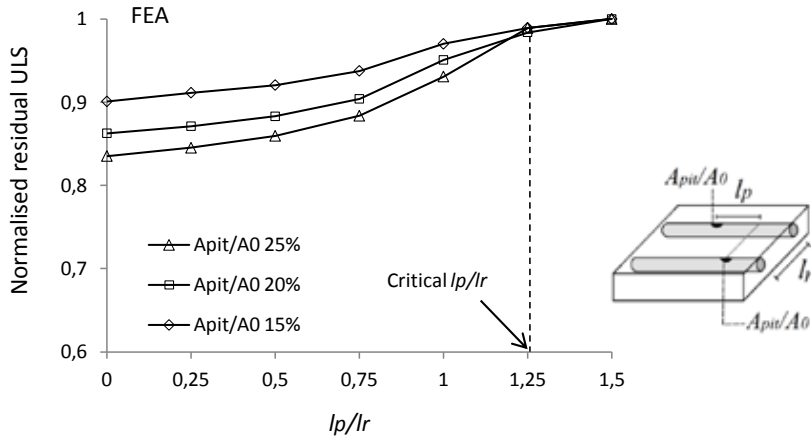


Figure 17 – Effect on the ultimate limit state (ULS) of varying ratios of pit distance to rebar distance on adjacent bar (l_p/l_r) for different steel cross section losses due to pitting corrosion. In all cases a 14% uniform steel cross section loss was assumed apart from the localised corrosion loss. Results are based on numerical analyses.

6. MODIFICATION OF ANALYTICAL FORMULA

Figure 18 indicates the normalised ULS based on analytical calculations for $l_p/l_r = 0$ and $l_p/l_r \geq 1.25$. They are based on using one, respectively two pits in an analytical strength evaluation of a cross section. The ULS reductions obtained from analytical evaluation are in good agreement with the numerical results, but it is clear that the current analytical design rules can not quantify the interaction effect of the ratio l_p/l_r and A_{pit}/A_0 for intermediate l_p/l_r ratios.

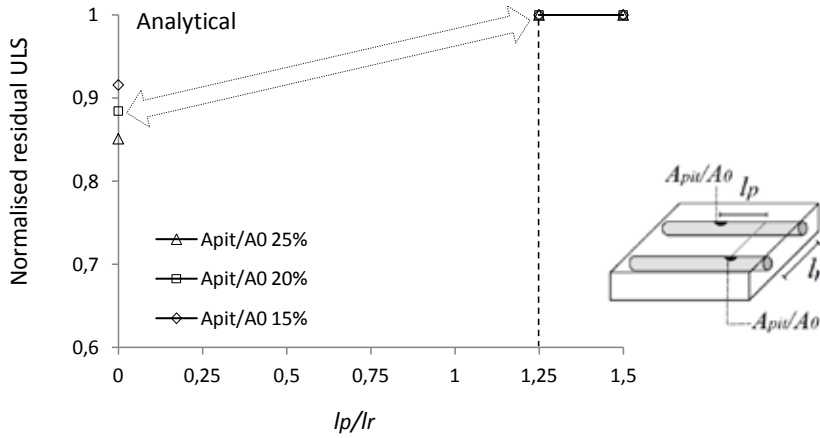


Figure 18 – Effect on the ultimate limit state (ULS) of varying ratios of pit distance to rebar distance on adjacent bar (l_p/l_r) for different steel cross section losses due to pitting corrosion. In all cases a 14% uniform steel cross section loss was assumed apart from the localised corrosion loss. Results are based on analytical analysis of the strength of the cross section.

As it discussed in section 4, the essential variables to bridge the gap in Figure 18 are l_p/l_r and A_{pit}/A_0 . It is proposed to use a modified total residual area of corroded rebars in an analytical analysis of the strength of the cross section:

$$\Sigma A_{res(mod)} = 2A_0 - (2A_{uni} + A_{pit} + \beta A_{pit}) \quad (11)$$

where $\Sigma A_{res(mod)}$ is the modified total residual area of two rebars after uniform and localised corrosion, A_0 is the area of one non-corroded rebar, A_{uni} is the uniform area loss of one corroded rebar, A_{pit} is the area of pit for one rebar. The interference is introduced by factor β which is a function of the ratio of longitudinal pit distance to rebar distance, l_p/l_r and possibly also by the ratio of pit size, A_{pit}/A_0 . Obviously, if $l_p/l_r = 0$ then $\beta = 1$ and if $l_p/l_r \rightarrow \infty$ then $\beta = 0$.

Upon substitution of Eq. (11) in the analytical formula for the ULS factor β can be expressed as:

$$\beta(l_p/l_r, A_{pit}/A_0) = \frac{ULS(l_p/l_r \rightarrow \infty) - ULS(l_p/l_r)}{ULS(l_p/l_r \rightarrow \infty) - ULS(l_p/l_r = 0)} \quad (12)$$

Substituting FE results presented in Figure 17 and approximating $ULS(l_p/l_r \rightarrow \infty) \approx ULS(l_p/l_r = 1.5)$ leads to results of Figure 19. The influence of A_{pit}/A_0 on β is limited, which supports the applied approximation $A_{pit}/(A_0 - A_{uni}) = A_{pit}/A_0$.

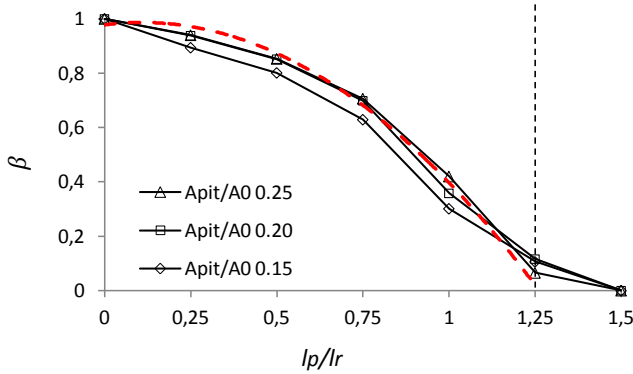


Figure 19- Pit interference factor β as a function of the ratio of longitudinal pit distance to rebar distance, l_p/l_r , for different A_{pit}/A_0 ratios.

The red line shows a proposed β , solely a function of l_p/l_r :

$$\beta = -0.76(l_p/l_r)^2 + 0.16(l_p/l_r) + 1 \quad (13)$$

Eqs. (11) and (13) can be used to quantify the possible interference of localised corrosion in connection with reassessment of corroded reinforced concrete structures. For this, (probabilistic) information on localised corrosion and pit distances is necessary.

7. CONCLUSION

In this work, the finite element modelling technique along with the response surface methodology (RSM) is employed to study the effect of four different variables, i.e. localised corrosion ratio, pit distance to rebar distance ratio, concrete compressive strength, and rebar tensile strength, on the residual ULS. From the results of FE analyses, supported by the RSM modelling, for one configuration of an under-reinforced RC beam with rebar distance $l_r = 80$ mm, the following conclusions can be drawn:

- The (interaction) effects of the ratio of pit distance to rebar distance (l_p/l_r) and the ratio of the localised cross section reduction to the original area of the rebar A_{pit}/A_0 were found significant.

Earlier work showed that interaction of pits leads to a gradual reduction of the ULS for decreasing l_p/l_r , starting at a critical ratio. For the investigated beam with $l_r = 80$ mm, regardless of pits size, the critical ratio was 1.25.

- For $l_p/l_r = 0$ and $l_p/l_r \geq 1.25$, the residual ULS calculated by analytical methods is in good agreement with numerical calculations. However, for $0 < l_p/l_r < 1.25$ current analytical rules are not able to calculate interference of pits on adjacent rebars.
- A modified analytical design rule was suggested to calculate the residual ULS by taking into account the ratio of pit distance in longitudinal direction on adjacent bars to rebar distance (l_p/l_r) when $0 < l_p/l_r < 1.25$ (Eq. 11 and 13).

To generalize these results additional parametric studies should be made in order to evaluate the effect of the varying rebar distance on the remaining ULS. For practical applications (probabilistic) information on pit sizes and pit distances is required.

ACKNOWLEDGEMENTS

This study has been carried out within COIN - Concrete Innovation Centre - one of presently 21 Centres for Research based Innovation (CRI), which is an initiative by the Research Council of Norway.

REFERENCES

1. Coronelli, D. and P. Gambarova, "Structural assessment of corroded reinforced concrete beams": Modeling guidelines. *Journal of Structural Engineering*, 2004. 130(8): p. 1214-1224.
2. François, R., I. Khan, and V.H. Dang, "Impact of corrosion on mechanical properties of steel embedded in 27-year-old corroded reinforced concrete beams", in *Materials and Structures/Materiaux et Constructions*. 2012. p. 1-12.
3. Torres-Acosta, A.A., S. Navarro-Gutierrez, and J. Terán-Guillén, "Residual flexure capacity of corroded reinforced concrete beams". *Engineering Structures*, 2007. 29(6): p. 1145-1152.
4. Azad, A.K., S. Ahmad, and S.A. Azher, "Residual strength of corrosion-damaged reinforced concrete beams". *ACI Materials Journal*, 2007. 104(1): p. 40-47.
5. Chung, L., H. Najm, and P. Balaguru, Flexural behavior of concrete slabs with corroded bars. *Cement and Concrete Composites*, 2008. 30(3): p. 184-193.
6. Du, Y., L.A. Clark, and A.H.C. Chan, "Impact of reinforcement corrosion on ductile behavior of reinforced concrete beams". *ACI Structural Journal*, 2007. 104(3): p. 285-293.
7. Hamada, H., et al. "Influence of localized corrosion of steel bars on structural performance of reinforced concrete beams". 2008.
8. Mangat, P.S. and M.S. Elgarf, "Strength and serviceability of repaired reinforced concrete beams undergoing reinforcement corrosion". *Magazine of Concrete Research*, 1999. 51(2): p. 97-112.
9. Rodriguez, J., L.M. Ortega, and J. Casal, "Corrosion of reinforcing bars and service life of reinforced concrete structures": Corrosion and bond deterioration. *International Conference on Concrete Across Borders*, 1994. 2: p. 315-326.
10. Kallias, A.N. and M. Imran Rafiq, "Performance assessment of corroding RC beams using response surface methodology". *Engineering Structures*, 2013. 49: p. 671-685.
11. Val, D.V. and R.E. Melchers, "Reliability of deteriorating RC slab bridges". *Journal of Structural Engineering*, 1997. 123(12): p. 1638-1644.
12. Kioumarsi, M.M., Hendriks, M.A.N., Geiker, M.R., "Interference of localised corrosion in adjacent reinforcement bar of a beam in bending", in *Concrete innovation conference_CIC*. 2014: Oslo, Norway.
13. Del Coz Diaz, J.J., et al., "The use of response surface methodology to improve the thermal transmittance of lightweight concrete hollow bricks by FEM". *Construction and Building Materials*, 2014. 52: p. 331-344.

14. Králik, J., "Nonlinear probabilistic analysis of the reinforced concrete structure failure of a nuclear power plant considering degradation effects". 2013. p. 1087-1098.
15. Rodriguez, J., L.M. Ortega, and J. Casal, "Load carrying capacity of concrete structures with corroded reinforcement". *Construction and Building Materials*, 1997. 11(4): p. 239-248.
16. DIANA, User's Manual, Release 9.4, in material library. 2010, TNO DIANA BV, Delft: The Netherlands.
17. fib, Model Code, fib Bulletin 55. "Federation Internationale du Beton". 2010.
18. Apostolopoulos, C.A. and V.G. Papadakis, "Consequences of steel corrosion on the ductility properties of reinforcement bar". *Construction and Building Materials*, 2008. 22(12): p. 2316-2324.
19. Cairns, J., Y. Dut, and D. Law, "Structural performance of corrosion-damaged concrete beams". *Magazine of Concrete Research*, 2008. 60(5): p. 359-370.
20. Du, Y.G., L.A. Clark, and A.H.C. Chan, "Residual capacity of corroded reinforcing bars". *Magazine of Concrete Research*, 2005. 57(3): p. 135-147.
21. fib, Bond of reinforcement in concrete, state-of-art report, fib bulletin 10. Federation Internationale du Beton. 2010.
22. El Maaddawy, T., K. Soudki, and T. Topper, "Analytical model to predict nonlinear flexural behavior of corroded reinforced concrete beams". *ACI Structural Journal*, 2005. 102(4): p. 550-559.
23. Kioumars, M.M., Hendriks, M.A.N., Geiker, M.R. "Effect of mesh alignment on simulated interference of localised corrosion on adjacent reinforcement rebars". in 2014. *XXII Nordic Concrete Research Symposium*, Reykjavik, Iceland.
24. Guan, X.L. and R.E. Melchers, "Effect of response surface parameter variation on structural reliability estimates". *Structural Safety*, 2001. 23(4): p. 429-444.
25. Kaymaz, I. and C.A. McMahon, "A response surface method based on weighted regression for structural reliability analysis". *Probabilistic Engineering Mechanics*, 2005. 20(1): p. 11-17.
26. Myers, R.H., D.C. Montgomery, and C.M. Anderson-Cook, "Response surface methodology: process and product optimization using designed experiments". 2009: Wiley.

Shear Resistance of Steel-Fibre Reinforced RC Beams with Small Circular Openings



Håvard Nedrelid¹
PhD, Researcher
havard.nedrelid@ntnu.no

Terje Kanstad¹
PhD, Professor
terje.kanstad@ntnu.no

¹Department of Structural Engineering, Norwegian University of Science and Technology, Trondheim, Norway

ABSTRACT

This paper reports test results from two experimental programs on RC beams with small circular openings under the combined action of bending and shear. Simple design rules are proposed and compared to the test results. The presence of openings leads to a disturbed stress flow which may result in early cracking and sudden failure if additional reinforcement is not provided close to the openings. This reinforcement is often tedious to place. Hence, it was decided to check if the reinforcement layout could be simplified by the inclusion of short discrete steel fibres in the concrete. Two experimental programs were undertaken: one with single openings and one with double openings. The main test variables were the amount of steel fibres (0 or 1.0vol%) and the layout of the shear reinforcement. It was found that all shear reinforcement could be left out by the inclusion of 1.0vol% steel fibres in the concrete. This also led to a more ductile post-peak behaviour of the structural members.

Key-words: Fibres, structural design, testing.

1. INTRODUCTION

RC beams are often constructed with openings to pass through utility pipes and ducts. Passing these through rather than below or above the beam results in less dead space and thereby an overall saving in total building height, especially for multi-storey buildings [1]. However, the presence of openings leads to a disturbed stress flow, e.g. as illustrated in Figure 1, which may result in early cracking and sudden failure if additional reinforcement is not provided close to the openings. This reinforcement is often tedious to place. Hence, a more effective reinforcement scheme might be obtained by letting short discrete steel fibres take on the role of both the beam shear reinforcement and any potential secondary shear reinforcement in the region of the openings. To check the feasibility of this concept, two experimental studies were conducted: one with single openings and one with double openings. The main aim of the test programs was to check if the beams could be constructed without any steel bars except for the main flexural bars. Since this most likely is only practical for relatively lightly loaded beams, the short vertical stirrups in the chords above and below the opening and the diagonal steel bars

next to the openings, sometimes used in more heavily loaded members, was not a parameter in the test programs.

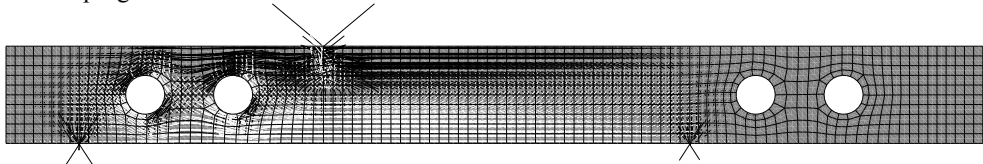


Figure 1 –Stress trajectories from an elastic finite-element analysis. The specimen geometry and loading arrangement are those of the test specimens with double openings.

Mansur has suggested that as long as beam theory applies, the opening may be termed as small [2]. Hence, if the section with the opening is subjected to pure bending, beam theory will cease to apply when the length of the compression chord above the opening becomes so large that instability failure occurs. Or, if the opening is subjected to combined bending and shear, beam behavior will transform into Vierendeel frame action as the size of the opening is increased. For circular, square or nearly square openings, this may be assumed to occur when the depth of the opening d_o is larger than about 40% of the overall beam depth h [3].

2. DESIGN APPROACH

The beams in the test programs were subjected to combined bending and shear. The ratio d_o/h was 0.47 for the single opening specimens and 0.40 for the double opening specimens, respectively. However, since no signs of Vierendeel frame action was observed in any of the tests, all openings are treated as small in this paper. Moreover, since the opening under the highest combination of bending and shear governed the failure (except for Beam A2 as seen in Figure 13), the shear resistance is assumed to depend solely on the opening closest to the applied load.

At present there is no mention of how to treat RC beams with small openings in EN 1992-1-1:2004 (hereafter EC2) [4]. However, Mansur has proposed a design method which is similar to the American Concrete Institute (ACI) Code approach for solid RC beams [5]. The approach used in this paper follows the line of Mansur, but it is based on the EC2 expressions rather than the ACI Code expressions. However, it should be noted that the variable strut-inclination method in EC2 is abandoned and the concrete term is reintroduced in the shear calculations. This is in agreement with the Level I Approximation to shear design as described in the new Model Code 10 [6]. The reason behind this choice is that it allows for the effect of the opening to be accounted for in a simple manner by modifying the effective depth of the critical concrete cross-section. The effect of fibres is calculated in a similar manner by modifying the fibre contribution expression given in COIN Project Report 29 [7]. This report contains the Norwegian design rule proposals for fibre-reinforced concrete. The final Norwegian design guideline for fibre-reinforced concrete is to be published as “Norsk Betongforening publikasjon nr. 38” in 2015.

According to Mansur, two types of failures must be accounted for in the design of RC beams with small openings: beam-type failure and frame-type failure. Typical crack-patterns for the two failure types are depicted in Figure 2. Beam-type failure is similar to the shear failure in a solid beam except that the failure plane passes through the center of the opening; frame-type failure is different in that the compressive and tensile chord above or below the opening is

assumed to act as an independent entity similar to that in a framed structure. In the following, the shear formulas used in this paper is briefly explained. The method is completely analogous to the design methodology proposed by Mansur, except that it is based on the EC2 rather than the ACI Code expression and, in addition, includes the effect of fibres on the shear resistance

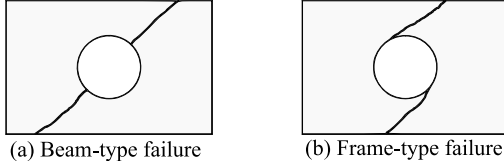


Figure 2 – Two possible modes of shear failure for a RC beam with small openings [3].

2.1 Beam-type failure

A 45 degree crack through the centre of the opening is assumed and the shear resistance is calculated by the expression

$$V_{\text{beam}} = V_c + V_s + V_f \quad (1)$$

where V_c is the shear resistance attributable to the concrete, V_s is the shear contribution from the stirrups crossing the crack, and V_f is the shear resistance provided by the fibres crossing the crack. The concrete term V_c is calculated according to EC2 clause 6.2.2(1) with the effective depth d replaced by $(d-d_o)$. If we ignore the material factor the expression may be written as

$$V_c = [C_{Rd,c} k (100 \rho_L f_c)^{1/3}] b(d-d_o) \quad (2)$$

where $C_{Rd,c}$ is an empirical factor 0.15 or 0.18 dependent on the size, amount or type of aggregate, $k=1+\sqrt{(200/d)}<2.0$ is the size factor, $\rho_L=A_s/(bd)<0.02$ is the flexural reinforcement ratio, and f_c is the cylinder compressive strength of the concrete. Similarly, the fibre term V_f is calculated according to COIN Project Report 29 with h replaced by $(h-d_o)$ such that

$$V_f = 0.6 f_{\text{fres},2.5} b(h-d_o) \quad (3)$$

where $f_{\text{fres},2.5}$ is the residual direct tensile strength at 2.5mm crack width as derived from three-point bending tests on notched prisms according to EN 14651 [8]. Equation 3 is based on the idea that the fibres act as a diffuse inclined reinforcement over the crack as illustrated in Figure 3. If present, the contribution from each bar or stirrup is given by

$$V_s = A_v f_{yv} \sin \alpha \quad (4)$$

where A_v is the reinforcement area, f_{yv} is the yield strength of the reinforcement, and α is the inclination of the reinforcement to the beam axis. The steel bars or stirrups available to resist shear across the failure plane are those next to the opening within a distance $(d_v-d_o)/2$ from either side, where d_v is the distance between the top and bottom longitudinal bars.

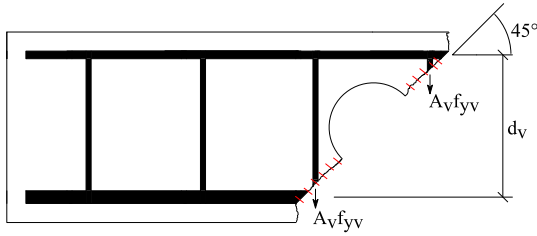


Figure 3 –Model of the shear resisted by the stirrups and steel fibres crossing the crack.

2.2 Frame-type failure

The compressive and tensile chord members are treated as separate beams. Each beam will be subjected to a portion of the applied shear and the axial force which arises due to bending of the beam as shown in Figure 4.

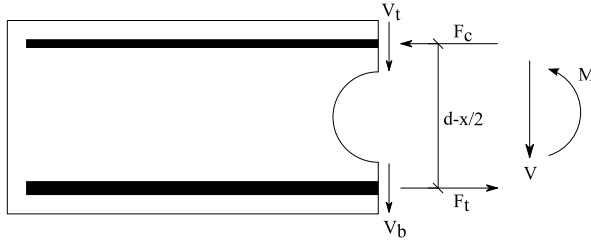


Figure 4 – Free-body diagram at beam opening.

The shear resistance is calculated according to EC2 clause 6.2.2(1) with the axial force term $k_1 \sigma_{cp}$ included. Or, if no flexural bars are provided in the chord members, the expression may be written as

$$V_c = [0.035 k^{3/2} f_c^{1/2} + k_1 \sigma_{cp}] b h_f \quad (5)$$

where h_f is the depth of the compressive or tensile chord and $\sigma_{cp} = N/A_c < 0.2 f_c$ is the normal stress transmitted through it. The factor k_1 is taken as +0.15 for compression and -0.30 for tension as suggested by the Norwegian Annex to EC2. The numerical value of the axial force is given by

$$N = F_c = F_t = \frac{M}{z} = \frac{V a}{d - x/2} \quad (6)$$

where a is the length of the shear span and x is the depth of the ultimate stress block (which obviously cannot be greater than the depth of the compressive chord). The overall shear resistance is calculated by adding together the various contributions to the shear resistance as follows

$$V_{frame} = V_t + V_b + V_f \quad (7)$$

where V_t and V_b is the shear resistance attributable to the top and bottom chord member respectively, and V_f is the contribution from the fibres. The fibre contribution term V_f is

calculated as for beam-type failure, since the total crack length over which the fibres act is the same. However, it should be mentioned that the Danish guideline for structural fibre-reinforced concrete neglects the effect of the fibres on the shear resistance for cross-sections subject to a tensile normal force [9]. If short vertical stirrups are provided in the chord members as shown in Figure 5, their contribution V_s can be added to the shear resistance of the respective chord members as for an ordinary beam.

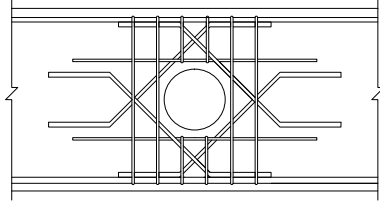


Figure 5 – Typical detailing of reinforcement around opening in a heavily loaded member. The vertical component of the inclined reinforcement provides resistance for beam-type failure, but is mainly placed for crack control.

3. RC BEAMS WITH SINGLE OPENINGS UNDER SHEAR

3.1 Details of specimens and loading arrangement

Three shear-reinforced RC beams with single openings, and an equivalent solid beam unreinforced in shear, were tested as shown in Figure 6. The dimensions of the beams were $b \times h \times l = 200 \times 300 \times 2500$ and the diameter of the openings was $d_o = 140$ mm. For all specimens, the tensile and compressive reinforcement consisted of $2\phi 20$ and $1\phi 12$, respectively, with 30 mm cover. The shear reinforcement varied as shown in Figure 7. For the fibre-reinforced specimens, the reinforcement layout was centred to promote a favourable flow of fibres during casting.

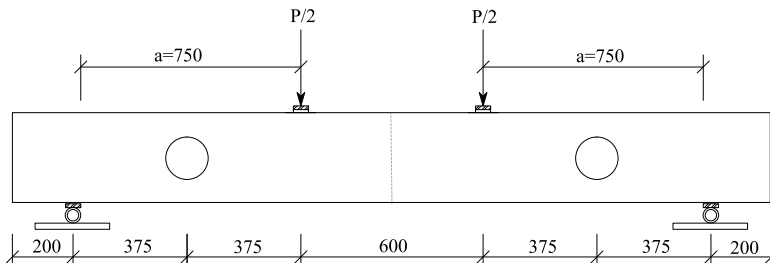


Figure 6 – Test set-up for the four RC beams investigated in the test program.

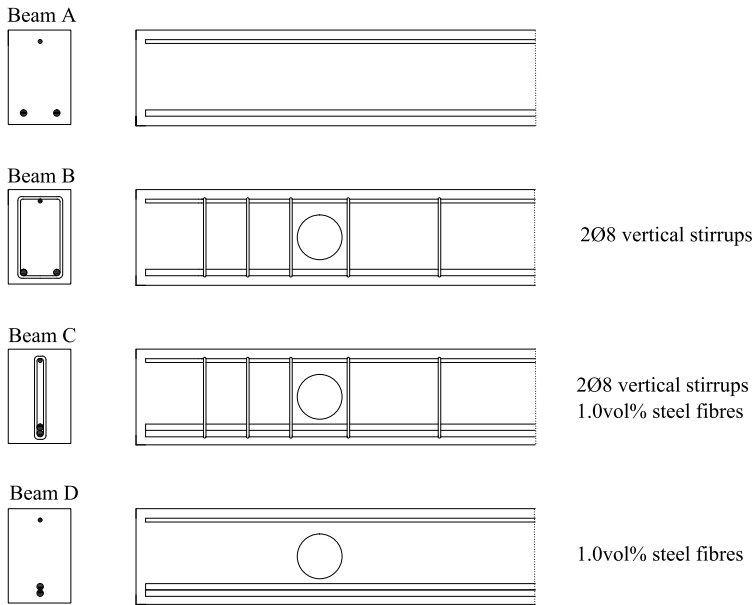


Figure 7 – Reinforcement layout for the four RC beams tested. The text to the right lists the reinforcement relevant for the shear resistance of the critical cross-section.

3.2 Materials

Two beams were made of ordinary concrete and two of concrete with 1.0vol% hooked-end steel fibres of the type Dramix 80/60. The fine aggregate was 0-8mm natural sand and the coarse aggregate was 8-16mm natural gravel. The compressive strength of the concrete f_c was established by multiplying the strength obtained from tests on 100mm cubes by a factor 0.8. The direct residual tensile strength $f_{fres,2.5}$ was derived from bending tests on notched 150x150x550 prisms by multiplying the measured residual flexural strength at 2.5mm crack width by the commonly used factor 0.37, as e.g. described in COIN Project Report 29. The yield strength of the steel bars f_y was assumed to be 500MPa.

3.3 Testing of specimens

The specimens were loaded by a hydraulic jack through a 50x200mm steel plate. A piece of chipboard was inserted between the loading platens and the specimen to ensure full contact over the entire loading area. The specimens were supported by a 50mm steel plate rotating on top of a steel pipe at both ends. To obtain a simply-supported condition, the left pipe was fixed by welding, whereas the right pipe was allowed to roll. The displacement at mid-span was measured by a LVDT connected to the floor.

3.4 Experimental results

Figure 8 and Table 1 summarises the results from the test program. In the calculations of V_{frame} , the shear resistance attributable to the compressive frame member has been calculated by

combining Equation 5 and 6 and solving for the unknown shear force V_c , whereas the contribution from the tensile frame member was neglected. This is a conservative approach since the force transmitted through the compressive frame member will in reality be larger if shear reinforcement or fibres is provided. The tensile frame member might also contribute slightly to the shear resistance, but its contribution can only be small due to the adverse effect of the normal tensile force on the shear resistance.

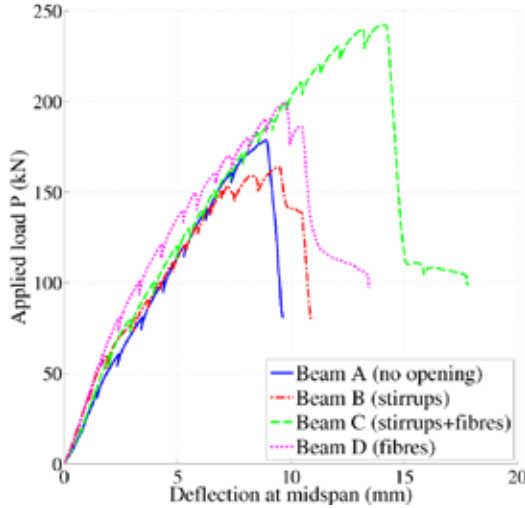


Figure 8 – Load-deflection behaviour of the single opening specimens.

It can be seen that when either 2Ø8 vertical stirrups or 1.0vol% steel fibres is used as shear reinforcement adjacent to the opening, the behaviour of the RC beams with openings (Beam B and D) is restored to that of an equivalent solid RC beam unreinforced in shear (Beam A). The RC beam with both stirrups and fibres (Beam C) on the other hand is about 50% stronger. It is also interesting to note that the failure of the RC beams without fibres is brittle, whereas the fibre-reinforced specimens exhibit some residual strength after the peak load.

Table 1 – Test parameters together with the estimated and experimental shear resistance.

Beam	f_c Mpa	$f_{\text{fibre},2.5}$ Mpa	a mm	d mm	d_o mm	A_v mm ²	V_{frame} kN	V_{beam} kN	V_{exp} kN	$V_{\text{exp}}/V_{\text{calc}}$	Failure type in tests
A	41	-	750	260	-	-	-	64.5	89.4	1.39	Beam
B	41	-	750	260	140	201	19.0	130	82.0	4.32	Frame
C	52	3.4	750	260	140	201	86.7	198	121	1.40	Beam?
D	52	3.4	750	260	140	-	86.7	97.5	100	1.15	Beam

3.5 Discussion

From Table 1 it can be seen that the shear resistance is predicted rather well for all specimens except Beam B. The reason is probably that the stirrup on the right side of the opening in Figure 8 crosses the critical crack in the compressive chord and thereby contributes to the overall shear resistance of the member. In fact, if the contribution from 1Ø8 stirrup (i.e. 50kN) is added to the frame-type predictions for beam B, C and D, the shear resistance is well predicted for all specimens, although the strength of Beam C is slightly over-predicted. It also seems to lead to

the correct prediction of the type of failure for all specimens, except maybe for Beam C. However, it should be noted that the exact failure type of beam C is not easy to pinpoint since the crack pattern seems to be a combination of beam-type and frame-type failure.

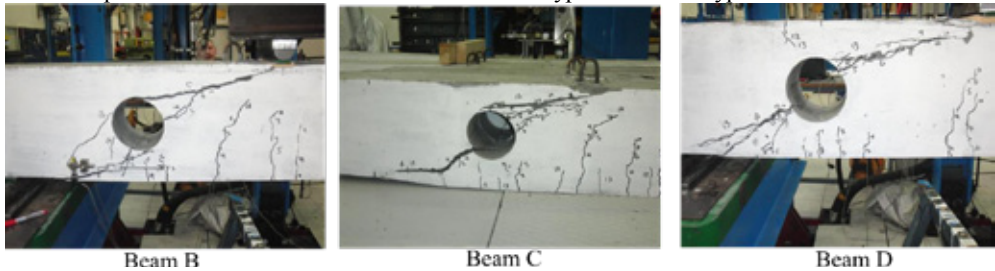


Figure 9 - Crack pattern after failure for the RC beams with single openings.

4. RC BEAMS WITH DOUBLE OPENINGS UNDER SHEAR

4.1 Detail of test specimens

Four RC beams with double openings were tested as shown in Figure 10. However, it should be noted that for Beam C the left and right support had to be moved 200 and 140mm toward each other, respectively, to ensure that shear failure occurred before yield of the main flexural bars. The shear reinforcement varied as shown in Figure 11. The dimensions of the beams were $b \times h \times l = 200 \times 400 \times 4000$ mm and the diameter of the openings was $d_o = 160$ mm. The tensile and compressive reinforcement consisted of $2\phi 25$ and $2\phi 12$, respectively, and $\phi 8$ s180 stirrups were used as shear reinforcement. This corresponds to the maximum spacing $0.6h'$ given by EC2 NA.9.2.2(6). Next to the openings the stirrups were moved 30mm in order to make room for the openings. This resulted in 210mm spacing adjacent to the holes and 150mm spacing in-between. In order to resist local bending moments, two 8mm bars with a length of 1000mm were placed in the chord members above and below the openings. These were removed in beam B, which served as reference for Beam C with fibres. In Beam D, only the tensile reinforcement was kept besides the fibres.

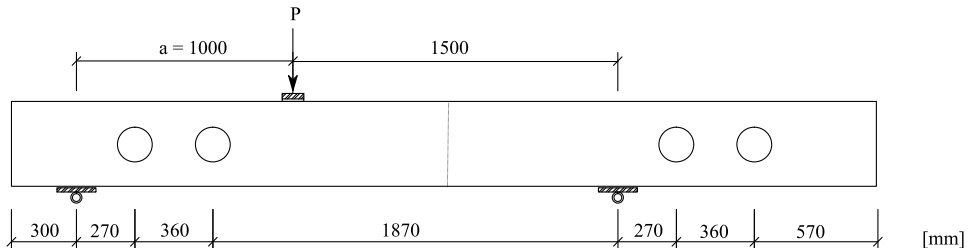


Figure 10 – Test set-up for the four RC beams investigated in the test program. Note that for Beam C the left and right support had to be moved 200 and 140mm toward each other, respectively, to ensure that shear failure occurred before yield of the main flexural bars.

4.2 Materials

Two beams were made of ordinary concrete and two of SFRC with 1.0vol% hooked-end steel fibres of the type Dramix 65/60. The fine aggregate was 0-8mm natural sand and the coarse aggregate was 7-14mm limestone gravel. The compressive strength of the concrete f_c was established from tests on 100x200mm cylinders. The direct residual tensile strength $f_{\text{fres},2.5}$ was

derived from bending tests on notched 150x150x550 prisms by multiplying the measured residual flexural strength at 2.5mm crack width by the factor 0.37. The yield strength of the steel bars f_y was assumed to be 500MPa.

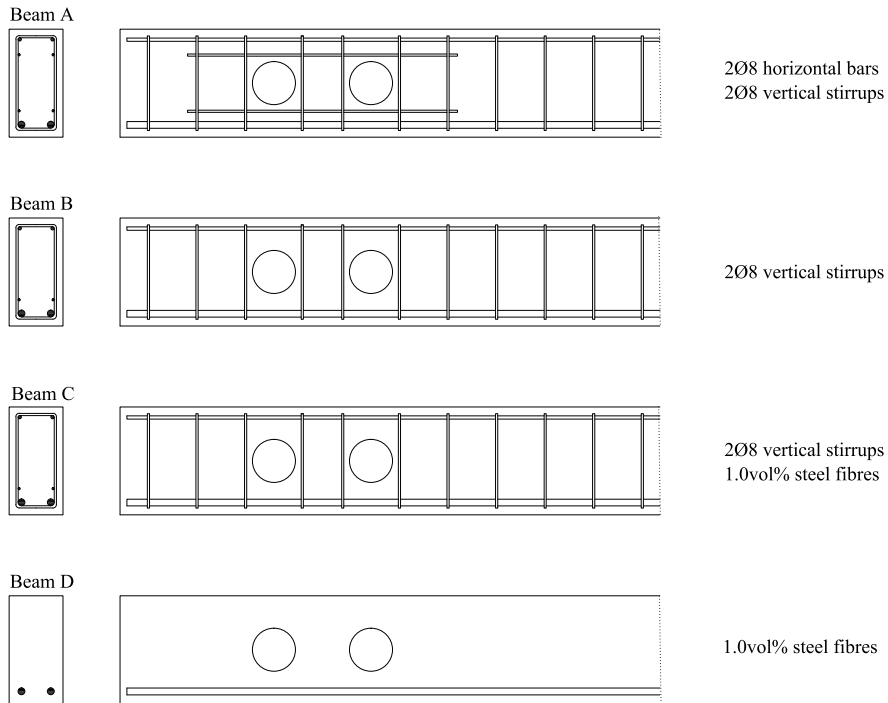


Figure 11 – Reinforcement layout for the four RC beams investigated in the test program. The text to the right lists the reinforcement relevant for the shear resistance of the critical cross-section.

4.3 Testing of specimens

The specimens were loaded by a hydraulic jack through a 100x200mm steel plate. A piece of chipboard was inserted between the loading platens and the specimen to ensure full contact over the entire loading area. The specimens were supported by a 180mm wide steel plate rotating on top of a steel pipe at both ends. To obtain a simply-supported condition, the left pipe was fixed by welding, whereas the right pipe was allowed to roll. The displacement of the loaded section was measured by a LVDT connected to the floor. Due to the asymmetric loading arrangement, the damage was mostly confined to the left region. Hence, after testing, the beam could be reverted and the test repeated for the other side.

4.4 Experimental results

Figure 12 and Table 2 summarises the results from the test program. The shear resistance was calculated in the same manner as for the specimens with single openings, but the factor 0.15 was used instead of 0.18, as dictated by the Norwegian Annex to EC2 for limestone aggregate. Note that contrary to the single opening specimens, two test results are obtained from each of the double opening specimens. However, for clarity of presentation, only the results from the second test (denoted A2, B2, C2 and D2) are shown in Figure 12. In Table 2, the strength results from the

first test (denoted A1, B1, C1 and D1) are also included. Nonetheless, in the following discussion it is simply referred to Beam A, B, C and D, since the first test and the replication led to similar results.

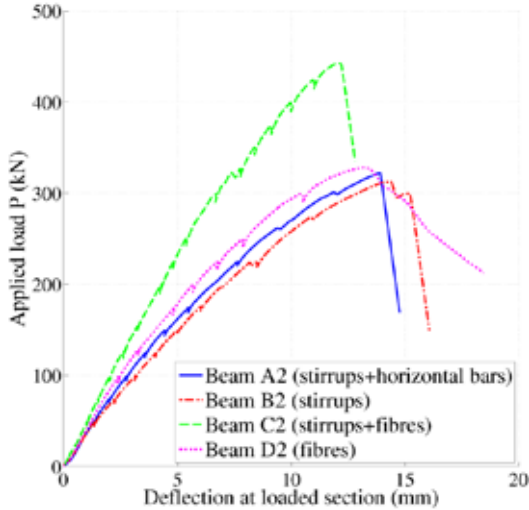


Figure 12 – Load-deflection behaviour of the specimens with double openings. For clarity of presentation, only the results from the second test on each specimen are shown.

By comparing Beam A and B, it can be seen that there is no effect of removing the horizontal bars in the chord members. This indicates that they probably are not needed in beams with small openings (except as anchorage for short vertical stirrups if present). It is also interesting to note that, as for the single opening specimens, the beams with either 2Ø8 vertical stirrups or 1.0vol% steel fibres as shear reinforcement, exhibits a nearly identical pre-peak behaviour (B and D) although the post-peak response is more ductile for Beam D with fibres. Further, as for the single opening specimens, the RC beam with both stirrups and fibres (Beam C) is about 50% stronger than the other specimens. However, it should be remembered that the loading arrangement for Beam C had to be slightly altered in order to obtain a shear failure before yielding of the main flexural bars, i.e. the behaviour of Beam C is not directly comparable to the other specimens. This is also the reason for the stiffer behaviour of this specimen.

Table 2 – Test parameters together with the estimated and experimental shear resistance.

Beam	f_c	$f_{fres,2.5}$	a	d	d_o	A_v	V_{frame}	V_{beam}	V_{exp}	V_{exp}/V_{calc}	Failure type in tests
	Mpa	Mpa	mm	mm	mm	mm ²	kN	kN	kN		
A1	60	-	1000	355	160	201	33.5	145	166	4.96	Frame
A2	60	-	1000	355	160	201	33.5	145	193	5.76	Frame
B1	60	-	1000	355	160	201	33.5	145	178	5.31	Frame
B2	60	-	1000	355	160	201	33.5	145	188	5.61	Frame
C1	57	4.5	800	355	160	201	158	274	267	1.69	Beam?
C2	57	4.5	800	355	160	201	158	274	266	1.68	Beam?
D1	57	4.5	1000	355	160	-	163	173	172	1.06	Beam
D2	57	4.5	1000	355	160	-	163	173	197	1.21	Beam

4.5 Discussion

From Table 2 it can be seen that, as for the single opening specimens, the predicted shear resistance for the beams with only stirrups (Beam A and B) is far off their experimental value. The reason is probably again that the full-length stirrups at the sides of the openings contribute to the frame-type shear resistance, due to the low inclination of the frame cracks. Since the shear crack-pattern in Figure 13 is distributed over the entire depth of both sides of the critical opening, it may seem like the stirrups on both sides of the opening contribute to the shear resistance. If this is the case, the contribution from 2Ø8 stirrups (i.e. 100kN) can be added to the frame-type shear resistance for Beam A, B and C. This leads to a better agreement with the tests results. It should also be noted that for Beam C, where the load application point is moved closer to the support, the main crack at failure nearly bypasses the opening and it also seems like the applied load flows more directly towards the support.

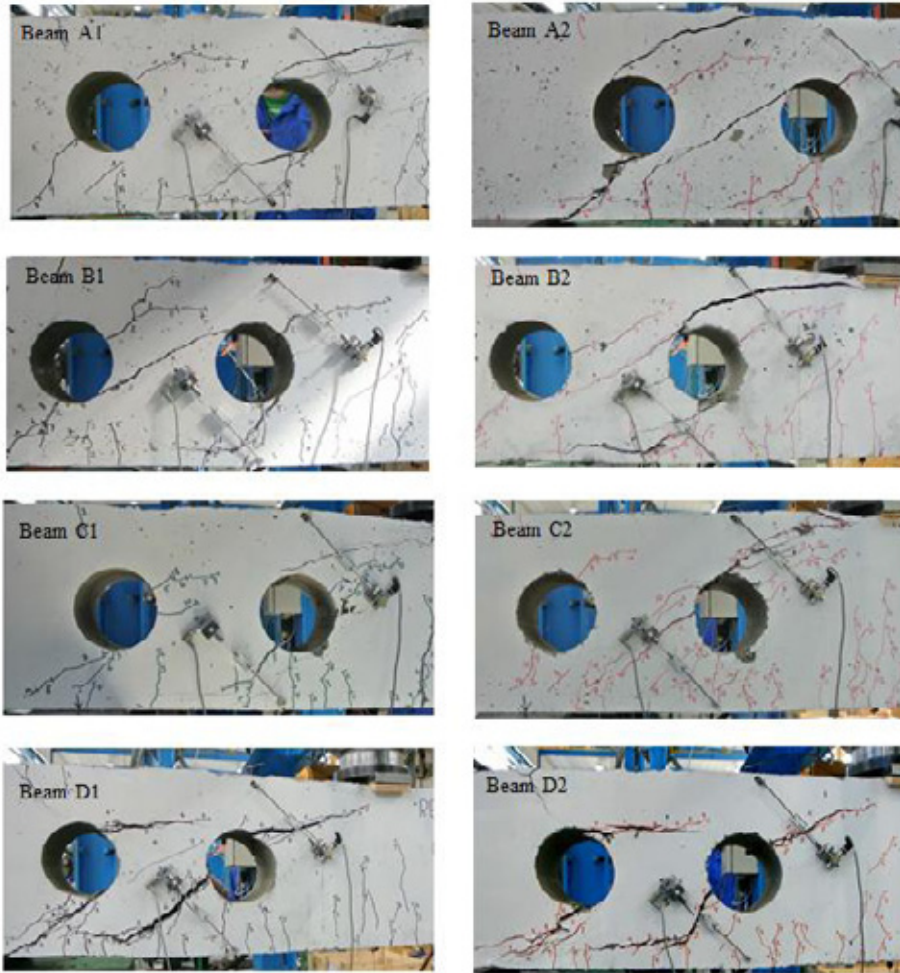


Figure 13 - Crack pattern after failure for the four RC beams with double openings.

5. FINAL REMARKS

It has been shown that both the beam shear reinforcement and the secondary shear reinforcement in the region of the openings can be left out by the inclusion of 1.0vol% hooked-end steel fibres in the concrete. Moreover, simple shear design formulas for RC beams with openings have been proposed based on the EC2 expressions for solid beams. The only material parameter used to account for the effect of fibres is the residual direct tensile strength at 2.5mm crack width as derived from three-point bending tests on small notched prisms. This led to safe strength predictions for all specimens, although the estimated resistance of the specimens governed by frame-type failure was overly conservative. It should be emphasised that the design methodology proposed in this paper is of a tentative nature and more experimental data is needed to check on its validity. Moreover, any favourable or unfavourable orientation of the fibres in the structural members compared to that in the “material” test specimens used to derive

the residual direct tensile strength, has not been investigated. However, the factor 0.6 in Equation 3, as proposed in COIN Project report 29, has been reduced from its theoretically deduced value of 0.8 (see e.g. [10]) and thereby indirectly account for any unfavourable orientation of the fibres in the structure.

REFERENCES

1. Mansur, M.A., Tan, K-H. "Concrete beams with openings – analysis and design". CRC Press LLC, 1999.
2. Mansur, M.A. "Effect of openings on the behavior and strength of R/C beams in shear". Cement and Concrete Composites, **20**, 477-486. 1998.
3. Mansur, M.A. "Design of reinforced concrete beams with web openings". Proceedings of the 6th Asia-Pacific Structural Engineering and Construction Conference , 104-120, 2006.
4. EN 1992-1-1. "Eurocode 2: Design of concrete structures – Part 1-1: General rules and rules for buildings". CEN, European Committee for Standardization, 2004.
5. Tan, K-H, Mansur, M.A, Wei, W. "Design of reinforced concrete beams with circular openings". ACI Structural Journal, **98**(3), 407-415, 2001.
6. fib, "Model Code 2010 - Final draft Volume 1", fib Bulletin no. 65, 2012.
7. Kanstad, T. et. al. "Forslag til retningslinjer for dimensjonering, utførelse og kontroll av fiberarmerte betongkonstruksjoner". COIN Project report 29, 2011.
8. EN 14651. "Test method for metallic fibre concrete. Measuring the flexural tensile strength (limit of proportionality (LOP), residual)". CEN, European Committee for Standardization, 2005.
9. SFRC Consortium, "Design guideline for structural applications of steel fibre reinforced concrete". Danish Technological Institute, 2014.
10. Klausen, A.B.E., "Steel fibres in load-carrying concrete structures. Guideline survey and practical examples". COIN Project report 17, 2009.

Is It Possible to Predict Formwork Pressure When Using SCC? – A Field Study



Richard Mc Carthy
MSc (Civil Eng), Researcher,
Head of Dissemination of Knowledge Section
The Swedish Cement and Concrete Research Institute (CBI)
SE-100 44 Stockholm
E-mail: richard.mccarthy@cbi.se



Johan Silfwerbrand
Professor & Department Head
KTH Royal Institute of Technology
School of Architectural & Built Environment
Dept. of Civil & Architectural Engineering
Division of Structural Engineering & Bridges
SE-100 44 Stockholm
E-mail: jsilfwer@kth.se

ABSTRACT

In Sweden, the market share of cast-in-place Self-Compacting Concrete (SCC) is only around 10%. Uncertainty concerning formwork pressure is considered to be one of the most important factors explaining the slow progression. During construction of a 400 m long, 6 m high and 0.27 m thick prison wall in northern Sweden, SCC alone was used. The formwork used consisted of steel-framed panels, instrumented with flush-mounted pressure sensors. Each concrete batch was tested for air content, slump-flow, concrete and air temperature. Besides tests on torsional moment or torque, L-box, and V-funnel were carried out. Relations between concrete properties, casting rate and time versus formwork pressure were investigated. The results confirmed that structural build-up of SCC has to be taken into account for predicting formwork pressure. The torsional moment was measured at three consecutive times at each casting and the time-dependent development of the torsional moment was subsequently used as indirect input in two simple formwork pressure methods that have been developed recently. The comparison between computed and measured formwork pressure shows that both these methods would be possible to use for predicting formwork pressure generated by SCC.

Key words: formwork pressure, fresh concrete properties, formwork pressure models, SCC.

1. INTRODUCTION

Self-Compacting Concrete (SCC) is a construction material with a great potential in the construction industry. Despite all the benefits, such as improved working environment and increased degree of productivity, the material still remains underused. The market share of cast-in-place SCC in Sweden is around 10%. The share in the precast concrete industry is substantially higher. The precast concrete production is carried out with the same trained and experienced working staff that is casting indoors without disturbances from weather, wind, rain, and snow. The precast concrete production is often run through long series enabling possibilities to take the advantages of repeatability into consideration. Consequently, the precast concrete production leads to concrete with constant properties and low scatter. Constant fresh concrete properties are beneficial for producing SCC. Contrary to precast concrete production, cast-in-place concrete production is carried out outdoors under varying weather conditions. The fresh concrete is usually produced in a ready mix plant and the transport between the plant and the site may vary in length due to differences in traffic intensity. The difference in transportation time is in turn influencing the fresh concrete properties which is challenging for the SCC production. Another difference between precast concrete production and cast-in-place concrete is that walls mainly are cast horizontally in the precast industry but vertically on site. The vertical casting requires more complicated formwork and the formwork pressure has to be taken into account when designing the formwork.

The difficulties in predicting formwork pressure when casting SCC in vertical formwork is considered to be one of the most important factors that have delayed the market share development of cast-in-place SCC. The fresh SCC has a lot of similarities with a liquid and when it was introduced in the 1990s, the formwork was designed for full hydrostatic pressure. However, more recent research has shown that this conservative design does not have to be used in all cases [1]. The structural build-up of SCC during rest means that a pressure that is substantially below the full hydrostatic pressure is developed, especially at low casting rates. Still, formwork pressure generated by SCC (and concrete in general) is difficult to predict and influenced by many factors. The most important ones are connected to the concrete properties (specific weight, rheological properties, and structural build-up), the formwork geometry (height and thickness) and other properties (friction and reinforcement), the casting rate (constant, step-wise, or varying), and the surrounding weather conditions (mainly temperature).

During 2008-2009, a unique SCC project was carried out in Sweden. A 400 m long, 6 m high and 0.27 m thick wall was constructed. It surrounds a new prison in Härnösand in the north of Sweden [2]. The first author measured the formwork pressure exerted in some of the casting sections as well as a number of fresh concrete properties. This paper contains efforts to compare measured fresh concrete properties and derived formwork pressure with measured formwork pressure.

2. ESTIMATING FORMWORK PRESSURE

2.1 Methods to estimate formwork pressure

The old Swedish method to estimate formwork pressure was developed during the 1960s [3]. It took casting rate R , slump S , and concrete temperature T at placing into account and was valid for $S < 150$ mm:

$$p_{\max} = 147.2 \cdot \left(0.75 + \frac{S}{600}\right) \cdot \left(\frac{R}{30}\right)^{(0.32+0.0042T)} \quad (1)$$

For $S > 150$ mm, the design pressure was considered to equal full hydrostatic pressure $\rho_c \cdot g \cdot h$, where, ρ_c = density of concrete, g = gravity constant ($g = 9.81 \text{ ms}^{-2}$), and h = casting height. Usually, the product $\rho_c \cdot g$ is replaced by γ_c (often: $\gamma_c = 25 \text{ kN/m}^3$). Other countries developed similar equations [4]. However, they have all the same shortcoming; they cannot be used for SCC.

During recent decade, a number of new methods for estimating formwork pressure when using SCC have been developed. Some of them are described in [5]. Their main characteristics are summarized in Table 1 [6-13]. All models have one condition in common; they all include a factor taking the time-dependent structural build-up of the SCC into account. However, this is done in several different ways. Some of these ways are fairly complicated and can hardly be conducted by others than the researchers. The authors have identified the methods developed by DIN [11] and Gardner et al. [13] as the easiest to use. They will be described more in detail in the following subsections.

Table 1 – Factors considered in some important formwork pressure models used for SCC.

Model	Specific weight of	Casting rate	Formwork height	Formwork thickness	Rebar diameter	Max aggregate	Slump-flow	No of other factors	How structural build-up is considered
Ovarlez & Roussel [6]	X	X	X	X				1	Static yield stress increase per time unit
Proske [7]	X	X		X	X			2	Time to force = 50 N gives indentation = 1 mm + further lab tests
Lange et al. [8]	X	X						3	Time to zero pressure for control test in vertical pipe
Perrot et al. [9]	X	X	X	X	X			1	Settlement of control test
Beitzel [10]	X	X	X	X				1	Static yield stress increase per time unit
DIN [11]	X	X	X					1	Time to force = 50 N gives indentation = 1 mm
Khayat & Omran [12]	X	X	X	X		X		2	Portable tixometer (Portable Vane)
Gardner et al. [13]	X	X	X				X	1	Time for max slump-flow to drop to 400 mm

2.2 The DIN 18218 [11] method

The German standard method DIN 18218 [11] was developed through a large German research program [14] containing both laboratory tests and field tests. In the German method, the following equation is used for determining the maximum formwork pressure p_{\max} .

$$p_{\max} = (0.8 + 0.16 \cdot R \cdot t_E) \cdot \gamma_c \leq p_{\text{hydrostat}} = \gamma_c \cdot H \quad (2)$$

where, R = casting rate (measured in m/h), t_E = setting time (h), $\gamma_c = 25 \text{ kN/m}^3$, $p_{\text{hydrostat}}$ = hydrostatic pressure of concrete liquid (kPa), and H = concrete height (m). The setting time is estimated in an approximate way by pushing the thumb with a 50 N force on a bag containing a sample of the actual concrete. The setting time is given by the time when the indentation in consecutive measurements passes below 1 mm (in practice the measurement value from the thumb test, defined as $t_{E,KB}$, is transferred to the setting time t_E inserted in Eq. (2) through the transition $t_E = 1.25 \cdot t_{E,KB}$). In Eq. (2) mean values are used. DIN [11] contains also an equation using characteristic values but it has been omitted since it is always more straightforward to compare measured values with mean values.

2.3 The Gardner [13] method

Gardner et al. [13] base their method on a large number of field tests. They are focusing on the time needed for the slump-flow SF to equal zero. Since slump-flow is a simple and well-known test method for testing fresh SCC, Gardner's method is simple to use. The following equation is used for determining the formwork pressure p :

$$p = \begin{cases} R \cdot \left(t - \frac{t^2}{2t_0} \right) \cdot \gamma_c; t < t_h < t_0 / 2 \\ R \cdot \left(t_h - \frac{t_h^2}{2t_0} \right) \cdot \gamma_c; t \geq t_h < t_0 / 2 \\ p_{\max} = R \cdot \frac{t_0}{2} \cdot \gamma_c; t \geq t_0 / 2 \end{cases} \quad (3)$$

where, the time t_0 (h) corresponds to a hypothetical time for the slump-flow SF to reach zero slump-flow. The SF is considered to decrease linearly with time after casting (Figure 1). Based on simple geometrical relationships in Figure 1, this time is determined with the following equation:

$$t_0 = t_{400} \cdot \left(\frac{SF_i}{SF_i - 400} \right) \quad (4)$$

where, t_{400} = time (h) required for the slump-flow to drop to 400 mm and SF_i = initial slump-flow (mm). The time limit t_h is equal to the time to reach a placement height h , i.e., $t_h = h/R$; where h = height between the measuring point and the top surface of the placement (that is the top of the last lift) and R = casting rate.

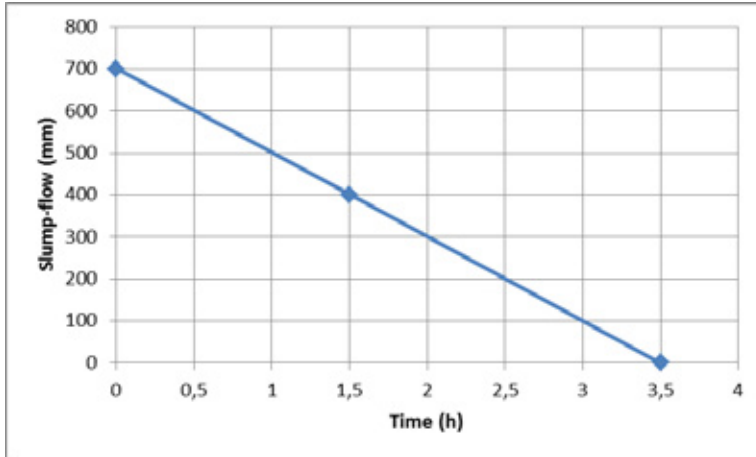


Figure 1 – Principle graph showing the relationship between slump-flow and time. In this example, $SF_i = 700$ mm, $t_{400} = 1.5$ h, and $t_0 = 3.5$ h. Please, note that Gardner et al. neglect the fact that in practice the SF cannot be lower than 200 mm = the diameter of Abram's cone. (The authors have drawn the figure in order to illustrate the ideas of Gardner et al [13].)

Gardner et al. [13] applied their method to three field castings (Figure 2). The correspondence between calculated and measured values is decent but not more. Most values are located below the line of complete correspondence indicating that the method is on the conservative side (calculation overestimates measurement).

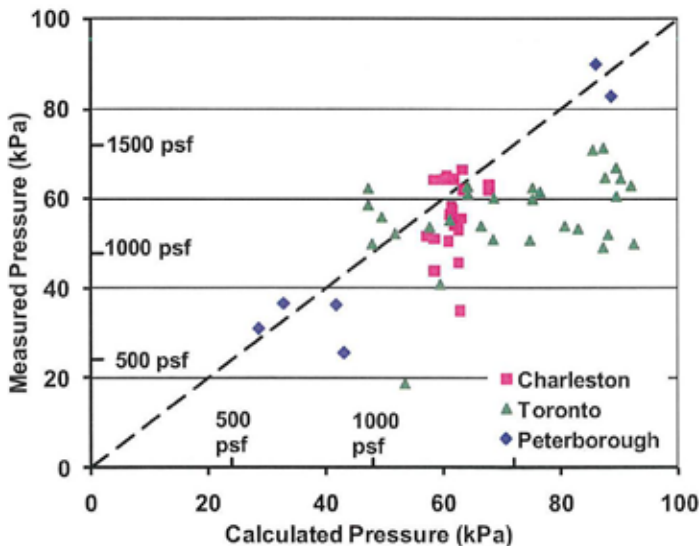


Figure 2 – Comparison of measured and predicted lateral pressures using Gardner's method and measuring data [13].

2.4 The Stockholm workshop

As stated in Section 2.1, lot of research has been devoted to SCC and efforts to determine and anticipate formwork pressure. In order to compare different models, summarized in Table 1, an international workshop consisting of round-robin tests was organized by the Swedish Cement and Concrete Research Institute in Stockholm during May 2012 [5, 15]. The workshop participants were the developers of the models. The test program included measurements of pressures generated in full-scale concrete forms using pressure transducers as well as load cells mounted on tie bars. Test parameters included wall height (4.2 or 6.6 m) and thickness (0.2 or 0.4 m), casting rate (2.7-6.4 m/h), and rate of structural build-up. The structural build-up was measured through a number of test methods (cf. Table 1) to suit the various researchers' needs. A total of eight castings were carried out during four days. Highest measured relative formwork pressure was 90 %. Billberg's conclusion is that all methods evaluated were comparable indicating that neither a "best" nor "worst" method could be identified [5].

3. AIM AND LIMITATIONS

The original aim of current research project was to investigate the influence of SCC properties on formwork pressure. The research question dealt with investigating any possible relationship between fresh concrete properties and formwork pressure exerted in full-scale concrete castings. Each concrete batch was tested for air content, slump-flow, and concrete and air temperature. Measurements were also conducted on torsional moment or torque as well as L-box and V-funnel tests. In addition, each slump-flow test was photographed. Torsional moment was measured at three different times after casting. Hence, it was also possible to evaluate the relationship between time-dependent changes of fresh concrete and formwork pressure.

The full-scale tests were carried out on a real project, a 400 m long prison wall. Measurements on a real project implies a lot of advantages (e.g., real conditions, no "lab-crete", experienced workers, and reduced costs) but also some disadvantages or limitations. The concrete mix design was made by the ready mix concrete plant in co-operation with the contractor and could not be varied which is desirable in any research project. Also the formwork height and thickness were constant. Furthermore, only twelve out of 33 castings could be instrumented and measured. All fresh concrete properties were not always measured at both plant and on site. The castings were conducted during winter which caused problems with some of the castings, measurements, and readings. Finally, the research project was planned and carried out already in 2007 and 2008-2009, respectively. At that time, no practical design methods (like [11] or [13]) were published. If they had existed, the testing program could easily have been expanded to cover the simple fresh concrete tests that constitute input data to their models.

4. DESCRIPTION OF THE PROJECT

4.1 General information on the project

The research project was carried out in connection to a new prison located in Härnösand, a city 450 km north of Stockholm, Sweden. The planning of the new prison, replacing an existing one, was initiated in 2003. In August 2007, the contractor NCC Construction was commissioned by the client Specialfastigheter Sweden. The prison was finished in two years (Figure 3). In average, one hundred people have been involved in the project. Two walls are surrounding the

prison, one 1000 m long outer wall and one 400 m long inner wall. This research project was carried out on parts of the inner wall that was 6 m high and 0.27 m thick.



Figure 3 – The new prison Saltvik was opened for use during the autumn 2010. It has room for 134 prisoners. Photographs from Wikipedia.

4.2 Castings

The wall was cast in 12 m sections (occasionally 10.8 m), using approximately 20 m³ SCC per section. The ready-mixed concrete was delivered by Grus & Betong i Norrland, a company within the Skanska group. Each section was normally cast in four lifts (single cases in five, six or seven lifts) that each was averaging 1.5 m in height. The casting rate varied between 1.3 and 3.5 m per hour and a concrete pump was used. The pump hose position was horizontally fixed during each casting. Concrete from the trucks were alternately pumped to the left and to the right (Figure 4). During each casting, pressure values were continuously monitored on the computer. Direct contact with staff at the ready-mix concrete plant and the pump truck driver made it possible to reduce the casting rate if the pressure values were too high.

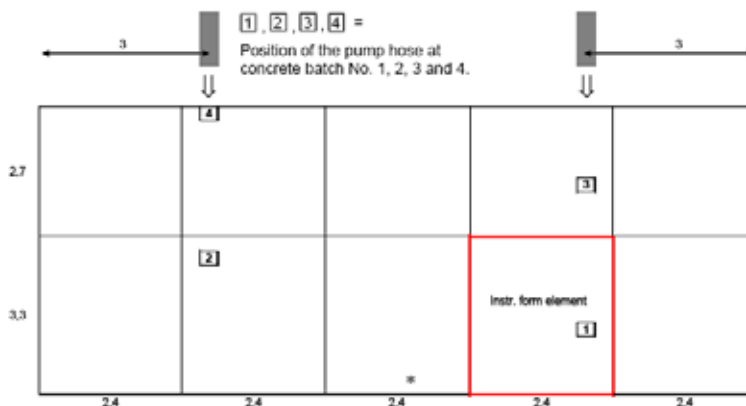


Figure 4 – Varying position of the pump hose. Measures in meter. *) Occasionally 1.2 m.

Requirements on concrete durability was established from exposure classes XC4 and XF3 in SS EN 206-1 [16], maximum $w/c = 0.55$. The selected SCC mix was frost resistant and designed to meet the requirements on compression strength class C32/40. The w/c was 0.50 (lower than the requirements in SS EN 206-1), and w/p was 0.33 with a paste content of 446 l/m³.

The ready-mix concrete plant was located just 250 m from the building site. The general mix design of the used SCC is shown in Table 2. The amount of admixtures was varied somewhat in order to maintain uniform fresh concrete properties.

Table 2 – Mix design of one cubic meter of the SCC.

Constituent	Weight (kg)
CEM II (Portland-limestone)	400
Limestone filler	200
Aggregate 0-8 mm (natural sand)	1015
Aggregate 8-16 mm (crushed)	485
Water	200
Plasticizer	Approx. 2.5
Air entraining agent	Approx. 1.1

The wall was built between August 2008 and May 2009. Measurements were made during twelve (of a total of 33) castings, see Table 3. Three different (but identical) form elements (Nos. 1-3) were used alternatively to enable an efficient production cycle.

Table 3 – Disposition of the castings and corresponding temperature and casting rate.

Date	Element No.			Outside air temp, mean value (°C)	Casting rate (m/h)	Note
	1	2	3			
2008						
8 Oct		X		+ 6	1.4	
10 Oct	X			+ 8	1.5	
15 Oct			X	-	1.5	
22 Oct	X			+ 7	1.3	
7 Nov		X		+ 3	1.5	
14 Nov			X	+ 2	1.5	
19 Nov		X		- 2	1.3	
2009						
14 Jan	X			- 2	1.3	The concrete was too stiff.
28 Jan		X		- 1	1.7	The concrete was too stiff.
11 Feb		X		- 10	2.5	
25 Mar		X		- 4	3.5	
27 Apr		X		-	3.3	

Note. The casting rate is defined as the average casting rate computed as total casting height divided with total time from casting start to end of casting. The measurements on Jan. 14 and Jan. 28 were omitted in the analyses since the needed fresh concrete measurements could not be performed.

4.3 Formwork, instrumentation and measurements

The formwork consisted of film faced 15 mm plywood panel mounted on steel frames. Each steel frame element was 2.4 m wide and 3.3 m high, consisting of two vertical KKR profiles (100×100×5 mm, KKR stands for the Swedish acronym for Cold Formed Rectangular Hollow Section, CFRHS) and horizontal VKR profiles (100×40×2.5 mm, VKR stands for the Swedish acronym for Hot Formed Rectangular Hollow Section, HFRHS). The formwork was supplied by the company PERIform Sverige. In average, two stages per week were cast. The walls were reinforced with a double mesh and 12 mm rebars. One of the elements was instrumented with pressure sensors and placed near the middle of the section, as shown in Figure 5.

The pressure sensors used were Honeywell ABH100PSC1B model with pressure range 0 to 689 kPa. The sensors were mounted in special made threaded steel plugs and sockets, with rubber wreaths around them to prevent leakage. They were flush-mounted, facing inwards, and placed in five different levels from the ground: 110, 530, 1130, 1730 and 2630 mm. In Figure 6, they are marked as red circles. The sensors were measuring deformation which then was transformed into voltage fluctuation (in mV). A logger (HBM Spider 8 with amplifiers SR 01) gathered the signals and transformed them for a connected computer using the software HBM Catman. The logger and the computer were stored inside a movable steel container, which was moved before each casting.



Figure 5 – Location of the instrumented form element in the actual section.

During the tests, also tension forces in the tie bars and strains in the formwork framing were measured. Comparisons between the three methods (pressure sensors, tie bar forces, and framing strains) show that the correspondence is fairly good [2], but in this paper only the pressure sensor measurements are used.

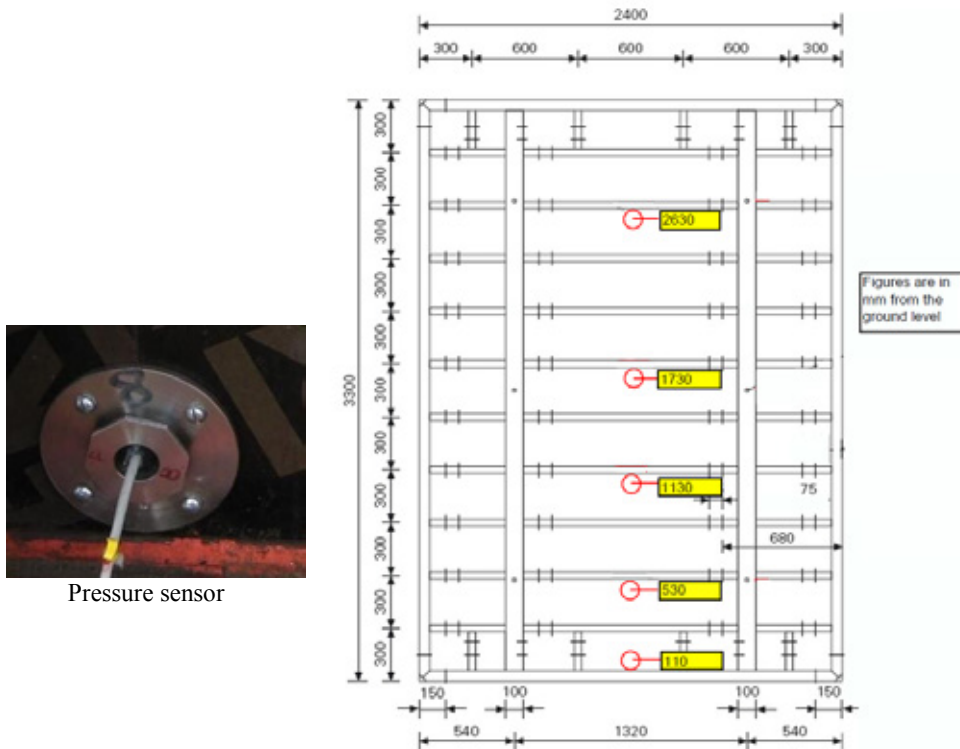


Figure 6 – Instrumentation of the formwork element.

Calibration of the pressure sensors and measurement uncertainty

In the laboratory, a pressure transducer (HBM P11, pressure range -20 to 20 kPa) was calibrated with the pressure calibrator (Fluke 718 100G, pressure range -82 to 689 kPa). These two gauges were mounted on a steel cylinder, 1.5 m tall and with 0.20 m diameter, with pressurized air in it. As a second step, the five pressure sensors were calibrated with the pressure transducer on the same steel cylinder. The logger used during the calibration was a HBM MGC Plus ML55B. The calibration provided conversion factors for the five pressure sensors as input for the used software. The total uncertainty of the pressure sensor measurements in the field consists of uncertainties in the following parts: (i) the pressure calibrator (0.05%), (ii) the pressure transducer (0.5%), (iii) the logger used for calibration (0.02%), (iv) the logger used in the field (0.2%), and (v) the pressure sensors (0.25%).

4.4 Fresh concrete testing

Each concrete batch was tested for air content, slump-flow, concrete and air temperature and torsional moment or torque as well as L-box and V-funnel tests. In addition, each slump-flow test was photographed. Slump-flow was measured according to SS-EN 12350-8 [17] (Figure 7, left).

Structural build-up at rest of concrete is typically assessed using a coaxial concrete rheometer, see [18]. In this project, a Portable Vane (PV) test, similar to that used to evaluate

the un-drained shear stress of soil, was used. The test method for soil is described in ASTM D2573-72 [19]. In this case a special equipment developed at the Swedish Cement and Concrete Research Institute was used (Figure 7, right). It consists of a cubic container with the sides made of 12 mm plywood. The interior dimensions of the container measure 300×300×300 mm. The four-bladed vane is attached through a ball bearing provided axle to a steel stand. The four blades are mounted in an orthogonal pattern. Each blade is 50×50 mm large and 2 mm thick. The gravity centre of the vane is placed 150 mm from the bottom of the container, i.e., at the centre of the fresh concrete. The measuring procedure is as follows:

1. Fill up the container with fresh concrete up to a height that should not exceed the container's height.
2. Mount the steel stand centred on the top of the container and tighten the screws slightly against two opposite exterior sides of the container.
3. Attach the torque meter, apply a torsional moment, and measure the torque that is needed to break down the structure of the fresh concrete.
4. Register the maximum value.

The torsional moment is registered as a value in Nm. The maximum value registered during the test is defined as the torsional moment T used in the analysis. There are expressions for converting the torsional moment to a shear stress but such a conversion has not been used since it is not needed for the aim of this paper. The torsional moment was measured at three different times; 0 (measured directly after pump), 20 and 40 minutes after casting. The measured increase of the torsional moment is a measure or at least substitute for the structural build-up of the SCC.



Figure 7 – Slump-flow test (left) and the Portable Vane, equipment for measuring torque (right).

The data from the L-box and V-funnel tests have not been used in the analysis for this paper. Descriptions on these test methods are therefore outside the scope of this paper.

5. RESULTS AND ANALYSIS

5.1 Introduction

The measurements were carried out on twelve castings (Table 3). Formwork pressure measurements were carried out during all twelve castings. The pressure sensors were located on five different levels (Figure 6). Since the casting of the formwork was made in several lifts,

there was a stepwise increase of the formwork pressure. The minor steps that also can be identified in the figure depend on the intermittent process of pumping. Simultaneously, there was a decrease of the formwork pressure due to structural build-up. A typical curve describing the formwork pressure development with time is shown in Figure 8.

All twelve castings were initially used for the entire analysis. However, the castings on 14 and 28 January, 2009, were omitted in the analysis in Section 5.3 since the SCC was too stiff to enable torsion measurements.

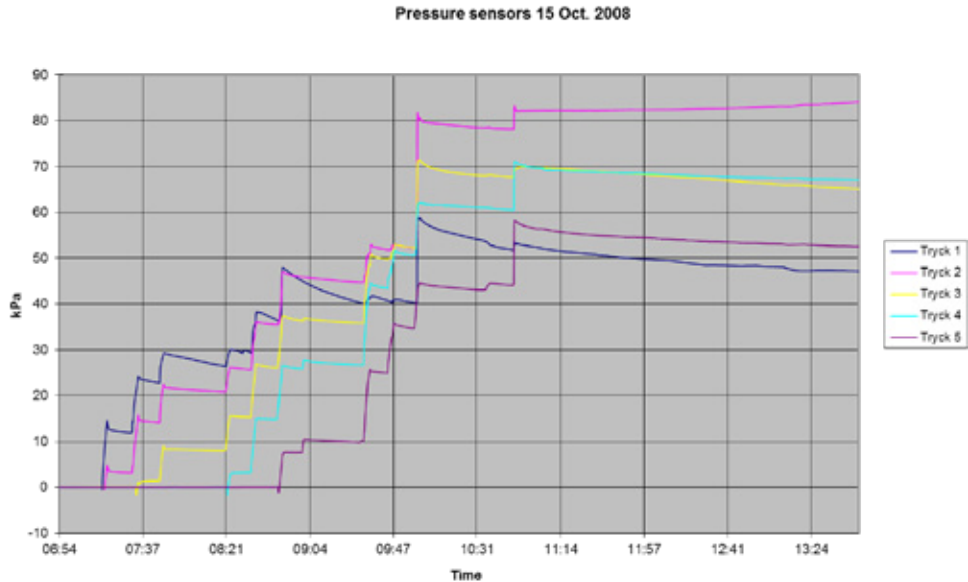


Figure 8 – Relationship between time (hour:min) and measured formwork pressure for casting on 15 Oct. 2008. The measurements at level 2, 0.53 m from bottom (indicated by “Tryck 2” in the legend), were used in the analysis. Casting started at 6.54 a.m. and maximum formwork pressure = 82.6 kPa was obtained at 10.50 a.m., i.e., 236 minutes after casting.

5.2 Simple relationships

In cases with all other parameters equal, it is anticipated that there should be an evident relationship between casting rate and formwork pressure. The concrete mix design was the same during the entire project but other conditions varied, especially the weather, cf., Table 3. Despite the non-consistent conditions, the relationship between casting rate and maximum measured formwork pressure was investigated (Figure 9). As anticipated, no correlation was obtained. The majority of the castings were conducted at a casting rate between 1.3 and 1.7 m/h and the graph shows that any value between 30 and 100 kPa could be obtained for the maximum formwork pressure.

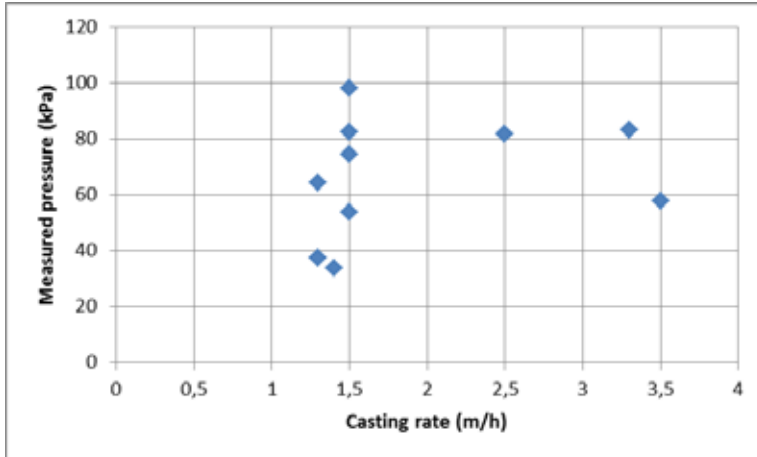


Figure 9 – Maximum measured formwork pressure, measured at 0.53 m from bottom, versus casting rate.

Figure 10 shows the relationship between measured slump-flow after pump and developed maximum formwork pressure at level 2, i.e., at 0.53 m from bottom. A decent correlation between the initial slump-flow and the measured pressure was obtained. The slump-flow corresponds to yield stress. Two concrete mixes with large difference in yield stress are likely to be different also in other respects, e.g., in structural build-up which current research has identified as one of the most important factors for obtaining formwork pressures below full hydrostatic pressure.

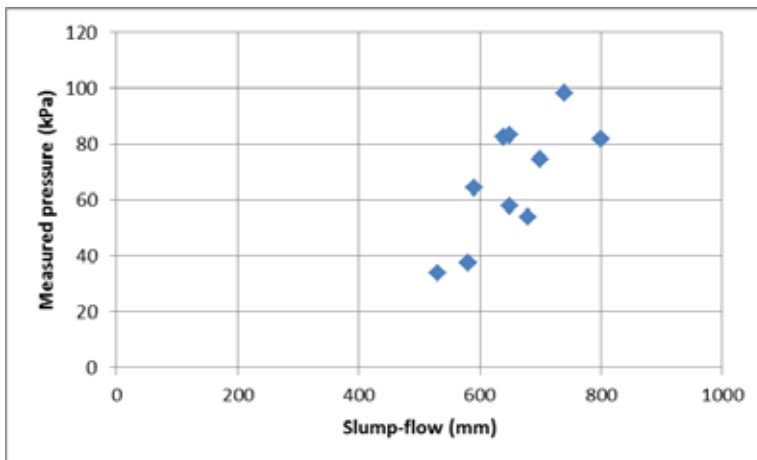


Figure 10 – Maximum measured formwork pressure, measured at 0.53 m from bottom, versus initial slump-flow.

5.3 Procedure and assumptions for estimating formwork pressure in the Härnösand study

Knowledge on consistency and casting rate is not sufficient to estimate formwork pressure. As stated above, we need to consider the behaviour of the self-compacting concrete at rest [5]. In current study in Härnösand, the measurement on torsional moment or torque T was the only test method used repeatedly during the casting procedure and is therefore the only possible indirect test method on structural build-up. It was measured at 0, 20, and 40 minutes after casting. In this section, the authors have tried to estimate the formwork pressure by combining the measurements on torsional moment with two simple methods from the literature; (i) DIN [11] and (ii) Gardner et al. [13]. The data from ten castings between 8 Oct., 2008, and 27 April, 2009, were used in the analysis. These castings were characterized by well-functioning measurements and gauges during the entire castings as well as by no signs of concrete segregation. In fact, these were the only castings that fulfilled these requirements.

Assumptions for using the two methods in the analysis are described in Table 4.

Table 4 – Assumptions in the analysis.

No.	DIN [11]	Gardner et al. [13]
1	The time-dependent structural build-up is assumed to be approximately linear and not only until 40 minutes (Figure 11) but even continuously until the setting time t_E .	The time-dependent structural build-up is assumed to be approximately linear and not only until 40 minutes (Figure 11) but even continuously until the setting time t_E .
2	A default value for the setting time used in the DIN test method is 10 h [11]. Slightly lower values (4-6 h) were obtained in the Swedish workshop (Section 2.4, [5]).	Measurements in [13] indicate that $t_0 \approx 3$ h with a large variation. In the Swedish workshop, higher values (4-11 h) were obtained.
3	Due to lack of measuring values and verified relationships, any influence of concrete mix and temperature is ignored. All other conditions equal, the low temperature in the Härnösand study ought to postpone the setting time.	Due to lack of measuring values and verified relationships, any influence of concrete mix and temperature is ignored. All other conditions equal, the low temperature in the Härnösand study ought to postpone the setting time.
4	The setting time is set to $t_E = 10$ h.	The zero slump-flow time is set to $t_0 = 4$ h.
5	Extrapolating and averaging the torsional measurements in Figure 11 indicates that $t_E = 10$ h corresponds to $T \approx 12$ Nm.	Extrapolating and averaging the torsional measurements in Figure 11 indicates that $t_0 = 4$ h corresponds to $T \approx 5$ Nm.
6	The evaluation has been conducted with individual measurements (every casting day is an individual measurement) using $T_{DIN} = 12$ Nm and $t_E = T_{DIN} / (\Delta T / dt)$, where $\Delta T / dt$ is the average measured torsional change rate (measured in Nm/h) between $t = 0$ and $t = 40$ min, i.e., $\Delta T / dt = (T_{t=40 \text{ min}} - T_{t=0}) / ([2/3]h)$.	The evaluation has been conducted with individual measurements using $T_{Gardner} = 5$ Nm and $t_0 = T_{Gardner} / (\Delta T / dt)$, where $\Delta T / dt$ is the average measured torsional change rate (measured in Nm/h) between $t = 0$ and $t = 40$ min, i.e., $\Delta T / dt = (T_{t=40 \text{ min}} - T_{t=0}) / ([2/3]h)$.
7	The calculated pressure p is computed with Eq. (2) and compared with the measured formwork pressure at level 2 (0.53 m above formwork bottom) starting with the first lift.	The calculated pressure p is computed with Eq. (3) and compared with the measured formwork pressure at level 2 (0.53 m above formwork bottom) starting with the first lift.

All assumptions may of course be discussed and criticized. Linear extrapolation (assumption No. 1) is an uncertain prediction method; however, this is the best one that can be used when evaluating this project afterwards. Please, note that the Härnösand case study was conducted one to three years prior to the publication of the two formwork pressure models. The use of the average time-dependent structural build-up for selecting the torsional moment corresponding to the setting time implies that the correspondence between measured and calculated formwork pressure will be fairly good. The interesting point is that this procedure makes it possible to compare individual test results with the corresponding calculated values. Faster (shorter setting time) and slower structural build-up (longer setting time) than the average will be reflected in lower and higher calculated formwork pressure, respectively, in cases with constant casting rate. Consequently, the comparisons between the ten castings and corresponding calculated values are interesting.

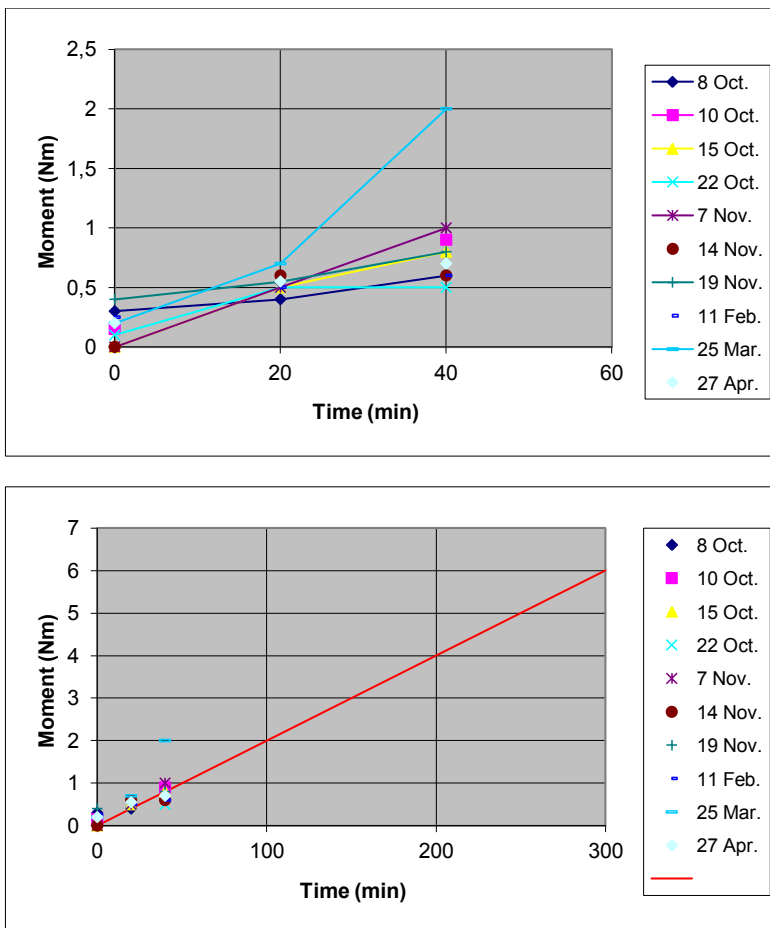


Figure 11 – The time development of torsional moment for selected concrete castings. The lowest graph contains an extrapolation of the measuring values up to $t = 300 \text{ min} = 5 \text{ h}$. This graph has been included to help the reader to obtain values of the torsional moment at times $t \gg 40 \text{ min}$. In Table 4, item 4, values after $t = 240$ and $t = 600 \text{ min}$ are used.

5.4 Comparison between calculated and measured formwork pressure in the Hårnösand study

The comparison between calculated values using the DIN method [11] and measured values is shown in Figure 12. Most of the values are rather close to the diagonal line that represents complete correspondence. There seems to be one outlier (from Oct. 8) and two groups (one above the line of complete correspondence between measurement and calculation and one below). However, no common denominator has been identified for the two groups, neither similar temperature, nor similar casting rate. Since the estimation procedure contains a series of assumptions, a better correspondence was hardly expected.

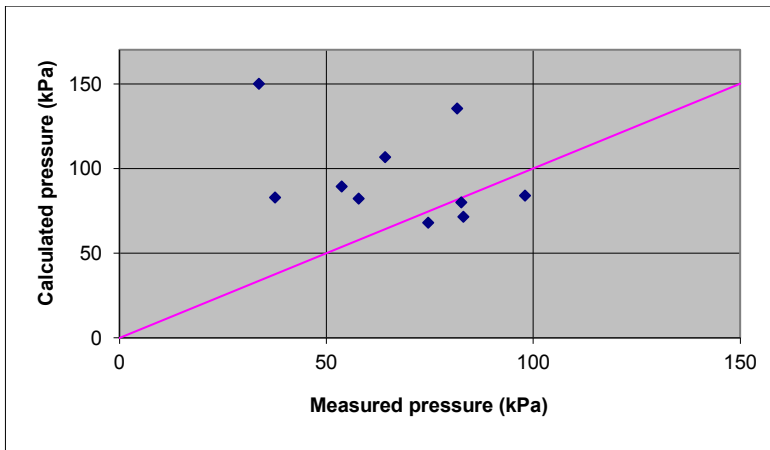


Figure 12 – The relationship between measured and calculated formwork pressure using the DIN method [11].

The comparison between calculated values using Gardner's method [13] and measured values is shown in Figure 13. The diagram points show a similar pattern as in Figure 12, however, all values are placed slightly lower, i.e., the calculated values are slightly smaller. This means that Gardner's method is less conservative than the DIN method. Still the obtained comparison is hardly worse than the correspondence obtained by the authors proposing Gardner's method, cf., Figure 2.

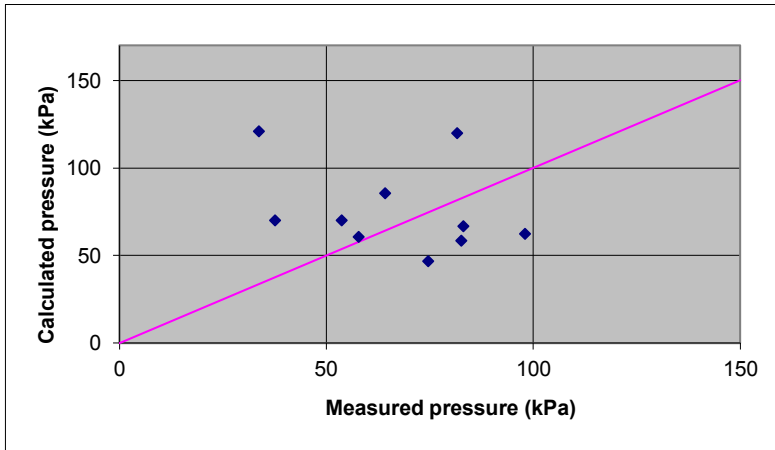


Figure 13 – The relationship between measured and calculated formwork pressure using Gardner's method [13].

6. CONCLUDING REMARKS

The construction of a new prison wall in the north of Sweden provided a unique possibility to carry out field tests on formwork pressure of SCC. A total of twelve castings were instrumented and measured during the winter 2008-2009. The formwork used consisted of steel-framed panels, instrumented with flush-mounted pressure sensors. Tests on fresh concrete properties as well as formwork pressure measurements were carried out for all twelve castings.

The tests show that previous formwork pressure methods, developed for vibrated concrete, cannot be used for determining formwork pressure of SCC. No clear correlations could be found between neither initial slump-flow nor casting rate and formwork pressure generated. This finding supports conclusions from previous research on formwork pressure generated by SCC.

In order to estimate the formwork pressure development, knowledge on the structural build-up of the SCC at rest has to be known or be possible to anticipate. In the Härnösand study, the structural build-up was measured through repeated tests on torsional moment. The torsional moment development with time has been used as an indirect measurement on the setting time t_E and zero slump-flow time t_0 used in the DIN method [11] and Gardner's method [13] to compute formwork pressure, respectively. Comparison between calculations and measurements show that both methods seem to be possible to use.

There is an urgent need of further research both in laboratory and in field to validate DIN method and Gardner's method for the large variety of conditions that are possible in the field. However, so far they seem to be promising for predicting formwork pressure generated by SCC.

ACKNOWLEDGEMENT

The authors wish to acknowledge the financial support from the Swedish Traffic Administration (previously Swedish Road Administration), the Development Fund of the Swedish Construction

Industry (SBUF) and the Swedish Consortium for Financing Basic Research in the Concrete Field. Special thanks to those who contributed with expert help regarding measurements: Stefan Trillkott and Claes Kullberg at the Division of Structural Engineering and Bridges, KTH Royal Institute of Technology in Stockholm. The great support from NCC Construction (especially Lennart Vestman and Per-Arne Källman) made this project possible and very rewarding. Finally, thanks to PERIform Sverige and Grus & Betong i Norrland for technical support. Last but not least are Dr. Peter Billberg, Strängbetong, and Eva Bertfelt, Swedish Cement and Concrete Research Institute, acknowledged for their assistance regarding planning and conducting of the measurements, respectively.

REFERENCES

1. Billberg, P., Silfwerbrand, J., & Österberg, T., "Form Pressures Generated by Self-Consolidating Concrete". *Concrete International*, Vol. 27, No. 10, October 2005, pp. 35-42.
2. McCarthy, R. & Silfwerbrand, J., "Comparison of Three Methods to Measure Formwork Pressure When Using SCC", *Concrete International*, Vol. 33, No. 6, June 2011, pp. 27-32.
3. Backsell, G., & Bydemar, B., "Dimensionering av vertikala formar" ("Design of Vertical Concrete Formwork"), *Report 44:1968*, The National Swedish Institute for Building Research, Göteborg, Sweden, 1968. (In Swedish).
4. Mc Carthy, R., Billberg, P., & Silfwerbrand, J., "An Investigation and Comparison of International Design Methods for Vertical Formwork". *Proceedings*, 5th International RILEM Symposium on Self-Compacting Concrete, Ghent, Belgium, September 3-5, 2007, Vol. 1, pp. 479-484.
5. Billberg, P., "Utvärdering av formtrycksmodeller vid gjutning med SKB" ("Evaluation of Formwork Pressure Models at Casting with Self-Compacting Concrete – An International Comparison with the Assembled Global Experts". *Technical Report*, Swedish Cement and Concrete Research Institute, Stockholm, Sweden, 46 pp. (In Swedish).
6. Ovarlez, G., & Roussel, N., "A Physical Model for the Prediction of Lateral Stress Exerted by Self-Compacting Concrete on Formwork", *Materials & Structures*, Vol. 39, No. 2, 2006, pp. 269-279.
7. Proske, T., "Frischbetondruck bei Verwendung von Selbstverdichtendem Beton – Ein wirklichkeitsnahes Modell zu Bestimmung der Einwirkungen auf Schalung und Rüstung (Formwork Pressure using Self-Compacting Concrete)", *PhD-thesis*, Technische Universität Darmstadt, Germany, 2007, 310 pp. (In German).
8. Lange, D.A., Birch, B., Henchen, J., Liu, Y-S., Tejeda-Dominguez, F., & Struble, L., "Modeling Formwork Pressure of SCC", *Proceedings of the 3rd North American Conference on the Design and Use of Self-Consolidating Concrete*, Ed. S. P. Shah, Chicago, USA, 2008, pp. 295-300.
9. Perrot, A., Amziane, S., Ovarlez, G., & Roussel, N., "SCC Formwork Pressure: Influence of Steel Rebars". *Cement and Concrete Research*, Vol. 39, Issue 6, 2009, pp. 524-528.
10. Beitzel, M., "Modeling Fresh Concrete Pressure of Normal and Self-Compacting Concrete", *Proceedings*, the 6th International RILEM Symposium on SCC and the 4th North American Conference on the Design and Use of Self-Consolidating Concrete, Ed. K.H. Khayat & D. Feys, Montreal, Quebec, Canada, 2010, pp. 243-254.
11. DIN, "DIN Standard on Formwork Pressure Updated – Standard Now Addresses Pressure Exerted by Self-Consolidation Concrete". *Concrete International*, Vol. 32, No. 6, June 2010, pp. 27-29.

12. Khayat, K.H., & Omran, A.F., "Field Monitoring of SCC Formwork Pressure and Validation of Prediction Models", *Concrete International*, Vol. 33, No. 6, June 2011, pp. 33-39.
13. Gardner, N.J., Keller, L., Quattrociochi, R., & Charitou, G., "Field Investigation of Formwork Pressures using Self-Consolidating Concrete", *Concrete International*, Vol. 34, No. 1, January 2012, pp. 41-47.
14. Graubner, C.-A.; Boska, E.; Motzko, C.; Proske, T.; & Dehn, F., "Formwork Pressure Induced by Highly Flowable Concrete – Design Approach and Transfer in Practice", *Structural Concrete*, Vol. 13, No. 1, 2012, pp. 51-60.
15. Donahey, R., "International Workshop on Formwork Pressure Generated by Self-Consolidating Concrete", *Concrete International*, Vol. 34, No. 8, August 2012, pp. 38-40.
16. SIS, "SS EN 206-1. Concrete – Part 1: Specification, Performance, Production and Conformity". Swedish Standards Institute, Stockholm, 2001, 74 pp.
17. SIS, "SS EN 12350-8. Testing Fresh Concrete Self-Compacting Concrete. Slump-flow Test". Swedish Standards Institute, Stockholm, 2010, 20 pp.
18. Omran, A.F., Naji, S., & Khayat, L.H., "Portable Vane Test to Assess Structural Buildup at Rest of Self-Consolidating Concrete". *ACI Materials Journal*, Vol. 108, No. 6, October-November 2011, pp. 628-637.
19. ASTM, "ASTM D2573-72. Standard Test Method for Field Vane Shear Test in Cohesive Soil". American Society for Testing and Materials, West Conshohocken, PA, USA, 1972.

Avoiding undesirable final results of bonded steel fibre concrete overlays – observations from tests and theoretical calculations



Dr Jonas Carlswärd
Betongindustri AB
Box 47312
SE-100 74 Stockholm
E-mail: jonas.carlsward@betongindustri.se



Prof, Dr. Mats Emborg
Div. Structural and Construction Engineering,
Luleå University of Technology
SE-971 87 Luleå
Betongindustri AB
Box 47312
SE-100 74 Stockholm
E-mail: mats.emborg@ltu.se / mats.emborg@betongindustri.se

ABSTRACT

Due to a high degree of damages and undesirable final results of bonded overlays, research has been conducted to develop recommendations on design and execution. Laboratory and half scale tests as well as theoretical analyses have been carried out including e. g. base and end restraint tests on overlays with various reinforcement, concrete qualities, substrate preparing and curing. Also, analytical and numerical calculations have been performed. Results reveal that the bond between overlay and substrate is the most critical parameter for a successful final result. Other key parameters are shrinkage and curing, while fibre and bar reinforcement generally proved to be less significant. Theoretical models work well on this case and will be further developed.

Keywords: Overlay, Shrinkage, Cracks, Curing, Bond, Steel fibres, Restraint stresses, Self Compacting Concrete

1. INTRODUCTION

1.1 Basic

Bonded overlays on concrete substrates are applied in a wide range of applications such as bridge deck overlays on structural concrete, finishing layers on prefabricated elements, repairs or strengthening of deteriorated bridge, parking decks and damaged industrial floors. In order to ensure that the overlaid system maintains durable and fully functioning during the intended service life it is essential to limit crack widths and to prevent delamination.

However, despite the fact that concrete is utilised on a regular basis for this application area, established practice regarding design and execution is lacking. A consequence is that misapplied

execution methods and wrong design are common, resulting in a far too high degree of undesirable final results. Cracking, debonding and edge lifting are among the most frequent problems, resulting from the differential shrinkage and thermal strain between the newly placed layer and the old sub-base material, see Figure 1.

To develop relevant guidance on how to design and execute overlays avoiding the problems above, research projects have been and are carried out at LTU in cooperation with Betongindustri AB, Strängbetong AB and Betongteknik AB with funding from Trafikverket, SBUF and also the university [1] – [3]. The work presented here summarises studies in Sweden mainly conducted within the doctoral thesis of first author [1] and on-going research. Focus is on test results and analysis. Some examples of theoretical calculations will however be given.

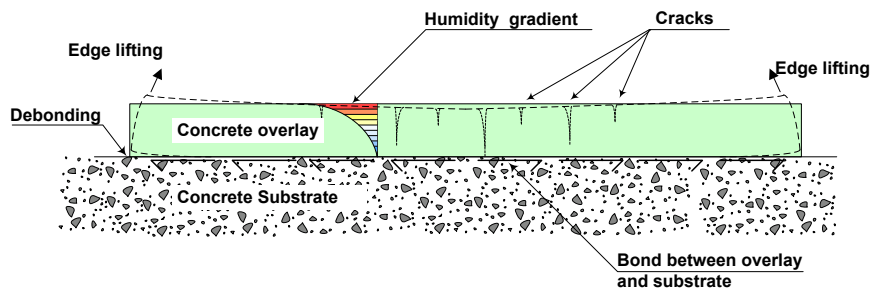


Figure 1. Cracking and edge lifting of overlay due to differential shrinkage [1].

1.2 Influencing factors

Many researchers and building clients have pointed out that the most important factor determining the service life of an overlaid structure is shrinkage of the newly cast overlay that is restrained by the underlying substrate [4-7]. On the other hand, as observed in recent studies, also temperature induced strains may have an influence on this matter. Nevertheless, the damages according to Fig. 1 are typical consequences of rather the difference in shrinkage and temperature strain between the overlay and substructure. In this paper, however, main focus is on the shrinkage induced effects.

Two measures may be undertaken to minimise the negative effects of restrained shrinkage: (1) reduce the shrinkage of the overlay concrete and/or (2) provide reinforcement to distribute and control cracks. Shrinkage reduction may be accomplished for example by adding Shrinkage Reducing Admixture (SRA) to the mix or by a proper mix design with as low cement paste and cement content as possible. The effect of SRA has been studied quite extensively over the last 15-20 years, leading up to 30 % reduction both in short and long term (> 200 days in own tests), see e. g. [8-10], and the technique may now be regarded as an accepted method to control concrete shrinkage.

Reinforcement is provided either by welded mesh or steel bars or by mixing fibres into the concrete matrix. An attractive feature of fibre reinforced concrete (FRC) is of course that the demanding handling of traditional reinforcement is eliminated. The improvement in working environment, and possibility to reduce labour intensity, is even more accentuated when fibres are combined with self compacting concrete (SCC). Experience from real overlay castings has further demonstrated that the use of SCC leads to improved surface finish with regard to flatness demands, thus reducing the need for expensive levelling screeds. These factors certainly give the

contractor incentives to select FRSCC, both from a productivity perspective as well as from a working environment and economical point of view.

Despite the fact that fibres, mainly steel, are used on a regular basis to control cracking there is no method available to design overlays. This means that the steel fibre addition is often selected/designed based on recommendations relying on experience. Several experience based design proposals are available according to [12]. Although such methods occasionally may prove to result in “crack-free” overlays it is obvious that more reliable approaches need to be developed for the future use of SFRC and SFRSCC in overlays. Thus, main incentives in present and future research as well as development are: (1) to experimentally verify the effect of steel fibres on widths and distribution of shrinkage cracks in thin overlays (2) to establish a theoretical model for the estimation of crack risk due to restrained shrinkage and to assess the contribution of steel fibres on crack widths and, last but not least, (3) to study the effect of the driving force on this phenomenon; the shrinkage.

2. OVERLAY TESTS

2.1 General

Various types of tests may be utilized for calibration of the models above; end-restrained test (1), base restraint tests (2) and ring tests (3), see Figure 2. Category (2) tests are clearly the most suitable from the viewpoint that the restraint condition represents the real overlay conditions. A drawback is that it is difficult to control the bond conditions, which means that the cracking response will rely on the particular restraint situation (bond quality) obtained in each test.

The ring test is certainly the most popular test method. Favourable features are the simplicity of the setup and that the degree of restraint is well defined. However, a review of results reported indicates that the ring test may overestimate influence of crack distribution [1], [11]. Multiple cracking is regularly obtained already at low steel fibre dosages and in fact also for plain concrete. As crack distribution would clearly not take place in unreinforced concrete this leads to speculations regarding the validity of the method assessing the effect of reinforcement.

Instead, end-restrained and base restrained tests have been used to assess the effect of steel fibres, restrained shrinkage and bond on cracking potential of SCC.

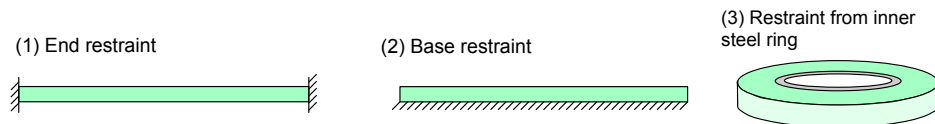


Figure 2. Common types of test methods used to study the effect of restrained shrinkage.

2.2 End-restrained test series

The test setup consisted of an HEA steel beam with a polished upper flange, giving a smooth and slippery surface to ensure that restraint would only develop at the ends of the specimen, see Fig. 3. L-shaped supports of steel 80x45 mm with 20 mm thick goods were bolted to the flange at a distance of 1 m.

measurement, see Fig. 6, with the same cross section but slightly shorter, however still representative as a dummy specimen (still same drying and shrinkage conditions). Target points for measuring deformation were glued to the surface immediately after demoulding at 24 hours. Shortly after this, a zero-reading was recorded on both restrained and unrestrained specimens.

2.3 Base restrained test series in laboratory

The base restrained tests consisted of narrow overlay strips (50x150x2500 mm) cast on large concrete bottom slabs, see Fig. 4 (a). Four slabs were produced approximately a year in advance to minimise the remaining shrinkage to maximise the differential shrinkage between overlays and slab. Different substrate preparations were applied in order to achieve a variation in bond quality for the slabs (grinded and dry at the time of overlaying, grinded and wet, milled and wet and milled and primed with MD 16 (Maxit). The grinding procedure gave a rather smooth texture while milling resulted in a rough texture, see Fig. 4 (b).

The ends of the overlay strips were fastened to the slabs by means of vertical expansion bolts in order to avoid complete delamination due to the well-known vertical tensile stresses, breaking off the overlay at the end. Ten overlay strips were cast on each slab; two strips of plain SCC, two steel bar reinforced strips SBRSCC (a centrally placed 10 mm steel bar i. e. 1 %), two strips with shrinkage reduced SCC (SRASCC with 1.5 % SRA type Sika Control 40) and four SFRSCC strips (two with 30 kg/m³ of fibres and two with 60 kg/m³ of the type Dramix RC-65/35-BN). The same basic concrete recipe and materials as for the end-restrained test series were used for all mixes (Table 1).

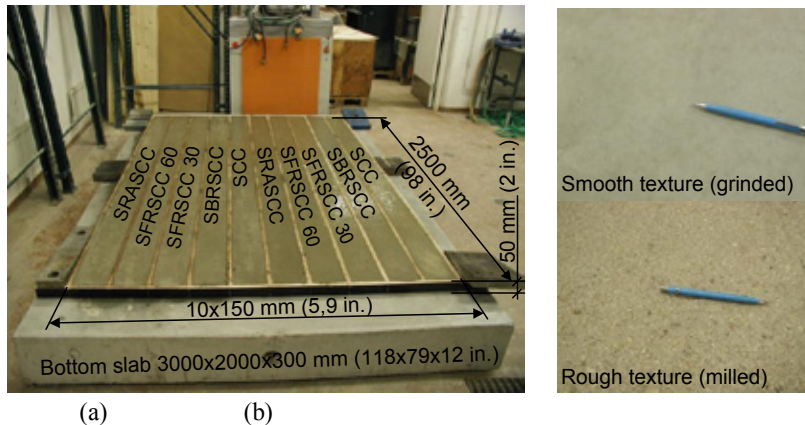


Figure 4. (a) Overlay strips on one of the slabs directly after casting. (b) Smooth and rough texture of substrate obtained by grinding and milling.

The overlays were cured underneath plastic coverage for five days before exposed to a rather harsh laboratory environment of 15-20 % relative humidity and 20°C giving a rapid drying shrinkage development and associated overlay cracking within a rather short period of time (prior to 30 days which is not so common in reality – i. e. cracking often occur later as the humidity often is higher). Cracking and debonding were followed for a period of about 3 months where more than 70 % of the total shrinkage has been reached.

Free unrestrained shrinkage was obtained in the same way as for the end-restrained test series under identical drying conditions, see Fig 9, despite a much shorter specimen as earlier

explained. A thickness of 50 mm was adopted in order to simulate the overlay strips and deformations were recorded at the bottom and upper faces of the specimens, using a handheld mechanical measuring device, to capture the shrinkage gradient.

2.4 Base restrained tests on large specimens

A series of “full or half scale” overlay tests was conducted on prestressed hollow core slabs (completely hardened, strength C45/55) of the type HD/F 120/27 at one prefabrication plant (Strängbetong AB). In total six slabs were used, each divided into four separate areas, in which different substrate preparations were applied in order to obtain a variation in the bond quality, see Figure 5 [3].

Preparations adopted (on thoroughly cleaned slabs) were pre-moistening, primer and none (dry). Pre-moistening was conducted approximately 1 hour prior to overlaying, which resulted in a film of free water on the substrate. Priming (Maxit Floor 4716) was conducted in two ways, the day before (primer 1d) and just before overlaying (primer 1h). Slabs 1, 3, 4 and 6 were overlayed at the same time with a 50 mm layer of Self Compacting Concrete (SCC). Slabs 1 and 4 were un-reinforced while slabs 3 and 6 were reinforced with steel bar mesh $\phi 8 \times 100$. Steel fibres (30 kg/m³, Sika Fiber CHO 65/35 NB) were then mixed into the SCC before the last two slabs were overlayed (slabs 2 and 5).

Two of the areas on each slab were air-cured while the remaining parts were covered by plastic foil, see Fig 5, which was removed 6 days later. However, the covering was not done until the morning the day after casting, which means that the surfaces were uncovered for approximately 17 hours. The mix design is given in Table 2. The cement was of the type CEM II/A-LL 42.5R (Byggcement, Cementsa). The aggregates were of a natural occurring type (Riksten).

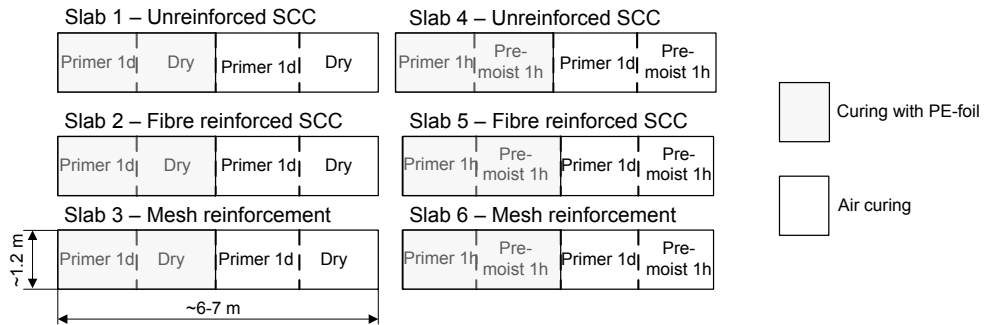


Figure 5. Full scale testing on hollow core slabs divided in four areas each with separate substrate preparation. Other parameters varied: type reinforcement and type of curing [3].

Table 2 - SCC mix composition. (Filler and superplasticiser, see Table 1)

Concrete grade	Cement kg/m ³	Sand 0/8 kg/m ³	Gravel 5/8 kg/m ³	Filler kg/m ³	Superplast kg/m ³	w/c
C35/45	445	1580	-	124	0.7%	0.47

3. RESULTS AND ANALYSIS

3.1 End-restrained test series

Material properties

– Some material properties measured in the test program are given in Table 3. The compressive strength was determined at an age of 28 days while flexural beam tests were conducted at times after 28 days. Flexural testing was performed in accordance with [16]. The procedure has been rather common in Sweden despite the fact that it was withdrawn in 2006 as a standard test method. Results obtained from the beam tests are the crack strength ($f_{fl,cr}$) and residual strength factors ($R_{10,x}$) as shown in the table. Residual strength is obtained by multiplying the crack strength with the residual factor. Thus, area of load deflection curve of four point bending tests is calculated for a certain deflection and compared with the area at first crack (when $f_{fl,cr}$ is reached), e. g. $R_{10,20}$ is residual factor for deflections 5,5 and 10,5 times the deflection at first crack respectively, see [16]. Logically, it is seen that the residual factor increases with the fibre content up to 60 % for 40 kg/m³ which means that the ductility is 60 % of the one at perfect plastic behaviour. Furthermore, it is observed that unreinforced concrete display almost no ductility after the cracking, as expected.

Table 3 – Cylinder compressive strength at 28 days and flexural strength and residual strength factors obtained from four point bending tests in accordance with [16].

Concrete type	$f_{cm}^{1)}$ MPa	Flexural and residual strength			
		$f_{fl,cr}$ MPa	$R_{10,20}$ %	$R_{10,30}$ %	$R_{10,40}$ %
SCC	30.5	4.2	4	2	1
SFRSCC 20	36.5	4.4	26	26	26
SFRSCC 30	39.0	4.2	37	38	38
SFRSCC 40	36.5	4.7	59	60	60

¹⁾ Mean cylinder strength.

Free shrinkage

As the bottom face of free shrinkage specimens were covered with air proof material, a nonlinear shrinkage distribution developed over the depth initially, which explains the difference in deformation that can be observed in Fig. 6. It can be seen that the response of the unrestrained specimens varied somewhat. In particular it may be observed that SFRSCC 40 had a somewhat slower shrinkage development. The variation is most likely related to a slight change in the relative humidity in the climate chamber during this test rather than to effects of the fibre addition. It may be noted that despite the rather small size of the free shrinkage specimen, the exact free shrinkage is not obtained due to noneven humidity and eigenstresses within the specimen. These effects, indeed influencing documented strains, are studied in a larger Scandinavian research project (Crack Free Con).

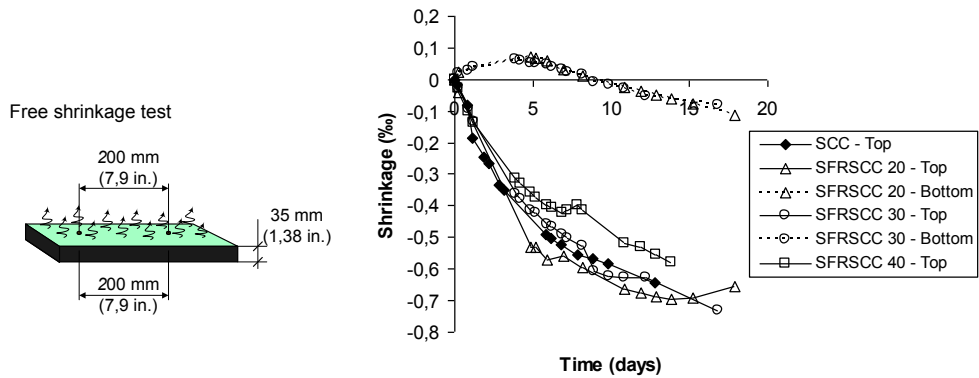


Figure 6. Free shrinkage test specimen and test results of the mixes within the test program. Recordings on the bottom face was conducted for mix SFRSCC 20 and 30 (kg/m^3) [1].

Restrained shrinkage

Strains obtained at the upper face of restrained specimens of SCC, SFRSCC 20, 30 and 40 (kg/m^3) are shown in Fig. 7 (a)-(d). It should be pointed out that only one crack developed, i. e. crack distribution due to the fibre additions was not observed. Thus, crack strain is the strain measured in the zone where the crack developed while strain in uncracked parts corresponds to the mean strain obtained in uncracked parts.

Even though steel fibres did not distribute cracks it is clear when comparing the results in Fig. 7 (a) with Figs. (b)-(d) that a positive contribution was obtained, resulting in a decreased crack strain and also in lower strain in uncracked parts. It can further be seen that the difference between the free shrinkage strain and the strain in uncracked parts was more significant for fibre reinforced mixes as compared to plain SCC. The reason is that the initially restrained specimens are completely relieved in case of unreinforced SCC, Fig. 7 (a), while some restraint remained after cracking in fibre reinforced specimens, Fig. 7 (b)-(d), due to fibres bridging the crack.

Although it is difficult to directly compare SCC and SFRSCC mixes as the final shrinkage was not reached at the end of testing it is quite clear that addition of 0.25 vol% (20 kg/m^3) of steel fibres (b) did not alter the response very much in comparison to plain SCC. Cracks developed at approximately the same time (≈ 5 days) and the crack strains were similar in magnitude.

From Fig. 7 (c) and (d) it may be seen that increased fibre amounts resulted in a more significant influence on the crack widths. A particularly good response was obtained for SFRSCC 40 (0.5 vol%) where only one of the specimens cracked. A rather good response was also obtained for one of the specimens of SFRSCC 30 in Fig. 7 (c). The reason for the poorer performance of the second specimen of the same mix is believed to be due to a lower number of fibres crossing the crack.

It can further be seen that the time to cracking seems to have been prolonged by increased fibre volume, compare i. e. the two specimens of SFRSCC 30. Note that a prolonged time to cracking for high fibre volume fractions has been reported in several previous studies [17, 18, 19]. This is usually believed to be due to fibres bridging and hindering cracks already at the micro stage.

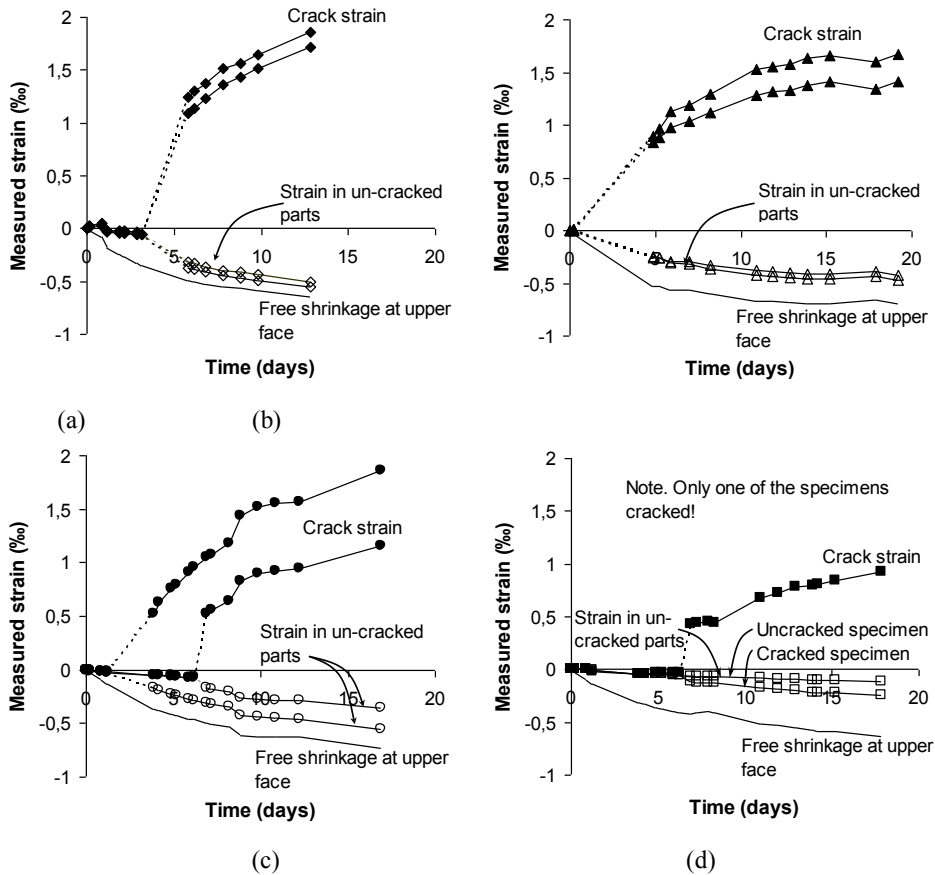


Figure 7. Strain development in cracked zone and uncracked parts compared to free shrinkage of unrestrained specimens. (a) Plain SCC. (b) SFRSCC 20, (c) SFRSCC 30, (d) SFRSCC 40.

The fact that the free shrinkage response differed somewhat between the tests (Fig. 6) makes it difficult to assess the effect of steel fibres on crack widths. Thus, for a reasonably fair comparison it was decided to select the measured crack width at the time when a similar free shrinkage value was recorded (0.6 ‰). Crack width results for this situation are given in Fig. 8. As the actual number of fibres crossing the crack did not always correspond with the amount of fibres added to the mix, the actual volume fraction in the crack zone was determined based on the counted number and by using fibre orientation theory [20, 21].

With one exception (one of the specimens of SFRSCC 30) it can be seen in Fig. 8 that crack widths decreased with increasing fibre volume fraction. Addition of 0.4-0.5 vol% of steel fibres reduced the crack width by approximately 50 %.

In the figure also an interesting comparison with the ring test is given. Two studies of ring tests [19], [22] which evaluated the effect of steel fibres on cracks were included. End-hooked fibres with length 50 mm and an aspect ratio of 50 were used in the first study while a crimped fibre with length 25 mm was used in the other study [22]. Noticeable is the substantial effect of fibres

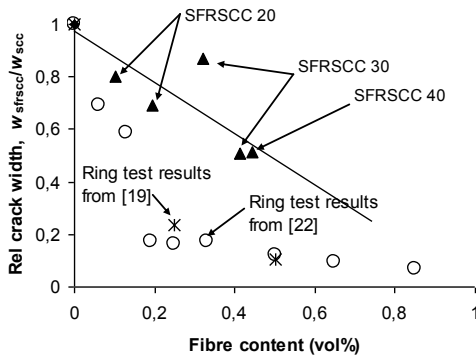


Figure 8. End-restrained test: effect of steel fibre addition on relative crack width = crack width of SFRSCC (w_{sfrscc}) divided by the crack width of plain SCC (w_{scc}). Comparison with results from two studies of ring shaped test-setup specimens [19, 22] see Fig. 2)

that was achieved already at dosages as low as 0.25 vol%. This implies that the ring shape gives a more favourable stress situation as compared to linear specimens as stated earlier in the paper. A thorough discussion of possible reasons for the difference can be found in [1].

3.2 Base restrained test series in laboratory

Free shrinkage

Measured free shrinkage development is shown in Fig. 9. Noticeable is the extensive difference in strain between the top and bottom faces of the specimens, resulting from the one sided drying conditions. It can further be seen that the addition of SRA reduced the average shrinkage by approximately 25 %. There were no differences between fibre reinforced and plain SCC, which verifies that the addition of fibres did not influence the shrinkage.

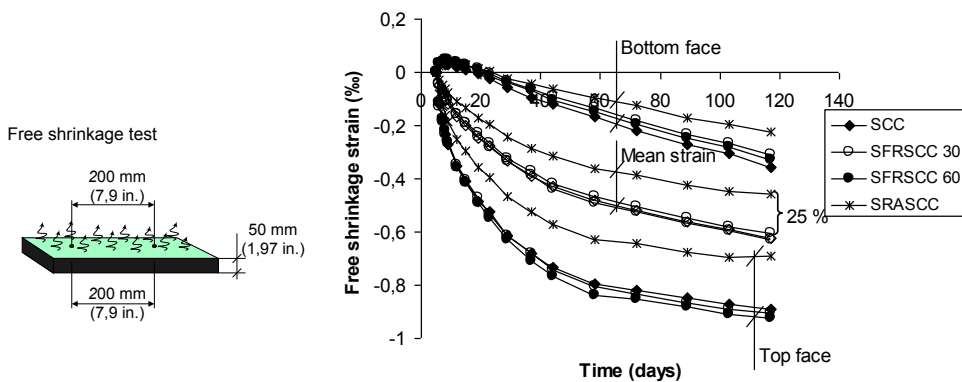


Figure 9. Free shrinkage test method and measured shrinkage at the upper and lower faces as well as the mean shrinkage of the mixes of base restrained test series.

Cracking and debonding

The first visible cracks were observed between 1 and 3 weeks after start of drying in most of the overlay strips and new cracks were then established until the end of the test period 3-4 months later. From the crack width summary given in Fig. 10 it can be seen that most of the cracks had a width of only between 0.05 and 0.25 mm while a few cracks with more significant widths developed in overlay strips of slabs 2, 3 and 4.

The reason why none of the cracks observed in overlays on slab 1 had a width that exceeded 0.15 mm is that the bond strength obtained was sufficiently high and evenly distributed to prevent debonding. The result was somewhat unexpected as a smooth and dry substrate is generally believed to be unfavourable from a bond perspective. For slabs 2-4 the bond situation was found to be considerably more varying, ranging from nonexistent to adequately high bond to prevent debonding. The result was quite surprising as the preparations of the substrates of these slabs were intended to provide better bond compared with slab 1. It is not fully clarified as to why the opposite situation occurred.

Major cracks always coincided with the development of a major, internal debonded zone, see example of crack mapping of overlays on slab 3, Fig. 11. For overlays with a major internal debonded zone (shaded area), a single crack developed for SCC, SRASCC and SFRSCC 30 and 60 (see SCC II, SRASCC II, SFRSCC 30 II and SFRSCC 60 II). This indicates that distribution of cracks, and corresponding crack control, was not achieved for the SFRSCC applied in the tests. It can however be seen that the crack in strip SFRSCC 60 II was only 0.2 mm and did not extend all the way through the width, implying that a 0.75 vol% steel fibre addition was

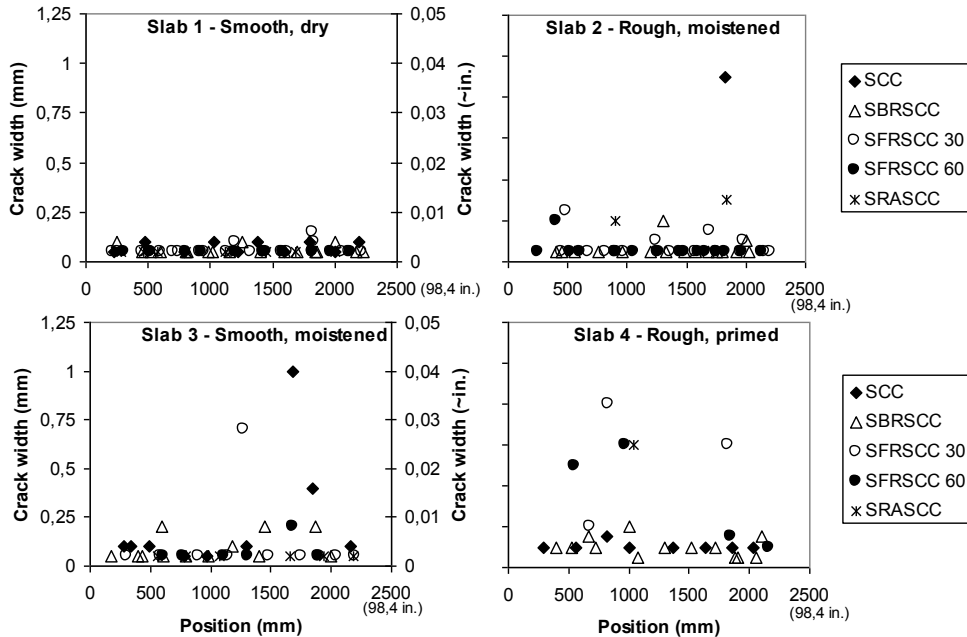


Figure 10. Measured crack widths at the end of the measuring period approximately 4 months after initiation of drying. (Smooth = grinded, rough = milled).

effective. For SBRSCC II an additional crack developed within the major debonded zone, proving that the centrally placed steel bar ($\phi 10$ mm) did give some crack distribution. The reason as to why sufficient bond strength seems to have been obtained for half of the strips (strips denoted I) while the remaining 5 strips (denoted II) seem to have been poorly bonded is unknown. Exactly the same preparation was applied and the strips were cast at the same occasion and cured in the same way. Furthermore, concrete from the same batch was used for the two strips of the same mix, for example SCC I and II. This clearly gives an indication of the sensitivity of the bond mechanism. The result also clarifies the difficulty in securing high and even bond in real overlay situations.

Effect of steel fibres on cracks

Based on the results presented above it can be concluded that steel fibres, or conventional steel bar reinforcement, are not required in cases when the bond strength is adequate to prevent debonding. In order to validate a possible effect of fibres it is necessary to consider the case where a major debonded area developed.

A summary of crack widths obtained for SCC and SFRSCC overlays in which a major debonded zone was established can be seen in Fig. 12. Observe that the crack widths have been normalised with respect to the debonded length recorded in the tests in order to enable comparisons. It should also be mentioned that the actual fibre contents were calculated based on the counted number of fibres crossing the crack by using fibre orientation theory [20, 21]. An interesting observation is that the actual fibre content was lower (3 cases) or equal (1 case) to the expected amount. This shows that the fibre content varied in the SFRSCC overlays and that a major crack is more likely to form in a section with low fibre content.

◦	0,35 mm (0,014 in)		0,05 mm (0,002 in)	0,05 mm (0,002 in)	0,05 mm (0,002 in)	0,05 mm (0,002 in)	0,1 mm (0,004 in)	0,1 mm (0,004 in)	◦	SCC I
◦	0,05 mm (0,002 in)	0,2 mm (0,008 in)	0,05 mm (0,002 in)	0,1 mm (0,004 in)	0,05 mm (0,002 in)	0,05 mm (0,002 in)	0,05 mm (0,002 in)	0,05 mm (0,002 in)	◦	SBRSCC I
◦	0,05 mm (0,002 in)	0,05 mm (0,002 in)	0,05 mm (0,002 in)	0,05 mm (0,002 in)	0,05 mm (0,002 in)	0,05 mm (0,002 in)	0,05 mm (0,002 in)	0,05 mm (0,002 in)	◦	SFRSCC 30 I
◦	0,05 mm (0,002 in)	0,05 mm (0,002 in)	0,05 mm (0,002 in)	0,05 mm (0,002 in)	0,05 mm (0,002 in)	0,05 mm (0,002 in)	0,05 mm (0,002 in)	0,05 mm (0,002 in)	◦	SFRSCC 60 I
◦	0,05 mm (0,002 in)	0,05 mm (0,002 in)	0,05 mm (0,002 in)	0,05 mm (0,002 in)	0,05 mm (0,002 in)	0,05 mm (0,002 in)	0,05 mm (0,002 in)	0,05 mm (0,002 in)	◦	SRASCC I
◦	0,05 mm (0,002 in)	1,0 mm (0,39 in)						0,05 mm (0,002 in)	◦	SCC II
◦		0,2 mm (0,008 in)			0,2 mm (0,008 in)	0,05 mm (0,002 in)	0,1 mm (0,004 in)		◦	SBRSCC II
◦					0,7 mm (0,027 in)				◦	SFRSCC 30 II
◦					0,2 mm (0,008 in)				◦	SFRSCC 60 II
◦					0,4 mm (0,016 in)				◦	SRASCC II
◦					1,4 mm (0,055 in)				◦	

Figure 11. Example of cracks in overlays on slab 3. Shaded areas indicate that the overlays have debonded. More examples of test results can be found in [1]. (Rings at the ends are the bolts attached avoiding debonding due to vertical end tensile stresses)

From the results in Fig. 12 it is quite clear that increased fibre content resulted in a decreased crack width. Based on the trend line it can be seen that a content of 0.5 vol% reduced the crack width by approximately 50 % while 0.75 vol% reduced the crack width to approximately one fourth of the width of cracks in plain SCC. This correlates rather well with the results of the end-restrained tests. The reason for this is believed to be that the restraint situations were similar as the overlay strips were restrained only at the ends of the debonded zones.

Important to recognise is however that as long as only a single crack develops (which was the case for SCC and SFRSCC overlays) the actual crack width will be proportional to the size of the debonded zone, and based on the present investigation it is thus not possible to determine a certain content of steel fibres required to limit crack widths in general cases. A distributed crack pattern would be required in order to enable crack limitation within a debonded zone.

3.3 Base restrained tests on large specimens

For the half scale/full scale tests (Section 2.3) the development of cracks was followed over a period of approximately 3 months from the time of overlaying [2], [3]. At the end of the period the crack widths were measured and the bond strength between overlay and substrates was determined by standard pull-out testing. Results from the bond strength measurements are given in Figure 13 (a) while crack widths are given in Figure 14 (a).

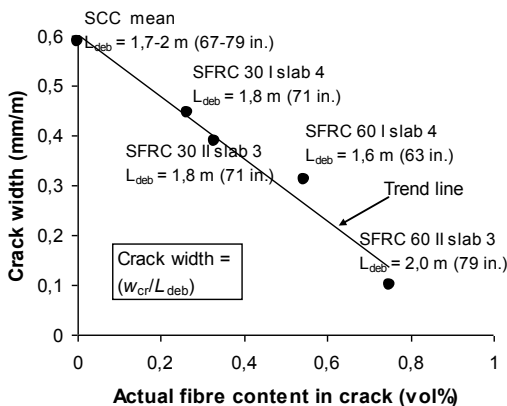


Figure 12. Crack width divided by debonded length as a function of steel fibre amount. Only the cracks that developed within major debonded areas have been considered [2], [3].

Regarding the effect of the substrate preparation on bond strength it is evident from the results in Figure 13 (a) that primer 1d was the best alternative irrespective of curing conditions. Dry substrate also gave reasonable bond strength in the areas that were cured under PE-foil (0.2 mm) while air curing resulted in zero bond strength for the same substrate condition. Curing thus seems to be extremely important if the overlay is cast on a dry substrate.

It can further be concluded from the results in Figure 13 (a) that late primer addition (primer 1h) and pre-moistening (premoist 1h) should be avoided considering that these preparation methods resulted in zero bond in most areas. The only exceptions were the primed areas (primer 1h) that were overlayed by fibre reinforced SCC. This implies that steel fibres may have a positive

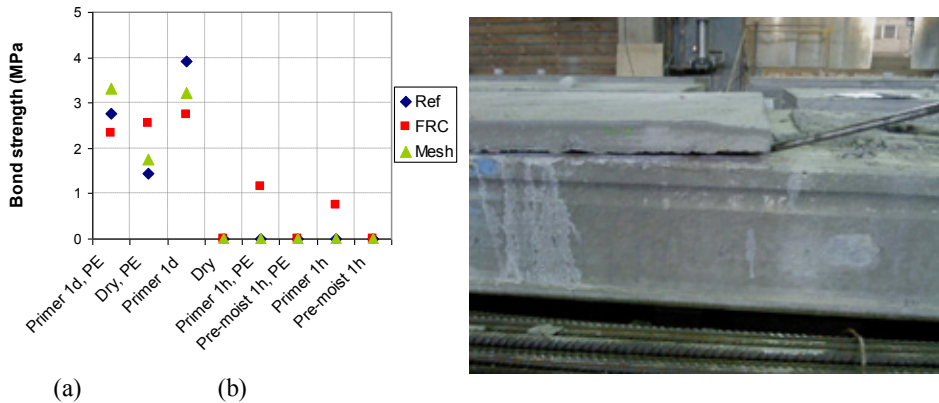


Figure 13. (a) Measured pull-out bond strength. (b) Overlays on slabs 4, 5 and 6 could easily be lifted off by means an iron-bar lever.

influence on the bond strength. The poor bond situation is illustrated by the photoshown in Figure 13 (b), where parts of the overlay on slab 4 are lifted off using an iron-bar lever.

It was expected that the poor bond of the areas with late priming and pre-moistening would give rise to large crack widths. However, this relation cannot be clearly discerned in the results given in Figure 14 (a), although the two largest cracks developed in low bond strength areas. A possible reason is that crack width growth was limited by the fact that most of the overlays on the slabs with late priming and pre-moistening debonded (see Figure 13 (b)). Regarding the effect of reinforcement the results imply that mesh may be favourable as none of the cracks in mesh reinforced areas exceeded 0.5 mm. However, it is not really possible to draw any clear conclusions except that reinforcement is clearly needed in case the bond strength is low (see crack in Figure 14 (b)).

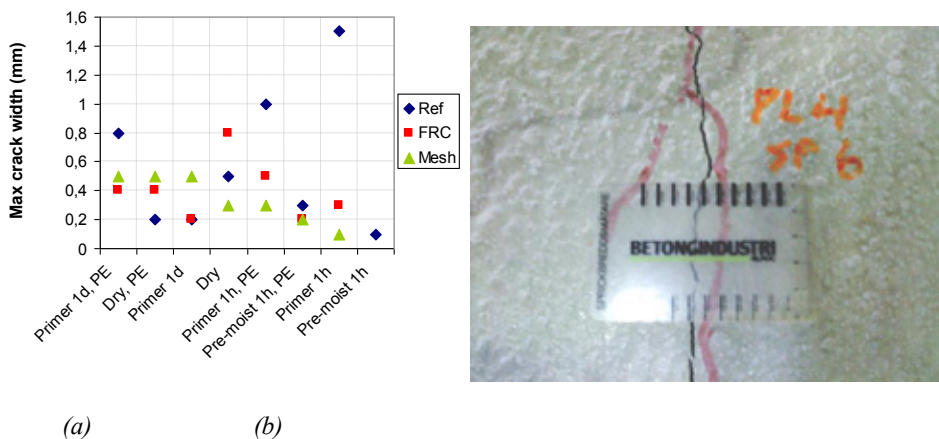


Figure 14 (a) Maximum crack widths measured at the end of the test period. (b) Photo showing the largest crack on slab 4 (ref).

4. THEORETICAL MODELS

4.1 General

An analytical model to determine the risk of cracking and the crack width of concrete overlays exposed to shrinkage has been proposed where the analysis is divided into two stages; (1) an analysis in the uncracked stage, and (2) crack width analysis, Fig. 15 [1][11]. In the uncracked stage tensile stresses are calculated based on composite beam theory. The analysis, see also [23], includes the rate of shrinkage and creep, the development of stiffness and tensile strength and the restraint situation. Two different situations are considered in the cracked stage, reached when the tensile stress exceeds the overlay strength: a) an internal debonded area developed and b) a still bonded overlay. In case of debonding, one single crack occurs in the unbonded region while a distributed crack pattern is the case for a bonded overlay. Further information is given in the references.

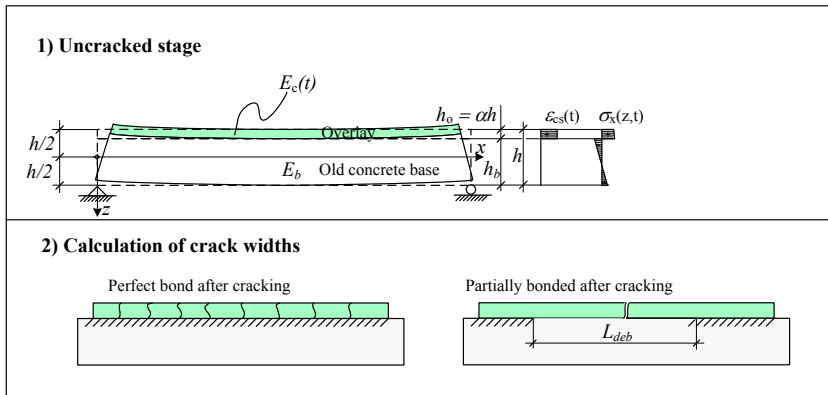


Figure 15. Proposed modelling: (1) initial stress analysis in uncracked stage and (2) crack width analysis [1], [11], [23].

4.2 Example of theoretical calculations of base restraint test situation

A comparison of measured and calculated strains at mid section at the upper face of some of the overlay strips of base restrained tests is given in Fig. 16 (a). The response of the overlay strips that were more or less completely debonded (see overlay strips denoted with II in Fig. 11) have been left out as the basic condition for the model is that the overlay is fully bonded to the base.

From the results shown in Fig. 16 (a) it can be concluded that the restraint was not 100 % even though the base slabs had a rather significant depth (300 mm) in relation to the overlay strips (50 mm), as such situation would have resulted in a zero strain reading. It can also be seen that the actual strain development was reasonably well captured by the theoretical calculation within the first 25-30 days. At this age however, some major cracks developed in mid section of at least two of the strips (SCC I and SFRSCC 30 I), which resulted in sudden strain changes.

Calculated stress development in reference overlays (SCC) and shrinkage reduced overlays (SRASCC) is shown in Fig. 16 (b). It can be seen that crack initiation (time at which the stress exceeds the strength) was estimated to approximately 20 days for the reference mix SCC and 30 days for the shrinkage reduced mix (SRASCC).

For the situation that the bond strength is insufficient to prevent debonding (case 2 in Fig 15) and assuming that the length of the debonded zone is known it can be shown that the theory gives reasonable results. This is seen in Fig 17(a) where a comparison of predicted and measured cracks widths within debonded areas of the overlay strips in the base restrained test series are shown.

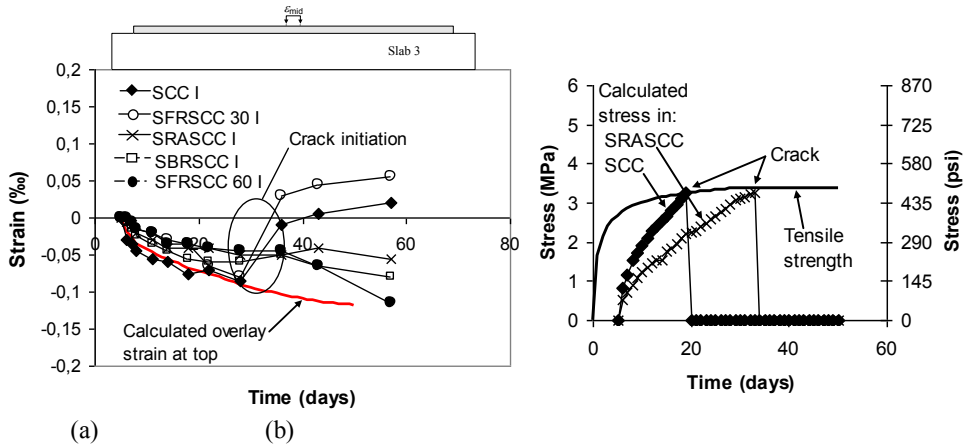


Figure 16. Base restraint tests; (a) Example of measured strain development at upper face of overlay strips (mid-section) compared to calculations using proposed theoretical model. (b) Calculated stress development in overlays of two concrete types [11].

The effect of steel fibres is shown in Fig. 17 (b), where relative crack width (w/L_{deb}), see [11] is given as a function of the fibre residual strength factor $R_{10,20}$ for overlay strips with a major debonded zone (> 1 m). The $R_{10,20}$ values in Fig. 17 (b) were estimated based on the actual volume fraction of fibres found in the crack zones, see [1] for details. It may be seen that calculated and measured crack widths correlated rather well. It is further evident that increasing $R_{10,20}$ resulted in decreased crack widths. A rather high $R_{10,20}$ value was however required in order to provide a substantial reduction in crack width. For an $R_{10,20}$ value of 80 %, corresponding to SCC with 0.75 vol% of steel fibres, the crack width was found to be reduced to approximately 0,1 mm/m. In case of a crack width demand of 0.2 mm, which is rather common, the debonded length may thus not exceed 2 m.

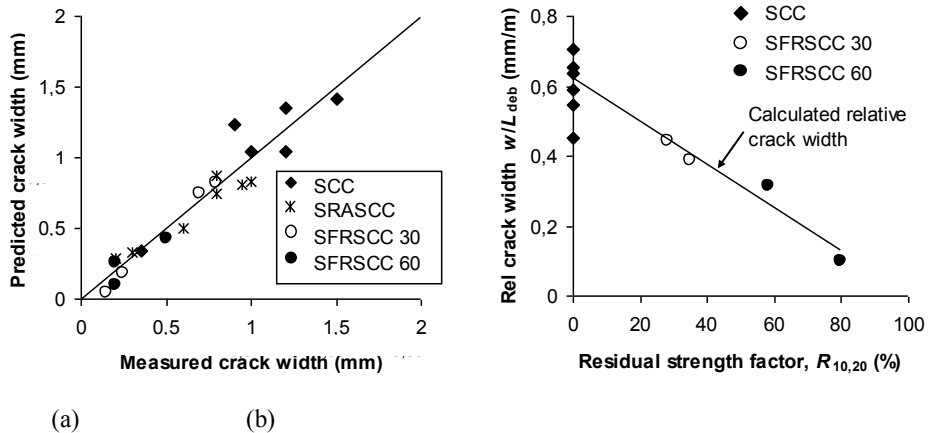


Figure 17 (a) Measured versus calculated cracks widths that developed within debonded zones of the base restrained overlay strips. (b) Measured and calculated relative crack width (crack width divided by debonded length) as a function of residual strength factor $R_{10,20}$ for cracks that developed in major debonded zones (> 1 m) in SCC and SFRSCC overlays of the base restrained test series.

5. DISCUSSION AND CONCLUSIONS

Results from the overlay test series, both in laboratory and at full scale, revealed that the choice of preparation of the substrate prior to overlaying is an extremely important parameter. Another parameter that was shown to influence the bond strength was the curing method. It was e.g. indicated that curing is particularly important if the substrate is dry at the time of overlaying.

Results from the end-restrained setup showed that increasing steel fibre contents resulted in a prolonged time to cracking and decreasing crack widths. At a volume fraction of 0,5 vol%, the crack width was approximately 50 % of that observed in unreinforced SCC. However, for the certain type of fibre and volume fractions considered in the study (≤ 0.5 vol%) only one crack developed, in other words crack distribution was not achieved. This implies that it is not possible to draw any conclusions based on test results regarding the volume fraction of fibres required for crack control in a real case of end-restraint.

The results were verified in the base restrained test series. In cases when a major internal debonded zone developed, giving a similar restraint situation as for the end-restrained test, only one crack occurred in SFRSCC. Although it was observed that increasing fibre contents did give smaller crack widths, the results still imply that the size of the debonded zone will be decisive for the crack width. In overlay strips with approximately equal debonded length the crack width for a steel fibre volume fraction of 0.75 vol% was found to be approximately equal to that obtained in steel bar reinforced SCC. This indicates that rather high amounts of steel fibres are required in order to control cracks.

It was further observed in the base restrained test series that, if high and even bond to the substrate is obtained, reinforcement is not required to distribute cracks in thin overlays (~ 50 mm). Test results revealed that a distributed pattern of fine cracks (0.05-0.1 mm) developed for this situation both for unreinforced and fibre reinforced SCC. A main conclusion from the base

restrained test series is, thus, that in order to ensure crack control for thin SCC overlays it is essential that sufficient bond strength is achieved.

The theoretical model to predict overlay cracking and crack widths showed a good correlation with the test. For the situation that the overlay is not sufficiently bonded to the substrate it is however difficult to predict potential crack widths of SFRSCC as the extent of debonding will be quite influential.

In the continued studies (PhD programmes at LTU) the theoretical models will be further developed, especially for the uncracked stage.

ACKNOWLEDGEMENTS

The authors of this paper would like to acknowledge the Development Fund of the Swedish Construction Industry (SBUF), Betongindustri AB, Betongteknik AB and the Swedish Transport Administration (Trafikverket) supporting the project as well as personell at Complab, LTU, executing the tests.

REFERENCES

1. Carlswärd, J. "Shrinkage cracking of steel fibre reinforced self compacting concrete overlays – Test methods and theoretical analysis," *Doctoral thesis 2006:55*, Division of Structural Engineering, Luleå University of Technology, 2006, <http://epubl.luth.se/1402-1544/2006/55/index.html>.
2. Carlswärd J. "Shrinkage cracking of thin concrete overlays". *Proceedings of XXI Nordic Concrete Symposium, Hämeenlinna, June 2011* Nordic Concrete Fed, Nord Concr Res 43:1
3. SBUF project nr 12001 "Steel fibre reinforced self compacting concrete overlays", Development Fund of the Swedish Construction Industry SBUF, www.sbuf.se
4. Granju, J.L., Sabathier, V., Turatsinze, A. and Toumi, A., "Interface Between an Old Concrete and a Bonded Overlay: Debonding Mechanism," *Interface Science*, Vol. 12, No. 4, 2004, pp. 381-388.
5. Rahman, M.K., Baluch, M.H. and Al-Gadhib, A.H., "Simulation of shrinkage distress and creep relief in concrete repair," *Composites*, Part B31, 2000, pp. 541-553
6. Weiss, J., Yang, W. and Shah, S.P., "Shrinkage Cracking of Restrained Concrete Slabs," *Journal of Engineering Mechanics*, Vol. 124, No. 7, 1998, pp. 765-774
7. Yuan, Y., Li, G. and Cai, Y., "Modeling for prediction of restrained shrinkage effect in concrete repair," *Cement & Concrete Research*, Vol. 33, 2002, pp. 347-352
8. Shah, S.P., Karaguler, M.E. and Sarigaphuti, M., "Effects of Shrinkage-Reducing Admixtures on Restrained Shrinkage Cracking of Concrete," *ACI Materials Journal*, Vol. 89, No. 3, 1992, pp. 289-295
9. Grzybowski, M. and Ohama, Y., "Properties of cementitious composites containing shrinkage reducing agents," *Report 36*, Structural Design and Bridges, Royal Institute of Technology, Stockholm, Sweden, 1996.
10. Weiss, J. and Shah, S.P., "Restrained shrinkage cracking: the role of shrinkage reducing admixtures and specimen geometry," *Materials and Structures*, Vol. 35, 2002, pp. 85-91
11. Carlswärd J., Emborg M "Predicting of stress development and cracking in steel fibre-reinforced self-compacting concrete overlays due to restrained shrinkage", ACI SP-274, proceedings: Fiber-reinforced Self-consolidating concrete: Research and application, 2010
12. Granju, J.L. and Turatsinze, A., "Repairs by the thin bonded overlay technique: the RILEM TC 193-RLS and last findings about the debonding mechanism," In: *Proceedings of the Conference on Concrete Repair, Rehabilitation and Retrofitting*, Nov. 2005, Cape Town, South Africa, pp. 43-52
13. Groth, P., "Fibre Reinforced Concrete – Fracture mechanics methods applied on self-compacting concrete and energetically modified binders," *Doctoral Thesis 2000:04*, Division of Structural Engineering, Luleå University of Technology, Luleå, Sweden, 2000.
14. Bissonnette, B., Morency, M., Von Fay, K., Vaysburd, A.M. and Brown, C.D. "Development of test method for cracking tendency of repair materials," In: *Proceedings of the Conference on Concrete Repair, Rehabilitation and Retrofitting*, Nov. 2005, Cape Town, South Africa, pp. 1045-1051.
15. Banthia, N., Yan, C. and Mindess, S. "Restrained shrinkage cracking in fiber reinforced concrete: A novel test technique," *Cement and Concrete Research*, Vol. 26., No. 1, 1996. pp. 9-14.
16. ASTM C1018-92 "Standard Test Method for Flexural Toughness and First-Crack Strength of Fiber-Reinforced Concrete (Using Beam With Third-Point Loading)," *Annual Book of ASTM Standards*, Vol. 04.02, Concrete and Aggregates, Philadelphia, USA, 1992, pp. 510-516.
17. Shah, H.R., Hossain, A.B., Mazzotta, G., and Weiss, J., "Time-dependent fracture in restrained concrete: The influence of notches and fibers," In *Proceedings of Advances in*

- Cement and Concrete IX: Volume Change, Cracking and Durability,” Copper Mountain, Colorado, Aug, 2003.
18. Shah, H.R., Hossain, A.B., and Weiss, J., “Using the Restrained Ring Test in Conjunction with Passive Acoustic Emission to Quantify the Role of Steel Fiber Reinforcement in Shrinkage Cracking Mitigation,” In *Proceedings of Conference on Fiber Composites, High-Performance Concretes and Smart Materials, ICFRC*, Chennai, India, Jan, 2004.
 19. Voigt, T., Bui, V.K., and Shah, S.P., “Drying Shrinkage of Concrete Reinforced with Fibers and Welded-Wire Fabric,” *ACI Materials Journal*, V. 101, No. 3, May-June 2004, pp. 233-241.
 20. Soroushian, P. and Lee, C.H. “Distribution and Orientation of Fibers in Steel Fiber Reinforced Concrete,” *ACI Materials Journal*, Vol. 87, No. 5, 1990. pp. 433-439.
 21. Löfgren, I. “Fibre-reinforced Concrete for Industrial Construction – a fracture mechanics approach to material testing and structural analysis,” *Doctoral Thesis*, Department of Civil and Environmental Engineering, Structural Engineering, Chalmers University of Technology, Göteborg, Sweden, 2005.
 22. Shah, H.R. and Weiss, J., “Quantifying shrinkage cracking in fiber reinforced concrete using the ring test,” *Materials and Structures*, Vol. 39, 2006, pp. 887-899.
 23. Silfwerbrand, J. “Stresses and strains in composite beams subjected to differential shrinkage,” *ACI Structural Journal*, Vol. 94, No. 4, 1997, pp. 347-353.
 24. Eurocode 2 “European pre-standard ENV 1992-1-1: Design of concrete structures. Part 1: General rules and Rules for Buildings, draft version, 2001.
 25. Concrete Report No 13, “Industrial Floors. Recommendations for the design, material selection, construction and maintenance (In Swedish),” *Swedish Concrete Society*, Report no 13, 2008.
 26. RILEM TC 162-TDF “Test and design methods for steel fibre reinforced concrete. Bending test,” *Materials and Structures*, Vol. 35, 2002, pp. 579-582.
 27. Shin, H-C. and Lange, D.A. “Effects of Shrinkage and Temperature in Bonded Concrete Overlays,” *ACI Materials Journal*, Vol. 101, No. 5, 2004, pp. 358-364.
 28. Bonaldo, E., Barros, J.A.O., and Lourenco, P.B. “Bond characterization between concrete substrate and repairing SFRC using pull-off testing,” *International Journal of Adhesion & Adhesives*, Vol. 25, No. 6, 2005, pp. 463-475.
 29. Júlio, E.N.B.S., Branco, F.A.B. and Silva, V.D. “Concrete-to-concrete bond strength. Influence of the roughness of the substrate surface,” *Construction and Building Materials*, Vol. 18, 2004, pp. 675-681.
 30. Silfwerbrand, J. and Paulsson, J. “Better bonding of bridge deck overlays,” *Concrete International*, Vol. 20, No. 10, 1998, pp. 56-61.
 31. Momayez, A., Ehsani, M.R., Ramezani pour, A.A. and Rajaie, H. “Comparison of methods for evaluating bond strength between concrete substrate and repair materials,” *Cement and Concrete Research*, Vol. 35, No. 4, 2005, pp. 748-757.
 32. Courard, L. “Adhesion of repair systems to concrete: influence of interfacial topography and transport phenomena,” *Magazine of Concrete Research*, Vol. 57, No. 5, 2005, pp. 273-282.
 33. Jonasson, J.-E. “Analysis of creep and shrinkage in concrete and its application to concrete top layers,” *Cement and Concrete Research*, Vol. 8, 1978, pp. 441-454.
 34. ConTestPro “User manual”, JEJMS Concrete, LTU, Cements, PeabAB, 2007, 200 pages

Strengthening of concrete structures using FRP – a guideline



Björn Täljsten Ph.D., Professor
Division of Structural Engineering, Luleå University of
Technology, SE-971 87 Luleå, and Sto Scandinavia AB,
Linköping, Sweden
bjorn.taljsten@ltu.se



Gabriel Sas, Ph.D
Division of Structural Engineering, Luleå University of
Technology, SE-971 87 Luleå, Sweden and Norut Narvi AS,
Norway
E-mail: gabriel.sas@ltu.se



Thomas Blanksvård, Ph.D.
Division of Structural Engineering, Luleå University of
Technology, SE-971 87 Luleå, and Skanska Sverige AB,
Göteborg, Sweden
E-mail: thomas.blanksvard@ltu.se

ABSTRACT

There is a need to retrofit existing concrete structures. There are many different ways to increase the performance of a concrete structure, FRP (Fiber Reinforced Polymer) strengthening being one. This method is commonly used across the world to improve the load-carrying capacity of concrete structures. In this paper, an overview of a Swedish guideline for the FRP strengthening of concrete structures is presented. The guideline covers designing for bending and shear as well as for confinement, and there is also a discussion of the need for proper workmanship and the choice of the right material for strengthening.

Key words: Concrete, Retrofitting, Strengthening, Upgrading, FRP, Composite Material

1. INTRODUCTION

1.1 General

Over the last few decades, there has been an increase in the need to maintain, repair and upgrade our existing civil structures and buildings, as the performance of the concrete used in them has deteriorated. Performance here relates to load-carrying capacity, technical function, durability or aesthetics.

There are at least two strong arguments why an existing concrete structure should be repaired or upgraded, instead of being replaced with a new one. First, there are the financial reasons – it is almost as economical or even more economical to repair or upgrade a structure as it is to

demolish and rebuild it. Second, there are the environmental reasons – by extending the life of the structure, the demand for natural resources is reduced.

There may also be a third reason. In general, the time to upgrade an existing structure is considerably shorter than building a new one. In addition, it is often possible to keep using the structure during the repair/upgrade. If the focus is placed on insufficient load-carrying capacity, then the reason for this can be split into two main areas:

1. Change in use: the structure has to withstand loads other than those for which it was originally designed.
2. Degradation of building material: the structure has deteriorated to a level where it can no longer carry the loads for which it was designed.

1.2 Change in use

Normally, building structures have a long life, for example a civil engineering structure, such as a bridge, is estimated or designed to have a lifespan of around 100 years. It is understandable that the demands on such structures or even their usage might change over time. Structures have not always been designed with contingencies to handle these changes so mitigating work, such as strengthening, might be needed. The underlying causes of such issues are often related to the following:

- Mistakes made in the planning or execution phase
- Demands related to increased load-carrying capacity or safety
- Change of function of the structure e.g. in relation to reconstruction

In all these cases, FRPs can generally be used for strengthening.

1.3 Degradation of material

Degradation of concrete structures can be caused by many different physical and chemical processes. Commonly, deterioration is due to chlorides from de-icing salts or sea water, or through carbonatisation of the concrete cover. Both these mechanisms cause steel corrosion. Other factors that might negatively affect the load-carrying capacity of concrete structures are freeze-thaw damage and lime leakage, that impair the strength of the concrete and, in some cases, lead to considerably reduced structural safety. The solution may be to demolish then build a new structure or repair and upgrade the existing one. The choice of which solution to use has to be analyzed on a case-by-case basis. In situations where the deterioration has not reached critical levels, and if the future deterioration can be halted, often FRPs can be used as a repair or strengthening measure. The suitability of using FRPs has to be decided by a specialist in each case.

1.4 Strengthening of concrete structures

Before a decision is taken regarding the strengthening of concrete structures, a proper assessment is recommended to clarify the reason for strengthening. Some commonly used methods to strengthen concrete elements are to increase the cross-sectional area, external prestressing, shotcrete, change of static system etc. Normally, these methods work well and have been used successfully for a long time. In the mid 1970s, a strengthening method using externally bonded steel plates was developed. During the 1970s and 1980s, the method was quite commonly used in central Europe, US and Japan [1]. At the beginning of the 1980s, the

use of FRP for strengthening concrete structures was researched [2]. The primary aims were to find methods and systems to improve the dynamic response of structures in relation to earthquakes. The results were very positive and continued research in the area led to the development of unidirectional FRP laminates for external strengthening [3]. Currently, external strengthening often uses FRPs and this method is fully accepted around the world. A common denominator for the strengthening systems has been carbon fiber, since this material has excellent mechanical properties for strengthening purposes. In Sweden, research in this area started at the end of the 1980s at Luleå University of Technology, first with bonded steel plates and, at the beginning of the 1990s, with composites [1]. This research is continuing at the university.

FRP strengthening has existed for approximately 30 – 35 years and steel plate bonding for more than 50 years. Early research in the field of strengthening was pragmatic, with the focus on understanding methods of strengthening and how much a structure could be strengthened. Later in the research, more refined design models were developed, evaluated and implemented. At present, there is, therefore, a good understanding of how to appropriately strengthen a structure, and how to design that strengthening.

In this paper, a brief summary of how to design for an increase in flexure, shear and confinement capacity will be presented.

2. MATERIALS AND STRENGTHENING TECHNIQUES

2.1 General

In contrast to traditional industries, such as space and aircraft manufacturers where composites have been used for a long time, composites in the construction industry must provide for longer lifespan. A structural lifespan of 50 years or more is a common requirement in the construction industry. Only those systems that have been extensively tested and used in full-scale concrete structures are possible candidates for external strengthening using FRPs. It is important to treat a proven system as a whole where its function has been verified through tests and applications.

Systems for FRP strengthening can be subdivided into prefabricated systems and in-situ systems. Prefabricated systems usually refer to pultruded flat profiles or rods, and in-situ systems refer to fabrics or sheets that are bonded together, using a resin, to form a composite on-site. Here, the systems are described in general terms and for design and strengthening works, the supplier's recommendations should be followed. There are three general steps that should be taken: pre-treatment, strengthening and post-treatment.

- Pre-treatment involves uncovering of aggregates, as well as leveling and cleaning the surfaces to be bonded. There must not be any dust, grease or water on the surfaces when bonding takes place.
- The strengthening process depends on the system chosen, but the bonding temperature must exceed 10°C to allow the adhesive to harden. For temperatures below 10°C , an external heat source or a heating device can be used.
- Post-treatment can involve fire protection, application of plaster, paint or other protection systems that are deemed necessary.

Different methods of strengthening building structures are shown in figure 1. FRP strengthening is suitable for concrete beams, walls, slabs and columns, but can also strengthen openings in slabs or walls. Another application is to strengthen structural elements by bonding FRP rods in the concrete cover, so-called NSM (Near-Surface Mounted) Reinforcement.

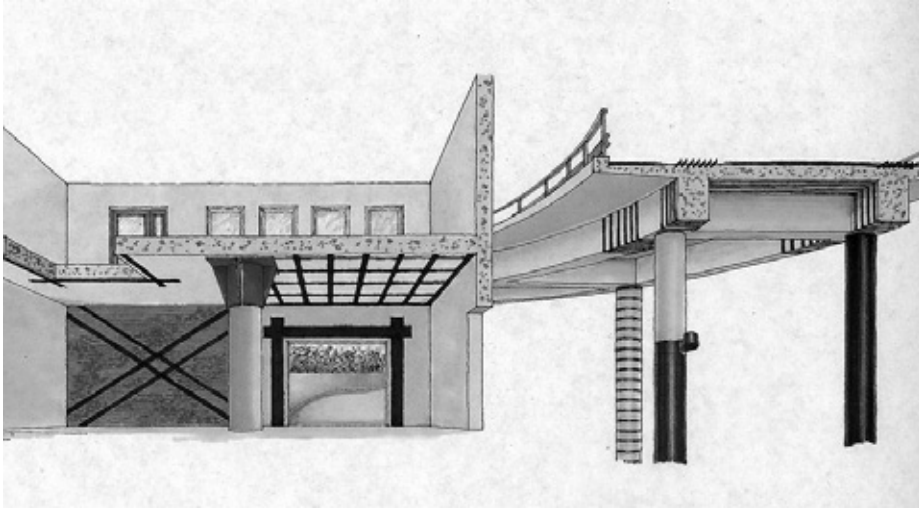


Figure 1 – Strengthening using laminates, sheets and NSM.

2.2 Laminates

The first applications using the CFRP laminate system were seen in Switzerland during the early 1990s [3], where a concrete bridge was strengthened after an accident that broke pre-stressing cables. Since then, a large number of objects have been strengthened worldwide. A laminate system consists of flat laminates with a typical size of $1.2 - 1.4 \times 50 - 150$ mm, but other dimensions are also available. The laminates can be obtained in different material grades, but normally the Young's modulus varies between 150 – 250 GPa, with a strain to failure between 0.4% up to 1.9%. Theoretically, the length of the laminate can be unlimited but, for practical purposes, the length is limited to 20 – 30 meters. Other components in the strengthening systems are primer and adhesive. The function of the primer is to improve the bond between the adhesive and the concrete. The adhesive used is a high viscosity filled paste such as epoxy adhesive. Typical bond layer thickness is 1 – 3 mm.

Laminates are most suitable for flat surfaces such as beams, walls and slabs. After the concrete has been pre-treated, the adhesive layer is placed onto the laminate and, in some cases, also onto the concrete surface. The two adherents are then mounted together and a light pressure is applied on the laminate. The system is then allowed to harden.

2.3 Sheets

Sheet systems are usually based on dry unidirectional fabrics, but bi-directional weaves are also used. These systems are more sensitive to the irregularities in the concrete surface and,

often, more pre-treatment is needed. However, the sheet systems are flexible and can be adapted to most surfaces. Sheet systems have been used for seismic retrofitting and the strengthening of curved structures, such as silos. These types of systems are also suitable in cases where openings in walls or slabs need to be strengthened. A typical sheet system consists of an epoxy primer, putty, dry or pre-impregnated fibre and a resin system.

Often the post-treatment consists of painting, but also plaster or a thin layer of polymer concrete has been used. The sheets normally used have a width of 200 – 400 mm with a weight of 200 – 400 g/m². The strengthening process for sheet systems takes a little longer than for the laminate system. First, the concrete surface is pre-treated. A primer is then applied and, in cases where there is significant unevenness, putty is used to level out these irregularities. The next step is to apply a thin layer of low viscosity epoxy adhesive to the concrete surface and then roll the carbon fibre sheet out over this surface. The fibres are stretched, and a roller is used to press out possible air voids; then a new layer of adhesive is applied. This process can be repeated such that there are 10 to 15 layers, depending on the strengthening system used.

2.4 Near-Surface Mounted Reinforcement

Near-Surface Mounted Strengthening (NSM) systems are used in cases where the strengthening system needs to be protected, for example where there may be possible physical impact. NSM systems are also suitable where the concrete surface is very uneven. Most NSM systems consist of circular or rectangular rods that are bonded in slots in the concrete cover of a structure. It is important to control the thickness of the concrete cover before this method is chosen; a typical concrete cover depth of at least 25 mm is normally needed. The pre-treatment for this method consists of sawing slots in the concrete cover. The rods are then bonded in these slots with an epoxy adhesive or a high quality cement grout.

It is of utmost importance that the slots are cleaned immediately after sawing; all concrete dust, wet concrete or ashes concrete must be removed. In cases where epoxy is used, the slot must dry prior to bonding and if cement grout is used, the slot must be pre-wetted before the grout is applied. The most important factor when NSM is used is the distance to the original steel reinforcement. Otherwise, the pre-treatment is quite easy and the method is relatively insensitive to irregularities in the concrete surface. In general, the force transfer from the concrete to the strengthening component is superior for NSM systems compared to laminate and sheet systems.

3. BENDING

3.1 General

FRP for strengthening is commonly used to increase the flexural capacity of concrete members. Strengthening can be achieved using laminates, sheets or NSM reinforcement. In general, laminates are most suitable for flat surfaces such as slabs, beams and walls. Sheets are used when greater flexibility is needed e.g. curved surfaces, columns etc. In this section, a brief description of design for bending is presented.

3.2 Design for increasing bending capacity

Calculation in SLS

Calculation in the Serviceability Limit State (SLS) involves assessing the stresses and strains due to service load. Here, a calculation is made to investigate whether the structure is cracked or not and there is also a calculation of the existing strain fields. Cross-sectional data are then needed when the strain field at the time of strengthening is calculated. For assessing the SLS, calculations regarding deflections and crack widths are carried out if necessary.

Estimation of material consumption

Before a detailed design calculation is carried out, it is recommended that an estimation be made of either the bending capacity based on the material to be used or the material needed to provide the desired bending capacity. The bending moment capacity can be calculated using:

$$M_d \approx 0.9(A_s f_y d + A_f \epsilon_f E_f h) \quad (1)$$

and, alternatively, the sectional area can be calculated using:

$$A_f \approx \frac{(M_d / 0.9 - A_s f_y d)}{\epsilon_f E_f h} \quad (2)$$

From this, a relatively good idea of the cost of the strengthening system can be generated. However, in the final design, it is always recommended to carry out the calculations and steps for the Ultimate Limit State (ULS).

Design for strengthening in the ULS

In this paper, only the design for single reinforced cross-sections is described. The method for designing double-reinforced cross-sections can be found in [4]. Figure 2 shows a cross-section of a rectangular strengthened concrete beam. In this figure, ϵ_{u0} is the actual strain in the bottom fiber, and ϵ_{c0} and ϵ_{s0} are the strains in the concrete and steel respectively, at the moment strengthening is carried out. ϵ_f is the strain on the FRP in the ULS (or at the level used in the calculation). $\Delta\epsilon$ refers to the additional contribution related to the loading in the ULS. In agreement with normal concrete design (EC2), the compressive strain in concrete, ϵ_c , should not exceed 3.5 ‰ in the ULS. In the analysis (to calculate the FRP area), use of equation (3) is suggested, where A_f and A_s are the cross-sectional area of FRP and reinforcing steel respectively, M_d is the moment capacity needed, f_y is the yield stress of steel and E_f is Young's modulus of FRP. Note that $\lambda = 0.8$ for $f_{ck} \leq 50$ MPa.

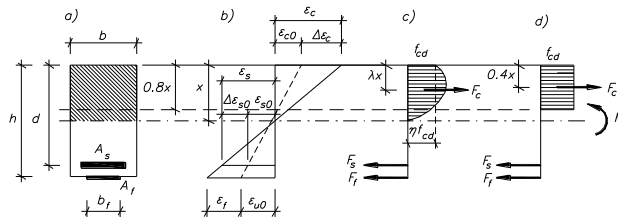


Figure 2 – Single reinforced cross-section

$$A_f = \frac{M_d - A_s f_y \left(d - \frac{\lambda}{2} x \right)}{\varepsilon_f E_f \left(h - \frac{\lambda}{2} x \right)} \quad (3)$$

To avoid brittle compressive failures, the following must be fulfilled:

$$\omega \leq \omega_{bal} \quad (4)$$

where

$$\omega_{bal} = \frac{\lambda}{1 + \frac{\varepsilon_f + \varepsilon_{u0}}{\varepsilon_{cu}}} \quad (5)$$

$$\omega = \frac{A_s f_y + A_f \varepsilon_f E_f}{b h f_{cd}} \quad (6)$$

In cases when $\omega > \omega_{bal}$, a more accurate procedure must be followed, see [4]. When designing strengthening in the ULS, different possible failure modes have to be considered. When strengthening for flexure, there are 7 modes that have been identified, see figure 3. These are:

1. Concrete compressive failure
2. Yielding in the tensile reinforcement (not necessarily a failure mode)
3. Yielding in the compressive reinforcement (not necessarily a failure mode)
4. Tensile failure in the FRP
5. Intermediate crack debonding
6. Peeling failure at the end of the laminate
7. Anchorage failure

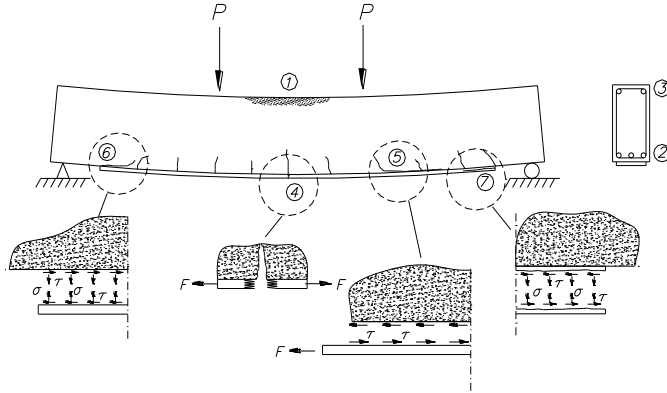


Figure 3 – Possible failure modes when strengthening for flexure.

In this paper, we will further describe intermediate crack debonding, peeling failure and anchorage failure. In the design often IC (Intermediate Crack) debonding is governed for laminates. For NSM often strain failure in the FRP or crushing of concrete is governed. The design guideline ACI-4402R-08 [5] forms the basis of the IC -debonding calculation, equation (7). However, also in this field considerably amount of research have been carried out, see [6] and [7].

$$\varepsilon_{fd,ic} = 0.41 \sqrt{\frac{f_{cd}}{nE_f t_f}} \leq 0.9\varepsilon_{fu} \quad (7)$$

where f_{cd} is the design compressive strength of concrete and n is the number of layers of FRP.

A peeling failure at the end of a laminate is related to the fact that, normally, the laminate cannot be anchored beyond the zero moment point. For a simple supported beam, there will likely be some distance between the support and the plate end. At this cut-off, end shear and normal stresses occur; these stresses interact and try to “peel” off the laminate from the structure, see [1] for a detailed analysis and [8] for a design procedure.

Anchoring the laminate properly is essential and, in general, the laminate should be anchored beyond a zero moment point if possible, otherwise it should be anchored outside a cracked area to avoid IC debonding. The anchor length is governed by the stiffness of the plate and the quality of the concrete. If debonding occurs, failure will most likely be in the concrete transfer zone. It is suggested that the anchor length is calculated using equation (8), where l_{ef} is the effective anchor length and f_{ctm} is the tensile strength of concrete defined by equation (9). However, it is also recommended that, when possible, an anchor length no shorter than 250 mm should be chosen.

$$l_{ef} = \sqrt{\frac{E_f t_f}{2f_{ctm}}} \quad (8)$$

where

$$f_{ctm} = 0.3 \cdot \sqrt[3]{f_{ck}^2} \quad f_{ck} = f_{cm} - 8 \text{ [MPa]} \quad (9)$$

The force that should be anchored in the laminate is split between the existing tensile steel reinforcement and the laminate, see [8]. The force in the laminate in the section to be anchored should not be allowed to exceed:

$$F_{f,e} = \varepsilon_{f,x} A_f E_f \quad (10)$$

where

$$\varepsilon_{f,x} \leq \sqrt{\frac{2G_f}{E_f t_f}} \quad (11)$$

and

$$G_f = 0.03k_b \sqrt{f_{ck} f_{ctm}} \quad (12)$$

$$k_b = \sqrt{\frac{2 - b_f/b}{1 + b_f/b}} \geq 1.0 \quad (13)$$

where k_b is a form factor that describes the size of the strengthened surface in relation to the unstrengthened surface, b_f is the width of the laminate and b the width of the structural member. Notice that the ratio $b_f/b \geq 0.33$ must be fulfilled (if $b_f/b < 0.33$ then the value of k_b should be $k_b = b_f/b = 0.33$).

4. SHEAR

4.1 General

The cause of shear failure is the result of a complex mechanism. A combination of the effect of shearing together with the influence of shear force creates a multi-axial stress state in the beam, where the maximum tensile stresses are generated at angles between $30 - 60^\circ$ (depending on reinforcement and loading) in relation to the construction's longitudinal axis. This leads to the formation of inclined shear cracks and ultimately to failure, see figure 4.

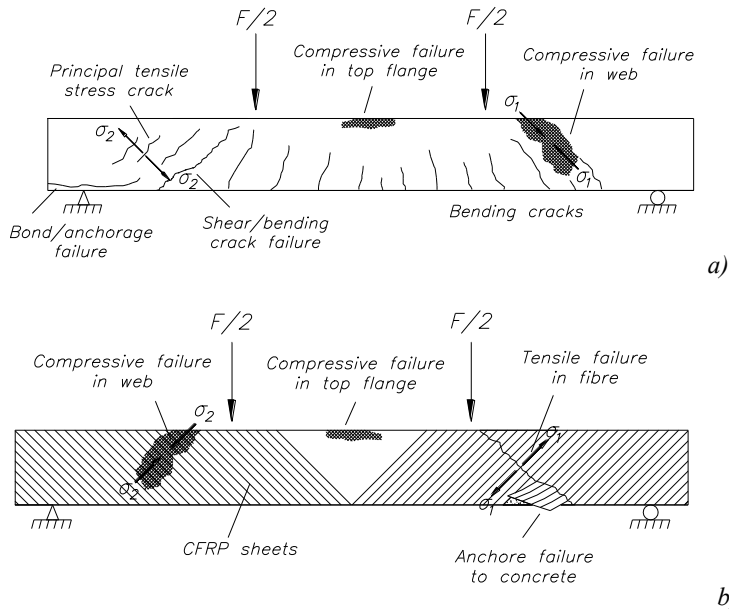


Figure 4 – a) Shear failure in an unstrengthened concrete beam, b) Possible failure modes in an FRP strengthened beam

We must have a basic understanding of the behaviour and different types of shear failures to be able to strengthen concrete structures in shear. In normal situations, a concrete structure is designed to withstand large deformations before failure, which means that the failure is often a bending failure. For a concrete beam with conventional steel stirrups, the shear failure can be characterized as follows:

- **Web shear failure:** this arises in those regions where the beam is not affected by bending cracks. The failure occurs when the principal tensile stress exceeds the concrete's tensile strength in the web. The failure is often a result of a lack of, or insufficient, shear reinforcement.
- **Bending shear failure:** the failure starts when bending cracks develop into inclined shear cracks. The crack grows from the structure's tensile zone towards the compression zone. The final failure is a crushing or splitting of the compressed zone. Shear reinforcement and external strengthening that cross the cracked zone contribute to the shear force resistance. The shear and bending reinforcement act as tensile bars while the concrete in the beam's compression zone and the inclined concrete struts between the shear cracks act as compressive bars in the truss model.

- **Compressive failure in web:** the failure is caused by compression failure in the inclined concrete struts in the truss. The failure can occur when the shear reinforcement is overdimensioned. In this case, the steel reinforcement does not reach the yield limit before the concrete's compression strength is reached.

When a concrete beam is also strengthened with external composites, another two failure modes can occur, see figure 4b:

- **Fiber failure in the composite:** this occurs when the fibre's critical strain capacity is exceeded. The failure is often characterized by a propagating failure where the composite gradually fails, especially with sheets. The failure is usually brittle. However, the orientation of fibers in relation to the greatest principal strain affects the ductility.
- **Anchorage failure:** this occurs when the concrete's external strength is too low or the anchorage area is too small to transfer the shear forces between the reinforcement and the concrete. In many cases, this type of failure can be avoided by wrapping the beam with fabric to create closed FRP stirrups.

When strengthening concrete structures for shear, it is essential to anchor the strengthening material properly. It is preferable to enclose, that is W-wrap, a structure with an FRP sheet system. However, this is not always possible e.g. for T-sections, which are common elements that are strengthened. Here, U-wrapped systems are recommended and if the end to the flange is mechanically anchored, or if sufficient anchor length can be provided, this is as effective as a W-wrap. Side-wrap, or S-Wrap, is not recommended. Most common FRP systems for shear strengthening are sheet systems, but laminates or NSM can, and have, also been used.

4.2 Strengthening for shear

In the design suggestion below, it is recommended that Eurocode is used [9]. By adding a component $V_{rd,f}$, the contribution from the FRP can be calculated. The total load-carrying capacity in shear is V_{Rd} , see chapter 6.2.2 in EC2 [9]. In the design model, see Figure 5, when strengthening for shear with FRP, there has to be a consideration of the contribution from the concrete and steel. The calculation of these contributions is defined in EC2.

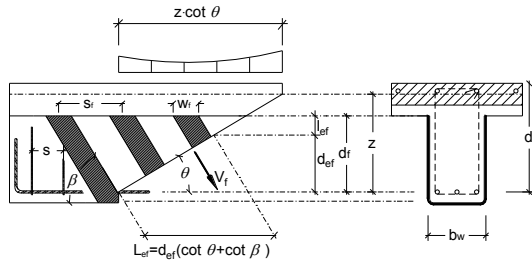


Figure 5 – Design model for FRP strengthening for shear

For a beam without shear reinforcement, but with FRP strengthening, the capacity is:

$$V_{Rd} \leq V_{Rd,f} \quad (14)$$

and for a beam with shear reinforcement and with FRP strengthening, the load-carrying capacity is calculated by:

$$V_{Rd} \leq \min(V_{Rd,s} + V_{Rd,f}; V_{Rd,max}) \quad (15)$$

where $V_{Rd,s}$ and $V_{Rd,max}$ are determined using section 6.2.3 in EC2 [9]. The contribution to the shear capacity can be calculated using equation (16) where the strain level is limited, see [8].

$$V_{Rd,f} = A_f \varepsilon_{fd} E_{fd} L_{ef} \sin \beta_f \cos^2 \alpha \quad (16)$$

where the anchor length l_{ef} is calculated using equation (8). The effective length, L_{ef} , is calculated as:

$$L_{ef} = d_{ef} \cdot (\cot \theta + \cot \beta_f) \quad (17)$$

and

$$d_{ef} = \begin{cases} z = 0.9d & \text{for } W\text{-wrap} \\ \min(z; d_f - l_{ef}) & \text{for } U\text{-wrap} \end{cases} \quad (18)$$

5. CONFINEMENT

5.1 General

If a column needs strengthening but its dimensions are to be maintained, then the most beneficial method to increase the load-bearing capacity of that column is to apply a confinement pressure. It has been proven by numerous researchers that a confinement pressure can enhance the load-bearing capacity of an axially-loaded member [10], [11]. In a traditional reinforced structural member, the confinement is achieved using lateral steel reinforcement. The lateral steel induces compressive confinement stresses on the concrete core, due to the elongation of the steel, which is caused by the expansion of the concrete, as described by the Poisson effect. When the axial strain increases, the confining pressure in the two transverse directions increases, and the strength of the concrete core in the axial direction is enhanced as well. The confinement of concrete columns is a well-established technique for improving both compressive behaviour and flexural response. Traditionally, for newly-built columns, this is handled in the design of the steel stirrups. However, for repair and strengthening of existing columns, this can be provided by wrapping with FRP. Depending on the purpose of the repair or strengthening scheme, the shear strength, axial strength and/or ductility can be enhanced. Using FRP for strengthening of columns has shown to be very efficient. The confinement effect is used in the calculation to create an increased compressive strength in the concrete. For uniaxially-loaded columns, this calculation is very straightforward and easy to carry out. However, in this guideline, the effect of a bending moment is also considered. The most common strengthening systems used for confinement are sheet systems, where FRP sheets are wrapped around a column. The system is most effective for circular columns but can also be used for rectangular columns with some reduction factors. The maximum increased compressive strength for a wrapped concrete column can be calculated as:

$$f_{cd,c} = f_{cd} + \alpha_{f,c} 3.3 \kappa_a f_l \quad (19)$$

and

$$f_l = \frac{2E_f n t_f \varepsilon_{fe}}{D} \quad (20)$$

where κ_a is an efficiency factor that takes into account the geometry of the cross-section (circular or not), $\alpha_{f,c} = 0.95$ and is a safety factor. The effective strain is given by:

$$\varepsilon_{fe} = 0.004 \leq \kappa_e \varepsilon_{fu} \quad (21)$$

where κ_e is an efficiency factor that takes into account possible premature failure as a result of the tri-axial stress states of wrapped sections.

5.2 Strengthening of columns

The design for confinement when a combined normal force and a bending moment act on an axial member is best explained by figures 6a) and 6b), see also [8]. Here, we calculate different stages for a rectangular member, A to D, before and after strengthening. Figure 6b shows the capacity before strengthening – the dashed curve, the need for strengthening, the X and the capacity after strengthening, the solid line.

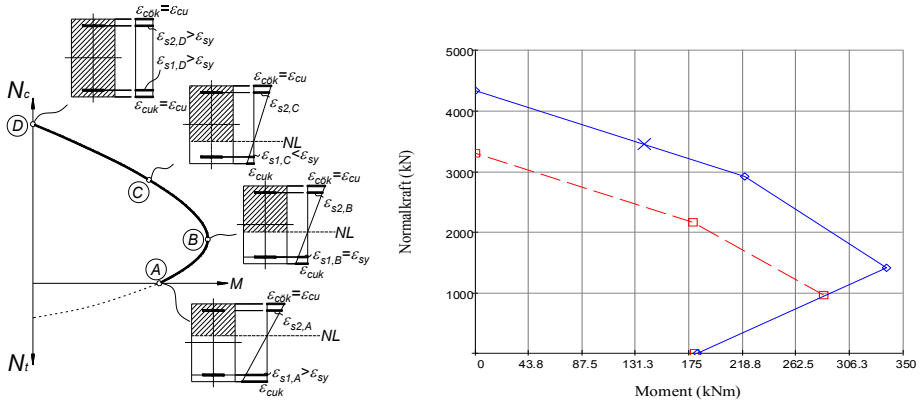


Figure 6 Strengthening for confinement a) General calculation, b) calculation for strengthening

6. WORKMANSHIP AND QUALITY CONTROL

The way in which the work is carried out is of tremendous importance if FRP strengthening is to be successful. To achieve this, the workmanship and quality controls during different stages in a project must be precisely followed. The strengthening work can be divided into three phases:

1. Before strengthening
2. During strengthening
3. After strengthening

All phases are important, but for different reasons. In the first phase, a detailed mapping of the structural component to be strengthened is carried out. The main purpose of this is to obtain a thorough understanding of the strengthening needs and the most suitable system. For example, where the steel reinforcement is placed in the concrete structures and what the quality of the concrete is, are two important considerations. In the second phase, during strengthening, handling regulations and conditions for strengthening should be rigorously followed, for example when an epoxy-based system is used, the temperature must exceed 10 °C during the hardening process. In this second phase, most of the quality control is carried out and followed up. In the third, and last, phase, a final investigation of the bond is carried out. Sometimes during this phase, surface treatments such as painting, plaster or fiber protection, are applied to the strengthening systems.

For concrete substrates, it is essential that the surfaces to be bonded are pre-treated to remove grease, dust or other contaminants that might destroy the effect of the strengthening system. The concrete surface should be sandblasted or grinded prior to strengthening. For concrete structures, it is also important that larger irregularities in their surfaces are leveled out. Where there is corrosion in the existing steel reinforcement, this must be taken care of before the strengthening is carried out. The adhesive application technique used will depend on the strengthening system chosen.

Quality control of the strengthening is also related to the three phases described above. In the first phase, an assessment of the structural component is made, for example, surface strength, irregularities, corrosion etc. In the second phase, the strengthening work itself is checked and in the third, and final, stage, possible voids in, for example, the bond line are handled. Voids can be detected simply by tapping on the composite with a coin or by using more advanced techniques that use active thermography or other non-destructive methods.

For long-term monitoring, different methods can be used, such as traditional electrical strain gauges for strain measurement or more advanced systems using fiber optic sensors which, in their most developed form, can be integrated into the composite.

It is suggested that recommendations from material suppliers are followed when carrying out strengthening work using FRPs.

7. DISCUSSION AND CONCLUSION

In this paper, a brief description of how to design the strengthening of concrete members using FRP has been presented along with the most important and most common applications of FRP strengthening in concrete structures. However, to produce a proper design for strengthening a structure, it is essential to have a solid understanding of concrete design and assessment of concrete structures. The experience of the authors regarding real cases where strengthening has been used shows that it is often the assessment of the existing structure that needs most focus. Without this understanding, it may sometimes be difficult to treat the “patient with the right medicine”. From experience, it has also been found that the execution of the strengthening work is of utmost importance – if this is not taken seriously e.g. through poor workmanship, the resultant strengthening may be inferior.

To the existing handbook, the authors wish to add some more information to the topics covering a) strengthening to improve the fatigue life of concrete structures and b) strengthening of openings in walls and slabs. Currently, research in this area is on-going and preliminary results from our research, and that of others, are very promising.

ACKNOWLEDGEMENT

The authors wish to thank in particular the Swedish Transport Administration (Trafikverket), SBUF (The Development Fund of the Swedish Construction Industry) and the European Union for research funding. Without this funding, our research would not have been possible.

REFERENCES

1. Täljsten B., 1994, *Plate Bonding, Strengthening of Existing Concrete Structures with Epoxy Bonded Plates of Steel or Fibre Reinforced Plastics*, Doctoral Thesis 1994:152D, ISSN 0348-8373, Luleå University of Technology, 1994, p 308.
2. Shinozaki, Hino, Aravinthan, Thiru, Pandey, Govinda Raj, and Mutsuyoshi, Hiroshi (2007) *Advancements in retrofitting reinforced concrete structures in Japan using FRP sheets*. ISBN 0-909375-78-X. Proceedings of the 23rd Biennial Conference of the Concrete Institute of Australia In: Concrete 07: Design, Materials & Construction: concrete for the future, 18-20 October 2007, Adelaide
3. Meier U., Deuring M., Meier H., and Schwegler G. (1992), *Strengthening of Structures with CFRP laminates, Research and Applications in Switzerland*, Advanced Composite Materials in Bridges and Structures, Proceedings ACMBs 1, 1992, pp 243-251.
4. Täljsten, B., (2006). *FRP Strengthening of Existing Concrete Structures - Design Guidelines - Fourth Edition*. ISBN 91-89580-03-6, p 230, Luleå University of Technology, Division of Structural Engineering.
5. ACI (2008). *Guide for the design and construction of externally bonded FRP systems for strengthening concrete structures*. ACI 440.R2-08, American Concrete Institute, Farmington hills, Michigan.
6. Smith S.T., Teng J.G. (2002). *FRP-strengthened RC beams-I: review of debonding strength models*, Engineering Structures 2002; 24(4), pp. 385–95.
7. Toutanji H., Saxena P., Zhao L., Ooi T. (2007). *Prediction of Interfacial Bond Failure of FRP–Concrete Surface*. ASCE Journal of Composites for Construction, July/August 2007, pp. 427-436.
8. Täljsten Björn, Blanksvärd Thomas och Sas Gabriel (2011), *Handbok för dimensionering och utförande i samband med förstärkning av betongkonstruktioner med pålimmade fiberkompositer*, Luleå University of Technology, p 186, ISBN 978-91-7439-146-6
9. EC2 (2008). *Eurokod 2: Dimensionering av betongkonstruktioner – Del 1-1: Allmänna regler och regler för byggnader*. Svensk standard SS-EN 1992-1-1:2005, Swedish Standards Institute.
10. Richart F.E., Brandtzaeg A. and Brown R.L., 1928, *A study of the failure of concrete under combined compressive stresses*, University of Illinois, Engineering Experimental Station, Illinois, 1928.
11. Mander J.B., Priestley M.J.N. and Park R., 1988, *Theoretical stress-strain model for confined concrete*, Journal of Structural Engineering, ASCE, Vol. 114, No. 8, 1988, pp 1804-1826.

Thermal Crack Risk Estimations of Concrete Tunnel Segments - Equivalent Restraint Method Correlated to Empirical Observations.



Anders Hösthagen, M.Sc. Ph.D. Student
Projektengagemang AB & Lulea University of Technology (LTU)
Div. Structural and Construction Engineering, SE-971 87 Luleå
Email: anders.hosthagen@projektengagemang.se



Prof, Dr. Jan-Erik Jonasson
Lulea University of Technology
Div. Structural and Construction Engineering, LTU
Email: jej@ltu.se



Prof, Dr. Mats Emborg
Div. Structural and Construction Engineering, LTU &
Betongindustri AB, Box 47312, SE-100 74 Stockholm
Email: mats.emborg@ltu.se / mats.emborg@betongindustri.se



Adjunct prof, Dr. Hans Hedlund
Skanska Sverige /Div. Structural and Construction Engineering, LTU
Email: hans.hedlund@skanska.se / hans.hedlund@ltu.se



Kjell Wallin, Consulting Engineer
Projektengagemang AB
Email: kjell.wallin@projektengagemang.se



Marcin Stelmarczyk, M.Sc. CEO
The Green Dragon Magic
Email: marcin@greendragonmagic.com

ABSTRACT

Avoiding thermal and moisture induced cracking in newly cast concrete structures implies large economical and technical benefits. Thus, it is of large interest to model one of the major influencing parameters correctly: the restraint. The present study deals with the correlation between numerical models and empirical observations regarding the restraint. The equivalent restraint method, ERM, is used which is established from calculations with the local restraint method, LRM. Casting of walls and roof in a tunnel construction is investigated. Correlation between models and empirical measurements is established in three steps: 1) the restraint situation is analyzed; 2) the calculated temperature developments are compared to empirical temperature measurements to calibrate the models; and 3) calculated strain ratios are compared with observed crack patterns. In general a good correlation is achieved.

Key words: Thermal and moisture cracking, early age concrete. local restraint method, equivalent restraint method, modelling

1. INTRODUCTION

The movements within newly cast concrete are inherited from temperature and moisture states and may cause cracking during the construction, see e.g. [1], [2], [3], [4] and [5]. For complex structures, such as bridges, tunnels, foundations and piers, comprehensive pre-calculations need to be performed in order to analyze the risk of cracking during heating phase and cooling phase. If high strains/stresses are predicted for any part of the structure, measures are needed to avoid cracking. Examples of measures are cooling of the young concrete, preheating of the adjoining construction and/or optimized concrete mix (alternative binders, lower cement content etc.). Such measures are described among others in [6], [7] and [8]. In the case of casting a section against an adjoining structure or a restraining entity (such as rock, subgrade), the restraint influencing on the newly cast concrete increases, and with high restraint the risk of cracking becomes higher, [1] and [9].

It is understood that to design the measures in a cost-effective fashion reliable predictions of restraint are crucial. However, it is known that the restraint usually is difficult to estimate correctly and therefore is an uncertain factor [6]. It is also known that models achievable to estimate the restraint and risk of cracking have different benefits and withdrawals. Here, the model called Equivalent Restraint Method, ERM [10], is used. Benefits of this method involve a possibility to extract the restraint analyzed by elastic 3D calculations and implement it into a compensated plane method for young concrete. These calculations are efficient from a time saving point of view compared with the use of a 3D viscoelastic-viscoplastic simulation for young concrete. Furthermore, the ERM makes it possible to analyze arbitrary measures/actions onsite in an easier way, such as cooling and/or heating.

This paper demonstrates the correlation between numerical models and empirical experiences specially regarding restraint modelling. By studying crack inventories and temperature measurements from a tunnel project and comparing to numerical models, conclusions regarding the correlation are made. The casting of wall and roof segments is investigated and to estimate the restraint situation Abaqus version 6.12 is used and the temperature and stress/strain ratio calculations are performed with ConTeSt version 5.0 [11].

2. AIMS AND OBJECTIVES

Besides evaluating the numerical model ERM (Equivalent Restraint Method) by correlating estimated crack risk to empirical observations of the resulting crack pattern the following aims and purposes of the present research are defined:

- To investigate the effect on the restraint when casting walls using a different casting order. The order of casting in a segmented wall is either as a series (Case 1) or casting a wall in between two completed walls (Case 2).
- To investigate the effect on the restraint when casting roof segments using different casting order. The order of casting the roof segments is either as a series (Case 3) or casting one segment in between two completed segments (Case 4).

3. THEORY

The Equivalent Restrain Method, ERM, is a method to analyze the risk of through cracking. ERM is a further development from the Local Restraint Method [10] and is an improved method to which arbitrary measures/actions against cracking can be applied. To the LRM only cooling is possible to model. Where the LRM is based on semi 2D analysis as a point wise calculation method the ERM is a semi 2D method where the restraint situation at every LRM step is combined into one ERM model by regression analysis. Since both LRM and ERM are based on linear line analysis they are denoted as semi 2D analysis methods. The establishment of the ERM is made in three steps;

The first step: *Estimation of the restraint situation.* By normalizing the restraint within young concrete according to:

$$|\alpha \Delta T 0.93 \cdot E_c| \equiv 1 \quad (1)$$

an elastic analysis shows the restraint situation for the young concrete. In Eq (1) α is the heat expansion coefficient; ΔT is the temperature change within the young concrete; E_c is the Youngs modulus for the mature, adjacent concrete; and 0.93 is a factor to convert the Youngs modulus from mature to young concrete. The system is set to be statically determined in order to simulate a self-balancing system. The maximum restraint for the axis of interest is searched and a 2D (position and restraint magnitude) restraint profile is exported into the second step.

The second step: *Calculation point wise stress/strain ratios with LRM.* The restraint profile given in the first step is used as input to the translation restraint parameter. Several files are created where the stress/strain ratio is calculated at different heights (or positions).

The third step: *Obtaining ERM by regression analysis with LRMs as a base.* A model is created where the translation and rotation restraint, resilience behaviour, construction length and restraining block design are varied to obtain a similar stress/strain ratio profile within the interesting span from the LRMs.

Using the same conditions (e. g. temperatures, measures/actions, material parameters) as for an empirical case into the model, post-calculations for the onsite crack risk can be made. Comparisons to observed crack patterns then tell whether or not the model gives reasonable results.

4. CALCULATIONS AND RESULTS

4.1 Geometries studied

Four different cases have been investigated. Two cases are dealing with casting wall segments in a tunnel construction (Case 1 and 2), and two cases with roof segment casting (Case 3 and 4). In Case 1 the end wall in a cast series is studied, see Figure 1. Case 2 handles the situation where the intermediate (second wall) is cast between two existing walls. The wall segments in Case 1 and 2 are parts of wall 1 in Figure 3. In Case 3 the end roof segment in a cast series is studied, see Figure 2, and in Case 4 the intermediate roof segment (second roof) is studied. Later in this paper the strain situation in the roof is compared to observed crack patterns. Since crack

patterns are only documented for the part of the roof between wall 1 and 2, see Figure 3, only this area is analyzed with the LRM and ERM.

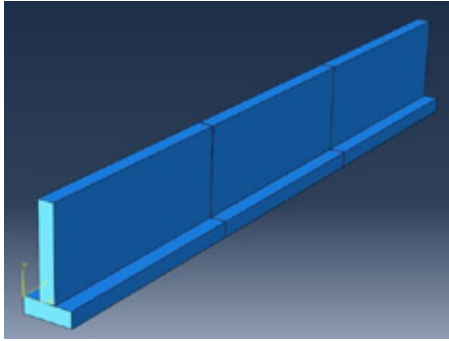


Figure 1 – Three casting sequences of typical case wall-on-slab. In Case 1, one of the end walls is the last casting, and in Case 2 the intermediate wall is the last casting.

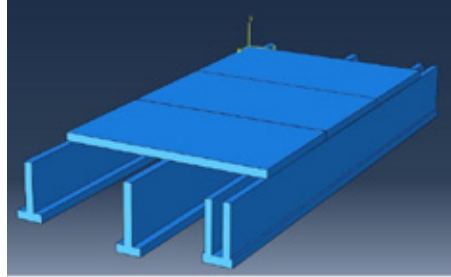


Figure 2 – Three casting sequences of roof segment. In Case 3, one of the end roof segments is the last casting, and in Case 4 the intermediate roof segment is the last casting.

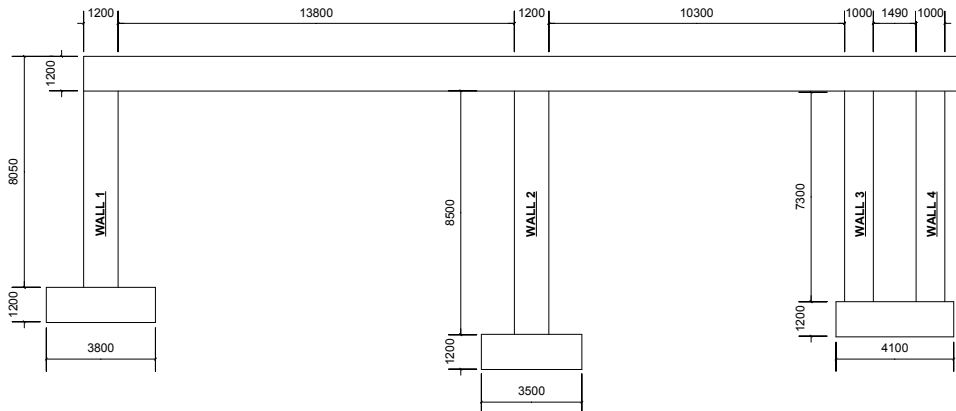


Figure 3 – Cross-section of studied tunnel geometries. Segments are 17.5 m long.

4.2 The first step, restraint estimation

General parameters

The restraint in the young concrete has been estimated in the 3D FEM calculations by use of an elastic modulus in young and existing (old) concrete of 27.9 GPa and 30 GPa respectively and a Poisson's ratio 0.2 in both young and old concrete.

The restraint, defined as the degree of hindrance of movements in the concrete, is obtained by modelling the geometry with the Abaqus 6.12 software. The normalization according to Eq (1)

implies that elastic Abaqus calculations show the restraint situation for the young concrete, formally represented by the calculated stresses.

An area is searched for where a representative restraint situation occurring. Only looking for the maximum restraint could be misleading since it often occurs at beginning (“the ends”) of casting joints. At these positions the restraint profile along the axis of interest is another than the profile at other locations in the construction. A 2D (position and strain ratio magnitude) restraint profile is exported to be used in the second step as earlier described.

The boundary condition, which provides the system in a static state in space, can be set in several ways. The current boundary conditions for the wall castings are set by four points as shown in Figure 4 (here for Case 2). For Case 1 the same boundary conditions are used and the same principle is used for the Cases 3 and 4.

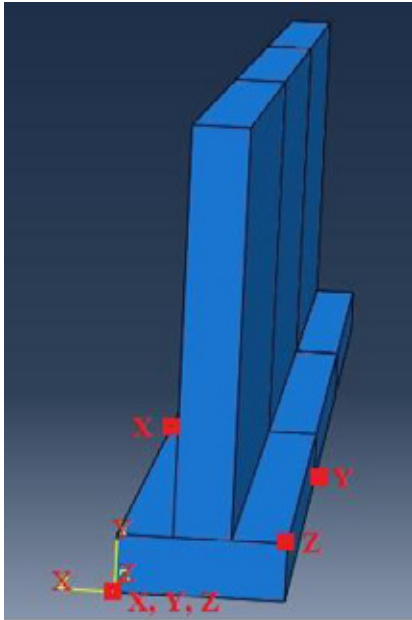


Figure 4 – Location of the four boundary condition points and the axis along which the translation movement is locked to make the system statically determined.

The restraint given by the calculations is the total restraint in all directions. In the result analysis of Abaqus it is possible to differentiate the restraint in any arbitrary direction.

Restraint conditions for the walls

The wall segments investigated in this paper are the segments in wall no 1 (Figure 1). For the wall the direction of interest regarding restraint is along the longitudinal direction (along the joint between the base slab and wall). The corresponding restraint for Cases 1 and 2 for elastic calculations when the newly cast concrete is contracting homogeneously is shown in Figures 5 and 6.

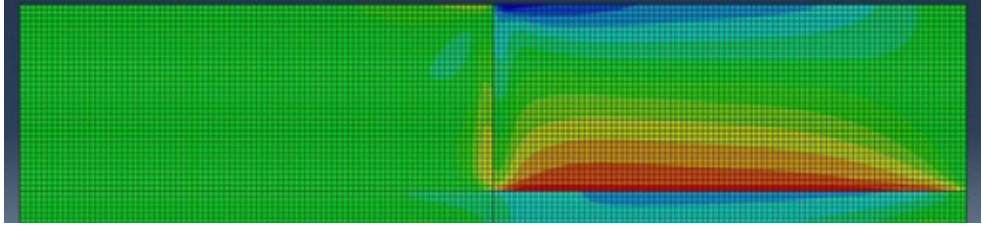


Figure 5 –Restraint values for Case 1 along the longitudinal direction of the tunnel. Maximum restraint is 0.76 and minimum is -0.64.

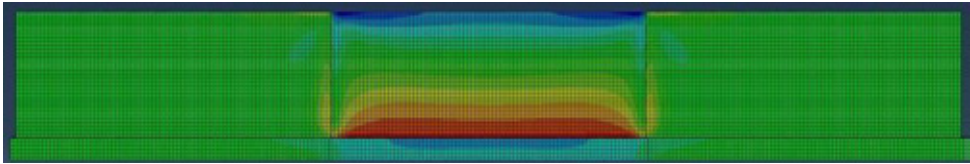


Figure 6 –Restraint values for Case 2 along the longitudinal direction of the tunnel. Maximum restraint is 0.76 and minimum is -0.64.

From the restraint analysis presented in Figures 5 and 6, it is seen that that the maximum value in the two cases are similar; 0.76. The main difference is that the distribution of the restraint in Case 2 displays a more extensive distribution of high restraint.

Restraint conditions for the roof segments

For the roof segments the directions of interest at restraint evaluation is along the axis parallel the joint to the wall and the casting joint to adjoining roof segment. The most significant restraint given by the walls origins from wall number 2 and the results are presented here. The corresponding restraints for Case 3 and 4 at elastic calculations are shown in Figures 7 - 9 where the newly cast concrete is contracting homogeneously.

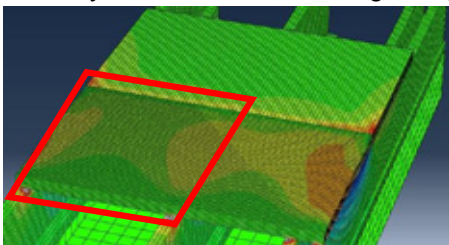


Figure 7 –Restraint values for Case 3 along the joints to the walls. Red square marks region studied. Maximum restraint is 1.00 and minimum is -0.84.

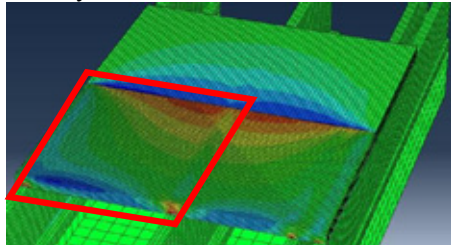


Figure 8 – Restraint values for Case 3 along the joint to the adjoining roof segment. Red square marks region studied. Maximum restraint is 1.00 and minimum is -0.58.

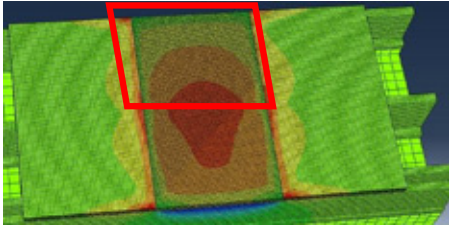


Figure 9 –Restraint values for Case 4 along the joints to the walls. Red square marks region studied. Maximum restraint is 0.70 and minimum is -0.97.

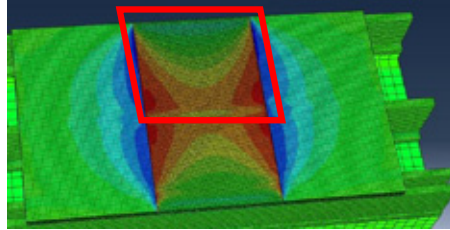


Figure 10 –Restraint values for Case 4 along the joint to the adjoining roof segment. Red square marks. Maximum restraint is 0.85 and minimum is -0.60.

4.3 The second and third step: development of LRM and ERM

General parameters

The stress/strain ratio of the young concrete has been estimated in the 2D FEM calculations by use of the following parameters:

- Concrete class: C35/45, $w/C = 0.40$ and $C = 430$ kg cement per m^3 .
- Wooden form, 21 mm. Heat conductivity 0.14 W/Km.
- Ambient air. Heat transfer coefficient 500 W/Km². Wind speed 3 m/s.
- Initial temperatures, see Table 1.

The restraint conditions in the first step are imported into the LRM calculations by use of the correct restraint value point-by-point performing one calculation at each position. The calculated strain ratio for every LRM position is then plotted, see marks “X” in Figures 11 to 14. The strain ratio is defined by calculated strain divided by the strain at rapture. A regression analysis is performed to obtain the corresponding ERM by varying the translation and rotation restraint, resilience behaviour, construction length and restraining block dimension. For the LRM and ERM calculations the computer program ConTeSt 5.0 was used.

The parameter settings for the LRM calculations and the resulting parameter settings for the ERM when performing the analysis of the wall are shown in Table 1. In Figures 11 - 14 the regression analyses are presented for Cases 1 to 4 as well as the restraint profiles imported from the first step.

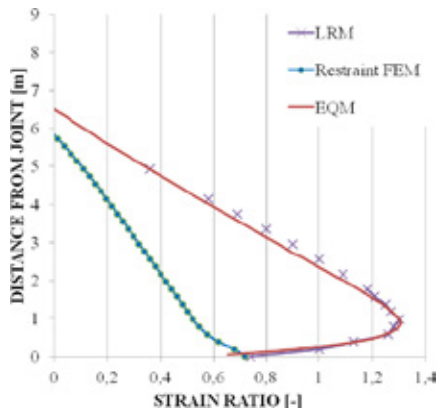


Figure 11 – Resulting ERM to resemble LRM strain ratios, Case 1.

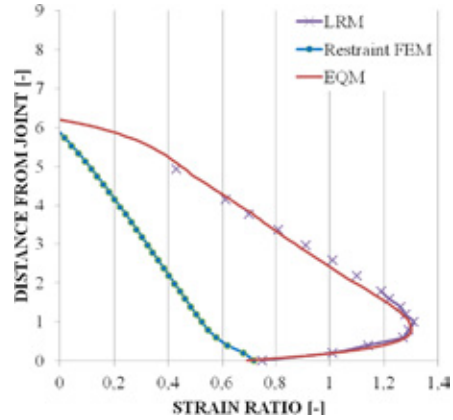


Figure 12 – Resulting ERM to resemble LRM strain ratios, Case 2.

Table 1 – Parameter settings for LRM and ERM, Cases 1- 4. Suffix after Case 3 and 4 refers to studied joint. Legend “Wall” determines the study of the joint between wall no 2 and the roof segment. “Roof” determines the study of the joint between mature roof and the newly cast roof segment.

	Tconcrete	Tair	Rotation restraint	Translation restraint	Resilience Structure length (m)	Reduction of L/H-ratio (-)	Restraining block(s) (# (m x m))
	(°C)	(°C)	(%)	(%)			
Case 1							
LRMs	15	0	1	varies	-	-	-
ERM	15	0	0.1	0.15	35	Yes	1 (3.5 x 1.2)
Case 2							
LRMs	15	0	1	varies	-	-	-
ERM	15	0	0.3	0.17	40	Yes	1 (3.5 x 1.2)
Case 3 - Wall							
LRMs	25	15	1	varies	-	-	-
ERM	25	15	1	0	53	Yes	1 (2.6 x 1.2)
Case 3 - Roof							
LRMs	25	15	1	varies	-	-	-
ERM	25	15	1	0	53	Yes	1 (10.5 x 1.2)
Case 4 - Wall							
LRMs	25	15	1	varies	-	-	-
ERM	25	15	0.8	0	-	No	1 (6 x 1.2)
Case 4 - Roof							
LRMs	25	15	1	varies	-	-	-
ERM	25	15	1	0	65	Yes	1 (10.5 x 1.2)

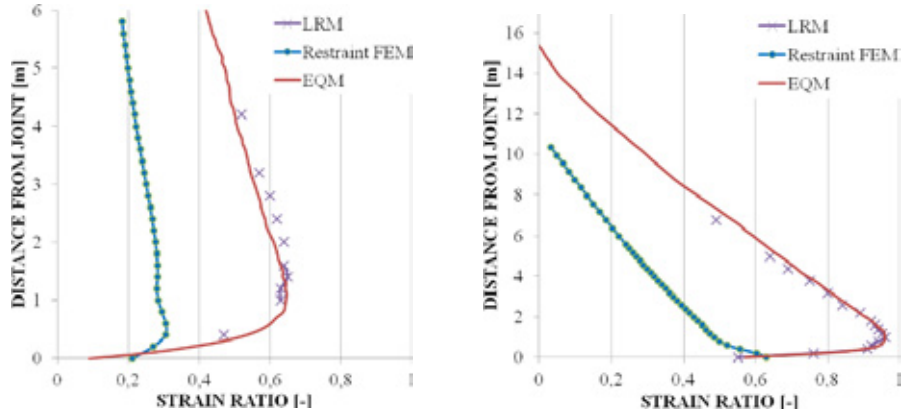


Figure 13 – Resulting ERMs to resemble the LRM strain ratios along the joints to adjoining wall (left) and roof (right) segments for Case 3.

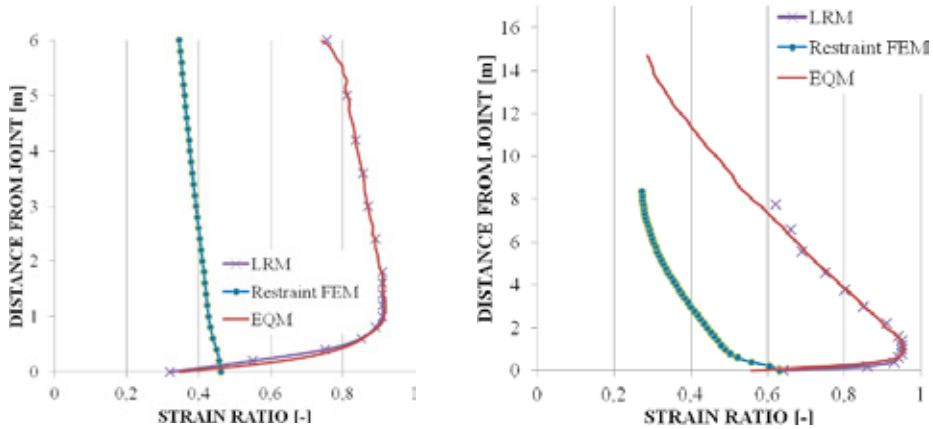


Figure 14 – Resulting ERMs to resemble the LRM strain ratios along the joints to adjoining wall (left) and roof (right) segments for Case 4.

4.4 Observed crack pattern and post-calculation

Onsite temperature measurements were performed for most of the castings within the tunnel project. The measurements together with corresponding crack inventory were used to single out interesting parts of the construction to analyze. In the frame of this paper it is of interest to study the restraint situation in those parts of the construction which show one or just a few cracks. This is because it could be expected that the strain ratio is just around the threshold for the formation of cracks. With the aim of meeting the requirements of a crack free situation, cooling pipes in the walls were used onsite, see Figure 15. However, despite the cooling, cracks occurred in some cast sections. In the post-calculations, the same conditions (e. g. temperatures, measures, and material parameters) as for the specific empirical case was implied into the ERM.

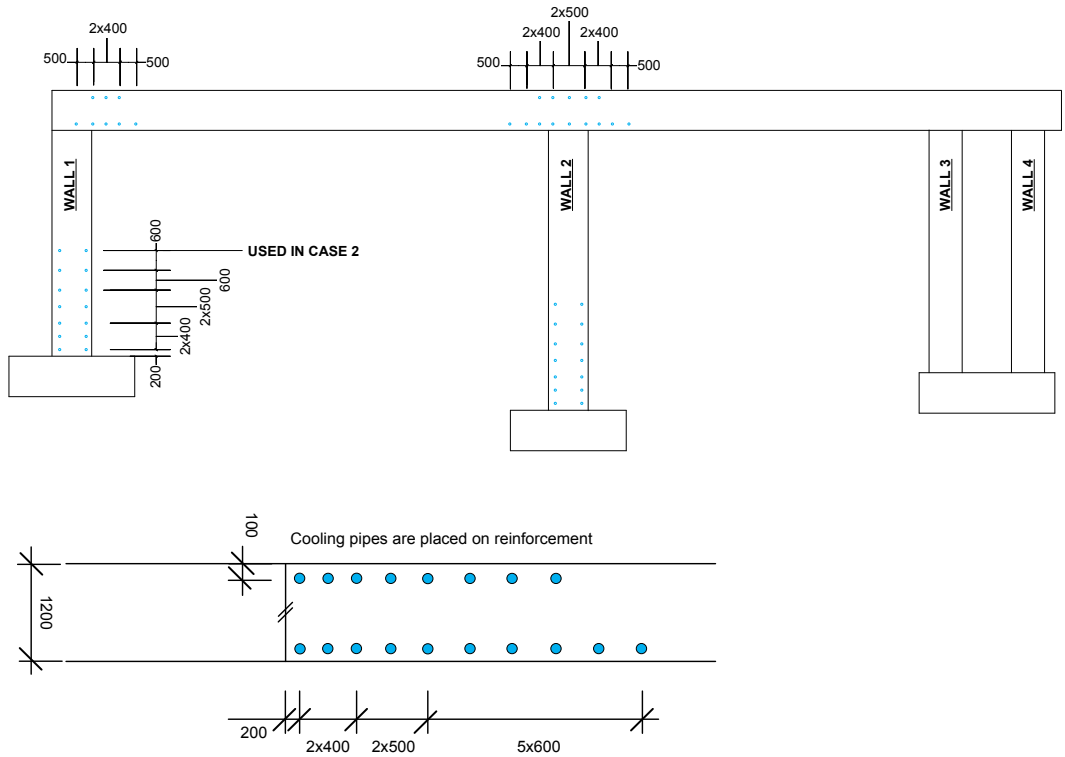


Figure 15 – Positions of used cooling pipes. The upper figure shows the cooling pipes above the joint to walls while the lower figure shows the cooling pipes to adjoining roof segment. Pipes over wall 3 and 4 are not shown.

Observed crack patterns

For the construction parts investigated, observed cracks have been documented. The castings within the tunnel project have proceeded during more than 2 year's time and only sporadic crack inventories have been made. Case 4 have been checked for cracks two times and the others one time each. Figure 16 shows the documented cracks and when they were observed.

Post-calculations

To perform the strain ratio post-calculations, simulations of the casting situation for the four cases are performed using the ERM with the existing cooling pipes and the registered environmental parameters. In Table 2 the following input parameters are listed: the initial concrete temperature, average ambient air temperature, form striking time, average cooling water temperature, and start and stop of cooling actions. The ambient air temperature and cooling water temperature are given as average values but indeed fluctuates over time. All parameters in Table 2 except form striking time are collected from onsite measurements. The form striking times are given by documentation since it could not be read from the measurements. To meet the measured temperature maximum in the cast concrete the heat parameters within the software have been adjusted. All given times are counted from start of casting.

The resulting strain ratio profile as a function of strain ratio versus distance from joint, and the strain ratio at the position of the maximum strain ratio as a function of time is shown in Figures 17 - 20 for Cases 1 - 4 respectively. Start time of casting is set to 200 h in the calculations to make the system adjust itself before calculating the young concrete. Some figures show a slight discrepancy in maximum strain ratio between the two plotted graphs. This is due to the graph showing maximum strain ratio as a function of time is hand selected for a specific height.

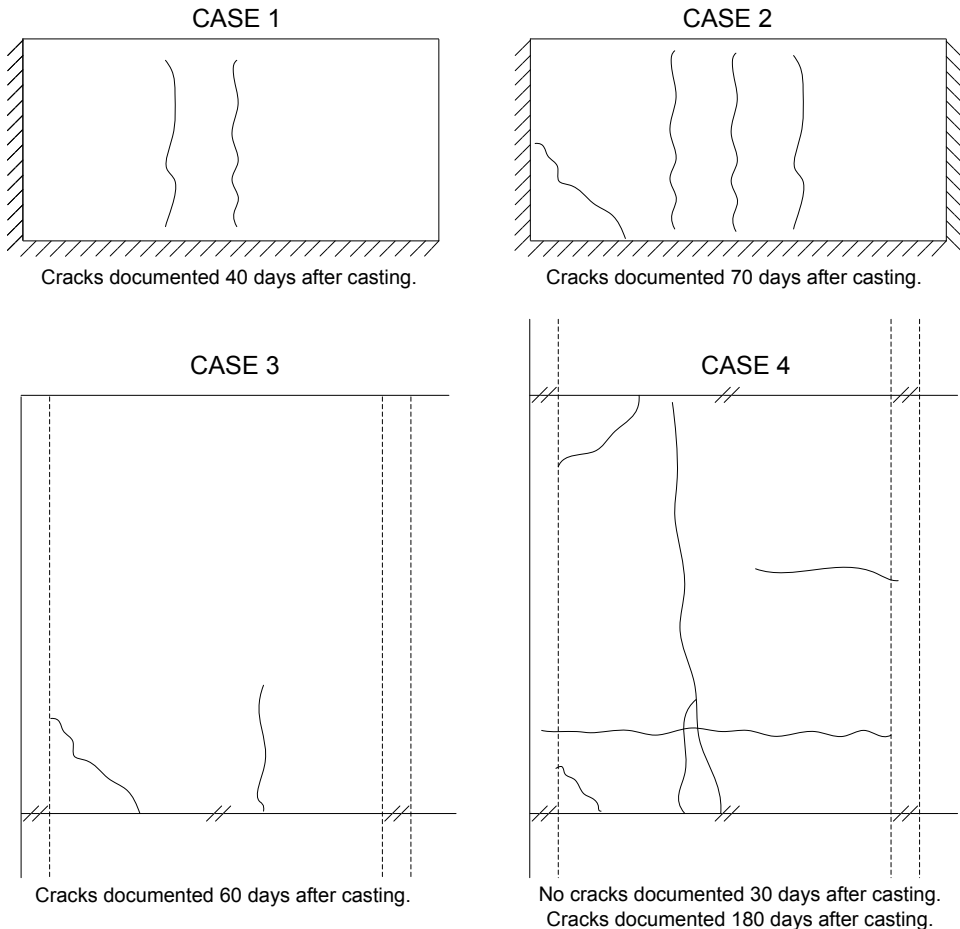


Figure 16 – Observed crack patterns and time of first observation for Cases 1 to 4. Crack widths are 0.1 mm or larger.

It can sometimes be hard to localize the exact height giving the maximum strain ratio. When looking at the figures it is important to bear in mind that follow up calculations of cracked situations states [12] that cracks were observed for estimated strain ratios of about 0.80 to 1.05.

In Figure 17 (Case 1) it is seen that the calculated strain ratio about 10 days (240 h) after time of casting reaches the maximum level of about 0.94, and that a high strain ratio remains for a rather

long period of time. The conclusion is that the numerical modelling gives a clear indication that the wall is in danger of cracking during the current parameter set. The observed status of the construction part (see Figure 16) shows a moderate crack pattern suggesting that the strain within the construction is just enough to create cracks.

In Figure 18 (for Case 2) the maximal strain ratio is 0.91 that is reached about 12 days (288 h) after time of casting. As for Case 1 a high strain ratio remains for a significant time period after the strain ratio peak. The high strain ratio for an extended time period implies that the wall in Case 2 is in danger of getting cracked. By comparing the post-calculation to observed crack patterns, see Figure 16, it is plausible that the high strain inside the wall causes the construction to crack. Compared to the crack situation for Case 1 there is more cracks in Case 2. By looking at the restraint distribution in Figures 5 and 6 it is clear that Case 2 have a more extensive distribution of high restraint. This could be one explanation why more cracks were observed in Case 2 than in Case 1 for the studied tunnel construction. Another explanation is that the time of crack documentation, counted from start of casting, differs between the two cases. Whereas in Case 1 the crack inventory was done 40 days after casting but as late as 70 days for Case 2. This implies that the strain due to temperature gradients had a longer time to make effect. Hence, more cracks could appear.

In Figure 19 (for Case 3) the strain has been analyzed along the joint between the newly cast roof segment and the walls. The strain presented is in the roof segment over wall number 2. Moreover, the strain along the joint between the newly cast roof segment and the adjoining mature roof segment is presented. At the casting joint to the wall the maximal strain ratio is 0.70 and is reached about 14 days (336 h) after time of casting. At the joint between roof segments, the maximal strain ratio is 0.82 reached about 13 days (312 h) after time of casting. The strain ratio remains close to the maximum for an extended time period after it peaked. Even though the strain ratio is just around 0.80 for a short period of time cracks has been documented 60 days after casting, see Figure 16. A contributing factor when cracks are formed during a rather long period might be local changes in time of the environmental conditions like temperature, wind speed, and moisture states.

In Figure 20 the strain has been analyzed along the joint between the newly cast roof segment and the walls (for Case 4). The strain presented is in the roof segment over wall no. 2. Furthermore, also the strain along the joint between the newly cast roof segment and the adjoining mature roof segment is presented. For the joint to wall the maximal strain ratio is 0.80 which is reached about 15 days (360 h) after time of casting. The maximal strain ratio at the joint between roof segments is 0.84 which is reached about 15 days (360 h) after time of casting. For this casting the cooling failed; for some reason it started 30 h after start of casting and ended 6 h later and the temperature of the cooling water was about 28°C. In Figure 20 it is observed a significant region from the joint to the wall and outwards with high strain ratios, 0.75 – 0.80. Furthermore, it shows that 0.5 to 1 m away from the joint between roof segments the strain ratio exceeds 0.80. The maximum strain ratios more or less don't decrease at all for both cases, even 33 days (800 h) after casting. When looking at Figure 16 no cracks were visible 30 days after casting but had appeared 180 days after casting.

Table 2 – Environmental parameters for casting of Cases 1 to 4

	Tconcrete (°C)	Tair average (°C)	Form striking (h)	Cooling temp average (°C)	Cooling time Start (h)	Stop (h)
Case 1	18	1	168	12	0	46
Case 2	16,5	4	288	9	0	34
Case 3	25	17	96	18	0	68
Case 4	25	20	240	28	30	36

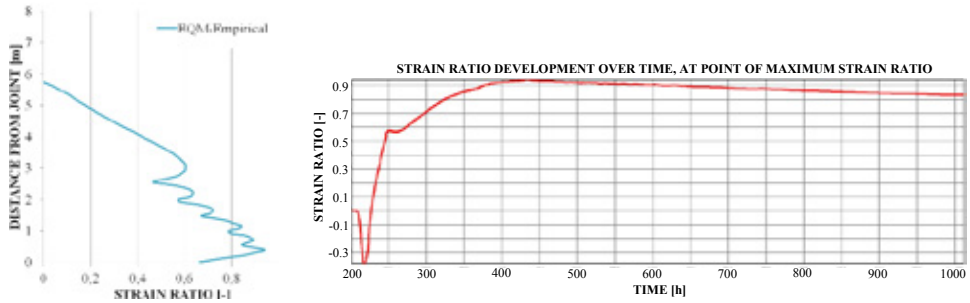


Figure 17 – Strain ratio profile at design position, and strain ratio versus time at position of maximum strain ratio for Case 1. Start time of casting is 200 h.

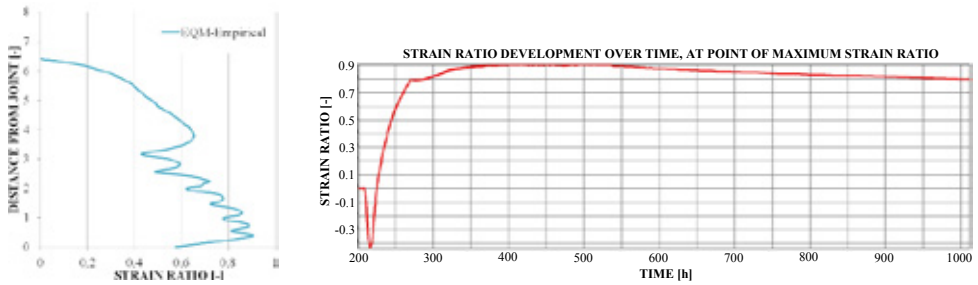


Figure 18 – Strain ratio profile at design position along the joints to adjoining wall (upper figure) and roof (lower figure) segments, and strain ratio versus time at position of maximum strain ratio for Case 2. Start time of casting is 200 h.

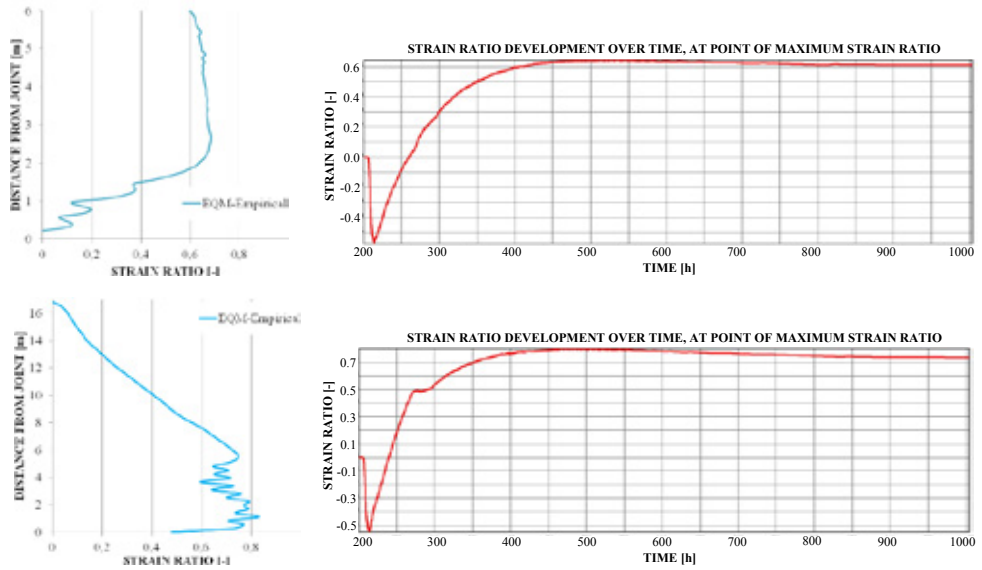


Figure 19 – Strain ratio profile at design position along the joints to adjoining wall (upper figure) and roof (lower figure) segments, and strain ratio versus time at position of maximum strain ratio for Case 3. Start time of casting is 200 h.

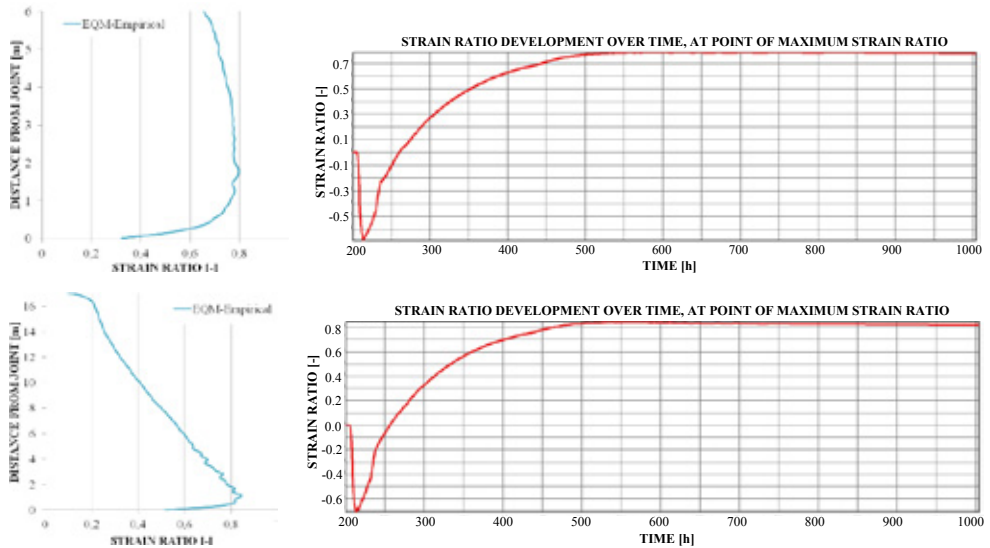


Figure 20 – Strain ratio profile at design position along the joints to adjoining wall (upper figure) and roof (lower figure) segments, and strain ratio versus time at position of maximum strain ratio for Case 4. Start time of casting is 200 h.

5. CONCLUSIONS

In the scope of this paper four typical casting situations were analyzed, two cases for wall segment castings (Cases 1 and 2) and two cases for roof segment castings (Cases 3 and 4). First a study of the restraint situation was performed. Secondly, the development of Equivalent Restraint Method was performed by subsequent regression analysis using ERM to resemble the Local Restraint Method calculations of strain ratio values. And finally, the developed ERMs were used to perform post-calculations for parts of a tunnel project representing Cases 1 to 4.

Regarding the objectives (Chapter 2) it can be concluded that analysis of the restraint in the wall segments (Cases 1 and 2) most likely explains why more cracks were observed casting intermediate wall than casting end walls, even though an extra pair of cooling pipes was added (see Figure 15). The effect of a more extensive restraint distribution, given by Abaqus, for Case 2, is not surprising. But that the magnitude is more or less the same as for Case 1 is interesting. When studying the observed crack patterns at these two cases, it is clear that for walls cast under the permissions of Case 2 more cracks are observed. An explanation could be that the total strain is larger than for Case 1. Added to this effect, there is slightly higher restraint above the point of maximum restraint in the construction for Case 2. Therefore a tendency of larger crack risk is present. For the studies of a cast end wall and a cast intermediate wall good correlations between the ERM and empirical observations were shown.

Furthermore, analysis of the restraint situation of the roof segments (Cases 3 and 4) shows an extended region of high strain ratio along the joint to the wall (upper part of Figures 19 and 20). The maximum strain ratio decreases slowly and as for Case 4 barely at all. This gives that a significant volume of the concrete is exposed to high strains under a long time. Along the joint to the adjoining roof segment the maximum strain ratio is just above 0.80. As for the joint to the wall, the maximum strain ratio decreases slowly, which strains that region for a long time and could therefore cause cracks. In Case 4 the cooling was poorly performed and the main reason why the strain ratio is not higher, especially when compared to Case 3, is favourable ambient temperature conditions and a long form striking time. If the form was stripped just after 4 days, as in Case 3, the roof segment most surely would show severe cracking within a day or two. For the studies of the roof segments an acceptable correlation between the ERM and empirical observations was shown.

The general conclusion from above is that a cast end wall experience a lower degree of total restraint compared to an intermediate cast wall. The same conclusion holds for roof castings when comparing restraint along the joint to the walls. The restraint inherited from adjoining roof segments is of the same magnitude for a end roof casting and an intermediate roof casting.

6. DISCUSSION

The work reported in this paper can be commented on as follows:

The onsite measurements that form the base of this paper, when it comes to correlate the ERM to empirical observations, are not as rigorous as hoped for. For example, systematic crack inventories with a short time span in-between would be beneficial to get a better view of when and where the cracks first start to appear.

There are more reasons that make the concrete crack than just movements caused by temperature development in the young concrete. For example the change of moisture gradients during time is one important factor which is not studied in the present ConTeSt calculations. The superposition of temperature strains and strain inherited from moisture gradients can be one factor that made the investigated concrete to crack.

To improve the comparison between the ERM model and empirical experience several parameters can be investigated further and calibrated. For example, the possible effect of self weight can be added to the Abaqus analysis on restraint. Furthermore, the temperature properties of the young concrete inside ConTeSt can be trimmed or updated.

To compare the post-calculations for these cases to each other could be misleading since the environmental parameters differ from each case. General assumptions such as differences in strain distributions can be done, but going into details should not be done. Comparisons of maximum strain ratios for the cases are therefore not valid due to the different parameter settings.

REFERENCES

1. ACI Committee 207, "Effect of Restraint, Volume Change, and Reinforcement on Cracking of Massive Concrete," ACI Committee 207.ACI207.2R-95. Reapproved 2002, 26 pp.
2. Emborg, M & Bernander, S., "Assessment of the Risk of Thermal Cracking in Hardening Concrete," *Journal of Structural Engineering*, ASCE, Vol.120, No 10, October 1994. pp. 2893-2912.
3. Mihashi, H., & Leite, J.P., "State of The Art Report on Control of Cracking in Early Age Concrete," *J. Advanced Concrete Technology*, 2004, 2 (2) pp.141–154.
4. Kianousha, M.R., Acarcanb, M, Ziari, A., "Behavior of base restrained reinforced concrete walls under volumetric change," *Engineering Structures*, 30, 2008, pp.1526–1534.
5. Cusson, D. & Repette, W., "Early-Age Cracking in Reconstructed Concrete Bridge Barrier Walls," *ACI Materials Journal*, 97(4), July/August, 2000, pp. 438-446.
6. Bosnjak, D., "Self-Induced Cracking Problems in Hardening Concrete Structures," Department of Structural Engineering, Norwegian University of Science and Technology Doctoral Thesis 2000, 171 pp.
7. Rostásy, F S, Tanabe, T., Laube, M., "Assessment of External Restraint. In: Prevention of Thermal Cracking in Concrete at Early Ages," Ed. by Springenschmid. London, England: E& FNSpon. RILEM Report 15. State of- the Art Report by RILEM Technical Committee 119, prevention of Thermal Cracking in Concrete at Early Ages.1998, pp. 149-177.
8. Emborg, M., "Development of Mechanical Behavior at Early Age," Ed. by R. Springenschmid. London, England: E & FNSpon. RILEM Report 15. State of- the Art Report by RILEM Technical Committee 119, Prevention of Thermal Cracking in Concrete at EarlyAges.1998, pp. 77-148.
9. Nilsson, M., "Restraint Factors and Partial Coefficients for Crack Risk Analyses of Early Age Concrete Structures," Lulea, Sweden, Division of Structural Engineering, Lulea University of Technology. Doctoral Thesis 2003, 170 pp.
10. Al-Gburi M., Jonasson J-E., Nilsson M., Hedlund H. & Hösthagen A., "Simplified Methods for Crack Risk Analyses of Early Age Concrete - Part 1: Development of Equivalent Restraint Method", Nordic Concrete Research No. 46, 2012/2.

11. ConTeSt Pro., "User's Manual - Program for Temperature and Stress Calculations in Concrete", Developed by JEJMS Concrete AB in co-operation with Lulea University of Technology, Cementa AB and Peab AB. Lulea, Sweden, 2003, 198 pp.
12. Larson M., "Estimation of Crack Risks in Early Age Concrete – Simplified Methods for Practical Use", Licentiate Thesis 2000:10, Luleå University of Technology, Luleå. 2000.

Determining the Chloride Threshold Value for Corrosion of Reinforcement Steel in Concrete: Influence of the Electrochemical Method and the Chloride Exposure



Dimitrios Boubitsas
CBI Betonginstitutet
c/o SP
SE-501 15, Borås
dimitrios.boubitsas@cbi.se



Tang Luping*
Ph.D., Prof
Chalmers Univ. of Techn.
Div. of Building Technology
SE-412 96, Gothenburg
tang.luping@chalmers.se

ABSTRACT

This paper describes a part of the work in the development of a “standard” test method for determining chloride threshold values required to initiate corrosion on reinforcement in concrete. The main objective of this study is to investigate the influence of corrosion monitoring techniques and the influence of increased concentration of the exposure salt solution on the measured chloride threshold values. Further, two different types of cement were studied. Two commonly used electrochemical techniques, that is, open circuit potential measurement and polarising current measurement under the potentiostatically controlled condition were used for monitoring the corrosion initiation. Both corrosion monitoring techniques were found to give reliable results in identifying corrosion initiation and no difference in the chloride threshold values could be observed between the monitoring methods. An increased concentration of salt solution from 6% to 12% sodium chloride did not accelerate the corrosion initiation time.

Key words: chloride-induced corrosion, chloride threshold values, surface condition

1. INTRODUCTION

Chloride initiated reinforcement corrosion is one of the major causes of deterioration of concrete structures [1]. Steel in concrete is protected by the high alkaline nature of the pore solution in concrete [2-5]. Iron oxides will form a thin protective film on the surface of the reinforcing steel (a passive layer), and in this passive state the corrosion rate is insignificant [4, 5]. However, in practice reinforcement corrosion due to the ingress of chloride ions from de-icing salts or sea water may occur resulting in premature damage which may lead to early failure of reinforced concrete structures [1, 2].

When chloride ions reach a certain critical concentration at the depth of the embedded reinforcement steel the passive film is broken down and the corrosion rate becomes significant, the exact mechanism is not well understood [5-7]. A lot of research has been devoted to try to determine this critical chloride concentration, or the chloride threshold value (CTV) as it is often referred to in the literature. Comprehensive literature reviews on the subject of CTV have been published by Angst et al. [8] and Alonso et al. [9]. A large scatter in the reported CTVs was found and it was concluded that the testing methods used contribute largely to the variability found in the reported CTVs [8, 9]. The need of a practice-related test method under conditions as realistic as possible to evaluate the CTV for embedded reinforcement steel in concrete was identified by Page [10]. Recently, the RILEM TC 235-CTC "Corrosion Initiating Chloride Threshold Concentrations in Concrete" is working for the development of a practice-related test method.

In the effort to develop a "standard" test method for determining chloride threshold values, under conditions reasonably comparable to those in service, with satisfactory reproducibility and as rapid as possible concerning the slow diffusion nature of the chloride ions in concrete, a series of studies intending to isolate parameters which can have a major influence on variability of the reported CTV-values were undertaken by the authors of this paper, as a pilot work of the RILEM TC 235-CTC. The starting point for the development of a "standard" test method is based on the work done by Nygaard and Geiker [11].

The "standard" test method should in the first stage be used in comparative purposes, for decisions such as the suitability of binders, admixtures, and reinforcement steel quality in different environments. At a second stage the aim is, after verification with field structures, to use the results as input to service life models.

The main objective of the study presented in this paper is to investigate the influence of corrosion monitoring techniques and the influence of increased concentration of the exposure salt solution on the measured CTV. Two commonly used electrochemical techniques, that is, open circuit potential (E_{corr}) measurement and polarising current (I_{pc}) measurement under the potentiostatically controlled condition were used for monitoring the corrosion initiation. Two salt concentrations that is, 6% and 12% sodium chloride (by weight of solution), were used as the exposure solutions for accelerating the test procedure. Further, two different types of cement was studied.

2. MATERIALS AND METHODS

2.1 Materials

The mix designs of concrete used in this study are given in Table 1 (w/c 0.50).

Table 1 - Concrete mix designs used in the experimental study

Cement type	Cement (kg/m ³)	Water (kg/ m ³)	Aggregate (kg/m ³)	Superplasticizer (% of cement weight)	Slump (mm)	Air (%)	Cube compressive strength (28 d) (MPa)
CEM I	380	190	1817	0.5	180	3	58
CEM II	380	190	1815	0.6	160	2.8	58

Two types of Swedish cement were used, a Portland cement for civil engineering (CEM I 42.5 N MH/SR/LA) and a Portland-limestone cement (CEM II/A-LL 42.5R). Relevant properties of cements are given in Table 2 (according to the supplier). The maximum aggregate size was limited to 10 mm due to the small cover depths.

Table 2 - Properties of the cements (according to supplier)

Cement type	CEM I	CEM II
Blaine fineness (m ² /kg)	310	470
C ₃ A (%)	2	6
Na ₂ O-equivalent (%)	0.6	0.9
Chloride content (%)	0.01	0.06

Four concrete specimens containing 2 sets of 4 embedded steel bars (i.e. a total of 8 bars in each specimen) were cast with the dimensions given in Fig. 1.

The eight plain reinforcement bars of cold-drawn carbon steel (SS260s) of diameter 10 mm were embedded in concrete with four different cover depths of 10, 15, 20 and 25 mm. The composition of the steel is given in Table 3 (according to the supplier).

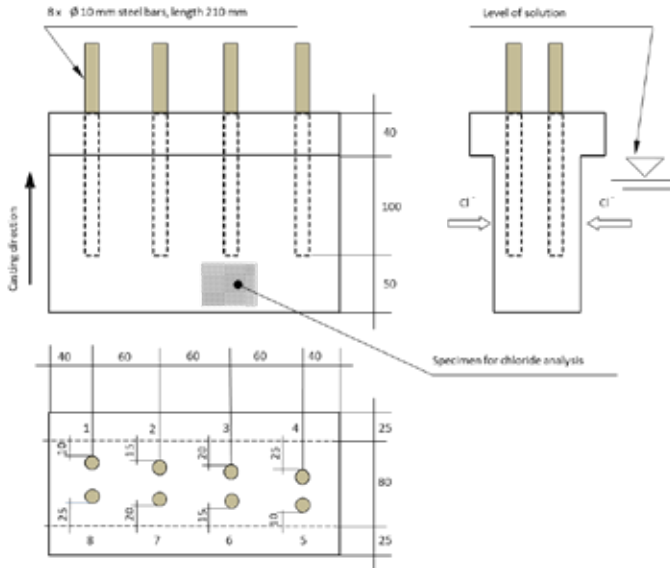


Figure 1 - Concrete specimen with embedded steel bars, the dimensions are given in mm.

Table 3 - Composition of the steel

Residual elements (% by weight)										
C	Si	Mn	P	S	Cr	Mo	Ni	V	Cu	N
0.11	0.29	1.26	0.008	0.014	0.039	0.001	0.04	0.007	0.035	0.0038

The surface condition of the embedded bars is shown in Fig. 2, presenting a photographic image (a) on the left hand side and a light microscopy optical image (b) on the right hand side. In Fig. 2(b) the light area is the steel base material and the dark area is the moulded plastic used to mount the specimen.

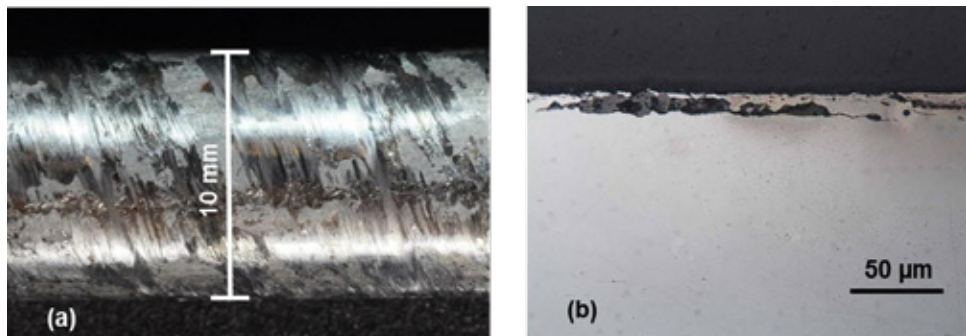


Figure 2 - Photo (a) and light microscopy image (b) of the steel bar surface condition.

The reinforcing bars were delivered in three meters lengths wrapped in plastic for protection against corrosion during the transportation from the production plant to the laboratory.

The bars had a bright metallic luster surface covered partially with strongly adherent mill-scale (Fig. 2(a)). Further, the microscopy image (Fig. 2(b)) shows localized cracks in the mill-scale and crevices between the steel surface and the mill-scale. In Fig. 2 (b) it can also be observed that in some locations in those crevices darker spots can be distinguished, probably some type of corrosion products. The delivered steel bars were cut into lengths of 210 mm and the ends were shaped to avoid sharp edges.

Two prismatic concrete specimens for each mix design (Table 1) with mounted steel were cast. Compaction was performed on a vibrating table. The moulds were first filled to half followed by 5 seconds of vibration and then the moulds were fully filled followed with additional vibration of approximately 5 seconds until air bubbles no longer appeared on the surface.

The reinforced concrete specimens were demoulded one day after casting and cured in sealed plastic sheets until the age of 14 days. The specimens were then cut by sawing to the T-shape form as shown in Fig. 1. After cutting, the concrete cover thickness of the steel bars, on each side, amounted to 10, 15, 20 and 25 mm.

Different concrete cover thicknesses were chosen for studying the effect of cover thickness and also eliminating the risk of undesired early corrosion of the bar at the smallest cover due to over-drying under the accelerated preconditioning (to be mentioned later).. The shape of the specimen is similar to that proposed by Nygaard and Geiker [11]. The major benefit with this kind of T-shape is to hinder sodium chloride crystals developing at the surface of the specimen. These salt crystals often 'climb' up to the top of the specimen and contaminate the protruding part of the steel bars causing crevice corrosion. Another advantage is that it is easier to detect defects such as air voids on a sawn surface, some air voids were observed in all specimens despite the compaction. After sawing, all the surfaces except the two sawn surfaces of each specimen were coated with epoxy resin for preventing the protruding bars to undergo crevice corrosion, and also for accomplishing a one dimensional chloride penetration. The coating was allowed to harden for one day and the specimens were then stored in tap water for six days.

At the age of 21 days the specimens were preconditioned for two weeks at a temperature of 20°C and a relative humidity of 50 %. This was for achieving some drying out and consequently an accelerated chloride penetration (resulting from a combination of capillary suction and diffusion) as it would have been very time consuming if saturated specimens had been exposed to the chloride solution for ingress simply by diffusion. After two weeks of preconditioning two of the specimens (one of each concrete mix) were exposed to a sodium chloride solution of 6% by weight (about 1 mole/l) and the other two were exposed to a sodium chloride solution of 12% by weight (about 2 moles/l). Different solution concentrations were used to see if the corrosion initiation time could be shortened without influencing the CTV. The exposure solution extended to a height of 130 mm from the bottom of the specimens (see Fig. 1).

In the following, the specimen with CEM I cement as binder exposed to the 6% sodium chloride solution is designated A6% and the specimen with the same binder exposed to the 12% sodium chloride solution is designated A12%, the specimens with CEM II as binder are designated by B6% and B12%, respectively.

2.2 Methods

Electrochemical measurements

Two different electrochemical techniques for monitoring the corrosion process were used: open circuit (free corrosion) potential (E_{corr}) and polarising current (I_{pc}) under a potentiostatically controlled condition. As have been pointed out in [8] the method for detecting active corrosion may influence the CTVs reported in the literature.

For each concrete specimen (see Fig. 1) embedded bars 1-4 were monitored by the open circuit potential E_{corr} , and embedded bars 5-8 were monitored by the I_{pc} under the potentiostatically controlled condition. In both cases a potentiostat developed by Arup and Sørensen [12] was used. The measurement principle is illustrated in Fig. 3. The E_{corr} for bars 1 to 4 (W2 in Fig. 3) was measured against the reference electrode (R). For bar 5 to 8 (W1 in Fig. 3) the I_{pc} was measured through the voltage drop across a $100\ \Omega$ build-in resistor in the potentiostat. More about this technique can be found in references [12, 13]. In principle, when corrosion is initiated, the open circuit potential E_{corr} will appear a sudden drop whilst the polarisation current I_{pc} will suddenly increase under the potentiostatically controlled condition.

Commercially available manganese oxide reference electrodes (ERE 20, made by FORCE Technology in Denmark) placed in the saline solutions and a data-logger were employed for data acquisition. Typical potential values measured with the manganese oxide reference electrode in saturated calcium hydroxide solution at 23°C are around $+200\ \text{mV}$ vs. saturated calomel electrode (SCE) according to the producer. This type of reference electrode possesses individual but relatively constant potential. The MnO_2 reference electrode used in the 6% solution measured $+178\ \text{mV}$ vs. SCE and in the 12% solution $+190\ \text{mV}$ vs. SCE. All the measured E_{corr} in this study were converted to “vs. SCE” for conformity. For the potentiostatically controlled monitoring a mixed metal oxide titanium mesh placed in the exposure solution as shown in Fig. 3 was used as a counter electrode (C) and the potentiostat was employed for maintaining the potential at a predefined level ($0\ \text{mV}$ vs. SCE).

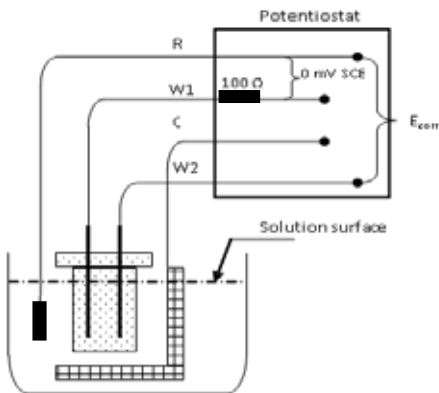


Figure 3 - Measurement principle for E_{corr} and I_{pc} .

The E_{corr} for passive steel in concrete depends on properties like the pH of the pore solution and oxygen availability (moisture content), and can vary over a wide range of potentials [14]. The E_{corr} was recorded every two hours; a sudden drop of the E_{corr} (>100 mV in a few hours) indicates depassivation.

For potentiostatically controlled monitoring the level of the applied potential has previously been found to influence the chloride threshold values. Alonso et al. [15] found that the chloride threshold values were independent of the potential if the level was more positive than -200 ± 50 mV vs. SCE and up to $+250$ mV. In this study the controlled potential was set at 0 mV vs. SCE, which is in the middle of the above range, as suggested by Nygaard and Geiker [11]. The current passed through each steel bar to maintain the steel bars at the fixed potential was recorded every two hours. This polarisation current was normally in a range of 0-5 μA for the passive steel bar. An abrupt increase of the current (>15 μA) indicates the initiation of corrosion [11, 12].

After the test period all of the steel bars were released from the specimens for visual examination of the corrosion status. The test period extended to 329 days for the bars cast in the A-specimens (CEM I) and 376 days for the bars cast in B-specimens (CEM II). Some of the steel bars were removed earlier, if corrosion initiation was indicated.

2.3 Chloride exposure and chloride threshold value determinations

All concrete specimens were continually submerged in the saline solution during the first 75 days. Gradually decreasing potential was noted for some of the steel bars in specimen A6% and B6% that were under the open circuit potential, which can be an indication of oxygen depletion [7]. Oxygen availability is one of the key factors for the electrochemical mechanism of corrosion of steel in concrete. Therefore, after 75 days all the concrete specimens were cyclically exposed to air ($T = 20$ °C and $\text{RH} = 50\%$) for three days and submerged for ten days. The aim of this procedure was firstly to try to make oxygen available, and secondly, this procedure can have an accelerating effect on the chloride ingress. After about two months cyclic exposure no corrosion initiation was found under this cyclic period. Hence this laborious procedure was terminated and the specimens were continually submerged from then on. It must be pointed out that no potential control could be achieved during the periods when the specimens were out of the saline solution. As can be seen in Fig. 4 after the cyclic exposure was started the trend of decreasing potentials stopped for the freely corroding bars in specimens A6% and B6%, and quite stable corrosion potentials (in the passive state) were maintained throughout the whole test period.

Chloride profiles were also determined during the test period. For a chloride profile measurements a concrete prism with the dimensions of approximately $50 \times 50 \times 80$ mm was cut out from the bottom end of each concrete specimen (see an example in Fig. 1). The prism was cut into small slices of 4 to 5 mm thickness in the penetration direction, and these small slices were then ground to powder. Four to six slices were cut for each profile. The acid-soluble chloride content in the powder (here assumed as total chloride content) was determined principally in accordance with AASHTO T260 [16]. An automatic potentiometric titrator (Metrohm 716 DMS Titrino) with chloride selective electrode and a 0.01 N silver nitrate solution was employed for the chloride analysis. After the chloride titration, the calcium content in the same solution was determined also using potentiometric titration with calcium selective electrode and a 0.1 N EDTA solution [17]. The cement content in each concrete sample could

then be estimated from the calcium content since the aggregates used did not contain any soluble calcium.

Ideally, the chloride content at the steel depth should be measured when the corrosion is detected. In this study with multi-bars in a concrete specimen, the destructive sampling of individual corroding bar may interrupt the test of the remaining passive bars. Therefore, instead of destructive sampling immediately after the depassivation, chloride penetration profiles were measured at five different occasions; after 75 days (for specimens A6% and B12%), 138 days (for specimen A6%), 182 days (for specimens B6%, B12% and A12%), 329 days (for specimens A6% and A12%) and 376 days (for specimens B6% and B12%) of exposure in the salt solution. The first three occasions were determined after detection of corrosion initiation of steel bars while the last two occasions were at the end of the test periods. These chloride penetration profiles were used to evaluate the chloride threshold values as described in the following.

A simple empirical model that considers the time dependence of both the surface chloride content and the apparent chloride diffusion coefficient, similar with that proposed by Nilsson [18] was used for predicting the chloride ingress. The principle of the model is to obtain the ‘apparent diffusion coefficient’ $D_a(t)$ and the ‘apparent surface chloride content’ $C_{sa}(t)$ by curve fitting the measured profiles to the error function solution to Fick’s second law (Eq. 1), after different exposure times t_1 and t_2 .

$$C(x, t) - C_{ini} = (C_{sa} - C_{ini}) \cdot \left[1 - \operatorname{erf} \left(\frac{x}{2\sqrt{D_a t}} \right) \right] \quad (1)$$

where C_{ini} is the initial chloride content in the concrete, $C(x, t)$ is the total chloride content (mass-% of cement) at depth x at time t . The time-dependent diffusivity $D_a(t)$ is given by Eq. 2, from which the age factor n can be calculated based on two measured chloride profiles.

$$D_{a2} = D_{a1} \left(\frac{t_1}{t_2} \right)^n \quad (2)$$

The apparent diffusion coefficient $D_a(t_{corr})$ at the time of corrosion initiation (t_{corr}) can then be estimated from the above equation. The time-dependency of C_{sa} is assumed to be linear between the two curve-fitting occasions. The chloride content, i.e. the chloride threshold value, at the time of corrosion initiation (t_{corr}) is calculated using again Eq. 1, with constant parameters $D_a(t_{corr})$ and $C_{sa}(t_{corr})$. It must be emphasized that in the actual experiment both capillary suction and diffusion processes were involved and hence Eq. 1 is not the correct solution of Fick’s second law but just as a purely empirical regression for interpolation between the exposure periods or slight extrapolation out of the curve-fitted occasions.

3 RESULTS

3.1 Corrosion monitoring

Figs. 4 and 5 show the measurements from the corrosion monitoring for the four concrete specimens containing a total amount of eight bars each. On the left hand side of Figs. 4 and 5 the

development of open circuit corrosion potential over time for the set of bars ‘freely corroding’ (E_{corr}) is showed, and on the right hand side the development of polarising current (I_{pc}) over time for the set of bars under the potentiostatic control.

In Fig. 4 (left hand side) a sudden drop to more negative potentials can be observed for three of 4 bars freely corroding for specimen A6%. For specimen B6% only the results for freely corroding bars 1 and 2 are shown, due to problems with the data acquisition. These results indicate corrosion initiation for bars 1 and 2 in specimen B6%. The visual examination showed corrosion initiation also for both bars 3 and 4 in the same specimen. In Fig. 4 (right hand side) the development of the polarising current with time shows that for both specimens A6% and B6% three of four bars indicate corrosion initiation.

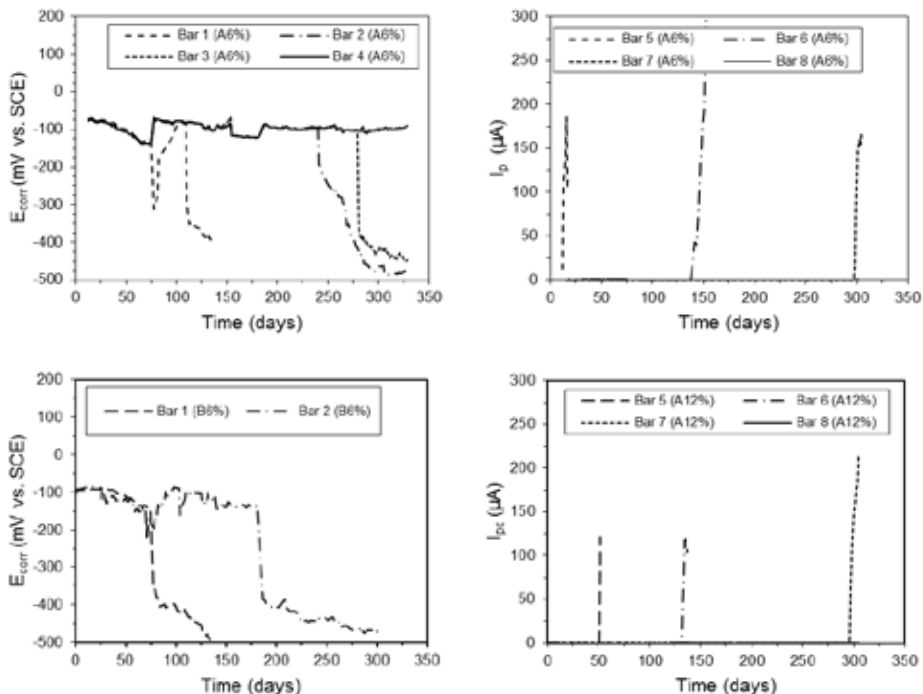


Figure 4 - Results for the specimens exposed to 6% sodium chloride solution.

In Fig. 5 (left hand side) corrosion initiation causing a sudden drop to a more negative potential can be observed for three of 4 bars freely corroding for both specimen A12% and B12%. In Fig. 5 (right hand side) the development of the polarising current with time shows that in specimen A12% three of four bars indicate corrosion initiation while only two bars in specimen B12% indicate corrosion initiation.

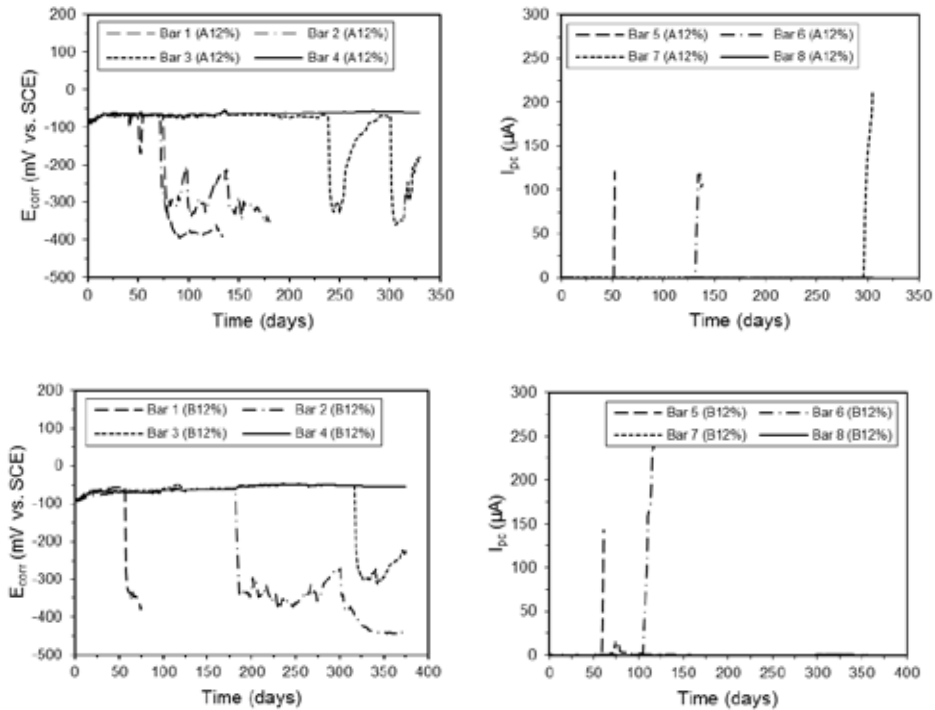


Figure 5 - Results for the specimens exposed to 12% sodium chloride solution.

Some freely corroding bars in Figs. 4 and 5 (especially bar 1(A6%) and bar 3(A12%)) show signs of corrosion initiation followed by a period where the potential returns to the initial less negative value and then drops again.

3.2 Visual examinations

From the visual examinations corrosion could be confirmed on the steel bars that indicated corrosion initiation according to the electrochemical monitoring. Further, no sign of corrosion was found on the steel bars not indicating corrosion initiation by the electrochemical monitoring. The location of corrosion attacks was always initiated on the side facing the direction of chloride ingress. The general feature of the corrosion immediately after removing the concrete cover was one or a couple of dark blue-greenish localized corrosion attacks surrounded with reddish-coloured rust. The corroded locations coincided sometimes with macro-pores (air voids) of size of a few millimeters which were present at the steel-concrete interface. In no case did corrosion cause visible cracks or any other break down of the concrete cover.

3.3 Chloride profiles and chloride threshold values

Fig. 6 shows some of the chloride profiles measured at different occasions during the exposure time. Left hand side chloride profiles measured for the specimens exposed to 6% sodium chloride solution (A6% and B6%) and right hand side chloride profiles measured for the specimens exposed to 12% sodium chloride solution (A12% and B12%). At least at two different occasions were chloride profiles measured for each concrete specimen. When two profiles were determined at the same occasion (as in the upper right hand side Fig. 6), a mean value of the regression parameters from the curve fitting procedure described in section 2.4 was used in the calculation of the chloride threshold values.

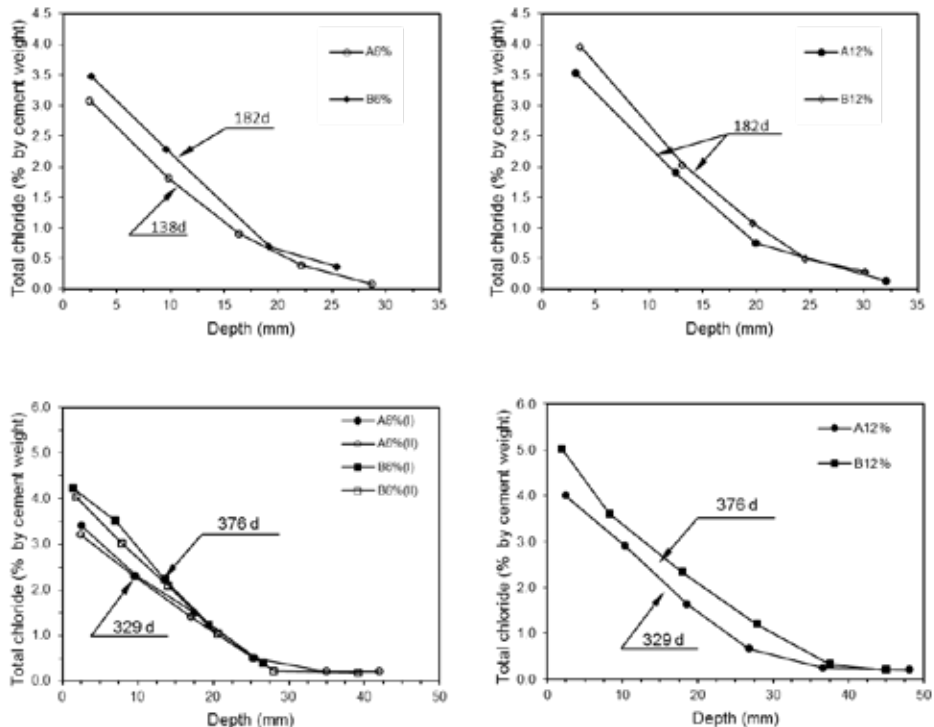


Figure 6 - Chloride profiles measured for the specimens exposed to 6% (left) and 12% (right) sodium chloride solution.

Fig.7 shows the corrosion initiation time and the CTV for all corroded bars. It is obvious that the corrosion initiation time is dependent on the concrete cover thickness and consequently the chloride content at the cover depth.

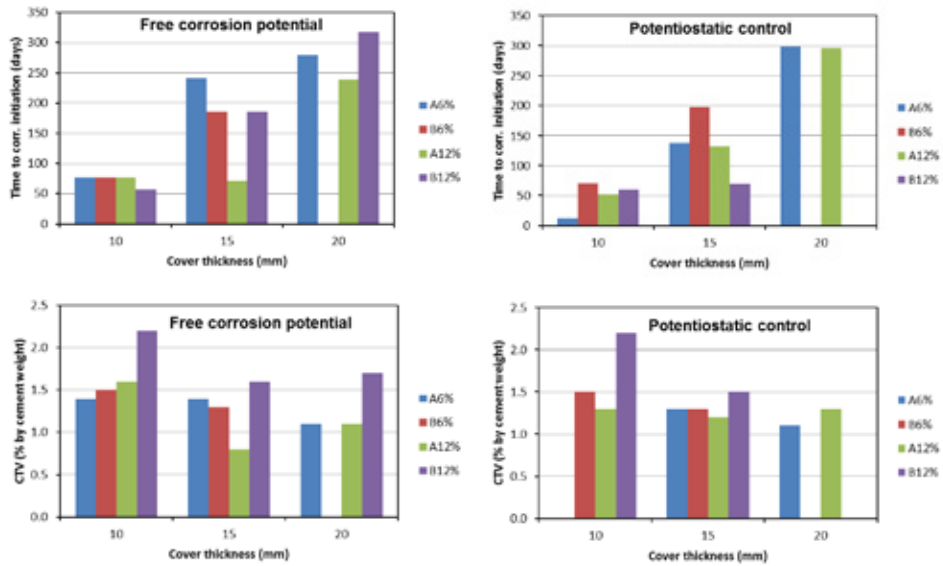


Figure 7 - Corrosion initiation time and the CTV for all corroded bars.

Fig. 8 shows the mean CTV for the corroded bars in each concrete specimen, the standard deviations are also included.

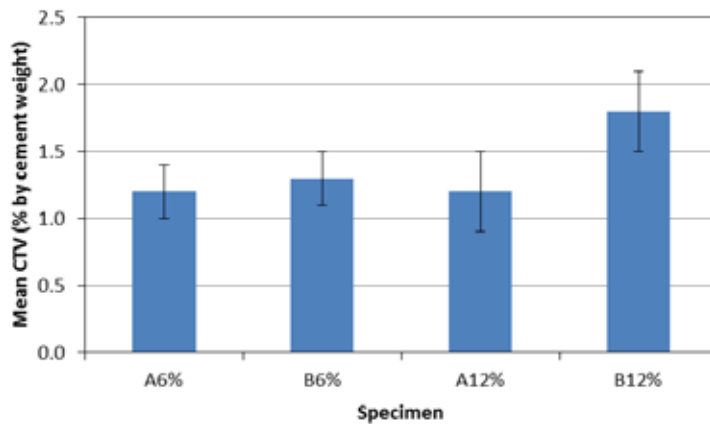


Figure 8 - Mean CTV for the corroded bars in each concrete specimen.

4 DISCUSSION

4.1 Corrosion initiation

In the passive state the E_{corr} of the freely corroding bars was between -100 and -50 mV vs. SCE. A sudden drop to more negative potential indicates corrosion initiation (Figs. 4 and 5). This was the case for all freely corroding bars at various times except for the bars with the thickest concrete cover (25 mm). Some bars (Bar 1(A6%) and Bar 3(A12%)) showed clearly corrosion initiation at an early stage but this indication was followed by a period where the potential returned to less negative values (Figs. 4 and 5). This phenomenon is called repassivation, although the mechanism by which actively corroding steel repassivates is not known with certainty. It has been suggested that in pitting corrosion a cap of porous corrosion products acts as a barrier and “seals off” the active local corrosion by limiting the exchange of local and bulk electrolytes [19].

Similar to the freely corroding bars almost all bars with the pre-set potential 0 mV vs. SCE showed also corrosion initiation at various times, with exception also here for the bars with the thickest concrete cover (Figs. 4 and 5), as well as Bar 7(B12%) with 20 mm concrete cover, in which no corrosion was detected or observed. The detection of depassivation for the corroding bars in this case is straightforward by a rapid increase of the current required to keep the pre-set potential. In one case a sign to repassivation was observed for Bar 6(B12%) (Fig. 5). Otherwise, due to the imposed potential the increase of the polarising current stopped only when the corroding bar was disconnected. These bars were then allowed to corrode freely (up to a month) whereafter the E_{corr} was recorded by the data logger and showed no repassivation.

It appears from Figs. 4, 5 and 7 that the two different methods of monitoring yielded different times of corrosion initiation in the same specimen, but the variation of CTVs between these two methods is not significant, probably due to the fact that the chloride increase at a certain depth is related to the square root of time.

As expected, when chlorides are introduced from an external source into concrete the most decisive parameter determining the time to corrosion initiation is the thickness of concrete cover (see Fig. 7).

4.2 Chloride threshold values

From the measured chloride profiles (Fig. 6) it appears that the chloride penetration rate was influenced by the concentration of the exposure solution and to some extent also by the binder type, being highest for specimen B12% followed by specimen A12%, and then by specimens B6% and A6%. However, the increased salt concentration did not accelerate the corrosion process or shorten the initiation time.

The average chloride threshold values of each group of specimens are shown in Fig. 8. The mean value of the chloride threshold for the corroding rebars embedded in the specimens with CEM I (A6% and A12%) as binder was 1.2 % by weight of cement with a standard deviation of ± 0.2 % for A6% and ± 0.3 % for A12%. For the rebars in the specimens with CEM II (B6% and B12%) as binder the mean value of the chloride threshold was 1.3 ± 0.3 % by weight of cement for the specimen B6% and 1.9 ± 0.3 % for the specimen B12%.

The mean CTV for the rebars embedded in specimen B12% is distinguished from the rest by being markedly higher. The CTVs for the rebars with the smallest cover depth represent the major contribution to this (see Fig. 7). This is difficult to explain as it would have been expected that the CTVs for the rebars in B12% and in B6% should be in the same range. Yonezawa et al. [20] showed that CTV can depend on the concentration of the exposure solution, but if so, in the present study that would have been the case also for the rebars in specimens A6% and A12%. Only one of the 20 corroded rebars showed a CTV lower than 1% by weight of cement. For the bars that did not corrode during the test period the chloride level at the cover depth (25 mm) was 0.8% for A6% and for B6%, 1.0% for A12% and 1.3% for B12% by weight of cement.

A large scatter of reported chloride threshold values is found in the literature [8, 9] and it is difficult to make a direct comparison between studies with different experimental setups due to the numerous parameters affecting chloride threshold values. However, the mean chloride threshold value for the bars in specimens A6%, B6% and A12% in this study is in line with the mean values reported in the statistical analysis of published chloride threshold values (1.24%) made by Alonzo and Sanchez [9], for what they referred to as “natural methods”. It can be pointed out that the mean value for the CTVs from potentiostatic methods were 0.82% by weight of cement, as reported by Alonzo and Sanchez [9].

The binder type has been pointed out as one of the influencing parameters on the susceptibility for chloride-induced corrosion [8]. As several authors [2, 3, 5] have pointed out, the high pH of the concrete pore solution has an inhibiting effect on chloride-induced corrosion. The pH in the pore solution depends mainly on the alkali content of the cement [21], as presented in Table 2 expressed as content of Na₂O equivalent for the cements used here. The content of Na₂O equivalent in CEM II is higher than in CEM I but it was only the bars in specimen B12% that showed a clearly increased CTV compared with the rest of the specimens which makes it difficult to directly attribute this to a higher pH in the pore solution.

4.3 Corrosion monitoring methods

Basically no difference in the CTVs could be observed between the monitoring methods (see Fig. 7) contrary to the data reported in [8, 9].

From the visual examinations it can be concluded that both corrosion monitoring methods gives reliable results in identifying corrosion initiation. In both cases the corrosion progress of all rebars was continuously monitored by using a data acquisition system, which has the benefits of a more precise registration of the corrosion initiation time, is less laborious, and hence, more cost-efficient than a manual registration method.

The drawback by monitoring only the E_{corr} is that the electrochemical potential can change because of other reasons than corrosion initiation, for instance oxygen depletion [14], or changes at the reference electrode and effects related to moisture or chloride ingress. A tendency of this decrease in potential can be seen in Fig. 4 during the first 75 days of immersion. If this tendency was kept longer, it might be difficult to distinguish the corrosion initiation time.

The potentiostatic controlled method can very clearly and sharply detect the initiation of corrosion, but is criticized for being an artificial state and not related to reality. For example, a phenomenon like repassivation as noted in Fig. 4 and Fig. 5 would not appear in the

potentiostatic controlled method as once corrosion has been initiated the current will continue to increase until the bar in the specimen is disconnected. In their literature review both Angst et al. [8] and Alonso and Sanchez [9] showed that generally lower CT-values were reported from potentiostatic tests than natural open circuit potential tests. However, this was not the case in this study as can be seen in Figs. 7 and 8. It must be pointed out that in this study the CTVs for the open circuit potential tests (E_{corr}) were determined at the first sign of depassivation and that repassivation was not considered. This can be the cause that the CTVs are equivalent for both monitoring methods. From the experience in this study the potentiostatic controlled method requires more knowledge in electronics and data acquisition systems. One drawback of this method is that it is not suitable for monitoring corrosion when simulating wet and dry periods.

The corrosion monitoring methods used in this study is not a critical parameter responsible for the scatter of the chloride threshold values reported in the literature. A much more decisive parameter influencing the CVT previously identified by the authors of this paper [22] and others [23, 24] is the rebar surface condition.

Further, the following suggestions can be given based on the experiences from this study for the improvement of the test method:

- Cast only one rebar per concrete specimen (for example 150x150 cube). This will make it easier to determine the exact chloride content at the corrosion initiation time without disturbing the corrosion monitoring of the rest of the rebars.
- Modify the preconditioning (harsher drying) to attain deeper initial chloride penetration in order to achieve corrosion initiation faster. A cover depth of 10-15 mm can be considered as sufficient to attain reliable results.
- Because studies of corrosion initiation always reveal a wide scatter of data [25], use at least 8 rebars with one cover depth to minimize the uncertainty in the results.

5 CONCLUSIONS

From this study, the following major conclusions can be drawn:

- Both open circuit potential and potentiostatic control techniques for corrosion monitoring give reliable results in identifying corrosion initiation and no difference in the chloride threshold values could be observed between these two monitoring techniques for the chosen level of polarisation.
- An increased concentration of salt solution from 6% to 12% by weight of sodium chloride did not accelerate the corrosion process or shorten the initiation time.

REFERENCES

- [1] Hobbs, D.W., "Concrete deterioration: causes, diagnosis, and minimising risk", *Int. Mater Rev*, Vol. 46, No. 3, 2001, pp. 117-144.
- [2] Tuutti, K., "Corrosion of steel in concrete", Dissertation, Swedish Cement and Concrete Research Institute, Stockholm, 1982, 469 pp.

- [3] Page, C.L., Treadaway, K.W.J., "Aspects of the electrochemistry of steel in concrete", *Nature*, Vol. 297, May, 1982, pp. 109-115.
- [4] Arup, H., "The mechanisms of protection of steel by concrete", Proceedings, Corrosion of reinforcement in concrete structures, London, June 1983, pp. 151-157.
- [5] Hansson, C.M., "Comments on electrochemical measurements of the corrosion of steel in concrete", *Cem. Concr. Res.*, Vol. 14, No. 4, 1984, pp. 574-584.
- [6] Benture, A., Diamond, S., Berke, N.S., "Steel corrosion in concrete - Fundamentals and civil engineering practice". Taylor & Francis, London, 1997, 201 pp.
- [7] Bertolini, L., Elsener, B., Pedersen, P., Polder, R., "Corrosion of steel in Concrete – Prevention, diagnosis, repair", Wiley-VCH, Weinheim, 2004, 392 pp.
- [8] Angst, U., Elsener, B., Larsen, C.K., Vennesland, Ø., "Critical chloride content in reinforced concrete – A review". *Cem. Concr. Res.* Vol. 39, No. 12, 2009, pp. 1122-1138.
- [9] Alonso, M.C., Sanchez, M., "Analysis of the variability of chloride threshold values in the literature", *Mater. Corros.* Vol. 60, No. 8, 2009, pp. 631-637.
- [10] Page, C.L., "Initiation of chloride-induced corrosion of steel in concrete: role of the interfacial zone", *Mater. Corros.* Vol. 60, No. 8, 2009, pp. 586-592.
- [11] Nygaard, P.V., Geiker, M.R., A method for measuring the chloride threshold value level required to initiate reinforcement corrosion in concrete. *Mater. Struct.* Vol. 38, No. 4, 2006, pp. 489-494.
- [12] Arup, H., Sørensen, H.E., "A proposed technique for determining chloride thresholds", Proceedings, Chloride penetration in concrete, International RILEM workshop, St-Rémy-lès-Chevreuse, France, October 1995, pp. 460-469
- [13] Nygaard, P.V., "Effect of steel-concrete interface defects on the chloride threshold for reinforcement corrosion", Master Thesis, Technical University of Denmark, 2003, 142 pp.
- [14] Elsener, B., Andrade, C., Gulikers, J., Polder, R., Raupach, M., "Half-cell potential measurements – Potential mapping on reinforced concrete structures", *Mater. Struct.* Vol. 36, No. 7, 2003, pp. 461-471.
- [15] Alonso, C., Castellote, M., Andrade, C., "Chloride threshold dependence of pitting potential of reinforcements". *Electrochim Acta*, Vol. 47, No. 21, 2002, pp. 3469-3481.
- [16] American Association of State Highway and Transportation Officials, "AASHTO-T260 Standard method of test for sampling and testing for chloride ion in concrete and concrete raw materials", (1997).
- [17] Tang, L., "Estimation of cement/binder profile parallel to the determination of chloride profile in concrete". SP Report 2003:07, SP Swedish National Testing and Research Institute, Borås, (2003), 30 pp.
- [18] Nilsson, L.-O., "A numerical model for combined diffusion and convection of chloride ion in non-saturated concrete". Proceedings, 2nd Int. RILEM Workshop on Testing and Modelling the Chloride Ingress into Concrete, RILEM Publications, Paris, 2000, pp 261-275.
- [19] E. McCafferty, Introduction to corrosion science, Springer, New York, 2010.
- [20] Yonezawa, T., Ashworth, V., Procter, R. P. M., "Pore solution composition and chloride effect on the corrosion of steel in concrete", *Corrosion*, Vol. 44, No. 7, 1988, pp. 489-499.
- [21] Taylor, H.F.W., "CEMENT CHEMISTRY", 2nd edition, Thomas Telford, London, 1997, 459 pp.

- [22] Boubitsas, D., Tang, L., "The influence of reinforcement steel surface condition on initiation of chloride induced corrosion", *Mater. Struct.* (accepted for publication).
- [23] Li, L., Sagüés, A.A., "Chloride Corrosion Threshold of Reinforcing Steel in Alkaline Solutions—Open-Circuit Immersion Tests", *Corrosion*, Vol. 57, No. 1 2001, pp. 19-28.
- [24] Hansson, C.M., Sørensen B., "The Threshold Concentration of Chloride in Concrete for Initiation of Reinforcement Corrosion", Proceedings, Corrosion Rates of Steel in Concrete, ASTM Spec. Tech. Pub 1065, Baltimore, USA, 1988, pp. 3-16.
- [25] Shibata, T., "Corrosion probability and statistical evaluation of corrosion data", Uhlig's Corrosion Handbook, 3rd edn. Wiley, New York, 2000, pp. 365-386.

Bridge deck concrete overlays –monitoring of cracking and general performance of two bridges



Martin Persson
M.Sc., Ph.D. Student
Div. Structural and Construction Engineering/Ramböll Sverige AB
Luleå University of Technology/Ramböll Sverige AB
S-971 87 Luleå/SE-104 62 Stockholm
E-mail: martin.persson@ltu.se/martin.persson@ramboll.se



Ulf Ohlsson
Ph.D.
Div. Structural and Construction Engineering,
Luleå University of Technology
S-971 87 Luleå
E-mail: ulf.ohlsson@ltu.se



Mats Emborg
Prof. Ph.D. /Head R&D
Div. Structural and Construction Engineering/Betongindustri AB,
Luleå University of Technology/ Betongindustri AB,
S-971 87 Luleå/100 74 Stockholm
mats.emborg@ltu.se/mats.emborg@betongindustri.se

ABSTRACT

Concrete overlays on bridge decks are expected to be more durable compared with the more common asphalt solution. Of interest is to evaluate the concrete overlay regarding traffic and shrinkage/temperature induced stresses. In a pilot study nondestructive test systems were evaluated in field observations with focus on detecting hidden defects that may have induced identified surface cracks. Studies using NonDestructive Test methods (NDT) and drill core analyses were performed as well as visual inspection. The methods were to some extent considered as time consuming obtaining data and unclear regarding analysis. However, interesting information regarding e.g. cracking has been achieved that will be a base for selection of methods in future field tests of a research project supporting future theoretical analyses and models.

Keywords: Concrete, Bridge deck overlay, Cracking, Modelling, Non-destructive testing.

1. INTRODUCTION

Bridge decks are important elements of the infrastructure. A critical detail of the decks is the top layer which protects the structural concrete of the deck against environmental loads such as rain, snow, de-icing chlorides etc. The most common solution is to apply an impermeable layer on the structural concrete with a wearing course of asphalt, Figure 1a. However, frequently this solution suffers from damages e.g. formation of bubbles in the impermeable layer early at

service stage, causing leakage of water and chloride ion entrainment, thus leading to costly repair. The construction process includes many stages and is complex and time consuming. An

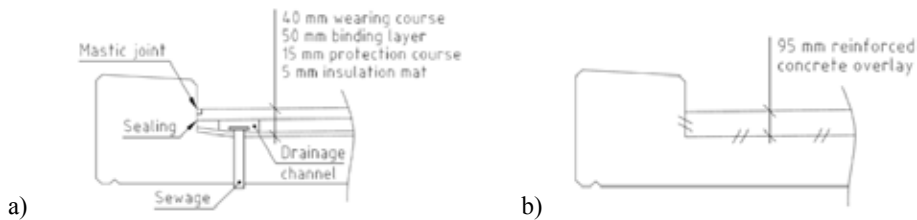


Figure 1 – Typical and common solutions for protection of structural bridge decks by insulation mat etc. (a) and directly cast concrete overlay (b).

alternative is an overlay of concrete cast directly on the structural concrete, Figure 1b. Approximately 500 bridges of a total of more than 11 000 concrete bridges in the regime of Swedish Transport Administration have been provided with the latter solution having reinforced concrete overlays on their bridge decks [1]. However, still, the share of total concrete bridges, using the second solution, is low - about 5%.

The system with directly cast overlays of concrete is environmental friendly; uses no epoxy primers, it is durable, has lower noise levels from traffic, is cost effective; leads to robust structure, has no drainage channels (avoidance of performance problems at construction and no expensive maintenance costs), gives light pavement (i.e. optical advantage) and includes few construction stages. Thus, concrete overlays are considered to be more wearing resistant and by that requiring lower maintenance in comparison to the solution with waterproofing layers and asphalt. Hence, fibre reinforced concrete might be preferred in regions where studded tires are necessary for long time periods or at places where the traffic intensity is high as well as for remote areas regarding recurring maintenance.

Important issues for concrete overlays are general performance with respect to external loads as well as cracking due to shrinkage and/or temperature strain and bond to substrate. The effects of these phenomena are however not fully understood and there is a lack of knowledge regarding performance, design, analysis, construction etc., especially when new types of concrete are used. Thus, the objectives of the newly started Ph.D. project (with support from the Swedish transport administration, Trafikverket) is to secure the performance of concrete overlays for a sustainable structure, i.e. concrete overlays with high durability, low maintenance cost and optimization regarding material consumption and global environmental loads. The project includes laboratory tests, full scale observations and theoretical analysis. This article is focussed on an initial field study.

Observations have been made on 23 bridges built in the 1990's in the north of Sweden [2]. The bridges studied were provided with steel fibre reinforced concrete overlays, poured directly on the newly cast structural concrete. The purpose of the observations were to determine if there was a need to worry about problems such as steel fibres at the surface, surface unevenness and surface cracks. Systematical problems were observed related to production technique, among other things resulting in high density of steel fibres on the surface at the bridge ends [2]. It was concluded that the problems probably were due to the compacting equipment used and

especially the difficulties to manoeuvre it close to the bridge ends. Thus, the concrete was processed manually instead resulting in poor finish.

Another problem reported in [2] are unevenness of the surface i.e. most of the bridges are not fulfilling the Swedish standard VÄG 94 [3]. A consequence might be that grinding the surface becomes necessary. In the context of grinding the surface, the author raise the problem of mechanical processing and risk of inducing undesirable micro-cracks in the overlay. Presence of surface cracks was also observed at some of the bridges.

To check whether the situation above is valid 15 years later and to explore if other types of documentation methods could be used than in the study above (mainly performed by visual inspection), on-site assessment of some of the bridges were initiated during autumn 2013. Thus, the article describes a field study of steel fibre reinforced concrete overlays on two bridge decks with the use of NonDestructive Test methods (NDT). The techniques and equipment used and discussed in this report are well known in Scandinavia and world-wide, see e. g [13] – [15] and the prevailing view is that they give accurate results and are fairly quick and easy to use, giving useful information. In the near future, based on the results of the two field studies, a new investigation will be performed on selected bridges of the ones included in the earlier examination.

2. METHOD

The present study was carried out in August 2013 with the help of a NDT-specialist [4] with a long international experience [13] – [15], often hired as a consultant in Scandinavia. The methods used were an impulse test method - *s'MASH*, thermography imaging and ultrasonic testing with the *Surfer* instrument. Also, visual inspection and drilling core examination were performed.

The bridges studied were one crossing the river Sangisälven, Långbacken, near Haparanda, denoted as A, and one crossing the creek Pierujoki at Pieruvaara, denoted as B. Both bridges are located in Norrbotten, Sweden, approximately 100 km and 200 km north east of Luleå, respectively.

The chosen bridges are in a potential deteriorating state with visible surface cracks. These cracks have been detected and reported earlier in the Swedish Transport Administration maintenance management tool¹ and have been categorized as an effect derived from the hardening process of the overlay for bridge A and due to traffic loading for bridge B. The crack pattern is similar for both the bridges, oriented approximately 40–50° relative its longitudinal direction i.e. the construction line. The purpose is now to evaluate if the NDT systems can detect hidden defects that may induce a crack initiation, resulting in delamination or debonding, as well as estimate the crack depths and widths. Furthermore, the study will give important input to future field studies within the Ph.D. research project.

¹Bridge and Tunnel Management, BaTMan

3. TEST SYSTEMS

3.1 Impulse test method *s'MASH*

The impulse response test method is used for both inspections of steel and concrete structures. However, the application of the methods is more known within the area of steel structures and has not got the similar attention as the impact-echo method [5] for concrete structures. In 2010, ASTM International (American Society for Testing and Materials) published a standard on how to interpret the impulse response when evaluating the condition of concrete structures [6]. An impulse response examination should not be used as a stand-alone tool to evaluate a concrete or a road structure. Hence, the method should primarily be considered as a relative method and should always be supplemented and verified with additional examinations like drilling cores examination, breaking up the concrete with other refined tools and visual inspection.

The impulse response method is utilised as a fast screening technique covering large areas of a structure with the purpose of detecting integrity troubled areas and locating possible defects. Typical information collected on bridges is delaminated and debonded areas, voids in the bridge deck and honeycombed² concrete. However, *s'MASH* does not give any depth indications of defects, hence only relative values of the various parameters can be evaluated for a structure. Thus *s'MASH* only caters for an indication of better or worse areas after calibrations has been done. The instrument may detect defects within a radius of approximately 300 mm from the test point and the maximum depths in which flaws can be detected are 250-300 mm, depending on the circumference of the flaws parallel to the surface tested [4].

The data collection starts with a sledgehammer, with a built in load cell, being struck against the surface creating the bridge deck to respond in a bending mode over a frequency range between 0 and 800 Hz, sampled by a velocity transducer. The use of a velocity transducer, a geophone, is known to be stable at low frequencies and robust in practice and therefore preferred as sampling device [7]. The time record of the impact force and the surface velocity are then processed using a fast Fourier transform algorithm and stored in a lap top. From the spectrum obtained by the Fourier transform algorithm of the hammer force and the velocity, the surface mobility plot is computed as the ratio of the velocity spectrum and the force spectrum, see further details in [5] and [7].

Interpretation of results by means of ASTM [6]:

Average Mobility - a parameter to compare differences in overall mobility among test points in the tested element. It can detect relative flexibility and is a function of plate thickness, concrete elastic modulus, support conditions and presence of internal defects. A higher mobility indicates that the element is relatively more flexible at that test point.

Mobility Slope - A high Mobility Slope has been found to correlate with locations of poorly consolidated (or honeycombed) concrete in plate-like structures.

Peak-Mean Mobility Ratio - A high ratio of the Peak Mobility to the Average Mobility has been found to correlate with poor support conditions or voids.

² Area on a concrete surface or a void inside the concrete that is coarse and stony.

Dynamic Stiffness - An indicator of the relative quality of the concrete, of relative thickness of the member, of the relative quality of the support conditions for suspended structural slabs.

Interpretation of iso-plot colour key for Average Mobility, Peak-Mean Mobility Ratio, and Mobility slope [4]: *White*: No damage, *Green*: No damage *Yellow*: Weak indications of possible damage, *Purple*: Clear indications of damage, *Red*: Clear indications of damage.

3.2 Thermography camera

Thermography imaging has in general a broad range of application areas and has been used for a long time e. g. visualisation of transmitted energy of a house or from defects in electrical installations. In this case the technique is used for the study of a surface layer of concrete. Figure 2 shows example of a concrete bridge deck being examined at its bottom surface aiming at localising delaminated areas. A schematic illustration of how the surface temperature of a bridge might vary for a sound and a damaged structure during a 24 hour cycle is shown in Figure 3.

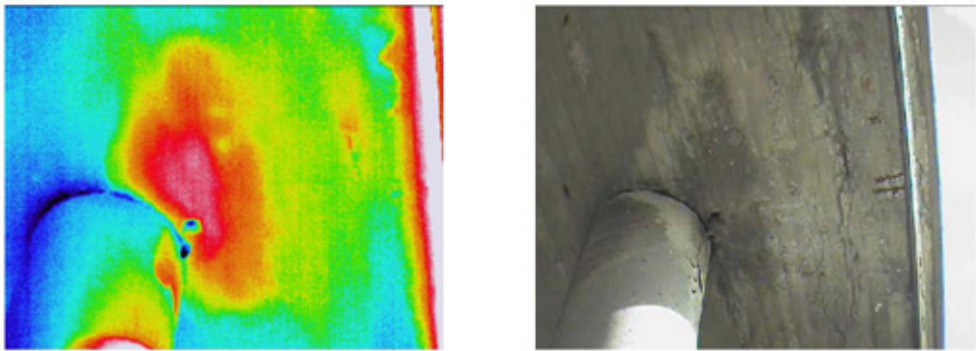


Figure 2 – Example of damaged area around a drainpipe mapped with a thermography camera.

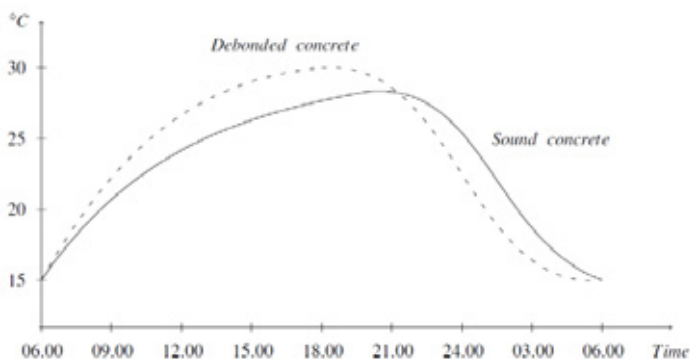


Figure 3 – Temperature variations measured with a thermography camera on the bottom surface of a bridge deck for a delaminated area (In principle) [8].

If the air temperature differs evidently during the day, a difference may be detected between delaminated or debonded areas and the bridge deck. If this temperature difference, is sufficiently

large it can be utilized as a result of estimating the loss of the structural integrity. If, however the daily temperature variations are small one may expect the two lines in Figure 3 to coincide and the risk of gaining zero information is imminent, even though the equipment used has a sensitivity of $\pm 0.05^\circ\text{C}$. It could be noted that this high sensitivity of the instrument might as well be diluted or consumed by the surface texture variation absorbing unequally amount of energy.

3.3 Sound velocity tester *Surfer*

The *Surfer* is an instrument measuring ultrasonic velocity and the time of longitudinal stress wave propagation in a solid material. In the present study, the main purpose using the instrument was to be able to measure the depth of vertical cracks close to the surface. However, the instrument might also have some other interesting features, for instance it caters for the possibility of estimating early-age strength development in concrete see [9]. In principle the instrument records the time it takes for the longitudinal stress wave to travel as a spherical wave front between the transducers located at a distance $L = 150\text{ mm}$. The depth d of a surface crack is given by the time delay of the signal when it is diffracted by the crack tip according to:

$$d = \frac{L}{2} \sqrt{\left(\frac{t_c}{t_p}\right)^2 - 1} \quad (1)$$

Where t_p is the time of propagation between the transducers parallel to the crack and t_c is the time of propagation between the transducers perpendicular to the crack. For this type of instrument the depth measurement range is approximately 10-50 mm.



Figure 4 – *Surfer* in practice (Displaying crack depth $d = 110\text{ mm}$) [9].

4. FULL SCALE OBSERVATIONS

4.1 Bridge data

As mentioned earlier two bridges were studied. The Bridge A is a two hinged slab frame bridge with a free span and width of 16 m and 8 m, respectively, and the frame legs are approximately 6.4 m high, Figure 5. The bridge surface is 141 m^2 and the bridge has four wing walls, almost equal in size, connected to the frame legs at an angel of 45° relative to the longitudinal direction.

Up till now the bridge (built 1994) has undergone some maintenance; however, no rehabilitation regarding the overlay has been carried out.

According to information from BaTMan the overlay on this bridge is a 50 mm thick steel fibre reinforced cement-based concrete overlay cast directly on the main structure without any additional binder or bituminous sealing layer according to present reference standard [10].

Bridge B is also a two hinged slab frame bridge with span and width of 12 m and 7 m, respectively, while the frame legs are approximately 5 m high, see Figure 6. The bridge surface is 98 m² and the bridge has four wing walls, almost equal in size, connected to the frame legs at an angel of 0° relative to the longitudinal direction. Information found regarding maintenance and repair history since completion in 1952 reveals that also this bridge had undergone some adjustments during its lifetime and up to now including a major rehabilitation in 1995 with an overlay exchange. Before 1995 the bridge had a wearing layer consisting of oil-impregnated gravel lying on top of a thin bituminous waterproofing layer. A 50 mm thick steel fibre reinforced concrete overlay was cast directly on a repair-concrete 20-95 mm thick attached on a water jetted surface of the deck. The thickness of the overlay at the centre of the bridge, in longitudinal direction, is 95 mm and 20 mm close to the edge beams. The reference standard valid at the time of rehabilitation was according to [11].

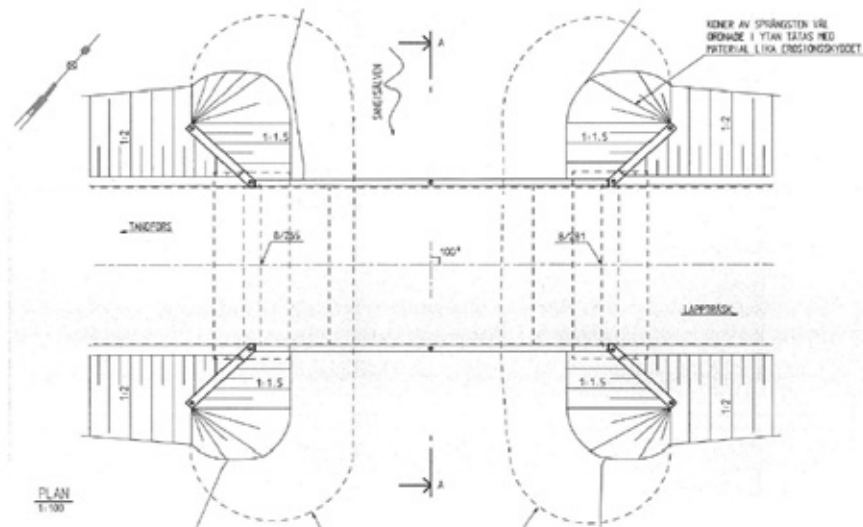


Figure 5 – Plan view of bridge A, near Haparanda.

4.2 Estimation of concrete properties and crack dimensions

Before executing the testing a 1×1 m² grid was created, covering the whole deck surface, see Figure 7. Test points were located at gridline intersections, corresponding to the grid used for the *s'MASH* results in Figure 8(a)-(d). A similar mapping approach was taken when collecting data from the crack dimension estimation. The crack depth and width were then collected with

the *Surfer* while the crack widths also were recorded by a measuring card³. The maximum crack depth and width were collected for each square meter. To be able to handle all the collected data, mean values were calculated based on the visible characteristics of the cracks. Based on crack width and depth the cracks were divided into three groups. These three groups are represented as grey areas visible in Figure 7. The size of the areas was determined by the shape of the crack pattern. The subdivision of the bridge surface also reflects the intensity of the dominating cracks. The cracks in the area on the left had a width in the range of 0.05-0.35 mm and depth of 29 mm. In the middle area the width was in the range of 0.20-0.80 mm and the depth was 30 mm. In the last area, the right part of Figure 7, the width was 0.15-0.60 mm and depth was 26 mm.

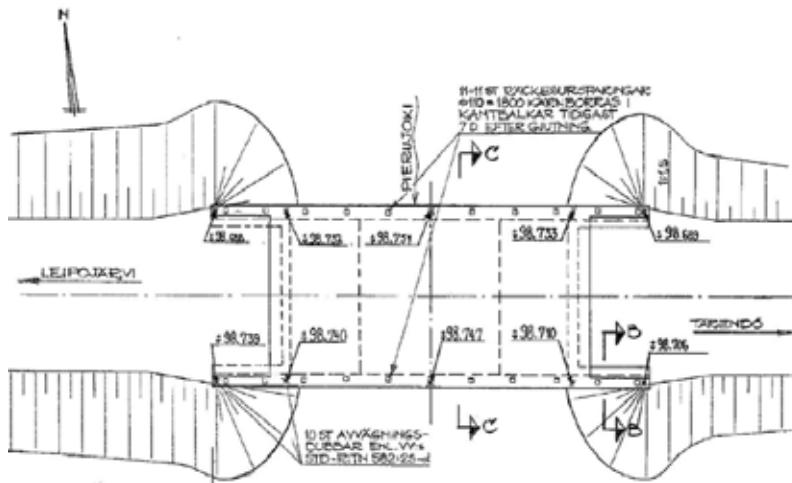


Figure 6 – Plan view of bridge B, at Pieruvaara.

³ A plastic card with a set of lines, with different thickness, used to compare with a crack.

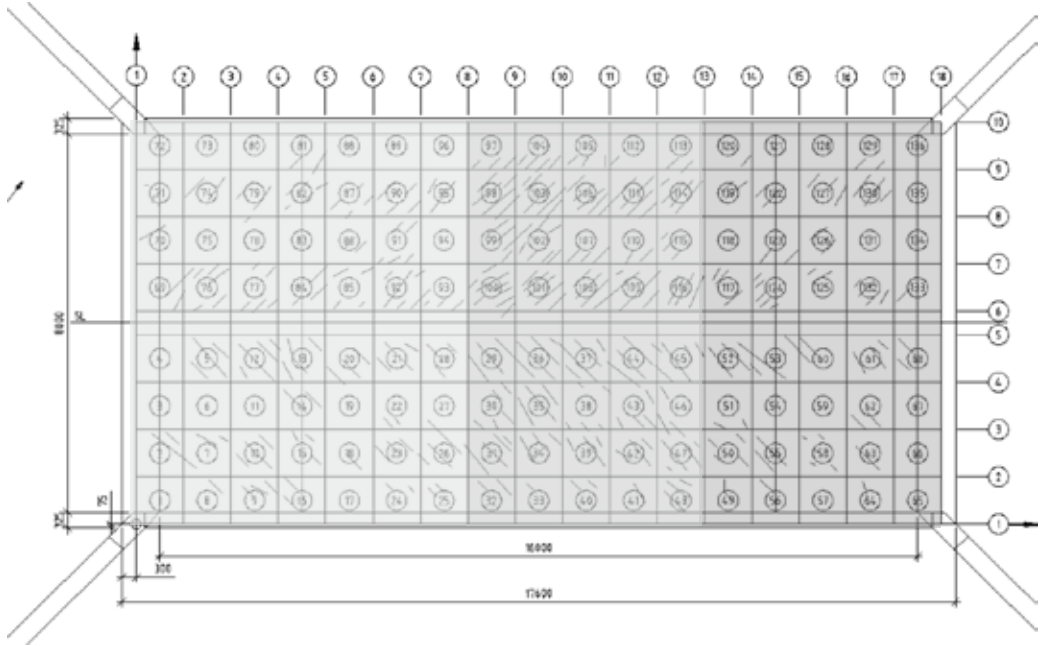
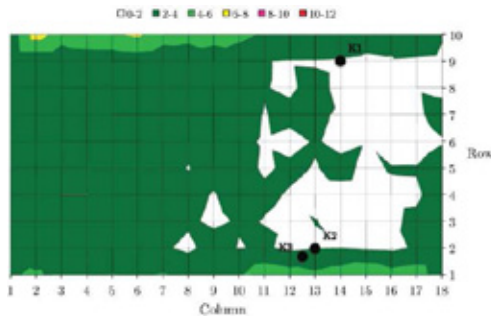
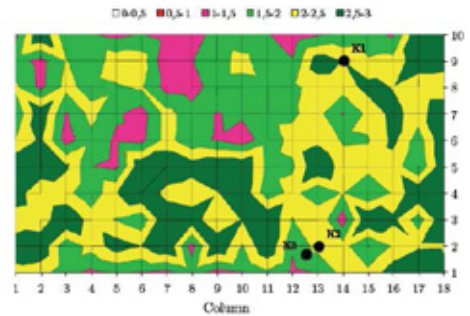


Figure 7 – Mapping of dominating cracks at bridge A. Three areas of crack widths and depths are defined by intensity of grey colour, see the text. No. in circles: testing points.

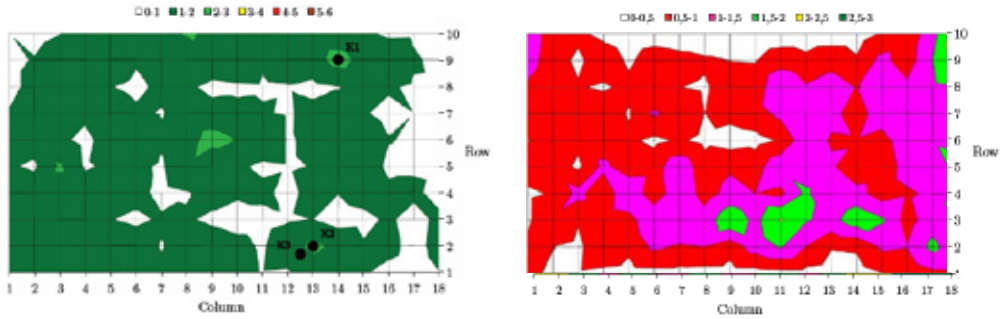
The results of the *s*'MASH-test measurements for bridge A, in Haparanda are shown in Figure 8 and were evaluated based upon the condition of the cores that were drilled out for calibration, see Table 1. Four graphs are shown and three of them were used to evaluate the condition of the bridge slab. Exact depths to flaws that might be detected are not catered for in these types of measurements, which only indicate of whether they are close to the surface or deeper in the deck. Core drilling for calibration of data was done at three locations.



a) Average Mobility, (m/s)/N.



b) Mobility Slope, (m/s)/N/Hz.



c) Peak-Mean Mobility Ratio, unit less.

d) Dynamic Stiffness, N/m.

Figure 8 – s'MASH output data (a)-(d) for bridge A. Interpretation of colours - see Section 3.1.

When evaluating data and determining the extent of damage, the interpretation is based on a standard scale recommended by [4]. Considering the results for this particular bridge slab the scale has been adjusted with the purpose to increase the sensitivity, though the normal scale did not indicate any defects. Since the scale has been adjusted the interpretation of the colours above should be considered with caution. In Figure 8(a) Average Mobility graph is shown indicating that the bridge plate is in good condition and that there are no signs of shallow delamination. In Figure 8(b) Mobility Slope graph is shown and no signs of honeycombed concrete are present. In Figure 8(c) Peak-Mean Mobility Ratio is shown, indicating good support of the overlay, interpreted that the bridge plate is in good condition and the risk of deeper flaws are negligible. In Figure 8(d) the Dynamic Stiffness shows the resulting effect from a combination of parameters such as geometry, quality of concrete and support conditions. No interpretation on Dynamic Stiffness has been made but it will possibly serve as a complementary result in future studies. The areas with the highest Peak-Mean Mobility Ratio selected for cores are located at test point 14;9 (K1) and 13;2 (K2). Core number K3 is located directly above a crack and is used as a calibration core of the depth measurements with the *Surfer*.

The same procedure was utilised at bridge B when categorising cracks and their characteristics. The size of the areas was determined by the shape of the crack pattern as for bridge A, see Figure 9. Cracks in the area on the left had a width of 0.05 mm and depth of 17 mm. In the middle area the width was 0.40 mm and the depth 30 mm and on the right width was 0.10 mm and depth was 17 mm. Two main cracks are present at the overlay of bridge B, distinguished from the other dominating cracks. Their orientation is parallel to the longitudinal direction of the bridge and located at the centre in the transverse direction. The crack to the left goes from 1;4.5 (33 mm) to 4;4.5 (0 mm) and one to the right from 12;4.5 (0 mm) to 14;4.5 (110 mm), see Figure 9.

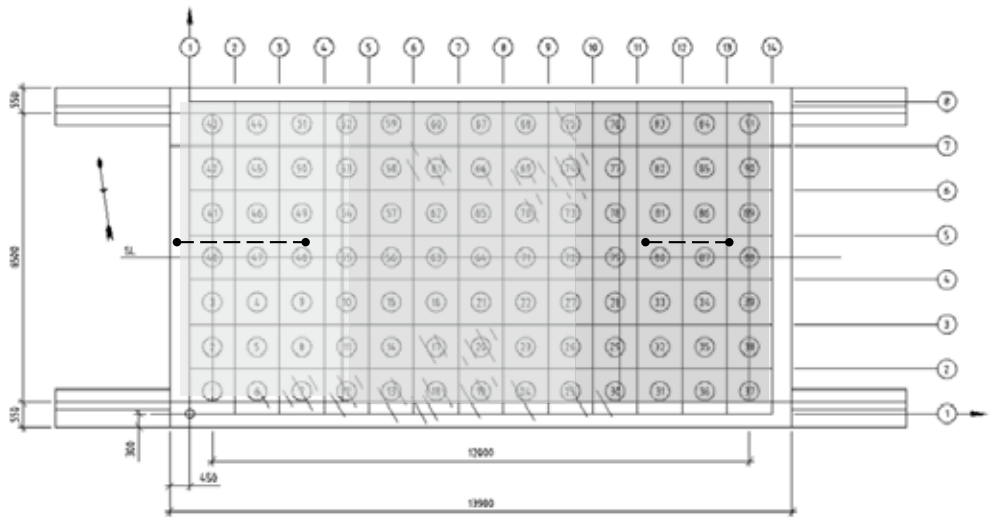
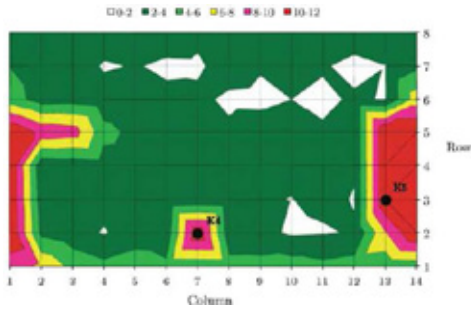


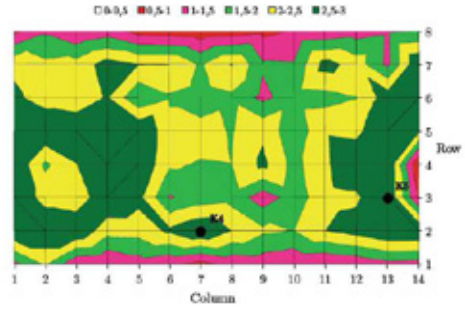
Figure 9 – Mapping of dominating cracks at bridge B. Three areas of crack widths and depths are defined by intensity of grey colour, see the text. No in circles: testing points. Two dominating cracks indicated by dashed lines.

The s'MASH-test measurements in Figure 10 were evaluated based upon the condition of the cores drilled out for calibration in the same manner as for bridge A, see K4 and K5 in Table 2.

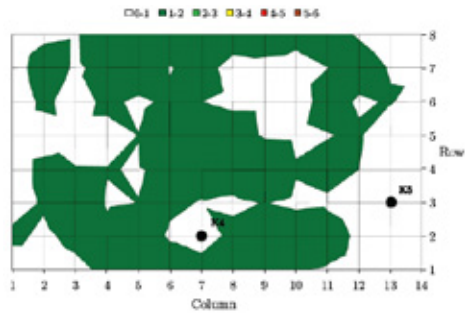
Data on Average Mobility, Figure 10(a), shows that the bridge plate is in a possible deteriorating state, with fairly large indications of debonding or delamination at both bridge ends, as well as at one location in the middle denoted 7;2 (beneath K4). The effect from the longitudinal crack on the west side is clearly visible. However, the crack on the east side is not that clear due to the surrounding delaminated area. Core K4 is located directly above a crack and is used as a calibration core of the depth measurements with the *Surfer*. In Figure 10(b) the Mobility Slope graph shows no signs of honeycombed concrete. The Peak-Mean Mobility Ratio graph, Figure 10(c), shows that the bridge plate is in good condition in general and the risk of voids is negligible. The Dynamic Stiffness of the structure shown in Figure 10(d) is influenced by a combination of parameters, such as geometry, quality of concrete and support conditions. Interpretation on the Dynamic Stiffness has not been made, but it will possibly serve as a complementing result in future studies.



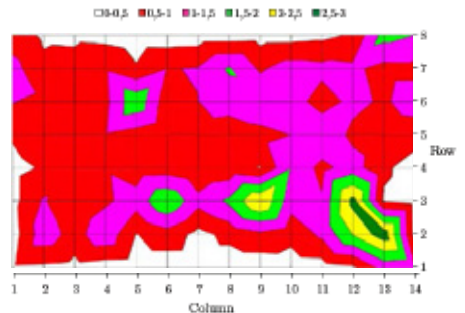
a) Average Mobility, (m/s)/N.



b) Mobility Slope, (m/s)/N/Hz.



c) Peak-Mean Mobility Ratio, unit less.



d) Dynamic Stiffness, N/m.

Figure 10 – *s'MASH* output data (a)-(d) for bridge B. Interpretation of colours - see Section 3.1.

4.3 Detection of cracks and flaws with thermography

Due to poor weather conditions at the time of the testing the infrared camera did not perform very well. It had been raining just before the examination, of bridge A, and the temperature variation during the last 24 hours had been less than 10-15 °C, which was not enough to give a clear indication. Based on the resulting data from the *s'MASH*, the expectations of finding flaws was fairly small anyway. Due to some logistic related problems the cores were drilled on 20th instead, now the weather was dry and the sun was shining at the location of the Haparanda bridge. The infrared camera was now tested once again, thus under new conditions. A selection from the result is shown Figure 11. No hidden defects were found, just surface related anomalies such as close to surface aggregate, missing aggregate in the surface and surface cracks you would be able to see anyway.

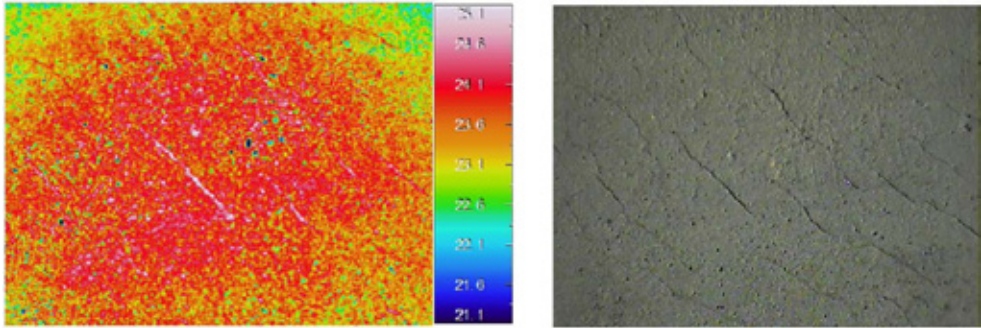


Figure 11 – Thermography plots, south side of bridge A (left). Hot spots in cracks and where aggregates are missing, as well as cold spots due to coarse aggregate close to the surface are shown. Typical crack pattern (right).

The conditions for using the infrared camera were also poor when testing the bridge B at 20th of August 2013, with a daily variation of temperature of less than 10–15 °C. However in Figure 12 the thermography camera seems to be able to detect the debonded area and the reason for it is probably due to its relatively shallow location. Based on the resulting data from the s'MASH the expectation of finding flaws was fairly good due to the debonded areas. No hidden defects were found, just surface related anomalies like the ones reported at bridge A, with the exception of the locally debonded area under K4.

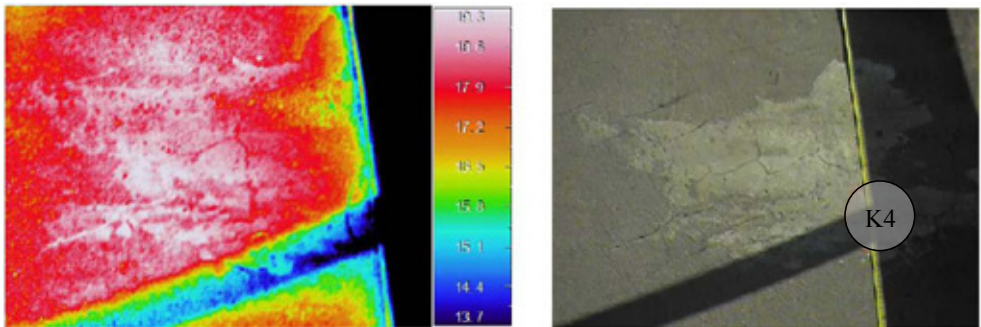


Figure 12 – Thermography plots, south side of bridge B (left). A smeared hot spot can be seen over a non-successful repaired area. Core K4 was taken here. A measuring tape was used to determine the position of the core and is visible as a yellow line. Typical crack pattern (right).

4.4 Core tests

The results from the drilling cores are shown in Table 1 and Table 2 with comments and analyses. Five core samples were taken, three at bridge A and two at bridge B.

Table 1 – Drilling cores (K1-K3) taken at bridge A




Id.	Core	Expectation
K1		Minor risk of small cracks deep in the concrete
		Condition
		Core intact in general. Steel fibre visible to a depth of 70 mm. A flat iron visible at bottom of the hole. A slightly high Peak-Mean Mobility Ratio indicates a void close to the flat iron or due to the flat iron itself, probably used for fixation of reinforcement bars.
Id.	Core	Expectation
K2		Minor risk of small cracks deep in the concrete
		Condition
		Core intact. No signs of internal defects in the core. Steel fibre visible to a depth of 70 mm. A slightly high Peak-Mean Mobility Ratio might indicate a void close to the reinforcement bar at the bottom of the core.

Table 2 – Drilling cores (ctd)

Id.	Core	Expectation
		Core taken above a crack to cater for the possibility of making a petrographical testing to evaluate the age of the crack
		Condition
		Depth of crack approximately 50 mm and 0.25 mm wide. Steel fibre visible to a depth of 70 mm. Concrete below wearing layer was intact, i.e. no propagation of the crack.

5. DISCUSSION

In general both bridges seemed to be working as expected in terms of cleanliness, i.e. only some gravel along the edge beams, and drainage. Although frictional or roughness measurements not were made, an engineering judgment on the frictional characteristics was performed and the observers contention is that both bridge decks surfaces do not suffer from frictional problems when interacting with rubber tires. Some indication of rutting⁴ was visible in the sense of differential surface texture that might have some impact on the frictional characteristics, however, only visible during certain light conditions. More interesting is that the inspection showed a macroscopic crack pattern, with a spacing of 100 mm, mainly oriented 40-50° relative to the longitudinal direction for both bridges, however mirrored at the longitudinal centre line for bridge A. The crack pattern was relatively distinct at bridge A, where the overall mean crack width was 0.36 mm with good bonding recorded, see Figure 13.

⁴ Groove in the wearing surface made by passage of vehicles.

Table 3 – Drilling cores (K4-K5) taken at bridge B.



Id.	Core	Expectation
K4		Core taken above a crack with the intention to verify the crack depth d measured with the SURFER.
		Condition
		Crack depth approximately 28-30 mm, equivalent to the thickness of the wearing layer at this point. Concrete below the wearing layer was intact i.e. no propagating crack. Bituminous material visible at both surfaces of the crack.
Id.	Core	Expectation
K5		Risk of minor cracks of poor bonding between the substrate and the wearing layer.
		Condition
		Core intact after coring, however, fairly easy to break. Bonding between wearing layer and substrate was weak. Thickness of wearing layer approximately 140 mm. Presumably bituminous materials visible at the crack surfaces (small brown spots). Additional reinforcement visible 110 mm below surface.



Figure 13 – North side of bridge A at mid-span. Macroscopic crack pattern mainly oriented 40-50° relative to its longitudinal direction.

A variation of crack widths were visible, however the depths were relatively constant. A constant crack depth was expected since the thickness of the overlay probably is more or less constant over the bridge deck surface, this based on structural drawings and the cores K1, K2 and K3. The variation in crack widths might be explained by a poor distribution of steel fibres or by the irregular geometric conditions; i.e. the slab has different thickness, although this may be unlikely. At the bridge ends the crack pattern was a bit more randomised with visible steel fibres at the surface.

Even though the cracks are randomised as well as diagonal the cause might be explained by plastic shrinkage in both cases. For roads and slabs associated with diagonal cracks the primary cause is rapid early drying, and the resulting effect is then plastic shrinkage, the same implies for the randomised cracks for reinforced concrete slabs according to [12].

In contrary to bridge A, the crack pattern on B was not that distinct, however, clearly visible for the naked eye. The dominating cracks at bridge B have approximately the same orientation, however, not mirrored at centre and they may be a bit more inclined for this bridge.

The variation in crack widths is slightly more distinct at this bridge. Steel fibres were also found at the bridge ends close to the surface. As mentioned before it might have something to do with a poor distribution of steel fibres or the irregular geometric conditions, i.e., the frame is haunched approximately between 1 and 5 as well as for 10 and 14, see Figure 10. The greatest difference in crack characteristics between the bridges are definitely the longitudinal cracks at the bridge ends at B and the non-mirrored pattern which might have been induced by traffic loading. To be able to consider the latter a petrographical test would be of interest to determine the age of the crack as a first approach.

6. CONCLUSION

The method used for mapping crack widths and crack depth is rather time consuming in relation to the time needed for the overall inspection, including *s'MASH*, thermography and other documentation such as taking photos. The method is thus more suitable when measuring a couple of selected cracks and not for hundreds. In terms of accuracy of the results for the two techniques used, *Surfer* and traditional measuring card are assumed to be good enough for this type of inspection and provide fairly reliable results.

In general, using *s'MASH* as a technique for detecting flaws like debonding, delamination or honeycombing in concrete structures is a rather rational approach. The results, however, are not straight forward to interpret without previous experience of testing such structures. One should be aware of the result scale since it is a relative measurement, and in general only valid for the specific structure or component investigated and should thereby always be verified via, at least, one core sample. As in most of the cases when operating on roads, time is of essence so to be able to determine where to take the cores you must be able to analyse the data on site.

Due to the difficulties in predicting the weather the thermography camera is not well suited for this type of inspection with instant information sampling. The required temperature variations, 10-15°C in 24 hours as mentioned above, is not that easy to fulfil, especially for the upper part of the slab, and is therefore not an alternative in further surveys. Another way to use the thermography camera, despite poor temperature variation, might be to sample pictures over time rather than just instant pictures as in this survey. Having a larger set of data, in the format of

time-history, for a specific area one might have a greater rate of success when evaluating the thermography data. The idea is that the first picture would then represent reference data for the next picture, and so on. One could possibly argue stronger and be able to compare thermography data with the other types of measurements using this latter approach.

All of the three test methods used in this article are to some extent subjective methods and should thereby be interpreted by the reader in the light of a strive to build a knowledgebase within the field of nondestructive testing.

The conclusions and experience above will serve as a base for selection of methods in future field tests of the Ph.D. research project e. g. supporting future theoretical analyses and model developments.

REFERENCES

1. H. Sundquist.(editor). "Robustare brobaneplatta, State-of-the-art och förslag till FUD program". Sveriges Bygguniversitet, 2011. (In Swedish)
2. M. Lindquist. Direktgjuten slitbetong på broar – en uppföljning av de broar som har byggts med direktgjuten slitbetong sedan 1992. Vägverket, avdelning teknik, Luleå,115 sidor., 1998 (In Swedish).
3. Vägverket Publ 1994:87 "Allmän teknisk beskrivning för vägar", VÄG 94, Cementbundna lager.
4. Jesper Stærke Clausen, NDT specialist, (personell contact), InSitu Test ApS, Emdrupvej 102, 2400 Copenhagen NV, Denmark.
5. Allen G. Davis Niels Saabye Ottosen, Matti Ristinmaa. Theoretical Interpretation of Impulse Response Tests of Embedded Concrete Structures. Journal of engineering mechanics, 130(9):1062–1071, 2004. ISSN 0733-9399. doi: 10.1061/(ASCE)0733-9399(2004)130:9(1062).
6. ASTM. ASTM Standard C1740-10, 2010, "Standard Practice for Evaluating the Condition of Concrete Plates Using the Impulse-Response Method". West Conshohocken, PA, 2010, DOI: 10.1520/C1740-10, www.astm.org, 2010.
7. Allen G. Davis. The nondestructive impulse response test in North America: 1985 – 2001. NDT E International, 36(4):185 – 193, 2003. ISSN 0963-8695. doi: [http://dx.doi.org/10.1016/S0963-8695\(02\)00065-8](http://dx.doi.org/10.1016/S0963-8695(02)00065-8).
8. Infratech Data Sheet No.1 "Concrete Delaminations", The Old Forge, Marston Magna, Yeovil, Somerset, BA22 8BZ.
9. GI. NDT Systems. Germann Instruments A/S, Emdrupvej 102, DK-2400 Copenhagen, Denmark, 2010.
10. Vägverket Publ 1988:6 "Allmän teknisk beskrivning för broar", Bronorm 88, Brodetaljer.
11. Vägverket Publ 1994:6 "Allmän teknisk beskrivning för broar", BRO 94, 6. Brodetaljer.
12. A.M. Neville and J.J. Brooks. Concrete Technology. Prentice Hall/Pearson, 2010.
13. Clausen J et al, "Monitoring of Ageing of Concrete Containments Based on Conditions Assessment by Means of Non-Destructive Testing Methods and Finite Element Analysis" International Conference, SMiRT 19, Toronto, 2007
14. Clausen J et al, "Inspection of Masonry Arch on Railway Bridges with Impact-Echo and Impulse Response, Structural Faults & Repair, 3rd – 5th July, 2012, Royal College of Surgeons, Edinburgh
15. Clausen et al, "Non Destructive Testing of Bridge Decks and Tunnel Linings using Impulse-response", 10th ACI International conference, Seville, 2009

Mineralogical, Physical and Chemical Characterization of Cementitious Materials Subjected to Accelerated Decalcification by an Electro-Chemical Method



Arezou Babaahmadi
PhD candidate
Division of Building Technology (Building Materials)
Chalmers University of Technology
S-412 96 Gothenburg, Sweden
arezou.babaahmadi@chalmers.se



Luping Tang
Professor
Division of Building Technology (Building Materials)
Chalmers University of Technology
S-412 96 Gothenburg, Sweden
tang.luping@chalmers.se



Zareen Abbas
Associate Professor
Department of Chemistry
University of Gothenburg
Kemivägen 4, SE-412 96, Gothenburg, Sweden
zareen@chem.gu.se

ABSTRACT

To facilitate the service life predictions regarding durability of nuclear waste repositories acceleration methods enhancing the decalcification process are needed. In this study an electro-chemical migration method to accelerate leaching of calcium from cementitious specimens of sizes 50×100Ø and 75×50Ø mm is presented. The mineralogical, physical and chemical properties of degraded samples are characterized. The results demonstrate that up to 70% decrease in strength, 50 % decrease in E-modulus, 90 % increase in gas permeability, at least 70% increase in chloride diffusion coefficient and 70 % increase in pore volume could be expected due to leaching of portlandite from concrete.

Key words: Acceleration method, Calcium leaching, Service life, Mineralogical properties, Diffusion, Adsorption, Mechanical Properties, Permeability

1 INTRODUCTION

Exchange of ions between cementitious materials and the surrounding environment due to concentration differences will result in dissolution or precipitation of minerals, and

consequently alteration in the microstructure and composition of the cementitious materials. One of the important factors in this process is the long-term contact between the concrete barrier and the surrounding groundwater [1, 2]. In concrete calcium hydrates are the major portion of hydrated cementitious material whilst the repositories are surrounded with low calcium content groundwater. As calcium leaching is a dissolution/diffusion governed transport process, decalcification will proceed, due to the calcium concentration gradients [3].

In repositories of nuclear waste where concrete is used in the engineered barriers to prevent the release of radio nuclides, detailed understanding of how the properties of the material are developed over the entire operational life of the repository is required. Of particular importance are the mechanical, physical and diffusion/adsorption properties of the degraded materials.

To account for the long term effect of degradation on properties of cementitious materials used in nuclear waste repositories several studies are reported in the literature regarding leaching of calcium from cementitious materials based on immersion of the solid cementitious specimens in water or enhancement of the decalcification process with acceleration methods [4-15]. However, although several conclusions can be drawn from these studies regarding the properties of aged cementitious materials these types of experiments are either very time consuming due to the slow kinetics of the decalcification process or small sample sizes should be implemented which limits further examination of the mechanical properties of the samples or their diffusivity. In addition it should be noted that there are not many studies reported in the literature with implication of concrete samples [16-19] of proper size rather paste specimens or powder samples have been used [4-7, 9, 10, 12-15, 20-22].

Moreover, although the common feature for both natural and accelerated leaching scenarios will be a total dissolution of portlandite and a significant decalcification of the CSH phases, other effects of the aging processes may differ considerably between specimens aged by different acceleration methods and comparably natural leaching methods. This emphasizes on the importance of reproducing accelerating tests and characterizing the aged samples to account for the comparability of the ageing function of different methods in order to produce databases with low variability and less uncertainties demonstrating properties of degraded cementitious materials.

It should be noted that in any acceleration method some involved processes may not be present in the natural situation. Characterization of the material after application of the accelerated method is of high importance in order to show the comparability as well as to build up a better base for further investigations.

Furthermore, as the rate of diffusion through concrete not only depends on molecular diffusion in pore solution, but also on the porosity and sorption properties of the cementitious materials, within assessments of diffusion properties of degraded cementitious specimens the changes in pore structure and adsorption properties should also be considered. As presented by Ochs et al. [23] an increase in sorption properties of degraded cementitious materials is expected after degradation, specifically for Cs ions. However, in general the available information in the literature regarding the sorption properties of cementitious materials exhibit a large variation and uncertainty due to considerable differences in the composition of the cementitious specimens which emphasizes on the importance of adsorption tests in parallel with investigations regarding diffusion properties. In addition, although combined effect of porosity, adsorption and molecular diffusion is of high importance, but available literature data on

adsorption have mostly been obtained from studies on powdered hydrated cement paste excluding the effect of changes in porosity and molecular diffusion.

All these implies that effective acceleration methods with comprehensible kinetic, simulating the calcium leaching process for specimens with a size suitable for further mechanical or physical tests are required. In this study a newly developed acceleration method simulating the leaching of calcium from cementitious materials is presented. The gradual changes of the physical, chemical and mineralogical properties of the samples are followed with the progress of the leaching process. Further, the diffusion properties of solid specimens of cement paste are investigated and the physical properties such as porosity, pore size distribution and specific surface area of decalcified samples are studied and compared with the untreated reference material. Moreover, the diffusive characteristics of Cs^+ , Na^+ and Li^+ ions are accounted for by means of a diffusion cell test and the adsorption characteristics for Cs^+ ions, as exhibiting no solubility limitation and only weak retention by fresh hydrated cement paste [23], is considered for both fresh and aged cementitious materials. Finally, the changes in mechanical and physical properties of solid concrete specimens are presented and the following properties have been studied: tensile strength, elastic modulus, permeability and water adsorption. In addition, the chloride diffusion coefficient of concrete samples has been studied in order to give an indication of the transport properties of the specimens.

2 MATERIAL AND METHODS

2.1 Specimen Preparation

In this study, all solid specimens were manufactured from pure cement paste and water in order to facilitate chemical and mineralogical analysis of the specimens. The paste specimens were casted from a mixture of Swedish structural Portland cement for civil engineering (CEM I 42.5N BV/SR/LA) and deionised water at a water-cement ratio of 0.5. The chemical composition of the cement is listed in Table 1. Fresh cement paste was cast in acrylic cylinders with an internal diameter of 50 mm and a length of 250 mm. The cylinder's ends were sealed with silicone rubber stops. The cylinders containing fresh paste were rotated longitudinally at a rate of 12-14 rpm for the first 18-24 hours of hydration to homogenize the paste, after which the rubber stops were removed and the ends of the cylinders were sealed with plastic tape in order to produce specimens with a homogeneous composition and structure. The specimens were stored for over 6 months in a moist plastic box and then cut to cylinders with the size of $\text{Ø}50 \times 75$ mm for use as specimens in the experiments. In order to prevent carbonation, saturated lime water was used at the bottom of the plastic box. The initial calcium and silica contents in the cement paste specimens presented in Table 2 were calculated with the assumption that the composition of CSH corresponded to $\text{C}_3\text{S}_2\text{H}_3$.

Table 1. Chemical characteristics of Swedish CEM I 42.5N BV/SR/LA

Chemical formulation	CaO	SiO ₂	Al ₂ O ₃	Fe ₂ O ₃	MgO	Na ₂ O	K ₂ O	SO ₃	Cl
Weight Percentage	64	22.2	3.6	4.4	0.94	0.07	0.72	2.2	0.01

Table 2. Initial calcium and silica contents in a cement paste specimen (Considering $C_3S_2H_3$ as the composition of CSH)

Total	Component	mole/gr paste	mole/specimen*
Calcium content	CSH	0.0044	1.02
	CH	0.003	0.68
	Other hydrates	0.0018	0.41
	Total	0.0092	2.11
Silica content	CSH	0.003	0.68

*Approximately 230 g paste/specimen

The Concrete specimens used in this study were cast using Swedish structural Portland cement for civil engineering (CEM I 42.5N BV/SR/LA) and crushed aggregates with maximum size of 16 mm. The specimens were casted in cylinders in two different sizes of Ø100×200 mm and Ø50×250 mm with two different water cement ratios. The ratios are decided according to the properties of the concrete used in The Final Repository for Short-lived Radioactive Waste, SFR, in Sweden [24, 25], Table 3. It should be noted that SFR consists of several parts with respect to the radioactivity level of the waste, the Silo (intermediate waste), BMA (intermediate waste), 1BTF and 2BTF (dewatered ion exchange resins) and BLA (low level waste) are the included parts. The observations from the slump test prior to casting was 25 mm slump for the concrete with W/C=0.48 and 35 mm for W/C=0.62. The specimens were cured in saturated lime water for more than 3 months after which they were stored for over 3 months in a moist plastic box and then cut to cylinders with the size of Ø50×75 and Ø100×50 mm to be used in electrochemical migration method.

Table 3. Properties of concrete used in SFR repository located in Forsmark

Properties	Silo ¹⁾	BMA ²⁾
Cement type	Swedish structural cement	Swedish structural cement
W/C	0.48	0.62
Cement content kg/m ³	350	300

1) Based on Emborg et al. 2007 [26] but with symmetrical deviation of 48±5 MPa in compressive strength instead of 43-58 MPa with mean 48 Mpa.

2) Estimated based on the previous Swedish concrete class K30.

2.2 Materials and Methods

The experimental set-up of the electrochemical migration method is inspired by the rapid chloride migration test developed by Tang, Figure 1 [27]. In this method, the specimen was placed between two electrolyte solutions providing a porous medium for ion migration. Specimens of size Ø50×75 and Ø100×50 were used. The curved surface of the specimen was

sealed using an asphalt tape which was extruded up to 2-3 times longer than specimen's height providing an empty volume of about 200 ml as the anolyte container. A plastic box with the capacity of 30 liters was used as the catholyte container. The anode was made of a titanium mesh which was equipped with a plastic support preventing direct contact with the specimen. The cathode was made of stainless steel which was mounted on a plastic support in a similar way as described in NT BUILD 492 [28]. The cells were connected to an external potential supplier with adjustable current and potential. In order to avoid a temperature-induced mechanical destruction of the specimen due to the Joule effect the current applied to the specimen was controlled. The choice of electrical current was based on the findings by Babaahmadi et al [29] showing that a constant current of 250 mA was suitable for a paste specimen of size $\varnothing 50 \times 75$ mm and also taking into consideration that the paste fraction of the concrete specimens used in this study and in which the leaching takes place was 30 percent of the total volume, Table 3.

Ammonium nitrate solution was used as catholyte solution in order to dissolve the calcium hydroxides and Lithium hydroxide solution was selected as anolyte solution. This was motivated by the fact that the Li^+ ions do not exist in the pore solution. Moreover, Li^+ ions with a crystallographic radius of 0.07 nm, have a high surface charge density and therefore they are strongly hydrated in water and acquire a large size [30]. The thick water layer around Li^+ in a solution will reduce the tendency for diffusion or migration and consequently will also reduce any competing potential in migration with calcium ions. Furthermore, with application of a hydroxide salt of lithium, the produced H^+ ions at the anode were neutralized and localized acidic characteristics in the anolyte solution with corrosive effects on the specimen were prevented.

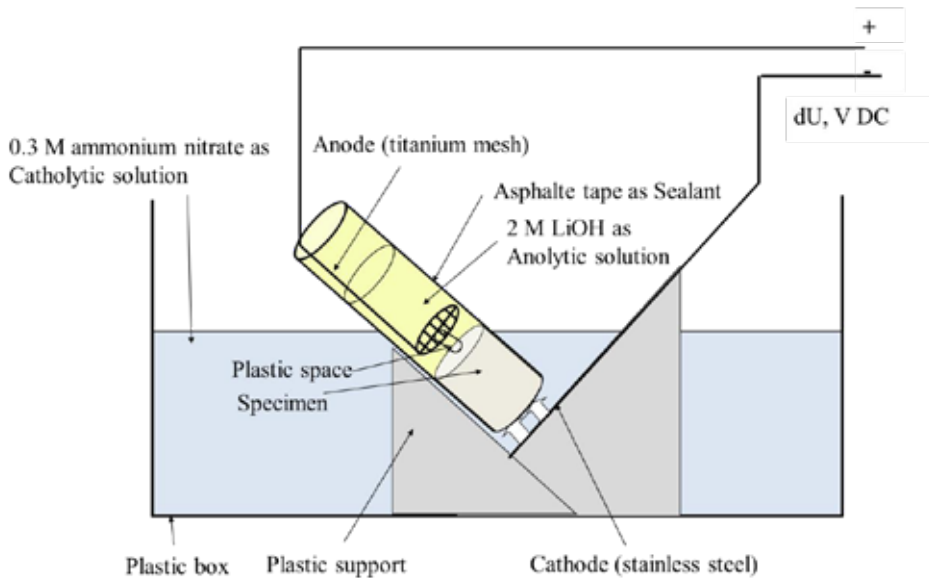


Figure 1. Setup design of electrochemical migration test

In order to maintain the pH level in the catholyte and anolyte solutions as well as to compensate for the consumed ions (OH^- ions in the anolyte solution and H^+ ions in the catholyte solution),

the solutions were frequently recharged. The quantities of the salts required for recharging were calculated according to the Faraday's rule of electrolysis as given in Equation (1).

$$I \cdot t = F \cdot z \cdot \left(\frac{m}{M}\right) \quad (1)$$

where, I : Current (A), t : time (seconds), F : Faraday number = 96485 C/mol, M : Molecular mass of substance (g/mol), m : mass of substance (g) and z : the valance number of ions.

With the application of a current of 250 mA, approximately 20 grams of ammonium nitrate and 6 grams of lithium hydroxide per specimen were needed to recharge the catholyte and anolyte solutions, respectively, for every 24 hours. When the current was set to 80 mA the catholyte solution was instead recharged with same amount of chemicals every 3rd day. The experimental time was set to approximately 6 weeks in order to reach to complete leaching of portlandite content as concluded by Babaahmadi et al. [29]. It should be noted that for the specimens with W/C=0.62 the experiment was terminated faster than for the specimens with W/C=0.48 as the portlandite content differs.

2.3 Instrumental analysis

To quantify the content of charged substances in the catholyte solution, Ion Chromatography (IC) was utilized. An IONEX (ICS 900) Ion Chromatograph was used in this study. Using this instrument the ions of interest were detected typically by conductivity or UV/visible light absorbance. The samples were injected in to the instrument with an auto-sampler. Moreover, the gradual change in the calcium concentration in the catholyte solution was analyzed by potentiometric titration on Metrohm Titrator 702 SM Titrino, using a calcium selective electrode and 0.1 N EDTA-solution as titrant.

Characterization of the crystalline phases in the solid samples was performed with X-Ray Diffraction (XRD) analysis. A Siemens D5000 ($\text{CuK}\alpha = 1.5418 \text{ \AA}$) X-Ray diffractometer, equipped with Gobel mirror was used. The measurements were carried out by using 0.050° per step and at a time step of 2 s. The powder sample was prepared by crushing and grinding the solid sample in a mortar while immersed in ethanol and vacuum drying after grinding. For each analysis 0.5 grams of the powder placed on a thin-walled glass sample holder was used. The results were calibrated using 0.05% mass of Si powder as standard.

Line scans quantifying the longitudinal changes in Ca/Si ratios of solid samples were performed by Laser Ablation- Inductive Coupled Plasma- Mass Spectrometry (LA-ICP-MS). Laser Ablation analysis was performed using a New Wave NWR213 laser ablation system coupled to an Agilent 7500a quadrupole ICP-MS (upgraded with shield torch and a second rotary vacuum pump). A 30 micron laser spot size, beam energy density of ca. 6 J/cm² and repetition rate of 10 Hz was used in line scan mode (scan speed 100 $\mu\text{m/sec}$).

The surface topography and elemental composition of the solid samples were analyzed with Scanning Electron Microscopy (SEM). A FEI Quanta ESEM 200 equipped with field emission gun and Oxford Inca EDX system was used to perform the analysis. Thin cubes of the solid sample of about 20×10 mm, thickness of 10 mm were used. The samples were vacuum dried prior to analysis. It should be noted that in order to prevent the samples from carbonation they were neither polished nor coated which may cause charging effects in the results as well as uncertainties due to uneven surface of the sample. The analyses were performed in high vacuum

mode and in 9-12 mm working distance. The reference sample and aged samples with different degrees of leaching were selected for the analysis.

The pore size distribution was studied with Mercury Intrusion analysis, using Micrometrics, Auto pore 9500 with a 5 ml penetrometer. Also the Brunauer-Emmett-Teller (BET) specific surface area was measured by N_2 adsorption with a Micrometrics, TriStar 3000.

2.4 Diffusion/Adsorption tests

The diffusion properties of the reference and the aged specimens were investigated for 0.5 M and 0.05 M solutions of LiCl, NaCl and CsCl respectively.

Conventionally, diffusivity of ions in a porous material is measured using a natural diffusion cell test at a certain concentration gradient [31]. Typically, two solution containers (cells) are separated by a slice of the specimen. The cell filled with a solution containing the ions of interest is called the upstream cell and the other cell, which is usually filled with deionized water, is called the downstream cell. Due to the concentration gradient between the cells, diffusion of ions through the specimen is always from the upstream cell to the downstream cell.

As shown in Figure 2, a paste specimen of $\varnothing 50 \times 15$ mm was assembled in the central part of the silicone rubber tube and kept in position with a clamp of stainless steel. Cells made of Plexiglas tube were attached to the ends of the silicone rubber tube using a clamp of stainless steel on each end of the tube. The upstream cell was filled with 250 ml of a selected solution and the downstream cell was filled with 250 ml of deionised water. A rubber stop was used to close the cells in order to prevent evaporation and carbonation. 10 ml of sample was taken from the downstream solution approximately every 10 days (replaced with deionised water) and chemically analyzed with Ion Chromatography in order to account for accumulated ionic content (Q_{ion}), diffused through the specimen, against time ($Q_{ion}-t$ curve). The experiment was terminated when a linear relationship observed from the $Q_{ion}-t$ curve, which was an indication of the steady state flow.

Moreover, in order to analyze the adsorption properties, reference and calcium leached paste specimens prepared according to the methods described in sections 2.1 and 2.2 respectively were hand crushed and powdered in a mortar. 3 grams of the powder was mixed with 30 ml of CsCl solutions with approximate concentrations of 0.3, and 5 ppm respectively in separate plastic tubes in a glove box filled with nitrogen gas in order to prevent any carbonation. The solutions were mixed by placing the tubes in a rotating chamber. The Cs concentration in the solutions was determined after 2 and 6 weeks with ion chromatography.

2.5 Mechanical tests

Splitting test

The tensile strength of the leached and reference materials was measured using a Toni-Technik compression testing machine with a maximum capacity of 100 KN. The concrete sample of size $\varnothing 100 \times 50$ mm was loaded across its vertical diameter. Plywood strips were inserted between the concrete cylinders and the top and bottom plates of the equipment to ensure homogeneous loading. 2 specimens representative for each W/C-ratio and each degradation state were tested to ensure reproducibility of the results.

Elastic Modulus

Elastic modulus of the specimens was obtained as the slope of stress-strain curves recorded by means of an ALPHA compression testing machine, Figure 3. The load cell had a maximum capacity of 50 KN and was loaded with a mechanical press at a constant rate of 0.01 KN/millisecond. The vertical stress was measured utilizing a calibrated LVDT (Linear Variable Differential Transformers) sensor. The end surfaces of the specimens, perpendicular to the longitudinal axis of specimen, were cut with a diamond saw and polished in order to have a smooth surface. The concrete specimens of the size $\text{Ø}50 \times 75$ mm were placed between two platens and positioned under the load cells. 4 LVDT sensors were used to measure the displacement of the bottom platen and 3 more sensors were employed to measure the displacement of the upper platen. The sensors were connected to a data-log system to record the gradient of strain as a function of stress. The calcium depleted samples were kept in 100% RH until being tested in order to avoid any internal cracks.

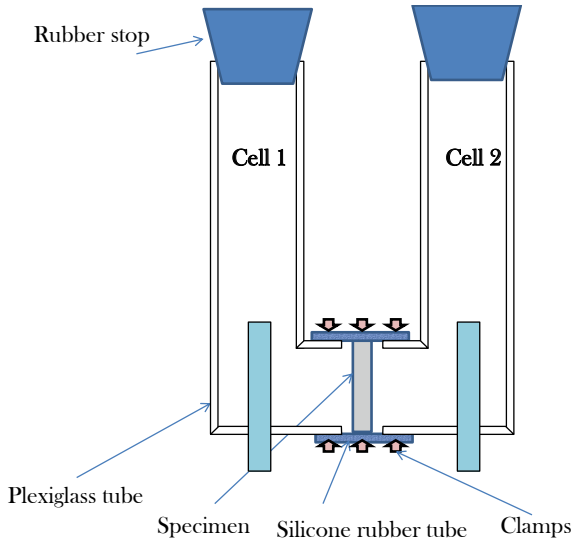


Figure 2. Diffusion cell test setup

2.6 Gas permeability and capillary water adsorption

The gas permeability and capillary water adsorption tests were performed according to state of the art report of Rilem technical committee 189-NEC [32] and the recommendations by Kollek (1989)[33]. The measurements were performed on concrete specimen of the size $\text{Ø}50 \times 75$ mm. The specimens were preconditioned for 2 weeks according to recommended procedures stated in Rilem technical committee 189-NEC [32] and the recommendations by Kollek (1989) [33] prior to the measurements. 2 specimens representative for each W/C-ratio and each degradation state were tested to ensure reproducibility of the results.

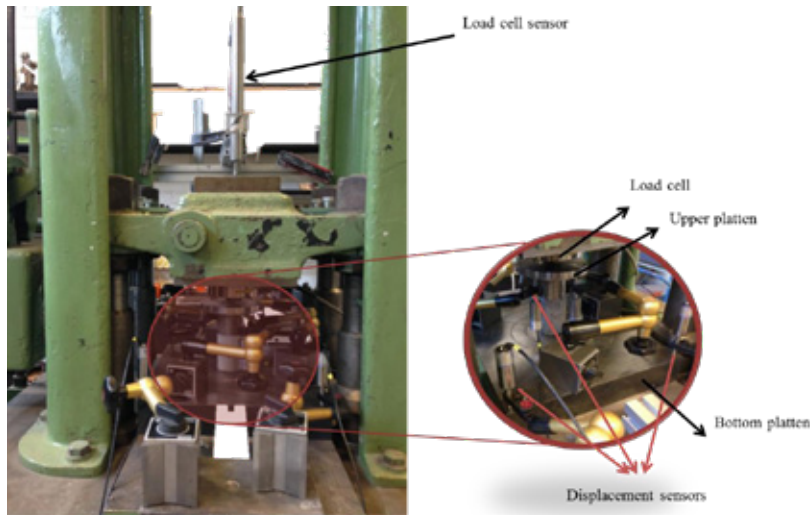


Figure 3. Instrumental setup concerning producing stress-strain curves

2.7 Rapid chloride migration test

The chloride diffusion coefficient of the pristine and leached specimens was studied by means of the rapid chloride migration test according to NT BUILD 492 and as described by Tang [27, 28]. It should be noted that in the case of the calcium depleted specimens owing to a reduced ionic concentration in pore solution compared to normal concrete specimens, adjusted shorter experimental duration was applied to these specimens. Moreover, due to a considerable increase in porosity of the calcium depleted concrete it is not easy to predict the proper test duration. In this study the test duration was set to 15 hours instead of 24 hours. However, chloride ions penetrated through the whole thickness of the specimens in this time duration. As a result the minimum chloride diffusion coefficient was calculated for the calcium depleted concrete specimens.

3 RESULTS AND DISCUSSIONS

3.1 Characterization of degraded specimens

In Figure 4, the Ca:Si ratio is plotted as a function of axial and radial position in the specimen and the number of days of leaching. In this figure it can be seen that leaching starts from the cathodic side of the specimen and propagates towards the anodic side. Considering the gradual changes in Ca:Si profile, the leaching develops towards a homogenized leaching level throughout the specimen (leached portlandite content).

The hypothesis regarding the preferential leaching of portlandite is investigated with XRD analysis. As shown in Figure 5. It is clearly shown that the portlandite peaks are dramatically reduced as compared to the pristine material. It should be noted that the ettringite peaks remain present in treated samples which, as discussed in part 2.2, should be due to low solubility of SO_3^{2-} ions as well as higher mobility of NO_3^- ions.

Figure 6 show SEM images of the pristine material and the leached specimens, respectively. As illustrated the aged samples show a higher porosity compared to the reference one. Moreover the detectable crystalline phases like portlandite, which are present in the reference sample, cannot be seen in the aged samples. The elemental composition of samples was analyzed and compared with the reference sample utilizing EDX method. The results are presented in Table 4, indicating a considerable lower Ca/Si in the aged sample compared to the reference sample. This is in good agreement with the LA-ICP-MS results.

Mercury Intrusion analysis results are presented in Figure 7. As shown the total porosity (cumulative pore volume) increased considerably for the degraded samples. As shown total pore volume of pores with sizes between 100-1000 nm increased whereas the total pore volume of pores with sizes between 1-100 nm decreased after leaching. The decrease in pore volume for smaller pores should be due to recrystallizations taking place during the leaching which might further dissolve after longer leaching time.

The changes in specific surface area of the aged samples as a function of pore distribution were studied by means of BET measurements. The results show that the pore area of the samples changes from 80 cm²/g to 160 cm²/g after degradation. As illustrated in Figure 8, the aged samples present a considerable higher N₂-adsorption and consequently a higher surface area than the reference samples. These results are in very good agreement with the results from mercury intrusion analysis presented in Figure 7.

Comparing the leaching depths in the specimens leached for 53 days (size Ø 50×75 mm) as shown in Figure 5, with the values reported in literature for natural leaching rates [4, 34-37] (leaching depth equal to 5-10 mm can be expected after up to 100 years and in 1000 years it is expected to be up to 8-20 mm), a considerable acceleration rate is demonstrated for presented method in this study. Moreover, The results are in good agreement with the pore distribution data from naturally leached samples as reported by Haga et al. [6] or reported results by Adondet and Buil [4] stating that total dissolution of portlandite content followed by progressive decalcification of CSH gel is expected in natural leaching process which was demonstrated to be similar for degraded samples in this study.

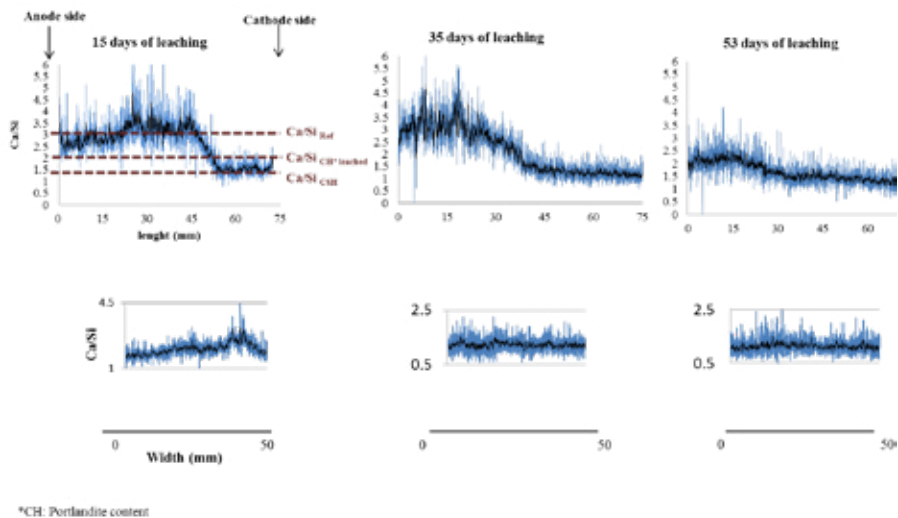


Figure 4. LA-ICP-MS analysis results

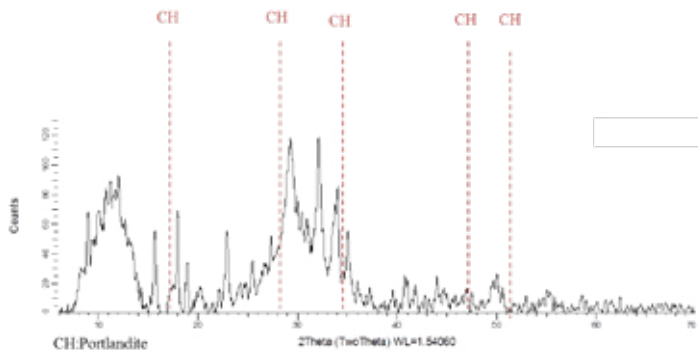


Figure 5. XRD analysis for degraded paste sample

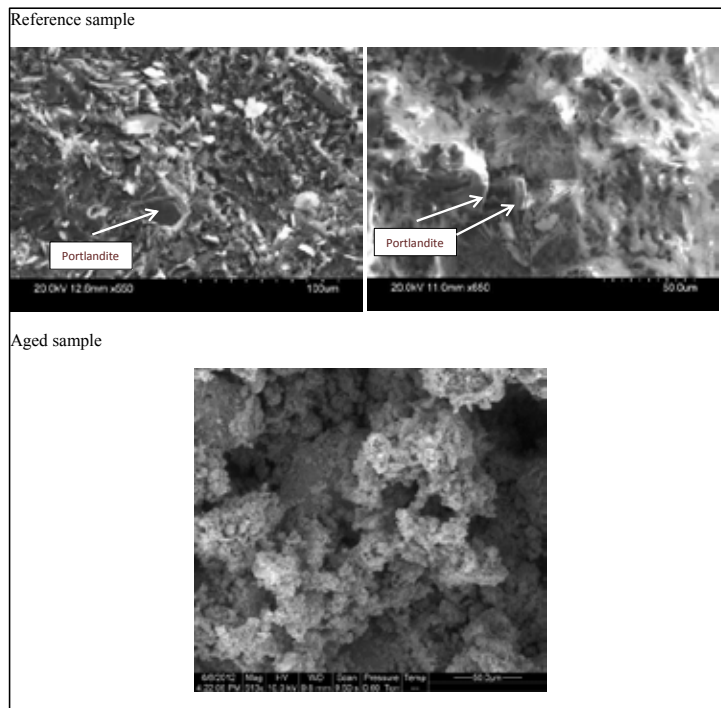


Figure 6. SEM analysis results

Table 4. EDX analysis results

Spectrum (% Atomic)		Al	Si	Ca	Fe
Reference	Mean	1.62	11.09	30.32	1.02
	Std. deviation	0.17	1.73	2.51	0.22
	Max.	1.8	13.14	33.08	1.37
	Min.	1.35	0.51	27.44	0.8
		Ca/Si : 2.73			
Aged	Mean	2.34	15.03	22.97	1.74
	Std. deviation	0.22	0.52	0.58	0.42
	Max.	2.97	15.91	24.28	2.91
	Min.	2.08	13.4	21.55	1
		Ca/Si : 1.52			

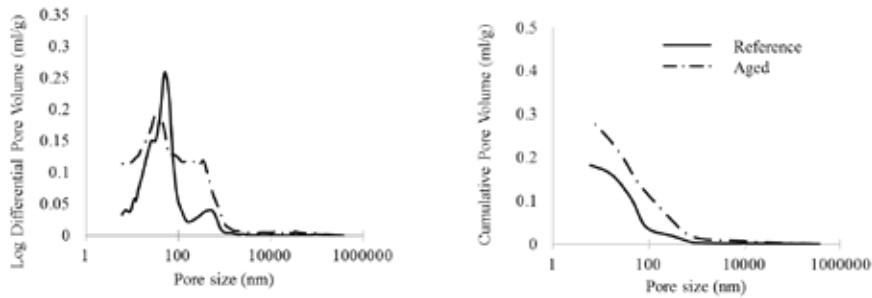


Figure 7. Mercury intrusion analysis results

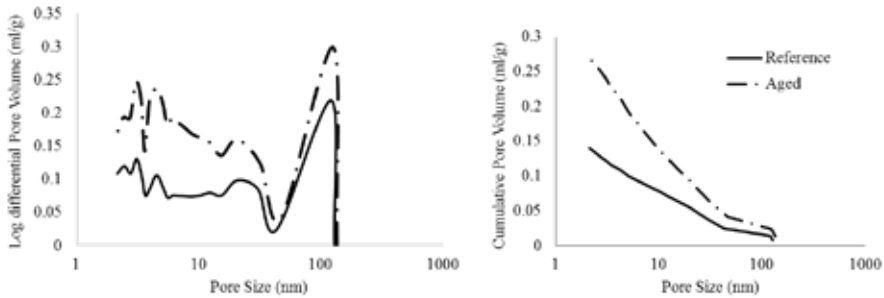


Figure 8. BET analysis results

3.2 Diffusion/Adsorption properties

As shown in Figure 9, the cement and CsCl mixtures reached equilibrium latest after 2 weeks. It is apparent from the figure that the free concentrations of cesium ions in the mixtures containing leached cement paste are considerably lower than the mixtures containing reference samples i.e., unleached specimens. This indicates a higher binding potential of aged cementitious materials, which has previously been reported by Ochs et.al [23].

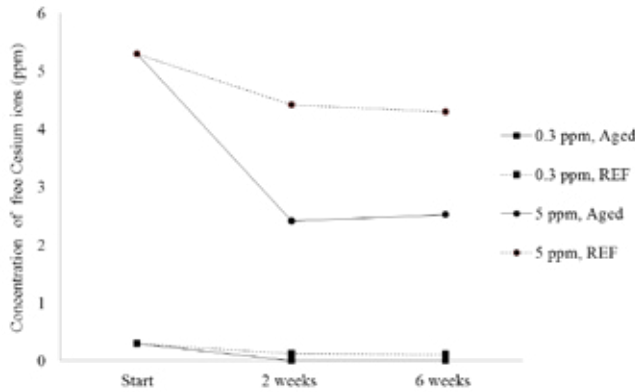


Figure 9. Adsorption test results

Figure 10, illustrates accumulated concentration of diffused ions in diffusion cell test as a function of time. As shown the diffusion rate is higher for all elements in the case of aged samples compared to the reference. Considering that decalcification changes the bulk density and the pore structure of the degraded cementitious materials, higher porosity in aged specimens reasonably causes a higher diffusion rate in these specimens.

Further, comparing plot (a) and (b) in Figure 10, it can be seen that the diffusion rate of Cs ions in the case of the aged sample is very close to diffusion rate of Na ions in plot (a), while it is considerably higher in plot (b). Considering higher mobility of Cs compared to Na ions, this can be due to adsorption/binding effect in the case of plot (a). However, a higher concentration gradient in the case of plot (b) overcomes this effect.

3.3 Mechanical properties

The results from the mechanical tests are presented in Table 5. As shown the average tensile strength (2 specimens for each W/C) for the specimens with a W/C ratio of 0.48 is reduced approximately up to 70 % due to calcium depletion whereas the reduction in tensile strength for the specimen with a W/C ratio of 0.62 is about 55%. Interestingly the residual tensile strength of the samples after degradation is similar in both water cement ratios, which indicates that although the different initial portlandite content in specimens would cause differences in strength properties, but similar residual strength can be predicted in specimens with different W/c ratios if leaching is propagated only up to leaching of portlandite content for all specimens. Moreover, the change in elastic modulus is also presented showing that the elastic modulus is reduced by 40% after leaching for both types of specimens.

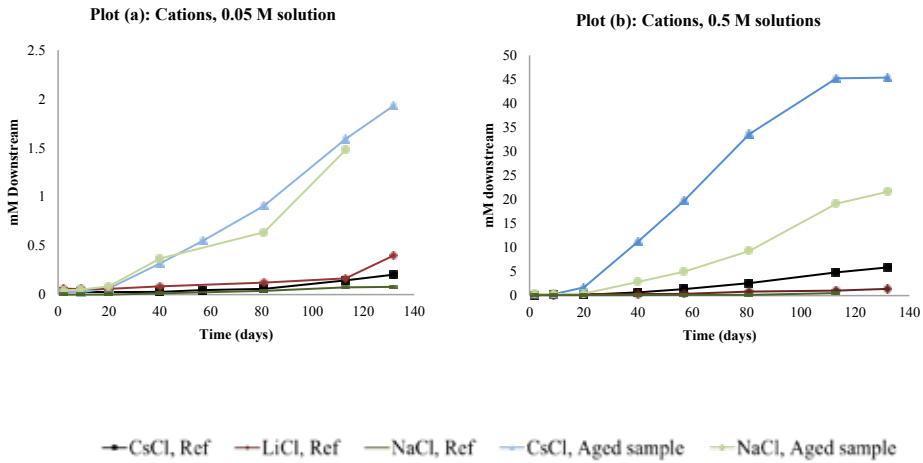


Figure 10. Diffusion cell test results

Table 5. Mechanical test results

	Tensile strength (MPa)			E-Modulus (GPa)		
	Ref	Aged	% Decrease	Ref	Aged	%Decrease
W/C=0.48	10	3	70	~ 50	~ 30	40
W/C=0.62	5.5	2.5	55			

3.4 Physical properties

Figure 11, illustrates the adsorbed water content as a function of time. As it can be seen up to 3-4 times of higher water adsorption rate for the calcium leached specimens is shown compared to pristine materials. The result indicate that a higher pore volume in calcium depleted samples which results mainly from dissolution of portlandite content has a detrimental influence on strength properties of cementitious materials [6, 8, 22].

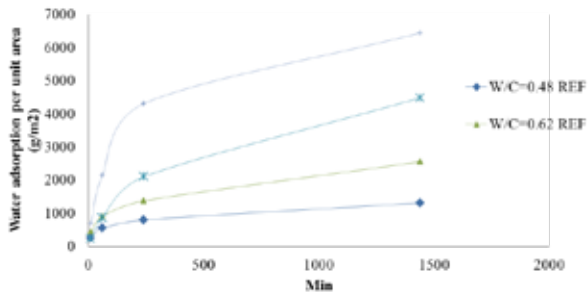


Figure 11. Capillary adsorption of water

Furthermore, the changes in gas permeability coefficient of the concrete due to degradation are presented in Figure 12, indicating up to 15 times of increase in gas permeability as a result of depletion in calcium.

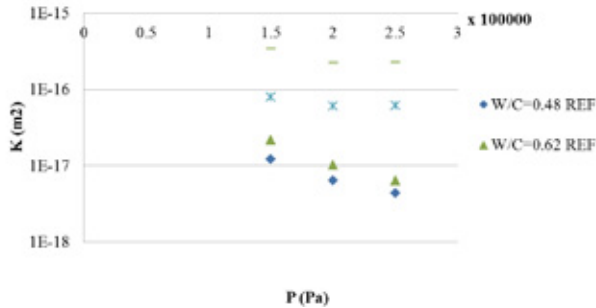


Figure 12. Gas permeability test results

Finally, the changes in chloride diffusion coefficient of the concrete samples due to degradation are presented in Figure 12. As it can be seen up to at least 70% increase in chloride diffusion coefficient is expected after calcium depletion. It should be noted that the presented results regarding the calcium depleted specimens are the minimum chloride diffusion coefficient owing to the full penetration through the specimen thickness as it was pointed out previously. The results are in good agreement with the presented results by Choi et al. (2013) [16].

Table 6. Rapid Chloride Migration test results

Average Chloride diffusion coefficient ($\times 10^{-12}$)		
	Ref	Aged
W/C=0.48	~28	>110
W/C=0.62	~51	>132

4 CONCLUSIONS

A newly developed acceleration method with the flexibility of producing decalcified cementitious specimens with different sizes suitable for further testing methods was presented. Electro-chemical migration method enhances ageing of cementitious materials with a rate far higher than natural leaching. The ageing function can be controlled and the sample size is flexible. Any acceleration method may involve some processes which may not be present in the natural situation. However, considering the changes in mineralogical, physical, chemical and mechanical properties of aged material is of high importance in order to show the comparability as well as to build up a better base for further numerical situations. One of the direct applications of this study is to provide experimental approaches to be able to supply databases in order to validate the risk assessment analyses regarding the functionality of engineered cementitious barriers. Based on the results presented in this study the following conclusions can be drawn:

- Leaching of portlandite from concrete followed by gradual degradation in CSH gel can be demonstrated by utilizing electrochemical migration method.

- The aged samples exhibit a higher binding potential for Cs ions. It was found that the specific surface area of aged samples was increased by up to 50%, which might be the reason to the enhanced adsorption of Cs^+ ions compared with the pristine material.
- The pore volume was increased by up to 40-50% after decalcification, which cause considerable increase in ionic diffusion rate of aged samples compared with pristine materials.
- Calcium depletion for sample with $\text{W/C}=0.48$ will lead to Up to 70% of increase in capillary water adsorption whilst 55% of increase is predicted for the case of $\text{W/C}=0.62$.
- Decalcification decreases the tensile strength and this reduction is proportional to the change in pore volume: 70% for $\text{W/C}=0.48$ and 55% for $\text{W/C}=0.62$.
- Up to at least 35% of decrease in E modulus is concluded whilst compressive strength at failure is shown to be reduced up to 50%.
- The gas permeability is shown to be increased up to 90% and at least up to 10 times higher water permeability is expected.
- The chloride diffusion coefficient is shown to increase at least up to 70%.

REFERENCES

1. Berner, U.R., *Evolution of pore water chemistry during degradation of cement in a radioactive waste repository environment*. Waste Management, 1992. **12**(2–3): p. 201-219.
2. Reardon, E.J., *Problems and approaches to the prediction of the chemical composition in cement/water systems*. Waste Management, 1992. **12**(2–3): p. 221-239.
3. Hinsenveld, M., *A Shrinkage Core Model as a Fundamental Representation of Leaching Mechanism in Cement Stabilized Waste*, Doctoral Thesis. 1992: Department of Civil and Environmental Engineering, University of Cincinnati, Cincinnati, OH.
4. Adenot, F. and M. Buil, *Modelling of the corrosion of the cement paste by deionized water*. Cement and Concrete Research, 1992. **22**(2–3): p. 489-496.
5. Faucon, P., et al., *Long-term behaviour of cement pastes used for nuclear waste disposal: review of physico-chemical mechanisms of water degradation*. Cement and Concrete Research, 1998. **28**(6): p. 847-857.
6. Haga, K., et al., *Effects of porosity on leaching of Ca from hardened ordinary Portland cement paste*. Cement and Concrete Research, 2005. **35**(9): p. 1764-1775.
7. Faucon, P., et al., *Leaching of cement: Study of the surface layer*. Cement and Concrete Research, 1996. **26**(11): p. 1707-1715.
8. Mainguy, M., et al., *Modelling of leaching in pure cement paste and mortar*. Cement and Concrete Research, 2000. **30**(1): p. 83-90.
9. Maltais, Y., E. Samson, and J. Marchand, *Predicting the durability of Portland cement systems in aggressive environments—Laboratory validation*. Cement and Concrete Research, 2004. **34**(9): p. 1579-1589.
10. Ryu, J.-S., N. Otsuki, and H. Minagawa, *Long-term forecast of Ca leaching from mortar and associated degeneration*. Cement and Concrete Research, 2002. **32**(10): p. 1539-1544.
11. Saito, H., et al., *Preliminary experimental study on the deterioration of cementitious materials by an acceleration method*. Nuclear Engineering and Design, 1992. **138**(2): p. 151-155.
12. Wittmann, F.H., *Corrosion of Cement-Based Materials under the Influence of an Electric Field*. Materials Science Forum, 1997. **247**: p. 107-126.

13. Carde, C. and R. François, *Effect of the leaching of calcium hydroxide from cement paste on mechanical and physical properties*. Cement and Concrete Research, 1997. **27**(4): p. 539-550.
14. Heukamp, F.H., F.J. Ulm, and J.T. Germaine, *Mechanical properties of calcium-leached cement pastes: Triaxial stress states and the influence of the pore pressures*. Cement and Concrete Research, 2001. **31**(5): p. 767-774.
15. Revertegat, E., C. Richet, and P. Gégout, *Effect of pH on the durability of cement pastes*. Cement and Concrete Research, 1992. **22**(2-3): p. 259-272.
16. Choi, Y.S. and E.I. Yang, *Effect of calcium leaching on the pore structure, strength, and chloride penetration resistance in concrete specimens*. Nuclear Engineering and Design, 2013. **259**(0): p. 126-136.
17. Nguyen, V.H., et al., *Chemo-mechanical coupling behaviour of leached concrete: Part I: Experimental results*. Nuclear Engineering and Design, 2007. **237**(20-21): p. 2083-2089.
18. Sellier, A., et al., *Behavior of HPC nuclear waste disposal structures in leaching environment*. Nuclear Engineering and Design, 2011. **241**(1): p. 402-414.
19. Marinoni, N., et al., *Long-term leaching test in concretes: An X-ray powder diffraction study*. Cement and Concrete Composites, 2008. **30**(8): p. 700-705.
20. Ulm, F.-J., E. Lemarchand, and F.H. Heukamp, *Elements of chemomechanics of calcium leaching of cement-based materials at different scales*. Engineering Fracture Mechanics, 2003. **70**(7-8): p. 871-889.
21. Saito, H. and A. Deguchi, *Leaching tests on different mortars using accelerated electrochemical method*. Cement and Concrete Research, 2000. **30**(11): p. 1815-1825.
22. Carde, C., R. François, and J.-M. Torrenti, *Leaching of both calcium hydroxide and C-S-H from cement paste: Modeling the mechanical behavior*. Cement and Concrete Research, 1996. **26**(8): p. 1257-1268.
23. Ochs, M., I. Pointeau, and E. Giffaut, *Caesium sorption by hydrated cement as a function of degradation state: Experiments and modelling*. Waste Management, 2006. **26**(7): p. 725-732.
24. Emborg, M., J.-E. Jonasson, and S. Knutsson, *Långtidsstabilitet till följd av frysning och tining av betong och bentonit vid förvaring av låg- och medelaktivt kärnavfall i SFR I*. 2007, Swedish Nuclear and Waste Management Company
25. Höglund, L.-O., *Project SAFE: Modeling of long-term concrete degradation processes in the Swedish SFR repository*. 2001, SKB Report: Svensk Kärnbränslehantering AB.
26. Emborg, M., J.-E. Johansson, and S. Knutsson, *Långtidsstabilitet till följd av frysning och tining av betong och bentonit vid förvaring av låg- och medelaktivt kärnavfall i SFR I*. 2007, SKB Report: Svensk Kärnbränslehantering AB.
27. Tang, L., *Electrically accelerated methods for determining chloride diffusivity in concrete - Current development*. Magazine of Concrete Research, 1996. **48**(3): p. 173-179.
28. NT BUILD 492, *Concrete, Mortar and Cement-based Repair Materials: Chloride Migration Coefficient from Non-steady-state Migration Experiments*. 1999: Nordtest, Esbo, Finland
29. Babaahmadi, A., et al., *Characterization of Cement Paste Subjected to Accelerated Decalcification by an Electro-Chemical Method*. Submitted to Cement and Concrete Research, 2014.
30. Abbas, Z., E. Ahlberg, and S. Nordholm, *Monte Carlo Simulations of Salt Solutions: Exploring the Validity of Primitive Models*. The Journal of Physical Chemistry B, 2009. **113**(17): p. 5905-5916.
31. Page, C.L. and Ø. Vennesland, *Pore solution composition and chloride binding capacity of silica-fume cement pastes*. Matériaux et Construction, 1983. **16**(1): p. 19-25.

32. *Non-Destructive Evaluation of the Penetrability and Thickness of the Concrete Cover - State-of-the-Art Report of RILEM Technical Committee 189-NEC*. 2007.
33. Kollek, J.J., *The determination of the permeability of concrete to oxygen by the Cembureau method—a recommendation*. Materials and Structures, 1989. **22**(3): p. 225-230.
34. Lagerblad, B., *Leaching Performance of Concrete Based on Studies of Sample from Old Concrete Constructions* 2001, Swedish Nuclear Fuel and Waste Management
35. Romben, L., *Aspects on testing methods for acid attack on concrete*. 1978, Swedish Cement and Concrete Institute.
36. Romben, L., *Aspects on testing methods for acid attack on concrete-further experiments*. 1979, Swedish Cement and Concrete Institute.
37. Trägårdh, J. and B. Lagerblad, *Leaching of 90-year old concrete in contact with stagnant water*. 1998, Swedish Nuclear fuel and Waste management.

Research Council and Editorial Board for Nordic Concrete Research

Prof. Dr. Olafur H. Wallevik, Chairman for the Research Council

Dr. Dirch H. Bager, Editor of Nordic Concrete Research

**Danish
Concrete
Association**

Dr. Dirch H. Bager
Lavendelparken 5
DK - 9310 Vodskov
Tel: +45 9829 2412
Mobile: +45 2049 7324
E-mail: dirch.bager@bbnpost.dk

Mr. Claus Pade
Concrete Centre,
Danish Technological Institute
Gregersensvej
DK - 2630 Taastrup
Tel: + 45 7220 2183
E-mail: cpa@teknologisk.dk

**Finnish
Concrete
Association**

Mr. Juha Valjus
Concrete Association of Finland
Unioninkatu 14 PL 381
FI - 00131 Helsinki
Tel: +358 41 533 6020
Mobile: +358
E-mail: juha.valjus@betoniyhdistys.fi

Lic.Sc.Tech. Klaus Juvas
Consolis Technology
Box 72
FI - 21291 Rusko
Mobile: +358 40 5160 316
E-mail: klaus.juvas@consolis.com

**Icelandic
Concrete
Association**

Dr. Jón E. Wallevik
Innovation Center Iceland
IS - 112 Keldnaholti
Tel: +354 522 9362
Mobile: +354
Fax: +354 522 9111
E-mail: jon.w@nmi.is

Prof. Dr. Olafur H. Wallevik
Innovation Center Iceland
IS - 112 Keldnaholti
Tel: +354 522 9000
Mobile: +354
E-mail: wallevik@ru.is

**Norwegian
Concrete
Association**

Dr. Terje F. Rønning
Heidelberg Cement NE / Cement
Product development & Implementation
P.O.Box 38
N - 3991 Brevik
Tel.: +47 3557 2347
Mobile: +47 9157 6046
E-mail: terje.ronning@norcem.no

Prof. Dr. Mette R. Geiker
Division of Concrete Structures
Department of Civil Engineering
N - 7034 Trondheim
Tel: +47 7359 4529
Mobile: +47
E-mail: mette.geiker@ntnu.no

**Swedish
Concrete
Association**

Adjunct. Prof., Tekn.Dr. Mikael Hallgren
Tyréns AB
Peter Myndes Backe 16
SE - 118 86 Stockholm
Tel: +46 104 522 351
Mobile: +46 70 661 05 33
E-mail: Mikael.Hallgren@tyrens.se

Tekn. Dr. Peter Utgenannt
CBI Swedish Cement and Concrete Research
Institute
P.O. Box 857
SE - 501 15 Borås
Tel: +46 105 166 870
Mobile: +46 706 452 008
E-mail: peter.utgenannt@cbi.se

18 November 2013

Active reviewers for Nordic Concrete Research as per December 2013

DENMARK	
Dr.	Dirch H. Bager
Dr.	Mette Glavind
Prof., Dr.	Per Goltermann
Mr.	Oscar Klinghoffer
Prof., Dr.	John Forbes Olesen
Mr	Claus Pade
Prof., Dr.	Eigil V. Sørensen
Prof., Dr.	Jens Peder Ulfkjær
FINLAND	
Dr.	Klaus Juvas
Dr.	Matti V. Leskala
Prof., Dr.	Jussi Mattila
Dr.	Jouni Punkki
Mr	Juha Valjus
ICELAND	
Mr.	Einar Einarsson
Mr.	Haukur J. Eiriksson
Dr.	Gisli Gudmundsson
Mr.	Karsten Iversen
Mr.	Torfi G. Sigurdsson
Mr.	Sveinbjörn Sveinbjörnsson
Dr.	Jon E. Wallevik
Prof., Dr.	Ólafur H. Wallevik
Prof., Dr.	Børge J. Wigum
NORWAY	
Dr.	Helge Brå
Ms.	Danielle Bosnjak
Mr.	Anton Gjørven
Mr.	Steinar Helland
Dr.	Bernt Jacobsen
Prof., Dr.	Terje Kanstad
Dr.	Terje F. Rønning
Mr.	Tor Kristian Sandaker
Mr.	Sverre Smeplass
Mr.	Hans Stemland
SWEDEN	
Prof., Dr.	Anders Ansell
Dr.	Thomas Blanksvärd
Prof.	Lennart Elfgren
Prof., Dr.	Mats Emborg
Prof., Dr.	Kent Gylltoft
Prof., Dr.	Mikael Hallgren
Prof., Dr.	Jan-Erik Jonasson
Prof., Dr.	Björn Lagerblad
Prof., Dr.	Karin Lundgren
Prof., Dr.	Tang Luping
Prof., Dr.	Per-Erik Petersson
Prof., Dr.	Johan Silfwerbrand
Dr.	Peter Utgenannt

